US LHC Technical Design Handbook

Table of Contents

I Introduction

This US LHC Technical Design Handbook describes the work being done by a collaboration of three US National Laboratories -- Brookhaven National Laboratory, Fermi National Accelerator Laboratory, and Lawrence Berkeley National Laboratory -- in support of the construction of the Large Hadron Collider (LHC) at the European Organization for Nuclear Research (CERN). The US contribution to the LHC accelerator is a subproject of the overall construction project and it is referred to as the US LHC Accelerator Project. The LHC consists of an accelerator and storage ring with two counter-rotating proton beams, each with an energy of up to 7 TeV. These beams collide in four interaction regions (IRs), where much of the work and deliverables from the US LHC Accelerator Project are focused. The LHC is fed by an existing chain of proton synchrotrons and will be constructed in the existing tunnel for the Large Electron-Positron (LEP) accelerator. US physicists are also important collaborators on the two LHC experiments that will explore physics up to the TeV mass scale, and the US contribution to the construction of the LHC accelerator will shorten the time required to bring the accelerator into operation. Furthermore, involvement in the US LHC Accelerator Project will provide an opportunity for the US National Laboratories to take part in forefront hadron collider research and to build the global cooperation that will be necessary to construct future colliders beyond the LHC.

The major thrust of the US LHC Accelerator Project focuses on the interaction regions and the RF straight section of the LHC accelerator. This involves the design, fabrication and integration of the specialized components required to provide adequate beam handling in these regions, especially the superconducting magnets. The US Laboratory Collaboration is responsible for the providing CERN with integrated inner triplet magnet systems for the four interaction regions at points 1, 2, 5 and 8. The Collaboration will design and build the front absorbers and neutral beam dumps, that are required at points 1 and 5. In the RF straight section at point 4, the US Laboratory Collaboration will provide specialized magnets and collaborate with CERN on the integration of these magnets into this region.

In addition to building these magnet systems, the US Laboratories will help CERN in the design and construction of LHC by providing technical support in several areas. The US Laboratories will participate in the R&D and perform production testing of the superconducting wire and cable in order to characterize it for use in the main LHC magnets. The US Laboratory Collaboration will also work with CERN on a number of special accelerator physics topics of mutual interest, which are focussed primarily, but not exclusively, on issues related to the US-provided hardware.

The Technical Design Handbook presents detailed descriptions of the hardware systems and technical support provided by the U.S. Laboratory Collaboration, including detailed requirements and specifications, detailed descriptions of the designs of hardware systems and of the technical support work to be carried out, and of the supporting R&D programs. It is the primary vehicle by which the specifications and requirements and the technical implementations are documented and approved by CERN. It is a controlled document of the US Project requiring approval of its initial contents and of any changes through the change control mechanism specified in the US LHC Accelerator Project Management Plan. Each chapter, corresponding to one major equipment item or task, is a separately controlled document, whose initial contents and any changes thereto must be approved by the LHC Project Leader and the official CERN contact person(s) for that task.

II Technical Systems

II.1 Interaction Regions

The U.S. Laboratory Collaboration is responsible for providing CERN with integrated inner triplet magnet systems for the four interaction regions (IRs) at points 1, 2, 5 and 8. The US Collaboration will design, develop and fabricate half of the high gradient quadrupoles that make up the final focus system, the other half being provided the KEK Laboratory in Japan. The US Laboratories will develop and build cryostats for all of the quadrupoles, and assemble U.S.-built and KEK-built quadrupoles together with correction coils and beam and cryogenic instrumentation provided by CERN into complete cryostatted systems. The US Collaboration will design and fabrication of the cryogenic feed boxes which provide interface between the superconducting magnet system and the CERN cryogenics, DC power distribution and instrumentation systems. In addition, the U.S. Laboratories will design and build the front absorbers and neutral beam absorbers, which are required at points 1 and 5. The U.S. Laboratories will have design responsibility, subject to CERN oversight and approval, of the inner triplet quadrupole system, including the assembly with CERN provided equipment, and the corresponding feed boxes.

The US and KEK built quadrupoles are built to the specifications with respect to gradient, magnetic and physical lengths, and field quality, but differ in diameter and operating current. Thus quadrupoles all of one type will be used in one interaction region. CERN has responsibility for ensuring that the KEK-provided quadrupoles meet their specifications and for the delivery of them to the US Laboratories for assembly. The KEK-provided magnets will be delivered to the US Collaboration after a full set of acceptance tests have been performed, and the responsibility of the US Laboratories will be limited to assembling them into their cryostats and measuring the position of their magnetic axes with respect to external fiducials. This document provides a detailed description of the quadrupole design chosen by the US Laboratory Collaboration and of the conceptual design of the cryostat and IR cooling system which will accommodate both the US- and KEK-provided magnets.

Fig. II.1.2-1 is an illustration of an assembled LHC interaction region inner “triplet.” Each inner triplet consists of four cold mass assemblies, three multipole correctors, two beam position monitors, and supplementary heat absorbers. The overall length of each triplet is approximately 30 m, not including the feed box.

The four superconducting quadrupoles in each triplet are named (starting at the interaction point) Q1, Q2a, Q2b, and Q3. The magnetic lengths are 6.3 m for Q1 and Q3, 5.5 m for Q2a and Q2b. It is currently thought that quadrupoles Q1 and Q3 will each be assembled into separate vacuum vessels and that Q2a, Q2b, and two multipole correctors will be assembled into a single cold mass and a single vacuum vessel for a total of three distinct cryostats. These three individual cryostats will be joined using welded connections to form the complete inner triplet.

Fig. II.1.2-2 shows a typical cross section through any of the inner triplet quadrupoles at a cold mass support location. Each cold mass is supported at two places along its length by top-mounted supports oriented at ±45° from the cold mass centerline. Using two supports produces a much more rigid cold mass mounting system than one that uses a single support and may be an advantage in trying to meet the stringent alignment requirements for interaction region magnets. Also, supports mounted as shown in Fig. II.1.2-2 provide sufficient radial clearance for the external He II heat exchanger and 1.8 K saturated He II supply tube or a pump line. One of the two support locations per cold mass assembly will serve as the axial anchor. The other will have a sliding interface between the support and cold mass to allow for thermal contraction during cooldown.

{where's figure?}

Fig. II.1.2-1. LHC interaction region triplet layout.

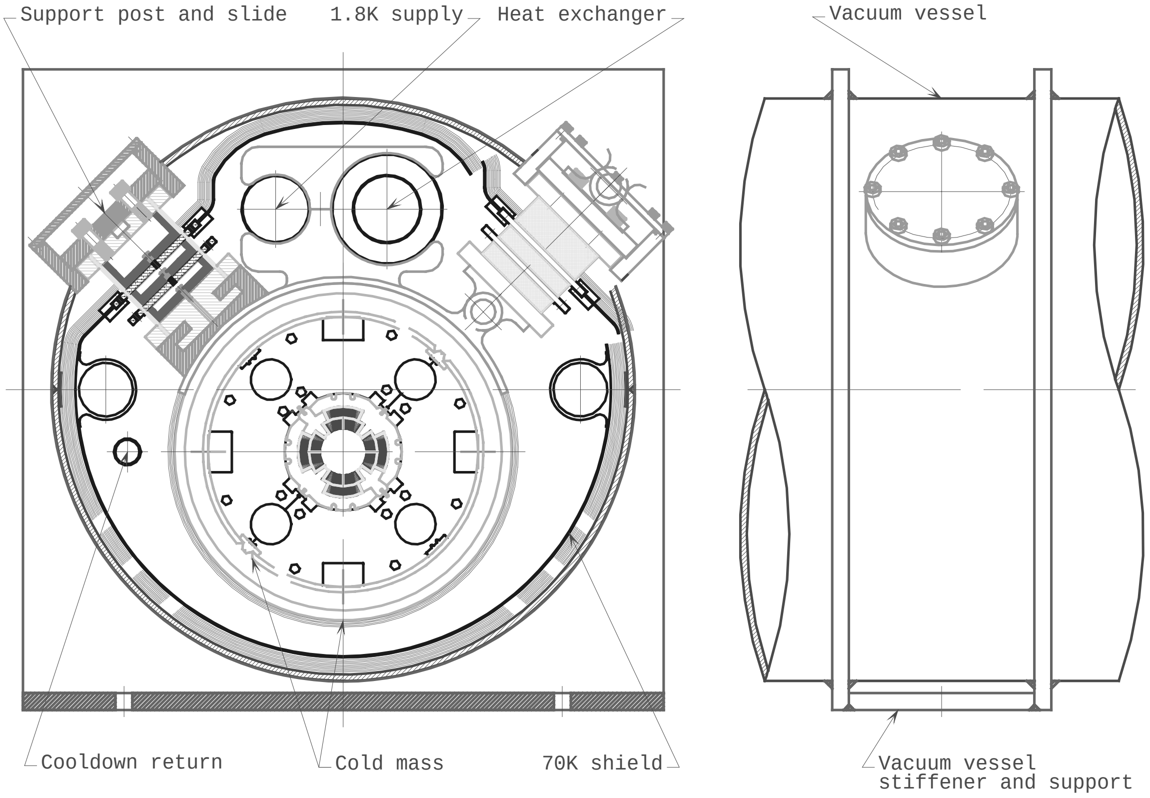

Fig. II.1.2-2. LHC interaction region quadrupole cryostat cross section.

The internal cold mass supports are coincident with the external vacuum vessel support rings. These support rings stiffen the vacuum vessel at the cold mass support points and serve as the interface between the vacuum vessel and the tunnel mounted support and alignment hardware. In the current conceptual design, the vacuum vessel is 864 mm outside diameter.

Ambient thermal radiation is intercepted by blankets of multilayer reflective insulation (MLI) immediately inboard of the inner vacuum vessel surface and by a 50-75 K helium cooled thermal shield. There is an additional MLI blanket on the cold mass.

There are two different outer diameters for the quadrupole cold mass helium vessels. Those being fabricated at KEK are 510 mm diameter while those being fabricated at Fermilab are 416 mm diameter. The current plan is to use an adapter on the Fermilab assemblies to increase their diameter at the cold mass attachment locations so that all cryostats will be identical regardless of the cold mass manufacturer. Each individual inner triplet uses cold masses with a single diameter, i.e. either all KEK or all Fermilab cold masses due to their having different operating currents. Fig. II.1.2-2 shows both cold mass diameters for reference.

A detailed description of the LHC cryogenic system is beyond the scope of this report but can be found elsewhere in the literature [1, 2]. With one exception, the cryogenic plants are installed at four points equally spaced around the LHC machine, and the refrigeration power is transported over a length of a 3.3 km octant by a separated cryogenic distribution line.

The inner triplet quadrupole magnets are cooled in static baths of pressurized He II at 1.9 K. The heat load is transported from pressurized He II to the flowing, saturated two-phase He II at 1.8K via a He II heat exchanger. This heat exchanger will be placed either inside of the cold mass, like for the LHC arc dipoles, or alongside of the cold mass in the cryostats.

The thermal design requirements and heat loads at various temperatures are listed in Table II.1-1. A thermal shield at 50 to 75 K is required to minimize the static thermal conduction and radiation heat loads.

Table II.1-1: Inner triplet heat loads vs. temperature

Temperature levels	*50 to 75 K*	*4.5 to 20 K*	*1.9 K*
Static heat loads (W)	170.7	3.2	10.0
Dynamic heat loads nominal (W)	0	0	146.5
Total heat loads (W)	170.7	3.2	156.5

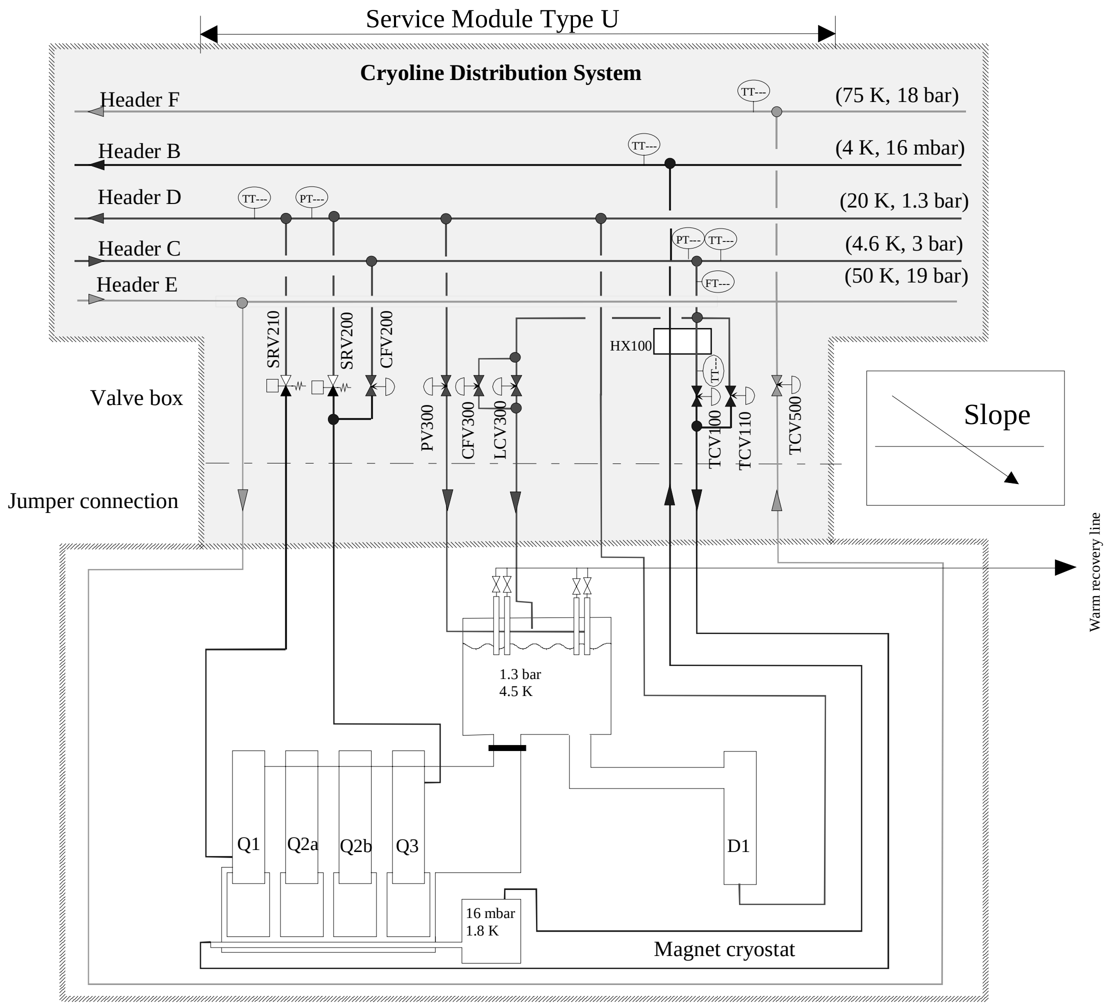

Fig. II.1.2-3. Simplified low schematic of cryogenic system for the LHC IR inner triplet (from CERN).

Fig. II.1.2-3 shows a simplified flow schematic (from CERN) of the cryogenic system for the inner triplet with an external He II heat exchanger design. The refrigeration power is transported by the cryogenic distribution line over a length of 3.3 km and is available for the inner triplet magnets in a standard way, like many parallel cells in the octants. Supercritical helium (3 bar and 4.5 K) from the sector refrigerator, distributed through Line C, is cooled within the counterflow heat exchanger by the returning low pressure cold helium vapor to 2.2 K and expanded through a J-T valve. The saturated helium flows through the copper heat exchanger tube, absorbing heat and gradually vaporizing as it flows. After heat exchange with the incoming supercritical helium in the counterflow heat exchanger, the low pressure helium vapor is pumped away via Line B. Line D, maintained at 20 K and slightly above atmospheric pressure, collects the helium discharged from the magnets during a quench and also provides cooling for the high-temperature superconductor current leads. Lines E and F circulate high pressure helium gas to cool the thermal radiation shield and cold mass support post intercept.

Fig. II.1.2-4 presents a detailed schematic of the cryogenic system for the inner triplet on one side of interaction point in which the feed box is located in the lower position. The cryogenic system for the inner triplet located on the other side of the interaction point is identical except the feed box is now on the higher position, so a pumping line is connected to the lower end of the He II heat exchanger to pump the helium vapor. The pumping line will replace the location of saturated helium supply tube in Fig. II.1.2-5.

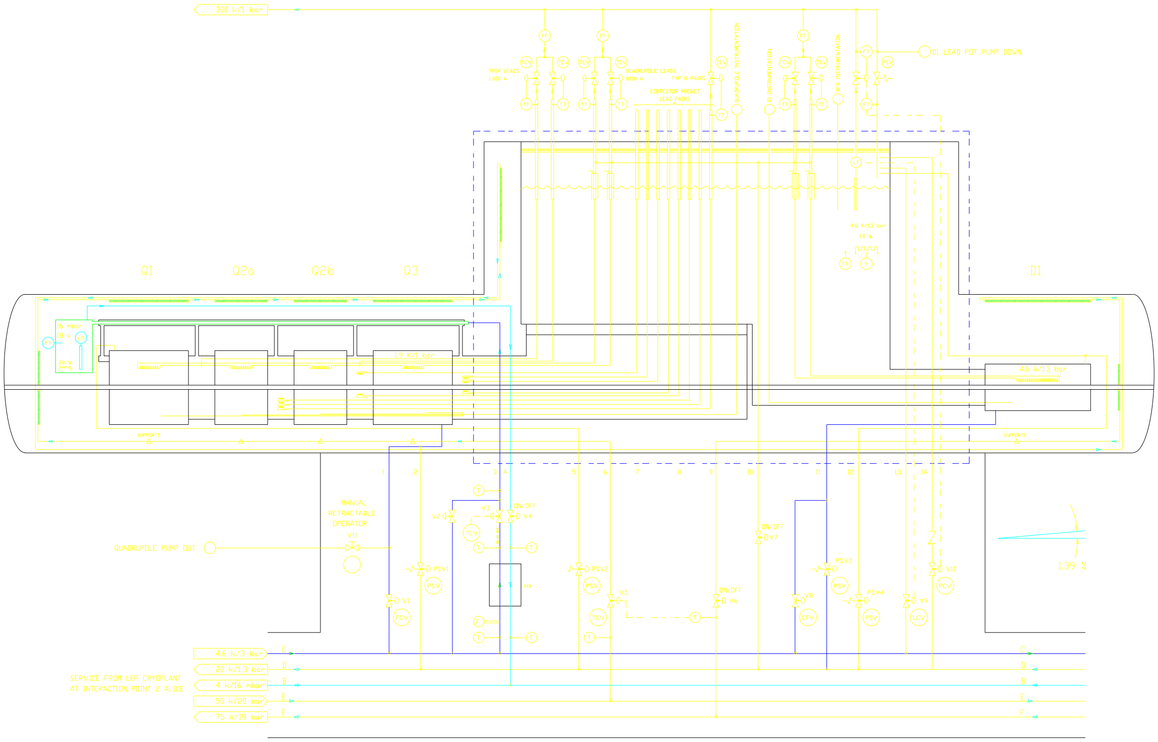

Fig. II.1.2-4. Flow schematic of cryogenic system for the LHC IR inner triplet.

The He II heat exchanger is a key component in the successful cooling of the inner triplets. The main function of He II heat exchanger is to extract both dynamic and static heat loads from the cold mass and maintain its temperature below 1.9 K during normal operation. The total temperature difference from the pressurized helium II around the cables to the saturated helium II at the DFB includes the following: the temperature drop within the pressurized He II from the cable to cooling holes in the iron yoke, the heat transport within the pressurized He II in the iron yoke out to the heat exchanger, the Kapitza thermal resistance on both sides of the heat exchanger, the thermal resistance through the heat exchanger wall, and pressure drop caused by the saturated, two-phase He II flow within the heat exchanger pipe. The thermal analysis results are summarized in the Table II.1-3.

Table II.1-3: Temperature differences from the pressurized helium II around the coils to the saturated helium II at the DFB for different situations.

Heat load (W)	*Liquid fraction (%)*	*Mass flow rate (g/s)*	*Interconnect dia (mm)*	*Total delta-T (mK)*
156.5	82.1 (expand from 3 bar, 2.2 K)	8.3	84.68 (3 IPS sch 5)	50.9
156.5	53.17 (expand from 3 bar, 4.5 K)	12.8	84.68	64.5
156.5	82.1	8.3	97.38 (3 ½ IPS sch 5)	42.6
156.5	53.17	12.8	97.38	56.2
234.8 (1.5 times above)	82.1	12.43	84.68	111.3
234.8	53.17	19.2	84.68	143.4
234.8	82.1	12.43	97.38	83.5
234.8	53.17	19.2	97.38	115.6

II.1.1.1.1.1 References

[1] The LHC Study Group, “The Large Hadron Collider,” *CERN/AC/95-05 (LHC)*, 20 October, 1995.

[2] Ph. Lebrun, “Superfluid Helium Cryogenics for the Large Hadron Collider Project at CERN,” *Cryogenics 34, ICEC Supplement* (1994), p. 1.

II.1.2 IR Quads

II.1.2.1 Introduction

The final focus in the low-β insertions is provided by inner quadrupole triplets together with four-quadrupole matching sections. The schematic layout of the LHC low-β triplet is shown in Fig. II.1.2.1-1. The low-β triplet optics and layout are described in Refs. [3 - 6]. It consists of four large aperture superconducting quadrupoles connected in a series and powered by a common power supply. The outer two quadrupoles, Q1 and Q3, are 6.3 m long, while the central one is divided into two identical units, Q2a and Q2b, each 5.5 m long. The inner triplet is protected from secondary particles by 1.8 m long copper absorber (TAS), located within the front shielding of the experiments.

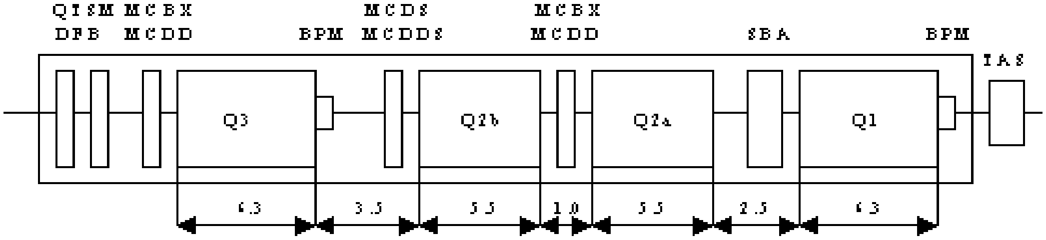

Fig. II.1.2.1-1. Schematic layout of the LHC low-β triplet.

The protection of the superconducting quadrupoles against the high flux of secondary particles emanating from the p-p collisions at nominal luminosity of 10^{34} $cm^{-2}s^{-1}$ at 7 TeV beam energy is an important issue in the design of the low-β triplets. The radiation induced heat depositions and magnet protection in the inner triplets have been studied by several groups [7, 8]. It has been found that Q2a, in which the radiation power density is the highest, can be better protected by optimizing its distance from Q1. Based on these studies, the separation between Q1-Q2a has been set to 2.5 m, sufficient for a approximately 1.5-m long supplementary beam absorber (SBA). Protection of the triplet as a whole will be further improved by optimizing the thickness of the quadrupole cold bore [9].

The 1 m space between Q2a and Q2b is reserved for the combined horizontal-vertical orbit corrector [6]. In this location the β-function has a maximum in one plane, while the maximum in the orthogonal plane occurs upstream of Q3, where an additional orbit corrector is envisaged. The space between Q2b and Q3 is used to adjust the optics of the single parameter low-β triplet to that of the matching section. The resulting drift of 3.5 m is slightly longer than otherwise needed for magnet interconnections, a beam position monitor (BMP) and multipole spool pieces.

The quadrupoles Q1-Q3 are single aperture superconducting magnets with a large cold bore [3]. Besides accommodating two fully separated beams at injection, they must provide a high field gradient and low multipole errors required for the colliding beams, and sustain high power density of the secondary particles. The required parameters and operating conditions for LHC low-β quadrupole are summarized in Table II.1.2.1-1.

Table II.1.2.1-1 Parameters of the LHC low-β quadrupole (requirements and operating conditions).

Parameter	*Unit*	*Value*
Nominal field gradient	T/m	200/210
Magnetic length	m	6.3/5.5
Inner coil diameter	mm	70
Peak beam-induced heat load	mW/g	1.2
Operating temperature	K	1.9

The nominal field gradient of 200 T/m is required for the high luminosity interaction regions. For the low luminosity IRs the nominal field gradient is slightly higher, 210 T/m, but the operational margins (critical temperature and critical current) could be lower because of much lower level of the beam induced heat deposition in these regions. Based on the above mentioned and cost reduction considerations, the same HGQ designed for the high luminosity IR will be used for the low luminosity IR.

To provide the required luminosity in the interaction point the high field quality in the quadrupole magnets has to be achieved. The preliminary field quality specifications for the inner triplet quadrupoles, formulated based on the first results of the dynamic aperture study and field quality analysis in the large aperture SC quadrupoles [10], are summarized in Table II.1.2.1-2 and Table II.1.2.1-3. Field quality requirements are imposed for all quadrupoles in form of systematic values (b_n, a_n), uncertainties in the systematic values (Δb_n, Δa_n) and random RMS spreads (σb_n, σa_n), where b_n and a_n are normalized to the main field component normal and skew harmonic coefficients (for b_n and a_n definitions see also §II.1.2.4).

Table II.1.2.1-2. Systematic errors and uncertainty at 1 cm reference radius (in 10^{-4} units of main field).

n	*3*	*4*	*5*	*6*	*7*	*8*	*9*	*10*
bn	0.0	0.0	0.0	0.0 (-0.1*)	0.0	0.0	0.0	0.0
Δbn	±0.2	±0.09	±0.04	±0.02(±0.04*)	±0.01	±0.004	±0.002	±0.0009
an	0.0	0.0	0.0	0.0	0.0	0.0	0.0	0.0
Δan	±0.2	±0.09	±0.04	±0.02	±0.01	±0.004	±0.002	±0.0009

* – at injection.

Table II.1.2.1-3. Random errors at 1 cm reference radius (in 10^{-4} units of main field).

n	*3*	*4*	*5*	*6*	*7*	*8*	*9*	*10*
σb_n	0.5 (1.3*)	0.3	0.07	0.03	0.008	0.003	0.0016	0.0005
σa_n	0.5 (1.3*)	0.3	0.07	0.03	0.008	0.003	0.0016	0.0005

* – at injection.

Taking into account a significant change of β-function along inner triplets the end field quality in the HGQ might be important. The end field effects on beam dynamics are now under extensive study [10]. The preliminary reference numbers (specifications) for the integrated systematic multipole coefficients in the end regions are presented in Table II.1.2.1-4. Reproducibility of magnetic length from magnet to magnet must be within 1 cm for the same magnet type.

Table II.1.2.1-4. Integrated harmonic coefficients in unit·m at 1 cm reference radius and end magnetic length for the HGQ.

Parameter	*Lead End*	*Return End*
$\langle B_6 \rangle$	0.27	0.046
$\langle B_{10} \rangle$	–0.0013	–0.0013
$\langle A_2 \rangle$	16	
$\langle A_6 \rangle$	0.010	
$\langle A_{10} \rangle$	–0.0005	

All components of the inner triplet must be precisely aligned with respect to each other and beam closed orbit. Magnet alignment is provided during fabrication and after installation in the tunnel. Extensive studies on the effect of quadrupole misalignment on the accelerator performance has been started [11, 12]. It was found that a 1 mm offset of the inner triplet cryostats on both sides of IR results in a vertax displacement by 0.6 mm, and exterior closed orbot distortions of about one beam sigma. To be within the dinamic range of the dipole correctors the relative transverse misalignments of IR quadrupoles inside the triplet should be less than 0.35 mm. The relative longitudinal quadrupole misalignment could achieve 10 mm. To ensure the luminosity degradation less than 10% the design of quadrupole support system should limit the short term displacements (vibrations) to a few microns. In general, transverse and roll IR quadrupole misalignments must be kept as small as is practically possible. Quadrupole alignment requirements will be studied and reviewed based on the accelerator physics study and IR quadrupole R&D results.

A detailed description of the LHC cryogenic system can be found elsewhere in the literature [1]. The heat load requirements to the inner triplet cryostat design at various temperature levels are listed in Table II.1.2.1-5.

Table II.1.2.1-5: Allowed cryostat heat loads.

Temperature, K	*50 to 70*	*4.5 to 20*	*1.9*
Static heat load, W/m	5.7	0.1	0.3
Dynamic heat load, W/m			4.9
Total, W/m	5.7	0.1	5.2

Each triplet consists of four quadrupoles, three multipole correctors, two beam position monitors, and two supplementary beam absorbers. The cold mass assemblies for Q1 and Q3 are approximately 7 m long. Those in Q2a and Q2b are approximately 6 m long. The multipole corrector assemblies are about 0.6 m long. The triplet assembly is divided in three units each with their individual cryostat:

- Q1 unit with BMP and SBA1. Its additional feature is the end dome welded to the cryostat end closest to the interaction point
- Q3 unit with SBA2 and multipole corrector
- Q2a-Q2b unit with BPM and two multipole correctors

These three individual units will be joined using welded connections and bellows to form the complete triplet. Cryogenics feed from one end of the magnet string and are terminated at turnaround pipes at the other end. The overall length of each triplet is approximately 30 m not including the feed box.

The IR Quadrupole project scope of work includes the development, fabrication, test and delivery to CERN the HGQ magnets for all LHC interaction regions. The important part of the project is a collaboration with CERN and KEK in the development and fabrication of the IR inner triplet components. Fermilab and KEK will provide the inner triplet quadrupole cold masses, 16 each plus spares. Multipole correctors and BPM will be provided by CERN. Cryostat design for both Fermilab and KEK quadrupole cold masses will be developed and provided by Fermilab. Magnet final assembly and test as well as delivery to CERN will be provided by Fermilab.

The project stages are presented below:

I. HGQ Conceptual Design Study (FY1996-FY1997)

- ☐ HGQ design and analysis
- ☐ Short tooling design/installation
- ☐ HGQ conceptual design report

II. HGQ R&D (FY1997-FY1999)

- ☐ Magnet R&D (6 short models)
- ☐ Cryostat R&D and cryostat design
- ☐ Tooling design/optimization (short/full-scale)
- ☐ MTF (test stands, test equipment)

III. HGQ Full Scale Prototype (FY-1999-FY2000)

- ☐ Prototype specs
- ☐ Full-scale tooling test
- ☐ MTF and procedure test
- ☐ Full-scale magnet and cryostat test

IV. Magnet Production (FY2001-FY2004)

This chapter describes the conceptual design (stage I) of the high gradient quadrupole magnets suitable for the LHC low-β inner triplets. Section II.1.2.2 describes the overall design of the high gradient quadrupole. The magnetic design and field quality analysis are presented in Sections II.1.2.2 and II.1.2.4. The analysis of the HGQ mechanical structure is given in Section II.1.2.5. The coil cooling system and results of thermal analysis are reported in Section II.1.2.6 and HGQ quench protection problems are analyzed in Section II.1.2.7. Finally, the plans and current status of the R&D program, which will be followed to optimize the design and to set final magnet specifications are summarized in Section II.1.2.8.

II.1.2.1.1.1 References

[3] The LHC Study Group, “The Large Hadron Collider,” *CERN/AC/95-05 (LHC),* 20 October, 1995.

[4] J.P. Koutchouk, R. Ostojic, T. Risselada, C. Rufer, W. Scandale, S. Weisz, “The Lattice Lay-out and Optics of the LHC, Version 4.1,” *SL/NOTE 95-38 (AP),* LHC Note 318, April 3, 1995.

[5] A. Faus-Golte, J.P. Koutchouk, A. Verdier, S. Weisz, "Modular Optical Design of the LHC Experimental Insertions," *Proc. of 5th European Particle Accelerator Conference (EPAC'96),* Barcelona, Spain, 1996.

[6] R. Ostojic, T.M. Taylor and S. Weisz, "Systems Layout of the Low-β Insertions for the LHC Experiments," *Proc. of Particle Accelerator Conference (PAC'97),* Vancouver, Canada, May 1997.

[7] A. Morsch, R. Ostojic, T.M. Taylor, "Progress in the Systems Design of the Inner Triplet of 70 mm Aperture Quadrupoles for the LHC Low-β Insertions, " *Proc. 4th European Particle Accelerator Conference (EPAC'94),* London, England, 1994, p.2274.

[8] J. Strait and N.M. Mokhov, "Optimization of the LHC Interaction Region with Respect to Beam-Induced Energy Deposition, " *Proc. 5th European Particle Accelerator Conference (EPAC'96*), Barcelona, Spain, 1996 (LHC Project Report 43).

[9] N.V. Mokhov and J.B. Strait, "Towards the Optimal LHC Interaction Region: Beam-Induced Energy Deposition," *Proc. of Particle Accelerator Conference (PAC'97),* Vancouver, Canada, May 1997.

[10] *The LHC Mini-Workshop on the IR Design,* Fermilab, October 7-8, 1997.

[11] A.Verdierr and S.Weisz, "Alignment of low-β insertion with beam," *CERN-SL-Note 95/118 (AP),* November 1995.

[12] S.Weisz, "Alignment of the low-β quadrupoles," *LHC Project Note 59*, 1996.

II.1.2.2 HGQ Design Description

II.1.2.2.1 Introduction

The current design of the HGQ consists of four, two layer shell-type superconducting coils connected in series, clamped by stainless steel collars, and surrounded by iron laminations. A two-layer geometry was chosen based on mechanical, thermal and quench protection considerations. This design concept provides better coil mechanical support and turn cooling conditions as well as lower magnet inductance as compared to a four-layer one. This approach rests solidly on the past experience [13, 14], and allows the use of existing tooling.

II.1.2.2.2 General Design Description

The magnet cross-section is shown in Fig. II.1.2.2-1. Each of the four coils consists of 14 turns in the inner layer, and 16 turns in the outer one. Inner and outer layer coils are connected by splices placed in the coil lead end region. Each octant has two spacers, one for each layer, which allow a fine adjustment of the field quality in the magnet straight section. The coil ends have the same block-wise layout of turns as in the magnet body. The block positions at the ends were optimized to reduce the maximum field and to improve field quality.

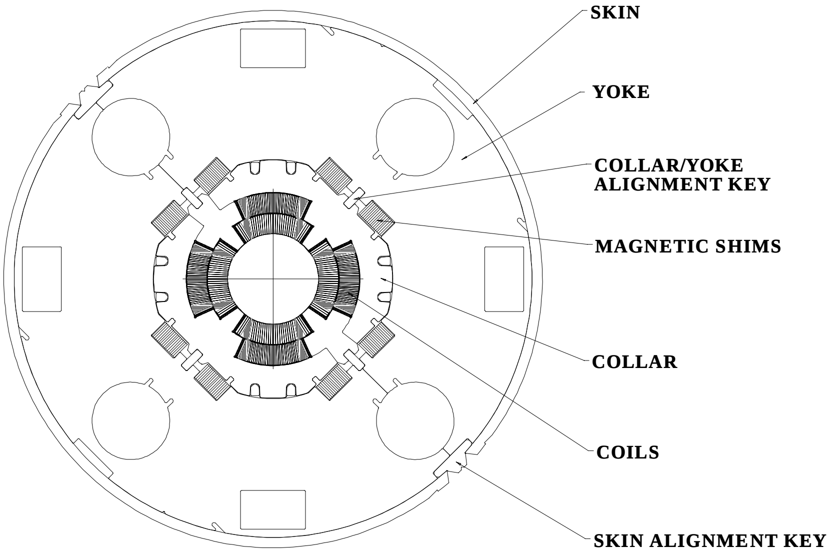

Fig. II.1.2.2-1. HGQ cross-section.

The coils are made of keystone Rutherford-type NbTi cables based on the SSC type strands. Different cable types are used in the two layers. Both cables have the same width but different mid-thickness. The cables are insulated with a multilayer Kapton insulation.

Magnet coils are pre-stressed and mechanically supported by means of stainless steel collar laminations. Collar laminations are locked in two perpendicular directions by four pair of tapered keys. The collared coil is centered inside the iron yoke with the help of special alignment keys. There is a small gap between collar and yoke laminations.

The yoke inner radius is 92.56 mm while the outer radius is 200 mm. The yoke laminations feature four round holes for the superfluid helium heat exchanger and four rectangular holes for housing of electrical connections, as well as special cutouts for fabrication purposes. In the pole regions, eight rectangular gaps between collar and yoke house the magnetic tuning shims for the field quality adjustment. In order to provide a good operating margin in the coil ends, the iron yoke is terminated at a distance of 150 mm from the lead end of the coil straight section and 50 mm from the return end.

A two-piece iron yoke is supported by stainless steel skin. Two skin shells are welded under some tension to provide tight contact of the iron blocks. Special keys are installed between skin shells for the longitudinal magnet alignment.

To restrict coil longitudinal motion under Lorentz forces applied to the coil ends, two stainless steel end plates welded onto skin are used. The quadrant splice assembly is mounted on the outer surface of the lead end plate.

The quadrupole coils are cooled by pressurized He II filling the cold mass (helium vessel) at a nominal temperature 1.9 K. The heat is transported from static pressurized He II to the flowing, saturated two-phase He II at 1.8 K via a He II heat exchanger. This heat exchanger could be arranged either inside of the cold mass (internal design) or outside of the cold mass (external design).

To reduce static heat leaks, the helium vessel (including cold mass and heat exchanger) is placed inside a vacuum vessel with the help of a special support system, and surrounded by additional thermal shield and multilayer thermal insulation.

II.1.2.2.3 Superconducting Cables

The HGQ superconducting cables use SSC type strands based on NbTi superconducting alloy. This superconductor has a critical temperature of 9.2 K and an upper critical magnetic field of 14 T. Nominal strand parameters are presented in Table II.1.2.2-1. The parameters of the inner and outer layer cable are listed in Table II.1.2.2-2.

Table II.1.2.2-1. HGQ Strand Nominal Parameters

Parameter	*Unit*	*Inner cable*	*Outer cable*
Wire diameter	mm	0.808	0.648
Filament diameter	μm	6	6
Copper-to-superconductor ratio		1.3:1	1.8:1
Residual Resistivity Ratio		100	100
Twist pitch	mm	13	13
Twist direction		left	right
Critical current @5 T & 4.2 K	A	600	320
Critical current density @5 T & 4.2 K	kA/mm^2	2.75	2.75

Table II.1.2.2-2. HGQ Cable Nominal Parameters

Parameter	*Unit*	*Inner cable*	*Outer cable*
Radial width, bare	mm	15.40	15.40
Minor edge, bare	mm	1.326	1.054
Major edge, bare	mm	1.587	1.238
Keystone angle,	deg	0.98	0.68
Cable packing factor		0.91	0.91
Number of strands		38	46
Strand diameter	mm	0.808	0.648
Transposition direction		right	left
Cable transposition pitch	mm	114	102

Since the two-layer magnet design requires cables with large aspect ratio, the mechanical stability of the cable during winding is a critical issue. Samples for both the inner and the outer cable have been produced by LBNL and winding studies have been carried out at Fermilab. Test winding was done to determine windability, cable lay (transposition direction) and winding tension. It was found that the optimal winding tension range is 303-500 N. Based on the coil windin results it was decided to fabricate both inner and outer cable to wind in the mechanically favorable direction - with right lay for the inner cable and left lay for outer one. To provide the better cable mechanical properties the twist direction of strand has to be opposite to the cable transposition direction – left for the inner strand and right for outer one.

II.1.2.2.4 Cable insulation

It is anticipated that all of the outer coil cable and some of the inner coil cable can be made entirely from existing SSC strands. Notice that SSC inner strand has a right twist direction. The possibility of utilization of inner SSC strand with right twist pitch is studied. Some quantity of new inner strand with the nominal twist direction will be purchased if required.Cable Insulation

The general requirements for the cable insulation are listed below:

- Azimuthal thickness of 75 μm after coil curing under compression. This requirement came from the magnetic design as a compromise between the turn separation and the high filling factor of the coil.
- Kapton film. This requirement is dictated by the radiation conditions during magnet operation.
- Multi-layer structure. This requirement is important for providing the mechanical and electrical reliability of cable insulation.

The fabrication experience shows that the cable insulation creeps during coil curing under compression and, consequently, it decreases the thickness by 20-30% in azimuthal direction. This reduction depends on the cable packing factor and coil curing conditions (temperature, pressure, time). Based on that, the non-deformed cable insulation has to be of 100 μm that corresponds to 25% azimuthal deformation after curing. The radial insulation thickness before and after curing is the same, 100 μm.

The above requirements lead to the two-wrap cable insulation design. The inner wrap in both cables is made of Kapton film 25 μm thick and 9.5 mm wide wound with 50% overlap. This wrap creates two insulating layers with the total non-deformed thickness of 50 μm.

The outer wrap of inner cable insulation is made of 50 μm thick and 4.8 mm wide Kapton film wound with a 2 mm gap. These channels increase the inner cable wet perimeter by an order of magnitude (13-14 times). That allows one to keep the inner cable temperature below the He lambda-point, and to take advantages of possible superfluid He penetration under the cable insulation involving it in a heat transfer along and across the cable. Although those helium channels decrease the E-modulus of the inner coil by a factor of two, it does not dramatically affect the field harmonic stability in the magnet operating current/gradient range. Moreover, the low E-modulus allows one to accommodate coils of a larger azimuthal-size variation without significant change of coil prestress range.

To provide the electrical and mechanical reliability of outer cable insulation and to increase the quench heater effectiveness there are no channels in the outer insulation wrap. It is made of Kapton film 25 μm thick and 9.5 mm wide with 50% overlap. This gives two additional insulating layers with total thickness of 50 μm. Another possibility is a butt outer wrap of 50 μm thick 4.8 mm wide Kapton film that is used for the outer wrap of inner cable.

Table II.1.2.2-3 summarizes the cable insulation parameters for the HGQ inner and outer cables. The cable insulation design will be finally optimized after tests of a series of HGQ short models.

Table II.1.2.2-3. HGQ Cable Insulation Parameters.

Parameter	*Inner cable*	*Outer cable*
Number of wraps	2	2
Inner wrap:		
-material	Kapton tape 0.025mm×9.5 mm	Kapton tape 0.025mm×9.5 mm
-adhesive	None	None
-wrap structure	Spiral wrap with 50% overlap	Spiral wrap with 50% overlap
--thickness	0.050 mm	0.050 mm
Outer wrap:		
-material	Kapton tape 0.050mm×4.8 mm	Kapton tape 0.025mm×9.5 mm
-adhesive	Liquid polyimide	Liquid polyimide
-wrap structure	Spiral wrap with 2 mm gap	Spiral wrap with 50% overlap
--thickness	0.050 mm	0.050 mm
Total thickness	0.1 mm	0.1
Wet perimeter	~60%	0%

II.1.2.2.5 Inner and Outer Coils

HGQ inner and outer coil assemblies are shown in Fig. II.1.2.2-2. Coil end parts are made of ULTEM 2300 with 30% glass fill machined into minimum cable stress shapes, produced by the BEND programs created at Fermilab. There are three types of end parts. On the return end there are keys, which are used to fill the pole area, spacers, which provide the termination for wedges and separate current blocks in the ends, and saddles, which provide support at the end for the final turn. There are identically named parts on the lead end, except where a turn transitions from one current block to the next. Here, the spacer is split into two pieces, called a spacer and filler.

The pole turn of each inner/outer coil pair needs to be spliced together. Splices are 114 mm long, which is approximately equal to the cable transposition pitch. Areas to be spliced are preformed, or filled with solder before the coil is wound. The tinned sections are then spliced after the magnet straight section is collared and keyed. Minimum stress preform shapes are generated by the program LEAD, which is similar to BEND.

Two different types of pole splice are being tried for the HGQ, internal and external. The configuration of both splices is shown in Fig. II.1.2.2-3. The external splice is made outside the coil perimeter. The internal splice is made within the radial space, which contains the outer coil.

Both splice designs have some advantages and disadvantages. Short models with each splice configuration will be manufactured and tested in the frame of HGQ R&D

program. Final splice design will be chosen based on the fabrication experience and magnet test results.

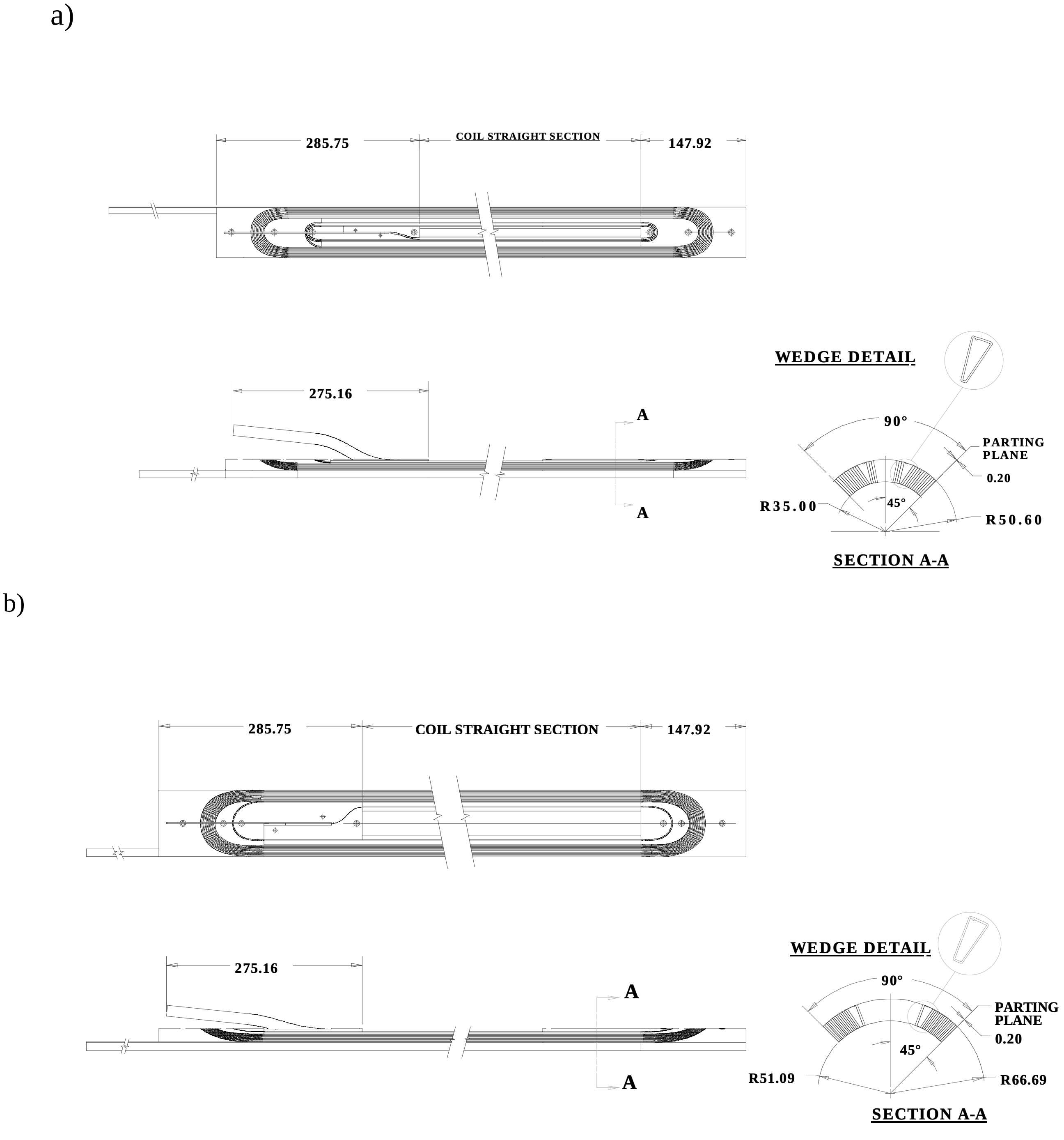

Fig. II.1.2.2-2. Inner (a) and outer (b) coil assemblies.

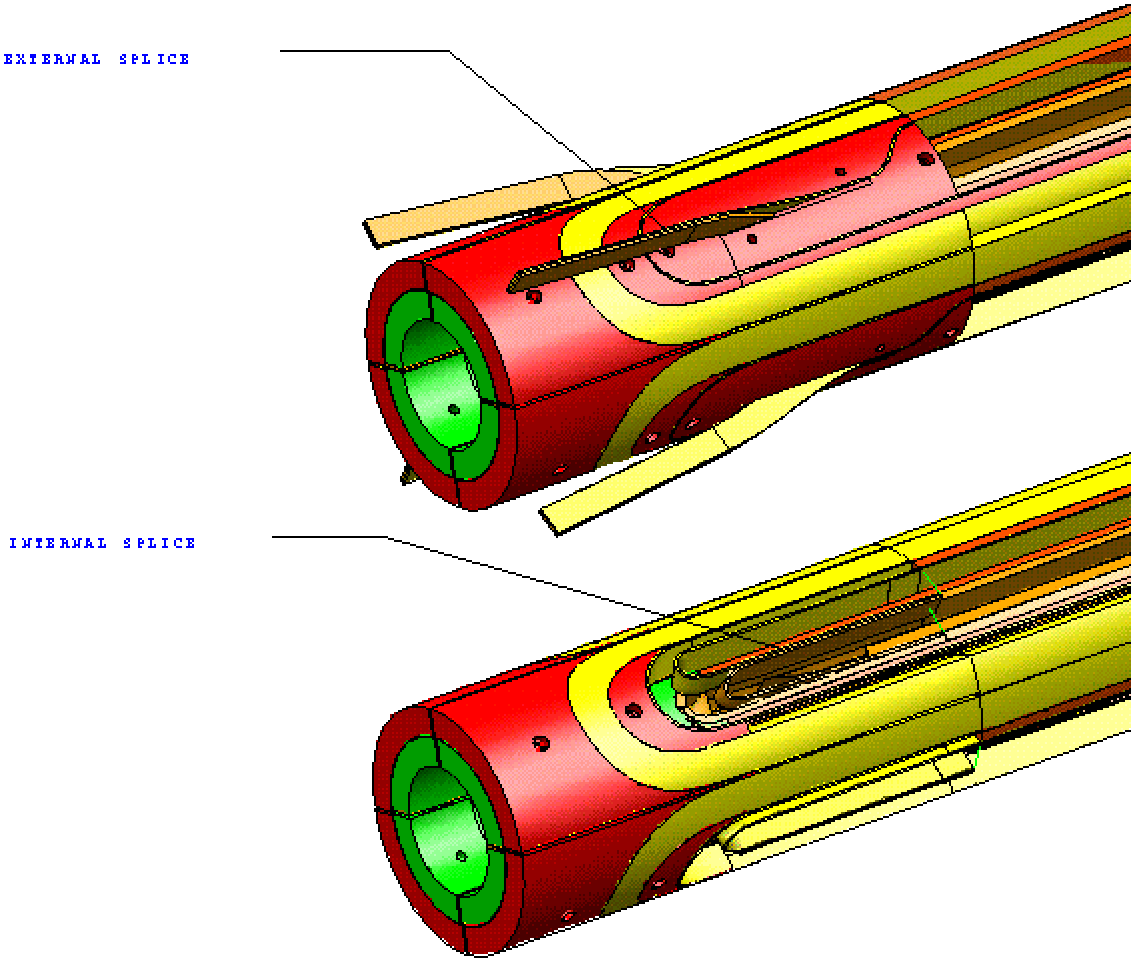

Fig. II.1.2.2-3 . External and internal splice view. Parts supporting the splice have been removed from the internal splice view to fully display the splice.

II.1.2.2.6 Coil Insulation and Ground Wrap

Coil insulation includes the ground wrap, interlayer insulation, and any other insulation materials, which are placed within the coil area. The main function of coil insulation system is the prevention of shorts between coils, quench protection heaters and collars (ground). It must allow for sufficient helium flow to the coils and it should be configured in such a way that assembly is efficient. The coil insulation system for the LHC IR high gradient quadrupole is shown in Fig. II.1.2.2-4.

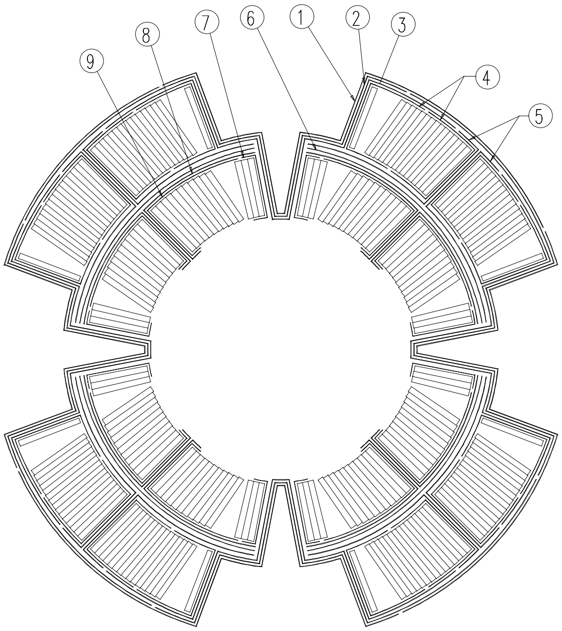

Fig. II.1.2.2-4. HGQ coil insulation system: 1,2,3 – pole ground wrap; 4, 7, 9 – coil caps; 5, 8 – parting plane layers; 6 – quench heater.

All insulating material is either 75 µm or 125 µm Kapton film. A minimum number of thickness and parts have been used within the constraints of the space allowed. At least 450 µm of Kapton insulation (consisting of four separate sheets) is placed between the collars and any coil surface. To allow tuning of the cross-section to eliminate systematic harmonics, the parting plane Kapton is 400 µm thick. All components to be electrically isolated have at least two sheets of Kapton between them. This allows each component to have at least one layer of Kapton separating it from any other component because, for assembly purposes, most pieces have azimuthal gaps between them, allowing a short path if a second piece is not used.

Ground wrap is split or perforated at the pole as it is shown in Fig. II.1.2.2-5. A passage is therefore provided for helium flow between the outer and inner edges of the coil area. The 3mm “corner” is sufficient to provide electrical insulation between inner coils and collars, while the 4mm opening is sufficient to provide helium flow. The 4 mm gap may be achieved either by using two separate pieces of Kapton or perforating a single piece with slots . Using a single perforated piece may be preferable for magnet assembly.

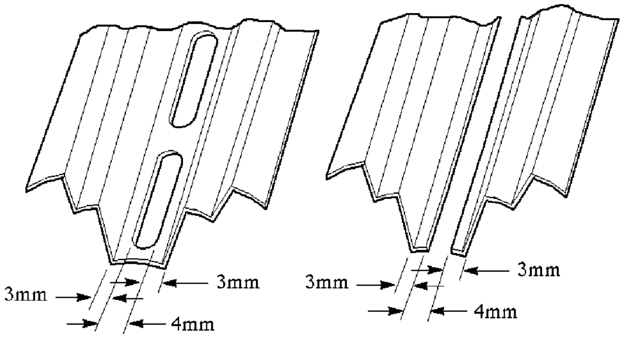

Fig. II.1.2.2-5. Ground wrap configuration at Inner Coil Pole.

The quench protection heater baseline design consists of a 25 μm thick stainless steel strip bonded to and sandwiched between two layers of 25 μm pieces of Kapton. The details of quench heater assembly is shown in Fig. II.1.2.2-6.

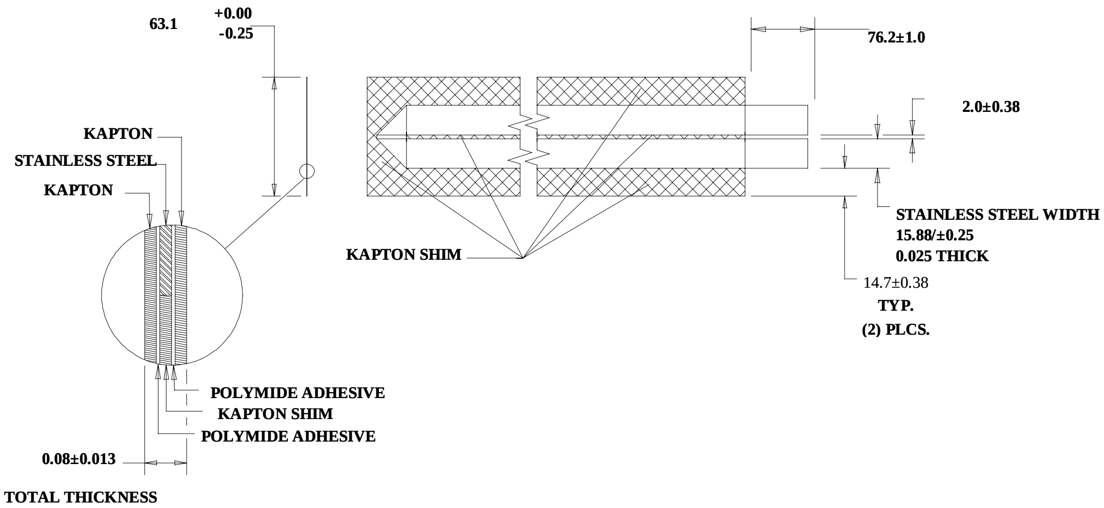

Fig. II.1.2.2-6. Interlayer quench protection heater assembly.

II.1.2.2.7 Collared Coil

There are three distinct sections of the collared coil: lead end, straight section and return end. Their cross sections are presented in Fig. II.1.2.2-7. The straight section consists of the coil, ground insulation with quench heaters, bearing strips, collars and keys. The bearing strips, made of brass, are placed on the inner and outer coil poles to provide a continuous load-bearing surface that protects coil insulation from damage during assembling, cooling down and operation. The collars are made of Nitronic 40 laminations of 1.5 mm thick. They are nominally 25 mm wide in the radial direction. The collars are manufactured by stamping that provides the geometry repeatability from part to part on the order of ±15 µm. Collar laminations are assembled vertically, stacked up with each new layer of laminations rotated 90° about the magnet axis from the previous layer. Collar layers are held together using two tapered, full hard phosphor bronze keys per quadrant.

The stacked assembly is inserted in a press, which pushes simultaneously on all four sides until the key grooves on adjacent collars align. At this point two keys are inserted per quadrant. After the press is released, the collars and keys support the coil compression load. To minimize stress concentrations, the key grooves are radiused. The collar is thickest at the midplane, which corresponds to the maximum Lorentz force location. The collars have an arc length of less than 180°, thus when assembled every other pole is filled with helium, allowing heat to pass from the beam tube through slots at the pole in the ground insulation, through collars, to cooling holes in the yoke.

a)

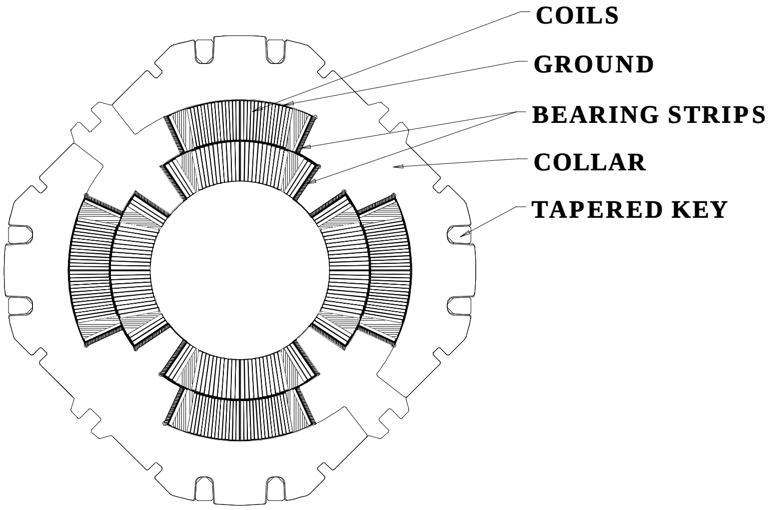
COILS
GROUND
BEARING STRIPS
COLLAR
TAPERED KEY

b)

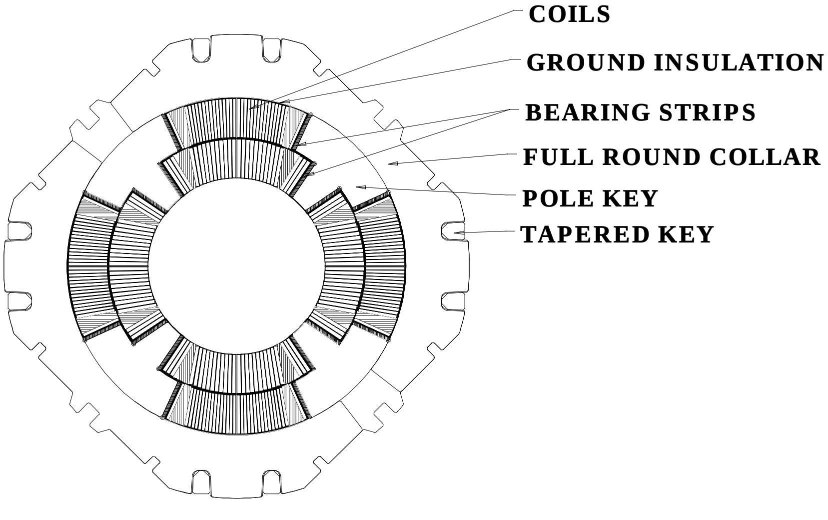
COILS
GROUND INSULATION
BEARING STRIPS
FULL ROUND COLLAR
POLE KEY
TAPERED KEY

c)

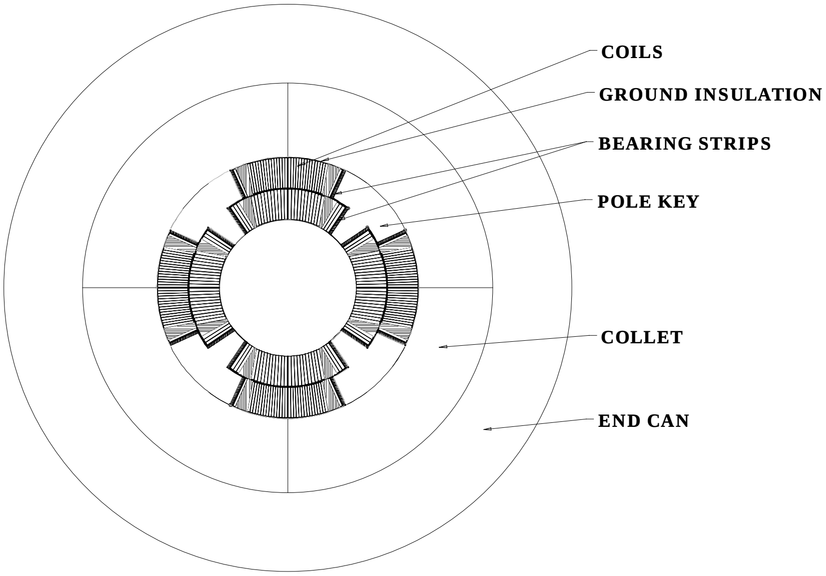

Fig. II.1.2.2-7. The collared coil cross section[HDG13]:
regular collar (straight section);
round collar (return end);
end can (lead end).

At the return end, the coils are supported similarly to the straight section except for modifications necessary due to coil end geometry. It differs from straight section geometry in two ways: the coils pass though the pole region and there is an additional layer of ground insulation. For this reason, the stamped collars of the straight section are modified by removing the poles and enlarging the inner radius to accommodate extra ground wrap. This modified lamination is the full round collar. It is used from the beginning of the coil key to the end of the coil saddles, a distance of 148 mm. The method of assembly is similar to and performed at the same time as that of the straight section.

On the lead end, the coil geometry is more complicated because the coil splice extends radially outward into the collar region. Therefore, a special support structure must be used. Instead of collars with a larger radius, a solid aluminum ring (end can) is used. It has 25/30 mm thick walls and a tapered inner diameter. Four ULTEM filler pieces, one for each quadrant with a 1 mm azimuthal gap between each, are placed between the coils and end can. The filler interface is also tapered so that the further the end can is pushed over the fillers, the more radial force is generated, resulting in higher coil compression and end can tension. The azimuthal gap between filler pieces guarantees that 100% of the end can radial compression force is transmitted to the coils.

The interlayer splices are contacted on both sides by a copper temperature stabilizer. The stabilizer has a 3 mm radius semi-circular channel that faces the cable, allowing the cable to be flooded with 1.8 K helium. The stabilizer and splice are wrapped together with Kapton tape. This package is laid into grooves in the filler pieces. The cross section of the lead end with internal splice is similar to the return end cross section. In the final assembly, it is supported azimuthally by ULTEM end parts. Radial support for the coils in the splice area is provided by full round collars.

II.1.2.2.8 Cold Mass

The five major components in the cold mass are the collared coil, iron yoke, skin, endplates, and quadrant splices. The 3D view of HGQ cold mass with both external and internal splice designs is shown in Fig. II.1.2.2-8 and Fig. II.1.2.2-9.

The iron yoke which surrounds the collared coil has no structural function; it is designed for purely magnetic and assembly criteria. It is comprised of 1.5 mm thick stamped iron laminations in the straight section, stainless steel laminations in the return end over a length of 200 mm, and stainless steel laminations in the lead end over a length of 300 mm. In the latter region, laminations are modified to fit over the end can assembly for the external splice. The yoke OD is 400 mm. There are several cut-outs in it: four 60 mm diameter cooling holes, cut-outs for buss bars, holes for magnetic shims, and notches for alignment and assembly. All of these features are placed maintaining quadrupole symmetry. Yoke laminations are formed by stamping which produces part to part repeatability of ±15 µm.

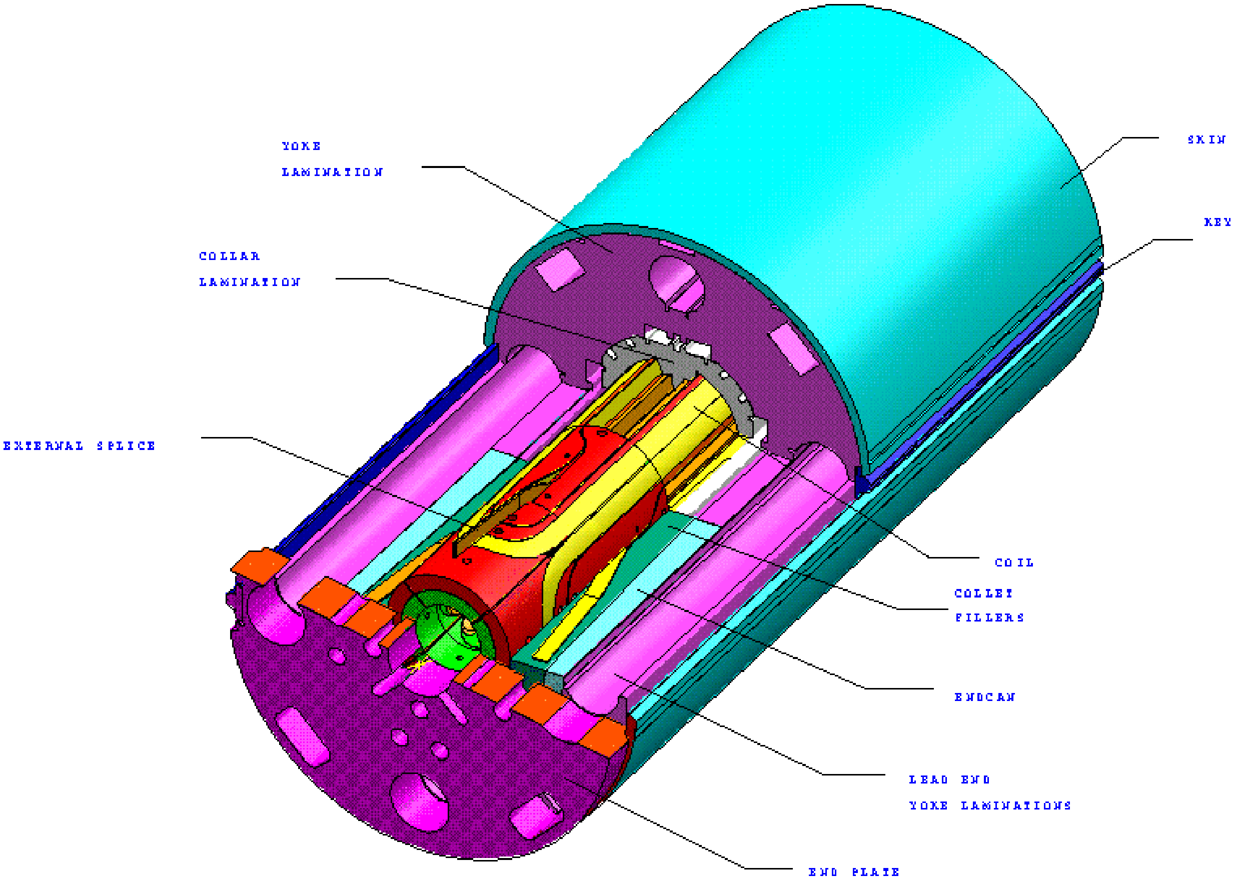

Fig. II.1.2.2-8. 3D view of HGQ cold mass with external inter-layer splices.

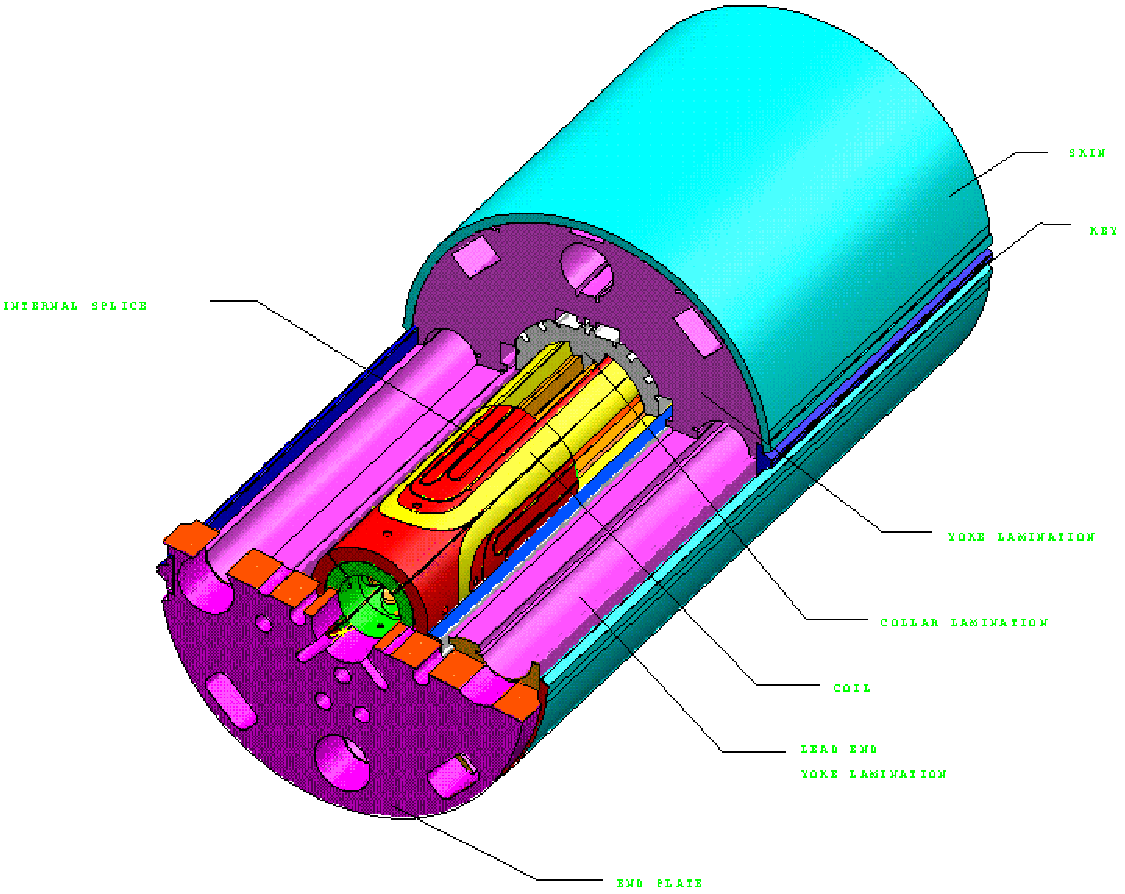

Fig. II.1.2.2-9. 3D view of HGQ cold mass with internal inter-layer splices.

The skin of the magnet compresses the iron halves together and forms the helium containment vessel. The key, which holds the skin together, also serves as an alignment mechanism. A key is fitted into precisely positioned notches in the iron stamping. This key also has an alignment feature, a notch, which runs the entire length of the magnet, which is the outside of the completed cold mass. The skin consists of two 8 mm thick stainless steel bump-formed half shells. These are assembled around the yoke in a press, which contacts the OD of the skin. Both skin halves are welded simultaneously to the key, which also serves as a backing plate for the weld. As the weld cools, the skin is stretched around the iron, resulting in a maximum tension of approximately 200 MPa.

End plates restrict the longitudinal end motion under Lorentz forces generated in the lead and return ends of the coils. The return end plate is shown in Fig. II.1.2.2-10. The forces are transmitted through 10 mm thick stainless steel flat plates, installed on the end of each coil quadrant, through short cylinders (bullets) to 50 mm thick stainless steel end plates welded onto the skin at the lead and return ends.

Each bullet senses the axial force in one quadrant via strain gauges mounted on its flat side. The bullets are threaded into the end plate and torqued so that they produce sufficient longitudinal compressive force at room and at helium temperature.

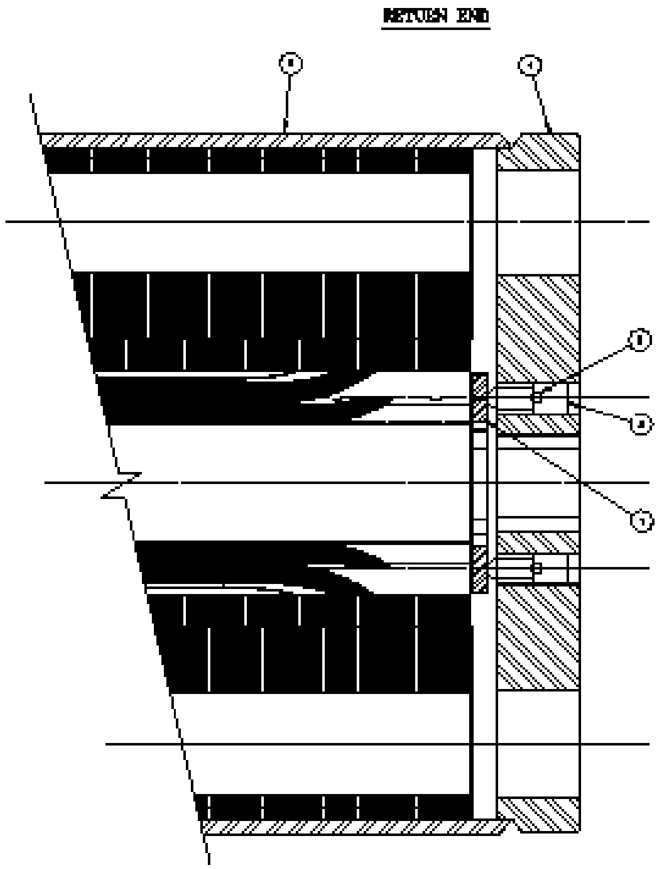

Fig. II.1.2.2-10. Return end cross section:
1 – pressure plate; 2 – bullet; 3 – adjustment screw; 4 - end plate; 5 – skin.

Four coils (quadrants) are connected in series with a help of three splices. The quadrant splice and power lead assembly is mounted on the outer surface of the lead end plate. Cables routed to ensure four quadrants are powered with proper polarity and assembly geometry chosen to maintain quadrupole symmetry to the extent possible. The last 120 mm of the cables are straight and are soldered together.

The details of quadrant splice assembly are shown in Fig. II.1.2.2-11.

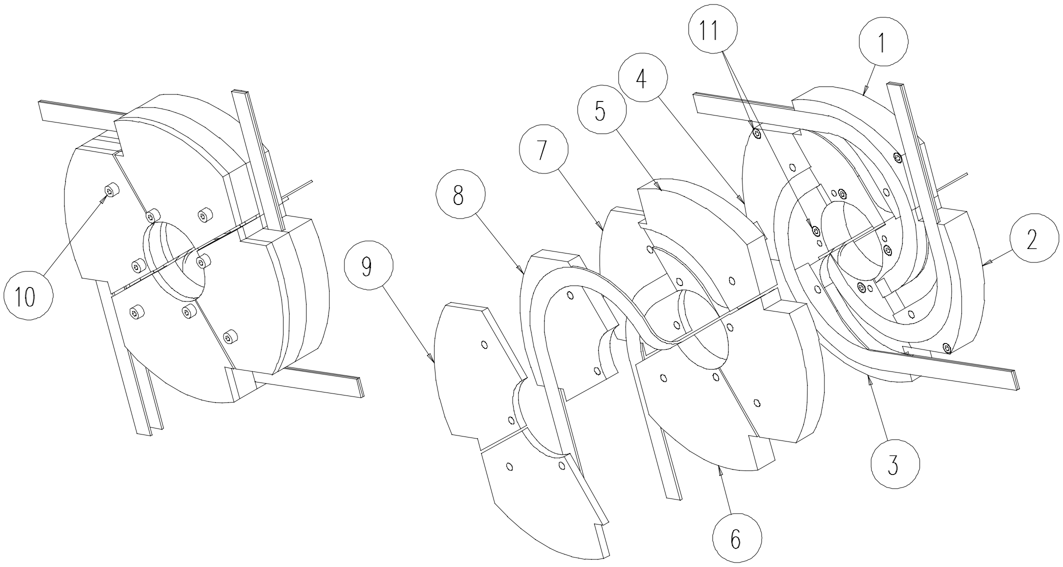

Fig. II.1.2.2-11. End view of quadrant splice and power lead assembly:
1, 2, 3, 4 – splice blocks;
5, 6, 7, 8 – intermediate blocks;
9 – support block cover;
10, 11 – screws.

II.1.2.2.9 Cryostat

The quadrupoles Q1, Q3 with adjacent multipole corrector and Q2a Q2b with two multipole correctors will be assembled into single cold masses and single vacuum vessels for a total of three distinct cryostats.

Fig. II.1.2.2-12 shows a typical cryostat cross section at a cold mass support location. Each cold mass is supported along its length by top-mounted supports (suspensions) oriented at ±45° from the cold mass center line. The HGQ cryostat and support structure designs are based on the designs developed and successfully tested for the SSC superconducting dipoles [15, 16]. Using two supports per cross section produces a much more rigid cold mass mounting system than one, which uses a single support and may be an advantage in trying to meet the stringent alignment requirements for interaction region magnets. Also, supports mounted as shown in Fig. II.1.2.2-12 provide sufficient radial clearance for the external He II heat exchanger, which must be above the cold mass for proper operation during cooldown, and 1.8 K saturated He II supply tube or a pump line. One of the two support locations per cold mass assembly will serve as the axial anchor. The other will have a sliding interface between the support and cold mass to allow for thermal contraction during cooldown.

The internal cold mass supports are coincident with the external vacuum vessel support rings. These support rings stiffen the vacuum vessel at the cold mass support points and serve as the interface between the vacuum vessel and the tunnel mounted support and alignment hardware. In the current conceptual design, the vacuum vessel has a 864 mm outside diameter.

Ambient thermal radiation is intercepted by blankets of multilayer reflective insulation (MLI) [17] immediately inboard of the inner vacuum vessel surface and by a 50-75 K helium cooled thermal shield. There is an additional MLI blanket on the cold mass.

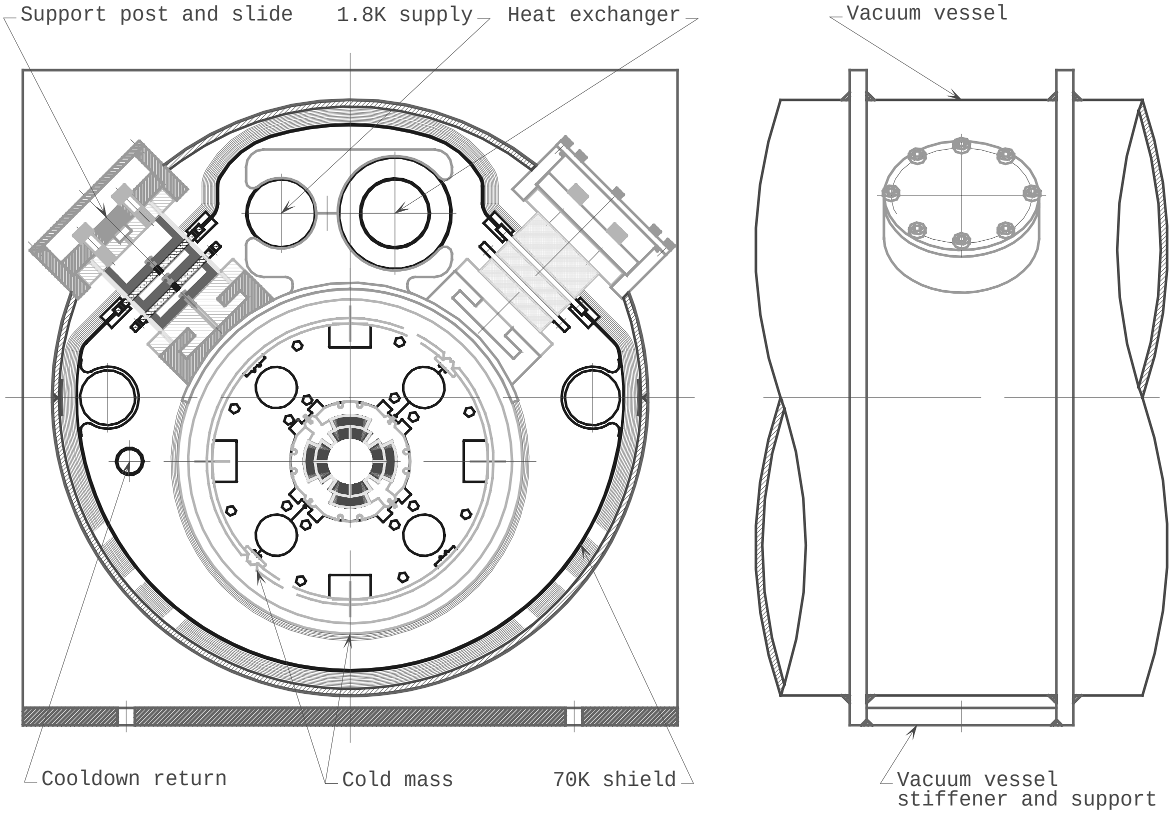

Fig. II.1.2.2-12. HGQ cryostat cross section.

There are two different outer diameters for the quadrupole cold mass. Those being fabricated at KEK are 510 mm diameter while those being fabricated at Fermilab are 416 mm diameter. The current cryostat design contain an adapter on the Fermilab assemblies to increase their diameter at the cold mass attachment locations so that all cryostats will be identical regardless of the cold mass manufacturer.

II.1.2.2.10 He II Heat Exchanger

The main function of He II heat exchanger is to extract heat from the cold mass and maintain its temperature below 1.9 K during normal operation. Several experiments have been carried out at CERN to study the thermal performance of the heat exchanger in which the heat is transported from static pressurized He II to the flowing saturated He II through either a smooth tube or a corrugated pipe [18, 19, 20]. These studies show that the heat exchanger exhibits a stable two-phase boiling liquid helium flow and performs as an efficient heat sink when vapor and liquid flow in the same direction. The He II heat exchanger, however, could be arranged either internally (within the cold mass) or externally (outside of cold mass) as long as the thermal design requirements are fulfilled.

There are four 60 mm holes in the iron yoke for the Fermilab and KEK designed quadrupole magnets, and the correction dipole magnets. The internal He II heat exchanger arrangement requires that the heat exchanger pipe be inserted all the way through from end to end of 30 meters in length. Thus, the positions of the 60 mm holes in the correction dipole magnets would be constrained to line up with those in the quadrupoles.

The external He II heat exchanger would eliminate this constraint if the thermal design requirements would be satisfied. The total allowable temperature drop from the pressurised He II in the magnet cold mass to the refrigerator is limited by the LHC cryogenic system, which is about 100 mK. For both the internally or externally arranged He II heat exchanger, the temperature drop must be maintained within 100 mK.

The design work for both internal and external He II heat exchanger arrangements is under way and the thermal analysis between the two is being compared. The final decision depends on several issues, such as the inner triplet cooldown regime from room to helium temperature, normal operation under various heat loads, peak quench pressure, and magnet cooldown regime after quench. The decision depends also on evaluation of the case of assembly given the mechanical complications arising from the requirement to accommodate both Japanese- and American-made quadrupoles with European-made correction coils.

II.1.2.2.10.1 References

[13] A.D. McInturff et al., “The Fermilab Collider D0 Low β System,” *EPAC Proceedings, Rome (Italy), v.2,* p.1264, June 1988.

[14] S. Caspi et al., “A Proposed IR Quad for the SSC,” *Supercollider 4,* Plenum Press, New York, 1992, p.243.

[15] T.N. Nicol, “Design Development for the 50 mm Superconducting Super Collider Cryostat,” *Super Collider 3, Vol.3,* Plenum Press, Ney York, 1991, p.1029.

[16] T.N. Nicol, “SSC 50 mm Collider Dipole Cryostat Single Tube Support Post Conceptual Design and Analysis,” *TM-1745, SSCL-N-765,* July 9, 1991.

[17] W.N. Boroski et al., “An Overview of the Multilayer Insulation System for the Superconducting Super Collider,” *XVIII International Congress of Refrigeration,* August 10-17, 1991, Monreal, Canada.

[18] A. Cyvoct, Ph. Lebrun, M. Marquet, L. Tavian and R. van Weelderen, “Heated Two-Phase Flow of Saturated Helium II over a Length of 24 m,” *CERN-AT/91-28 (CR), LHC Note 169,* (1991).

[19] J. Casas, A. Cyvoct, Ph. Lebrun, M. Marquet, L. Tavian and R. van Weelderen, “Design Concept and First Experimental Validation of the Superfluid Helium System for the Large Hadron Collider (LHC) Project at CERN,” *Cryogenics, vol. 32, ICEC Supplement,* (1992), p. 118.

[20] A. Bezaguet, J. Casas-Cubillos, Ph. Lebrun, M. Marquet, L. Tavian and R. van Weelderen, “The Superfluid Helium Model Cryoloop for the CERN Large Hadron Collider (LHC),” *CERN AT/93-21 (CR), LHC Note 233,* (1993).

II.1.2.3 Field Gradient and Short Sample Limit

II.1.2.3.1 Introduction

The conductor and iron configurations have been optimized [21] both to minimize the deviations froma pure quadrupole field and to maximize the short-sample limit gradient. This section describes the coil and iron yoke configurations for both the body and the ends and presents calculations of the load lines and of the short sample limit based on SSC strand critical current specifications. The expected magnetic field quality is discussed in the next section.

II.1.2.3.2 HGQ Magnetic Design

II.1.2.3.2.1 Magnet straight section

Fig. II.1.2.3-1 shows the coil cross section for one octant. The four blocks of the reference octant will be labeled as follows:

- B1: block 1 (15 turns) for outer layer, mid-plane side
- B2: block 2 (1 turn) for outer layer, pole side
- B3: block 3 (11 turns) for inner layer, mid-plane side
- B4: block 4 (3 turns) for inner layer, pole side.

Within each layer, the conductors are numbered from the mid-plane side to the pole side.

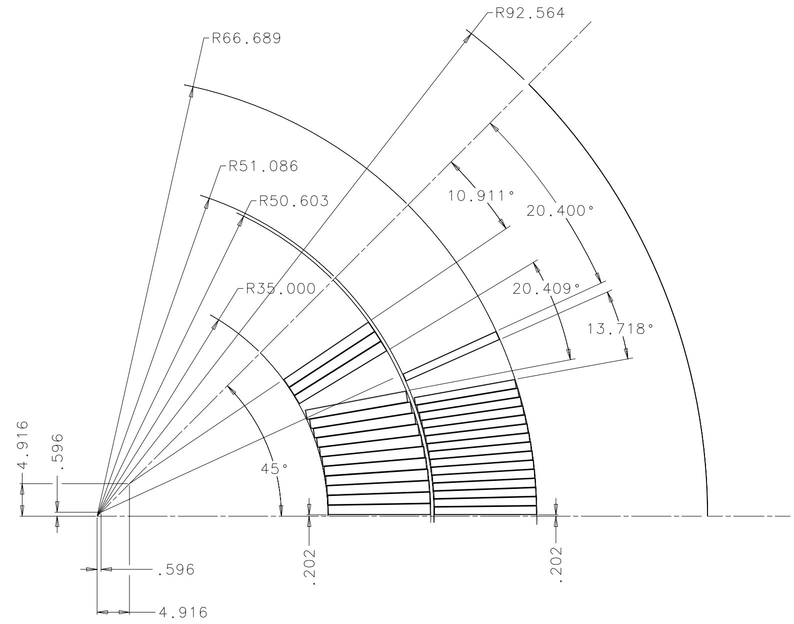

Fig. II.1.2.3-1. HGQ magnetic design.

II.1.2.3.2.2 End region

Fig. II.1.2.3-2 and Fig. II.1.2.3-3 show the longitudinal cross-section at the pole angle of the HGQ return and lead end. In both cases the z-axis is directed outwards from the magnet body. The iron yoke starts at z = –15 cm for the lead end, at z = –5 cm for the return end. In the lead end, the splice ramp starts at z = –13.78 cm for both the inner and the outer coil.

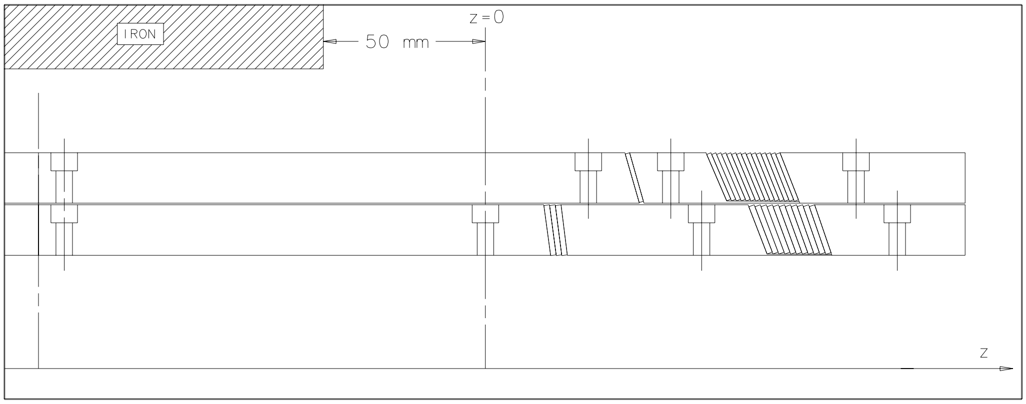

Fig. II.1.2.3-2. HGQ return end magnetic design.

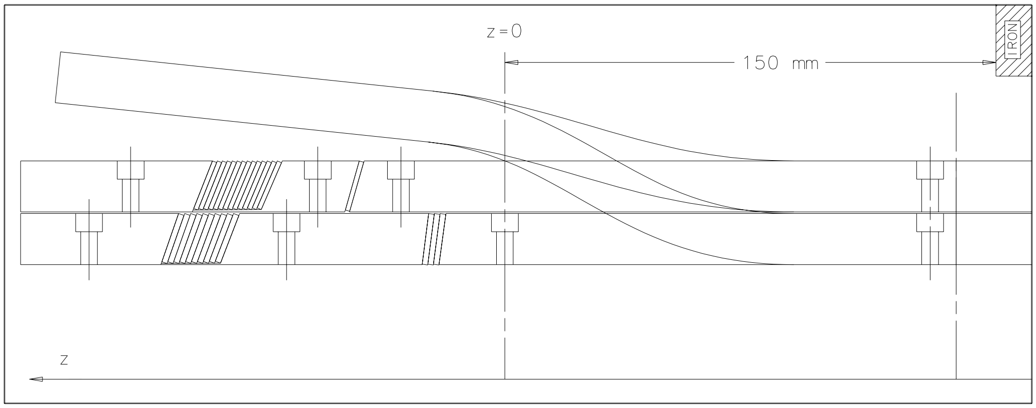

Fig. II.1.2.3-3. HGQ lead end magnetic design.

The 3D model for the coil end regions is built by extrusion along the z-axis, starting from a 2D model of the magnet cross-section. The data for the 3D extrusion is obtained by reading into the ROXIE program [22] the BEND [23] coordinate files, which specify the cross-sections of each conductor at small intervals along z.

For the return end, 20 cross-sections have been specified from the edge of the iron yoke to the coil termination. The cross-sections are spaced more closely in those regions where the bending radius is smaller. The resulting geometry for the return end is shown in Fig. II.1.2.3-4.

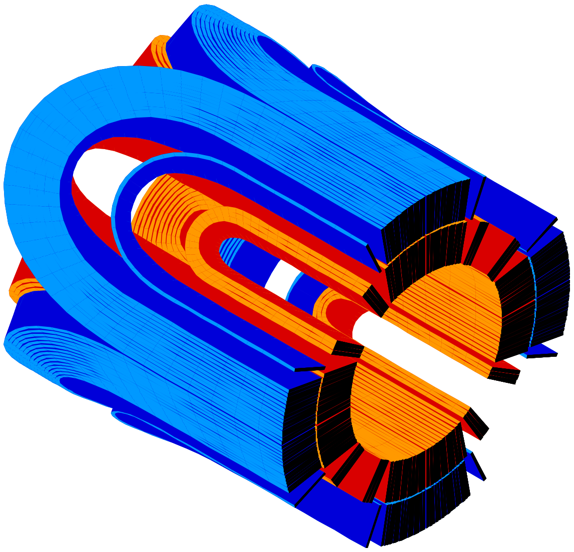

Fig. II.1.2.3-4. ROXIE-BEND model for the HGQ return end

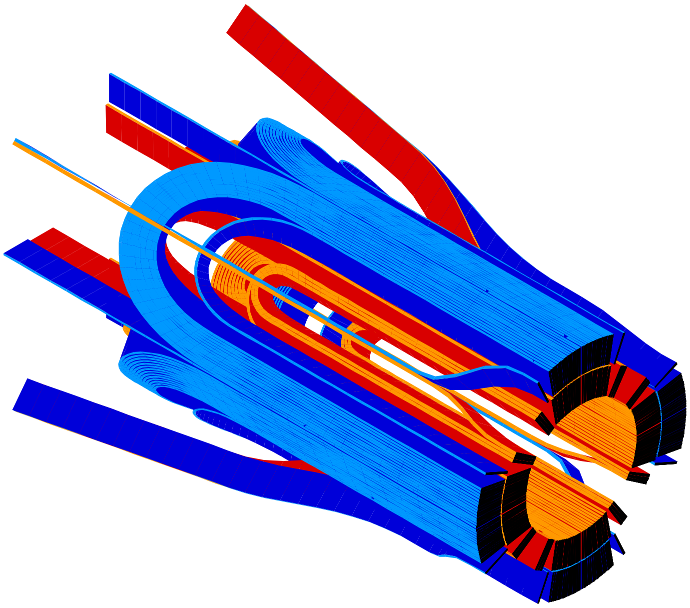

Fig. II.1.2.3-5. ROXIE-BEND model for the HGQ lead end (external splice design).

For the lead end, where the coil is not symmetric with respect to the pole plane, both the left and the right side of each quadrant (coil) have been defined. For the 3D extrusion, 30 cross-sections have been specified from the edge of the iron yoke to the coil termination. The resulting geometry is shown in Fig. II.1.2.3-5.

For both the lead and return end, the model also includes a straight section extending from the edge of the iron yoke for 1.5 m in the negative z direction. The coil to coil splice length is 11.43 cm. The quadrant splices are not included in the model. For each coil, the two connection conductors extend straight from the magnet body in the z direction and are truncated at z = 15 cm.

The field calculation is based on the Biot-Savart law. The iron yoke is regarded as a magnetic mirror of circular shape (inner radius 9.256 cm) with infinite permeability. For the ROXIE calculation, each conductor has been subdivided in current filaments, one for each strand. The total number of strands is 38 in the inner layer, 46 in the outer layer.

II.1.2.3.3 Gradient and Field Load Lines

Table II.1.2.3-1 reports the field load line coefficients for each block in the HGQ cross section computed using ROXIE. The following cases are considered:

- Case 1: no iron yoke

- Case 2: circular iron yoke with a linear B-H characteristic (μ=3000), inner radius Rin=92.564 mm and outer radius Rout = infinite.

Table II.1.2.3-1. Field load line coefficients and field gradient in each block.

Case	*B1, T/kA*	*B2, T/kA*	*B3, T/kA*	*B4, T/kA*	*G, T/m/kA*
1	0.532	0.525	0.587	0.639	16.669
2	0.588	0.589	0.643	0.699	18.221

The peak field for the inner layer is obtained in the pole turn (conductor 14). For the outer layer, depending on the yoke configuration, the peak field is obtained either in conductor 16 (pole turn, block B2) or in conductor 15 (pole turn, block B1). The gradient load line coefficients are 16.669 T/m/kA for case 1, 18.221 T/m/kA for case 2. The relative contribution of the iron yoke to the gradient is about 9%.

Field distribution, computed using POISOPT [24] with the real yoke lamination design and a non-linear B-H characteristic, is shown in Fig. II.1.2.3-6. Table II.1.2.3-2 reports the field and gradient load lines. A packing factor of 98% has been assumed for the yoke laminations. Based on this result, the operating current for a nominal gradient of 200 T/m is 11.11 kA and for the 210 T/m – 11.68 kA.

Table II.1.2.3-2. Gradient and field load lines for the real iron.

I , kA	*G, T/m*	*B1max, T*	*B2max, T*	*B3max, T*	*B4max, T*
1	18.34	0.596	0.588	0.649	0.707
6	109.36	3.551	3.500	3.869	4.212
8	145.15	4.709	4.639	5.135	5.590
10	180.64	5.854	5.764	6.391	6.957
12	215.61	6.980	6.868	7.627	8.303
14	249.75	8.072	7.936	8.834	9.618
16	283.40	9.145	8.984	10.024	10.914

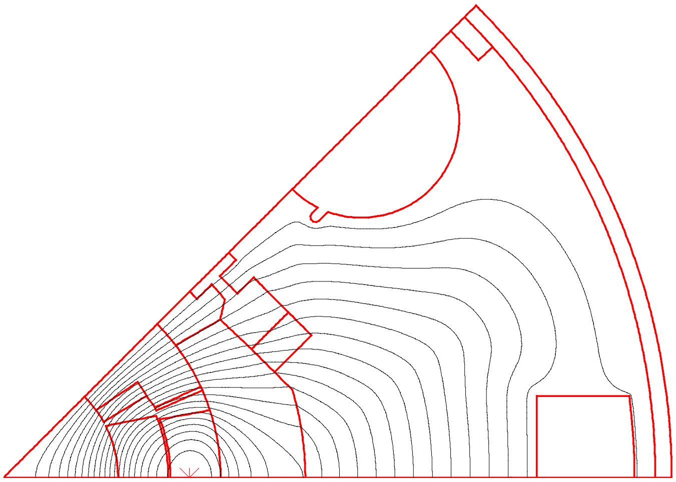

Fig. II.1.2.3-6. Field lines distribution in HGQ cross section.

For the 3D peak field calculation, the method implemented in ROXIE does not allow to take into account the contribution of the iron yoke. This means that the field values calculated in the proximity of the edge of the iron yoke (z = –50 mm for the return end, z = –150 mm for the lead end) are incorrect. However, the actual peak field normally occurs in the coil end area,where turns are bending around the pole, and previous calculations show that the distance from the edge of the iron yoke to this region is sufficiently large to ensure that the contribution of the iron yoke can be neglected.

Table II.1.2.3-3. Field load line coefficients in the HGQ straight section, lead and return end.

Block number	B_{max}/I, *T/kA*			
	Lead end	*Straight section*		*Return end*
	I=1-14 kA	*I=1 kA*	*I=14 kA*	*I=1-14 kA*
1	0.576	0.596	0.576	0.599
2	0.401	0.588	0.567	0.541
3	0.597	0.649	0.631	0.599
4	0.639	0.707	0.687	0.656

The linear coefficients for the maximum field in each block of the lead and return end as well as in the magnet body (taking into account the iron saturation and the detailed iron cross-section) as function of current are reported in Ref???. A comparison between these values shows that the peak field in the first-pole block of the outer layer (block 1) is higher in the return end than in the magnet body and consequently the critical current in this point determines the magnet short sample limit. Fig. II.1.2.3-7 shows the variation of the magnetic field along the z coordinate for some relevant conductors of the return end. For each block, the conductor where the maximum field occurs has been chosen. As can be seen, the behavior of block B1 (conductor/turn C15) is anomalous in the sense that the field keeps increasing all the way until the coil termination, while for the other conductor groups a peak is reached in the area where the conductors start bending, then the field starts to decay. This unusual behavior can be explained by an enhancement of the local field at the position of conductor C16 due to the relative positions of block B1 (outer layer) and block B3 (inner layer), as shown in Fig. II.1.2.3-8.

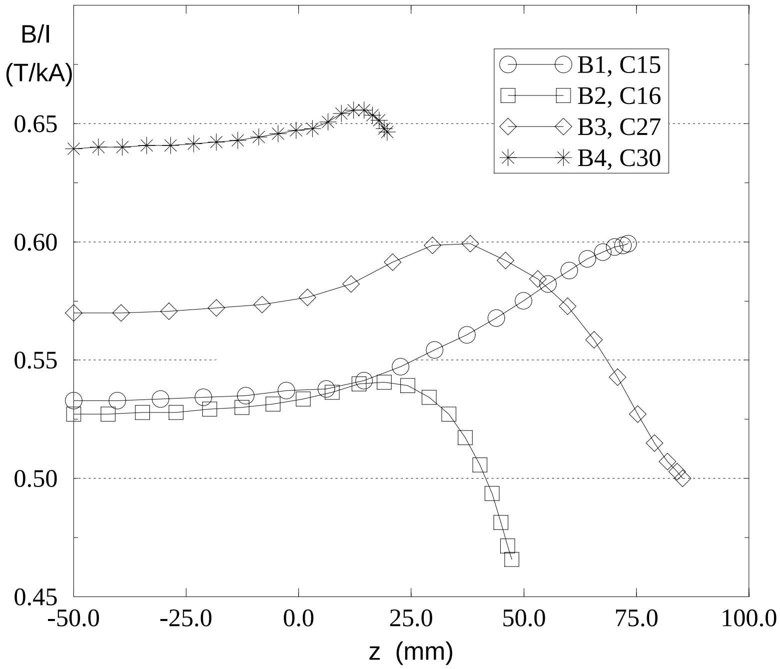

Fig. II.1.2.3-7. Field load line along z for some conductors in the return end. For each block, the conductor where the maximum field occurs has been chosen.

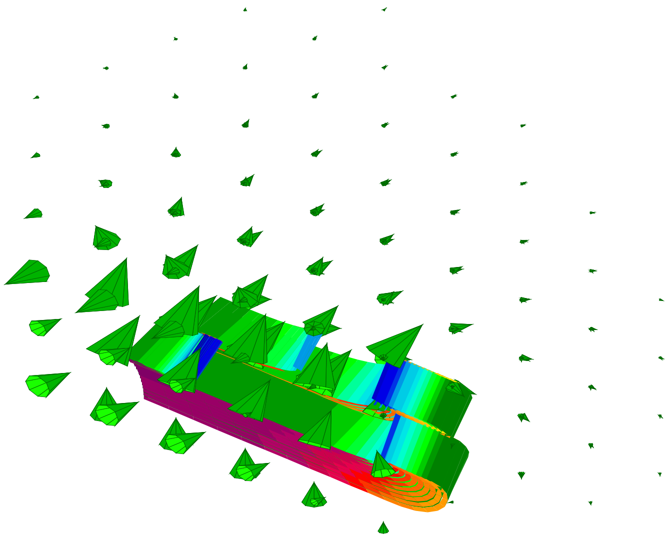

Fig. II.1.2.3-8. Magnetic field enhancement at the position of conductor C16, resulting from a constructive interference of the contributions of block B1 and block B3.

The variation of the magnetic field along the z coordinate for the most relevant conductors of the lead end is shown in Fig. II.1.2.3-9 (outer layer) and Fig. II.1.2.3-10 (inner layer). It can be seen that the peak field enhancement at the position of conductor C15 is still present, however the actual value is lower here than in the return end (0.576 T/kA instead than 0.599 T/kA). This can be explained by the fact that in the lead end both second-wound groups have one less conductor than in the return end. No particular problem arises in the inner layer, as well as at the location of the splice ramps and current leads.

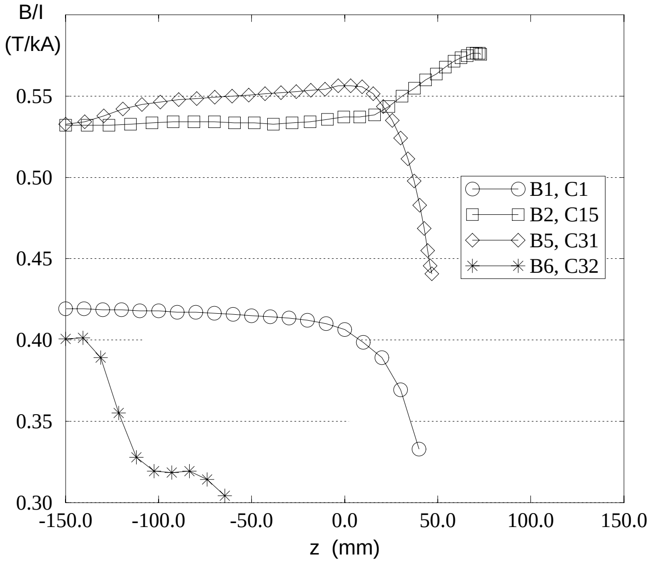

Fig. II.1.2.3-9. Field load line along z for relevant blocks/turns in lead end (outer layer).

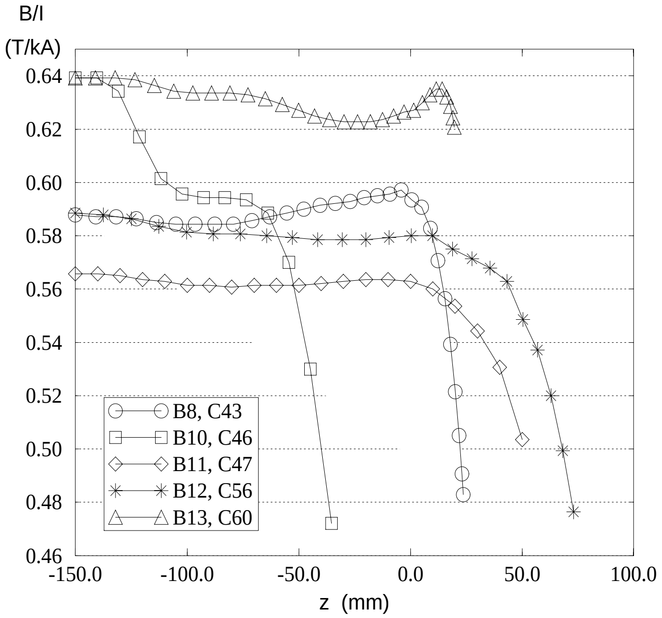

Fig. II.1.2.3-10. Field load line along z for relevant blocks/turns in lead end (inner layer).

II.1.2.3.4 Short Sample Limit

The calculated peak field load lines and measured cable critical currents for the HGQ inner and outer layers are shown in Fig. II.1.2.3-11 and Fig. II.1.2.3-12.

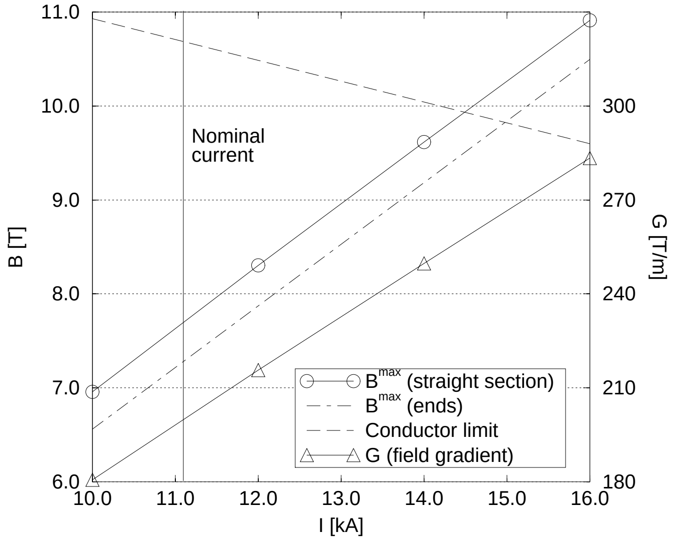

Fig. II.1.2.3-11. Field load lines and cable critical current for the HGQ inner layer.

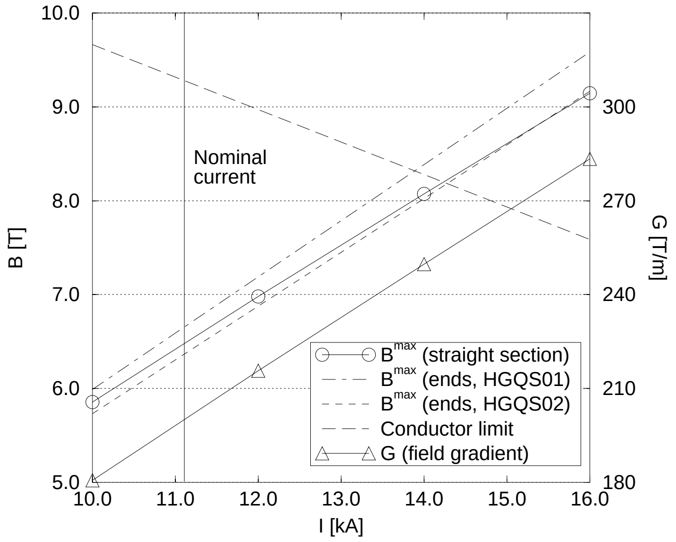

Fig. II.1.2.3-12. Field load lines and cable critical current for the HGQ outer layer.

Table II.1.2.3-4 reports the calculated maximum current in the inner and outer layer of the HGQ straight section and return end as well as the corresponding field gradient in the magnet bore. The calculations are based on the assumptions and the results discussed in the previous sections for the real iron yoke design with the nonlinear B-H iron characteristic. The contribution of the iron yoke to the end field is neglected.

Table II.1.2.3-4 . HGQ critical current and maximum field gradient.

	Iss, kA		*Gss, T/m*
	Inner layer	*Outer layer*	
Straight section	14.5	14.2	254
Return end	15	13.9	248

As can be seen, for the current HGQ design and the SSC superconducting strands the HGQ critical current and maximum field gradient are determined by the outer layer in the return end.

II.1.2.3.5 Summary

The calculated short sample limit for the first HGQ short model based on the presented above end magnetic design with the SSC strands at 1.9 K is 13.9 kA. It corresponds to the maximum field gradient in magnet bore of 248 T/m. The limitation comes from the return end region.The short sample limit for the magnet body is 14.2 kA which corresponds to a maximum gradient of 254 T/m. The reduction of maximum field in the end regions has been done during HGQ magnetic design optimization. This problem has been fixed by shifting the end block 2 of the coil outer layer by 20 mm along the magnet axis in both lead and return end. This allows to increase the HGQ short sample limit up to its maximum value 254 T/m for the chosen magnet design and conductor. A new optimized end design will be used starting from the model #2. Further end magnetic design optimization is planed during HGQ short model R&D program.

The nominal field gradient of 200 T/m is achieved at nominal current of 11.1 kA, that is by 20% lower than the HGQ short sample limit. The high critical current margin should minimize the number of training quenches required to reach the operating gradient and provides adequate temperature margin for the substantial beam heating experienced by these magnets.

II.1.2.3.5.1 References

[21] S. Caspi, “LHC IR Quad Magnetic Design: II.1.1.3. Field Quality,” FNAL/LBL/CERN videoconference, May 1, 1996.

[22] S. Russenschuck, “A Computer program for the design of superconducting accelerator magnets,” *CERN AT/95-39*, September 1995.

[23] J. Cook, “Strain Energy Minimization in SSC Magnet Winding,” *IEEE Trans. on Magnetics, MAG-27, 1991, p. 1976.*

[24] R. Holsinger & C. Iselin, “The CERN-POISSON package user guide”, CERN Program Library long writeup, August 1984.

II.1.2.4 Field Quality

II.1.2.4.1 Introduction

The expected field errors in the HGQ straight section as well as in the lead and return ends will be discussed in this chapter.

The field quality in magnet central cross-section is described in terms of multipole coefficients according to the following expression:

$$B_y(x,y) + iB_x(x,y) = \sum_{n=1}^{\infty}(B_n + iA_n)\left(\frac{x+iy}{R_{ref}}\right)^{n-1} \qquad (1)$$

where

Rref - reference radius (for the LHC magnets *Rref* = 1 cm),

B_n and A_n - normal and skew harmonic coefficients.

In an ideal quadrupole magnet, all the harmonic coefficients except B_2 are zero. The quadrupole gradient G can be obtained from the B_2 coefficient as $G=B_2/Rref$. The harmonic coefficients normalized to the main field component B_2 are determined as follows: $b_n = (B_n/B_2)\times 10^4$ and $a_n = (A_n/B_2)\times 10^4$.

An expansion similar to (1) is used for the integrated transverse magnetic field in the end regions. To make this approach valid the integration intervals start deep enough in the magnet body and finish far enough from magnet ends. Their axial coordinates with respect to coordinate systems shown in ??? and ??? have been chosen [–35, +25] cm for the lead end and [-25, +25] cm for the return end. As in the magnet straight section, the integrated/average multipole components in the ends $\widehat{b}_n$ and $\widehat{a}_n$ are expressed in standard units (10^{-4}) of the main integrated quadrupole component $\hat{B}_2$: $\widehat{b}_n = (\widehat{B}_n/\hat{B}_2)\times 10^4$ and $\widehat{a}_n = (\widehat{A}_n/\hat{B}_2)\times 10^4$. The magnetic length is defined as the length of straight section that would have an equivalent integrated gradient: $L_m = \hat{B}_2 / B_2$.

II.1.2.4.2 Design Harmonics

Table II.1.2.4-1 reports the first three allowed harmonic coefficients for the design coil 2D geometry, computed by ROXIE [25] using an analytical model (Biot-Savart law) for the iron yoke having a linear B-H characteristic with $\mu = 3000$, inner radius $R_{in} = 92.564$ mm and outer radius $R_{out} = \infty$. All other normal and skew harmonics with $n < 14$ are zero. The current flow in the cable is modeled by defining a current filament at the position of each strand (2×19 filaments for the inner cable, 2×23 filaments for the outer cable).

Table II.1.2.4-1. Design field harmonics in the 2D HGQ central cross-section at 1 cm and 2 cm reference radius.

n	*Rref*	6	10	14

b_n	1 cm	-0.002	-0.000014	-0.000018
b_n	2 cm	-0.025	0.0037	-0.074

II.1.2.4.3 Field Quality in the Magnet Straight Section

II.1.2.4.3.1 *Field error sources*

The following effects on the field quality in the magnet straight section have been analyzed.

Mechanical effects. Due to insufficient keystoning of the cables, the coil turns become progressively more non-radial moving from the mid-plane towards the wedge in both the inner and outer layers. The non-radial turns do not occupy the full radial cavity in the curing mold making their radial position not well defined. It is expected that after curing the turns will be aligned to the outer mold radius. The validity of this assumption will be checked as part of the model magnet program. The uncertainty range corresponds to alignment of all turns to the inner mandrel radius.

The magnetic design was optimized assuming room temperature part dimensions and absolutely stiff collars. The collared coil deformation during cooling down and under nominal pre-stress, as well as its deformation under Lorentz forces with respect to the warm unstressed geometry produce systematic field errors. The Lorentz force effect is negligible at injection and maximal at collision.

Deviations from nominal pre-stress and turn or coil block displacements due to manufacturing tolerances contribute to the random errors.

Magnetization effects. The coil magnetization is determined by the critical current density in the superconductor, filament diameter, Cu/Sc ratio, etc. This effect is maximal at injection and becomes negligible at collision. The uncertainty is related to the accuracy of the model and the parameters of the conductors. .

The magnetization of the stainless steel collars and beam pipe (internal beam absorber) produces current independent field harmonics, which depend on geometry and magnetic permeability. A nominal collar permeability of 1.003 was expected. The larger values up to 1.006 were also studied and included as uncertainty in the systematic value . A beam pipe/absorber with 27mm inner radius, 6 mm thickness and magnetic permeability 1.005 has been analyzed. Both the systematic effect and the random contribution due to beam pipe/absorber misalignment were found to be negligible if the offset is below 0.5 mm.

The yoke cross section was optimized to minimize the change in the harmonics due to iron saturation and to compensate the harmonics due to collar magnetization. The uncertainty is related to a precise knowledge of the iron B-H characteristic which is not known yet.

Iron is the material of choice for the cryostat vacuum vessel. The cold mass is placed off-center with respect to this shell. The effect on the harmonics has been analyzed and found to be negligible.

Magnetic measurements. The field quality of each HGQ magnet will be determined during magnetic measurements. Measurement errors contribute to the uncertainty in the systematic harmonics and to the harmonic RMS spread. Since the measurement system is still being designed, the estimates have been done based on data available in [26, 27].

II.1.2.4.3.2 Systematic errors

The systematic errors for the non-allowed harmonics are assumed to be zero with zero uncertainty, therefore disregarding the effect of possible asymmetries and imperfections in the components and in the tooling equipment. For the allowed harmonics, the systematic errors are expressed in terms of an expected value and an uncertainty range with respect to this value. The uncertainty range is in general not symmetric around the expected value. No assumption is made here regarding the probability to obtain a particular value of the harmonics within the uncertainty range.

Design systematic errors and error uncertainty range are summarized in Table II.1.2.4-2. The total calculated systematic value of b_6 at injection is –0.09 with uncertainty [-0.14, +0.04], and at collision b_6 is +0.01 with uncertainty [-0.14, +0.02]. Table II.1.2.4-3 shows the expected uncertainty in the systematic errors resulting from the accuracy of magnetic measurements.

Table II.1.2.4-2. Design systematic field errors and error uncertainty range at 1 cm.

Effect	b_6		b_{10}		b_{14}	
	Expected contribution	Uncertainty range	Expected contribution	Uncertainty range	Expected contribution	Uncertainty range
Coil optimization	-0.002		-0.000014		-0.000018	
Turn alignment	0.0	+0.0 -0.134	0.0	+0.0 0.00063	0.0	+0.0000041 -0.0
Prestress at 1.9 K and I=0	0.029		0.00017		-0.0000003	
Lorentz force at 13 kA	-0.017		0.000028		0.0000007	
Coil magnetization at injection	-0.11	+0.03 -0.03	-0.00013	+0.000035 -0.000035	0.0000018	+0.0000003 -0.0000003
Collar magnetization	-0.018	+0.0 -0.018	0.000076	+0.000076 -0.0	-0.0000001	+0.0 -0.0000001
Yoke geometry	0.016		-0.00001		-0.0000001	
Iron saturation	0.005	+0.001 -0.001	0.000001		-0.0000003	

Table II.1.2.4-3. Expected measurement field errors at 1 cm.

n	a_n , b_n
3	±0.16
4	±0.085
5	±0.042
6	±0.020
7	±0.0095
8	±0.0044
9	±0.0020
10	±0.00087
11	±0.00038
12	±0.00017
13	±0.000073
14	±0.000031

II.1.2.4.3.3 Random errors

Table II.1.2.4-4 and Table II.1.2.4-5 present the expected random errors in the HGQ harmonics due to both random displacements of turns and blocks in the coil during magnet fabrication and expected RMS of measurement data. The expected block displacement ranges in both radial and azimuthal directions were ±50 microns and the turn displacement ranges were determined by the possible turn misalignment in the curing mold. Analysis shows that for the normal and skew harmonics with n<7 the random errors will be dominated by the geometrical errors (basically block displacement) during magnet fabrication, while for higher order harmonics (n>7) the RMS spread of the measurement results will dominate.

Table II.1.2.4-4. Normal random errors at 1 cm.

n	*Block*	*Turn*	*Measurement*	*Total*
3	0.954	0.178	0.080	0.97
4	0.345	0.0216	0.042	0.35
5	0.0873	0.0178	0.021	0.092
6	0.0249	0.00817	0.010	0.028
7	0.00648	0.00153	0.0047	0.0082
8	0.00168	0.000622	0.0021	0.0028
9	0.000387	0.000130	0.00098	0.0011
10	0.0000972	0.0000347	0.00044	0.00045
11	0.0000241	0.0000104	0.00019	0.00019
12	0.00000586	0.00000256	0.000084	0.000084
13	0.00000157	0.000000631	0.000036	0.000036
14	0.00000176	0.000000001	0.000016	0.000016

Table II.1.2.4-5. Skew random errors at 1 cm.

n	*Block*	*Turn*	*Measurement*	*Total*
3	0.937	0.189	0.080	0.96
4	0.323	0.0854	0.042	0.34
5	0.0876	0.0189	0.021	0.092
6	0.0224	0.00418	0.010	0.025
7	0.00656	0.00156	0.0047	0.0083
8	0.00155	0.000249	0.0021	0.0027
9	0.000377	0.000132	0.00098	0.0010
10	0.0000928	0.0000418	0.00044	0.00045
11	0.0000247	0.0000110	0.00019	0.00019
12	0.00000579	0.00000393	0.000084	0.000084
13	0.00000148	0.000000554	0.000036	0.000036
14	0.00000000	0.000000000	0.000016	0.000016

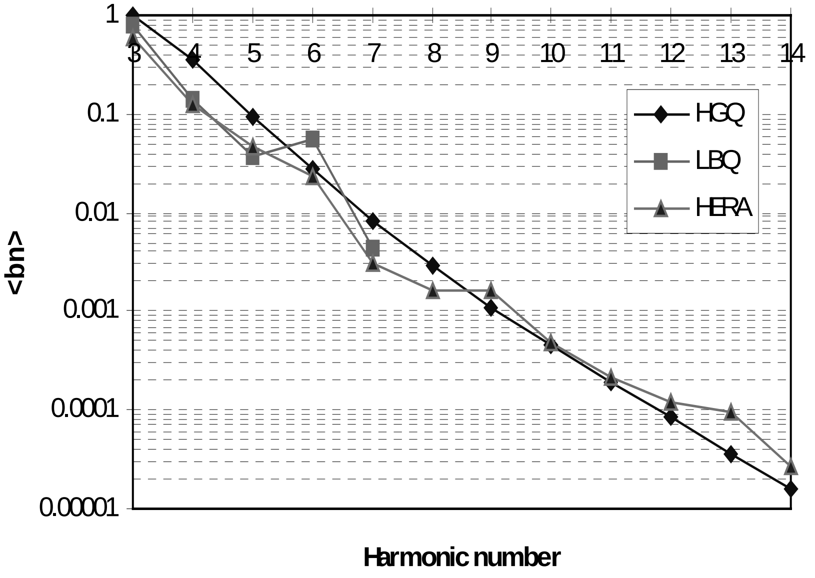

Comparisons between the predicted random errors for the HGQ and the results of measurements of the random field errors for FNAL LBQ [28] and HERA arc quadrupoles [29] presented in Fig. II.1.2.4-1 and Fig. II.1.2.4-2. LBQ magnets have been designed and fabricated at Fermilab, Saclay-HERA arc quads have been designed by Saclay and produced by industry.The HGQ results are given at a reference radius of 10 mm, corresponding to 1/3.5 of the HGQ bore radius. The HERA and LBQ experimental data have been scaled to a reference radius corresponding to the same fraction of the magnet bore. The resulting reference radii are 10.87 mm for LBQ and 10.71 mm for HERA quadrupoles. These magnets have been chosen for the following reasons: magnet design utilizes two layer coils; bore radius is comparable with HGQ bore (75 mm for Saclay-HERA quad; and 76 mm for FNAL LBQ)

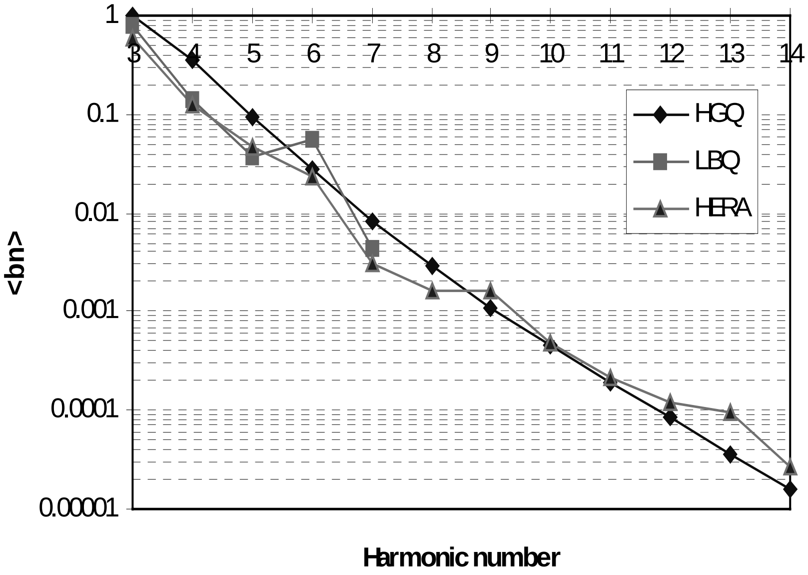

Fig. II.1.2.4-1. Random normal harmonic coefficients.

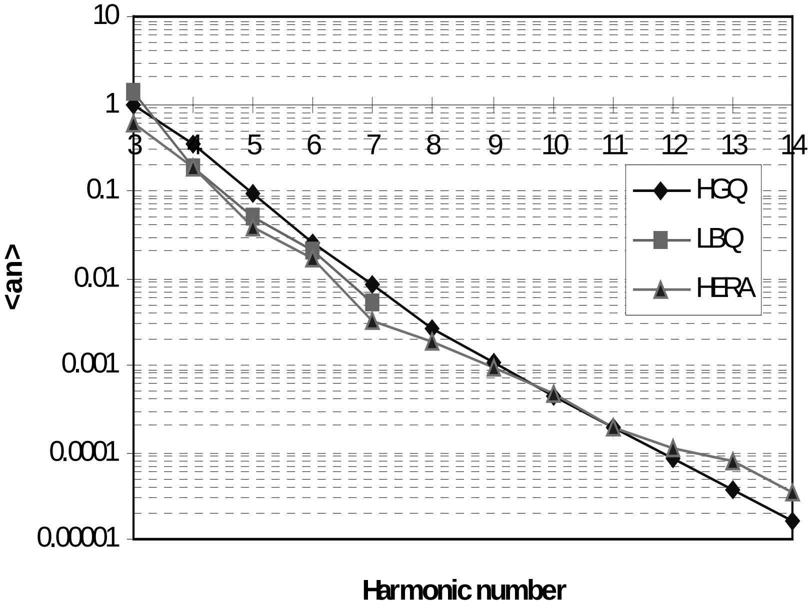

Fig. II.1.2.4-2. Random skew harmonic coefficients.

As can be seen, the expected random field errors for the HGQ are in a good agreement with the random field errors measured in LBQ and HERA quads. However, the experimental data indicate that the HGQ random errors for non-allowed low order harmonics (n<9) might be lower than the calculated values presented in this report.

II.1.2.4.4 Field Quality in the Ends

Practical experience shows that in the end regions the systematic field errors due to the coil geometry dominates with respect to all other systematic and random effects. The integrated/average systematic multipole coefficients and calculated magnetic length for the lead and return end are presented in Table II.1.2.4-6.

Table II.1.2.4-6. Integrated harmonic coefficients at 1 cm reference radius and magnetic length for the HGQ lead and return end.

Parameter	*Lead End*	*Return End*
End magnetic length, m	0.4072	0.3178
$\hat{b}_2$	10000	10000
$\hat{b}_6$	0.597	0.048
$\hat{b}_{10}$	-0.0032	-0.0041
$\hat{b}_{14}$	-0.000015	-0.000017
$\hat{a}_2$	42.8	0
$\hat{a}_6$	0.025	0
$\hat{a}_{10}$	-0.0011	0
$\hat{a}_{14}$	-0.000006	0

The uncertainty in the data presented in Table II.1.2.4-6 is related to the accuracy of the computation model. It is estimated as ±1% for the end magnetic length, ±10% for the low order multipoles ($n \leq 6$) and ±1% for the higher order multipole coefficients.

The multipole coefficients $\bar{b}_n$ and $\bar{a}_n$ for the orders n = 2, 6, 10 averaged along the small integration intervals $[z_p, z_q]$ of 2 mm as function of those interval longitudinal pozition z in the lead and return end are reported in Fig. II.1.2.4-3 through Fig. II.1.2.4-8. The data presented on these plots show the contribution of different regions along the magnet ends into the average end field harmonic coefficients presented in Table II.1.2.4-6.

II.1.2.4.5 Summary

Analysis of the field quality in the HGQ show that it is close to the preliminary specification presented in Section II.1.2.1. Some correction of systematic and random errors for the low order harmonics can be required. The possibilities for such correction are reserved in HGQ design.

The systematic error correction scheme relies on modification of the coil geometry using pole and mid-plane shims in each octant, independently for the inner and outer layer. Larger corrections may be obtained by changing the thickness of the bearing strips, while for fine tuning of the harmonics insulation layers 25 μm thick can be added or removed. The analysis shows that corrections of the systematic harmonics at nominal gradient within the predicted range of variation are possible using the existing tuning capability. Should larger effects appear the cross-section iteration might be considered.

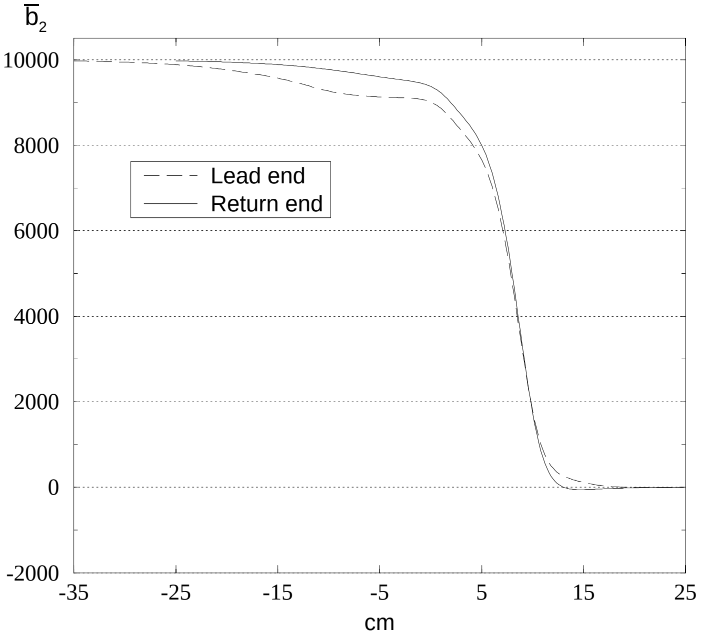

Fig. II.1.2.4-3. b_2 in the lead and return end.

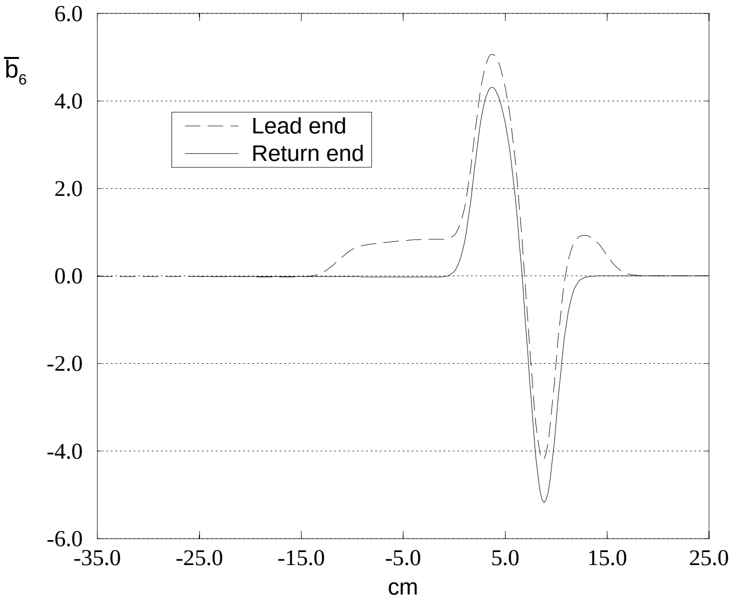

Fig. II.1.2.4-4. b_6 in the lead and return end.

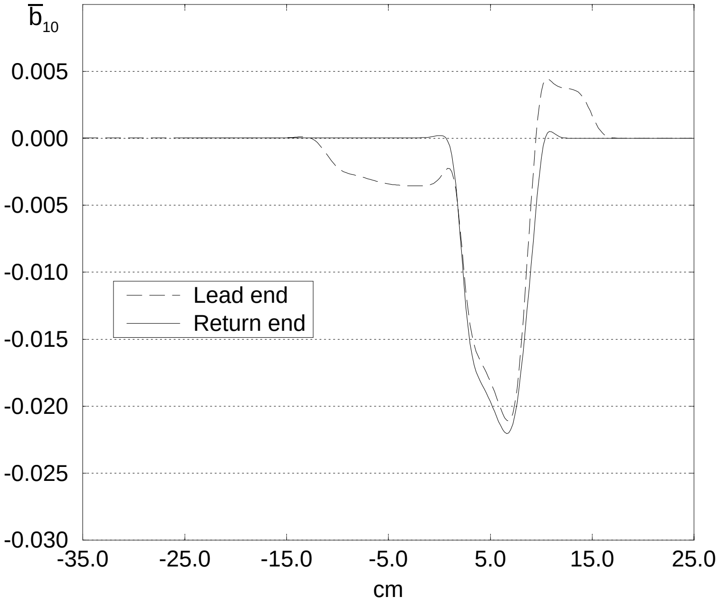

Fig. II.1.2.4-5. b_{10} in the lead and return end.

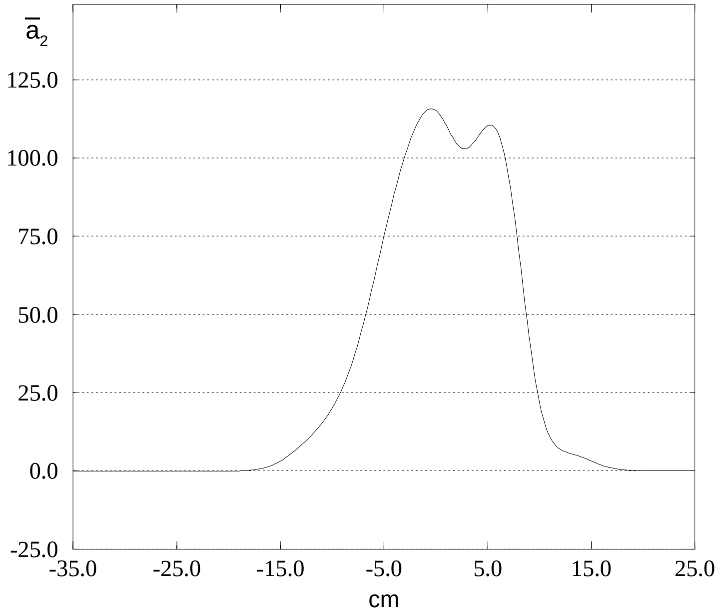

Fig. II.1.2.4-6. a_2 in the lead end.

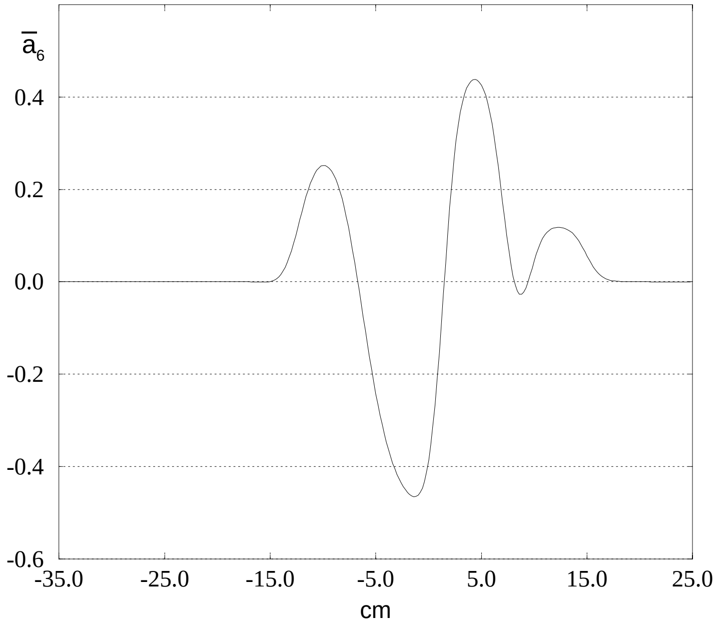

Fig. II.1.2.4-7. a_6 in the lead end.

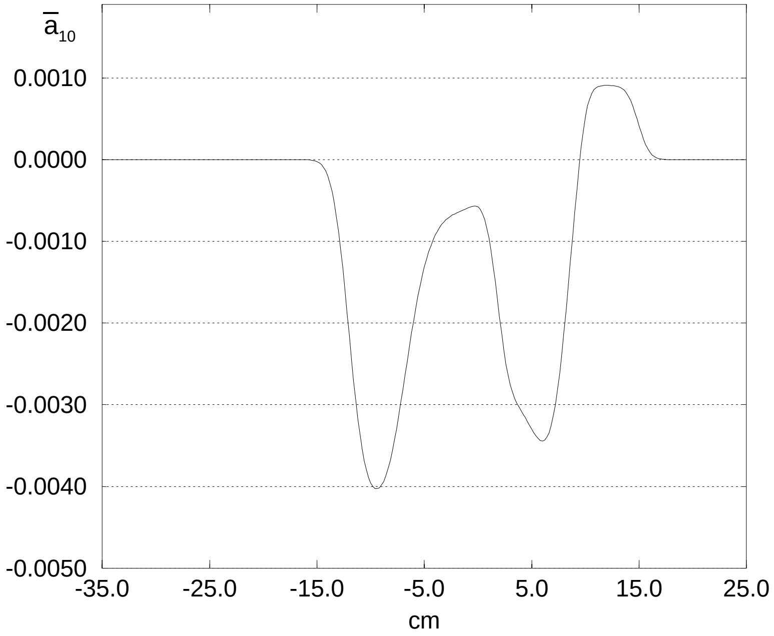

Fig. II.1.2.4-8. a_{10} in the lead end.

The RMS spread in the harmonics may be reduced either by coil re-shimming after warm magnetic measurements or by the use of iron tuning shims. The first method provides a current-independent correction, but it is labor-intensive and subject to some uncertainty as the harmonics is not exactly reproducible after collared coil reassembling. The second method is very attractive in terms of required effort and reproducibility, but the resulting correction is current-dependent due to saturation effects and is effective only for the few lowest order harmonics. Preliminary calculations indicate that only 50% of the correction capability at low current is preserved at nominal gradient. The HGQ magnetic design optimization and field quality correction scheme will be studied as part of the model magnet R&D program.

II.1.2.4.5.1 References

[25] S. Russenschuck, “ROXIE: The routine for the optimization of magnet x-sections, inverse problem solving and end region design,” *CERN AT/93-27 (MA),* August 1993.

[26] R. Meinke, “Methods for production measurements of superconducting magnets,” *DESY, HERA 90-06*, April 1990.

[27] N. L. Smirnov, “The Methods for Production of UNK SC Dipole Magnetic Measurements,” *IHEP 91-78*, Protvino, 1991.

[28] R. Hanft et al., “Magnetic Performance of New Fermilab High Gradient Quadrupoles,” *IEEE Particle Accelerator Conference (PAC91),* S. Francisco, May 1991.

[29] J. Perot & J. M. Rifflet, “Measurement Data Taken During the Industrial Fabrication of the HERA Superconducting Quadrupoles,” *Supercollider 3,* Plenum Press, NY, 1991, p.313.

II.1.2.5 Mechanical Analysis

II.1.2.5.1 Introduction

To stabilize the magnetic field characteristics of HGQ in operating field range and to reduce the probability of spontaneous quenches caused by turn motion, it is necessary to ensure the mechanical stability of turns in the coil. Turn mechanical stability is achieved by applying the prestress to the coil during magnet fabrication and by supporting the compressed coil during operation with a rigid support structure. The required prestress value is determined by magnet design, nominal operating field (field gradient) and mechanical properties of structural materials.

Coil mechanical support and prestress in the current HGQ design is completely provided by the stainless collars. Thick end plates are used to restrict the longitudinal coil motion under Lorentz forces. The prestress applied to the magnet coils at room temperature has to be sufficient to compensate the prestress decrease caused by collar spring back after the press load release, coil creep, difference in the coil and collar thermal contraction and Lorentz forces during magnet excitation.

Finite element analysis using ANSYS models has been performed to optimize HGQ coil prestress, to minimize stress in major elements of coil support structure and to determine the magnet cross-section deformation at room and helium temperature. The goal of this analysis is to develop a robust mechanical design, which is tolerant of manufacturing uncertainties in prestress and part sizes.

II.1.2.5.2 Finite Element Model Description

The ANSYS finite element models have been developed to analyze the mechanical characteristics of HGQ design during coil collaring, cooldown, and excitation to the maximum gradient.

II.1.2.5.2.1 Straight section and return end models.

2D ANSYS models of the HGQ collared coil straight section with regular collars and the return end with round collars are shown in Fig. II.1.2.5-1. Models include inner and outer coils, ground wrap and interlayer insulation, two layers of collar laminations, and two keys per quadrant. Frictionless contact elements are used as interfaces between components. Radial contact elements are used between the inner and outer coil, outer coil and collar. Azimuthal contact elements are used between the coils and collar pole faces, collars and keys. The two layers of collars produce reactions, which balance each other against the key. Quadrant symmetry is accomplished using radial and azimuthal couples between the horizontal and vertical surfaces of the coils: collars are coupled radially and azimuthally from the front collar at 0° to the back collar at 90° and from the front collar at 90° to the back collar at 0°.

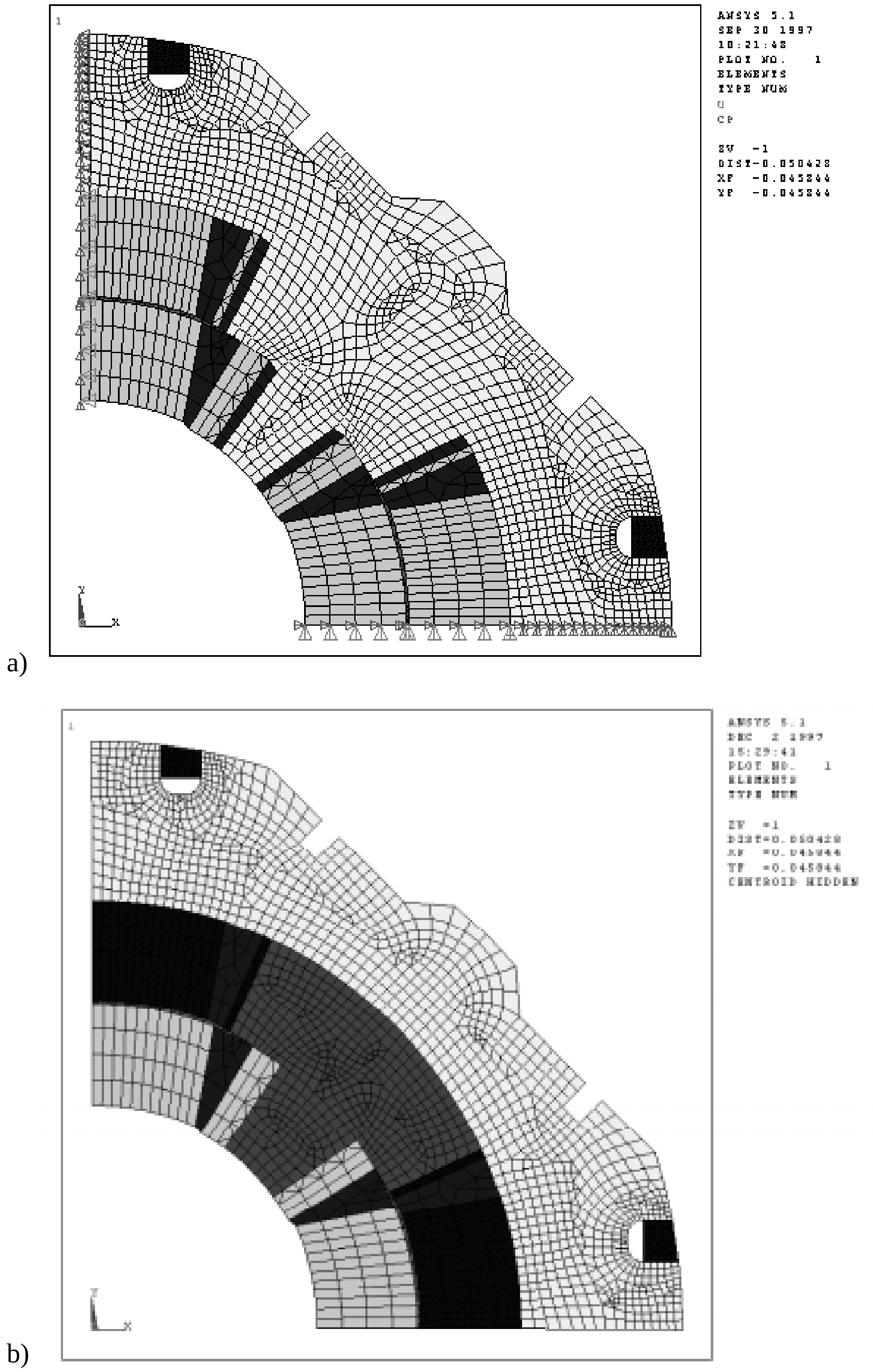

Fig. II.1.2.5-1. 2D ANSYS models of the HGQ collared coil straight section (a) and return end (b).

II.1.2.5.2.2 Lead end (end can) model.

A 2D ANSYS model of the end can (magnet lead end) is presented in Fig. II.1.2.5-2. The model includes the inner and outer coils surrounded by the Kapton ground insulation, ULTEM collet and pole insert block. An aluminum ring restrains the radial motion of all parts of the model. The geometry corresponds to the cross-section at the collared-coil/endcan interface where the Lorentz forces are largest. Octant symmetry is used in the model.

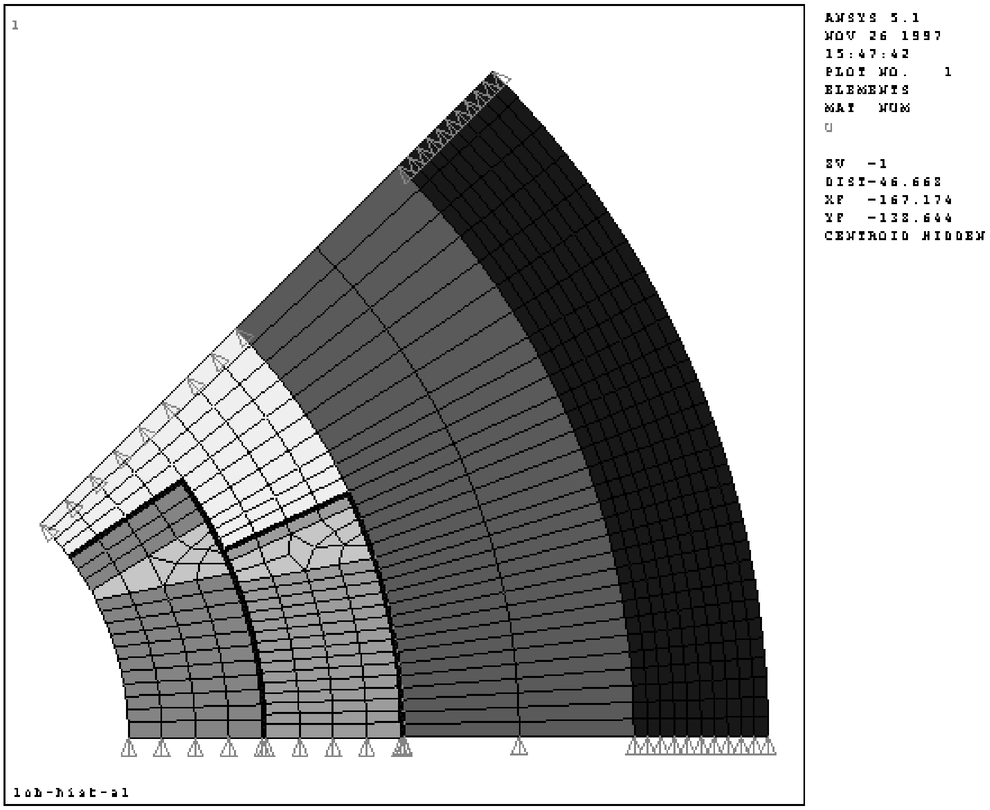

Fig. II.1.2.5-2. 2D ANSYS model of the HGQ lead end.

In the above models, all design components are represented with 4-node plane quadrilateral elements (PLANE 42). Material interfaces are modeled with one-dimensional gaps (COMBIN 40) oriented perpendicular to the interface without friction. The coil prestress induced during collaring, is simulated by imposing an azimuthal coil oversizing in the midplane. Cooldown to operating temperature is approximated by a uniform temperature change utilizing integrated thermal contraction coefficients from 300K to 1.8 K. Lorentz forces extracted from a magnetic analysis on a geometrically similar model at 13 kA, which corresponds to a gradient of 235 T/m, are also included in the models.

II.1.2.5.2.3 End plates

A 3D ANSYS end plate model is shown in Fig. II.1.2.5-3. The model consists of the thick end plate and skin, with the skin length extended back to the lead end cross section. The end plate includes a central round hole for the magnet beam pipe, round cooling holes, and rectangular holes for the bus bars. Octant symmetry is used in the model. The lead slot is simulated by removing the symmetry boundary conditions at that location.

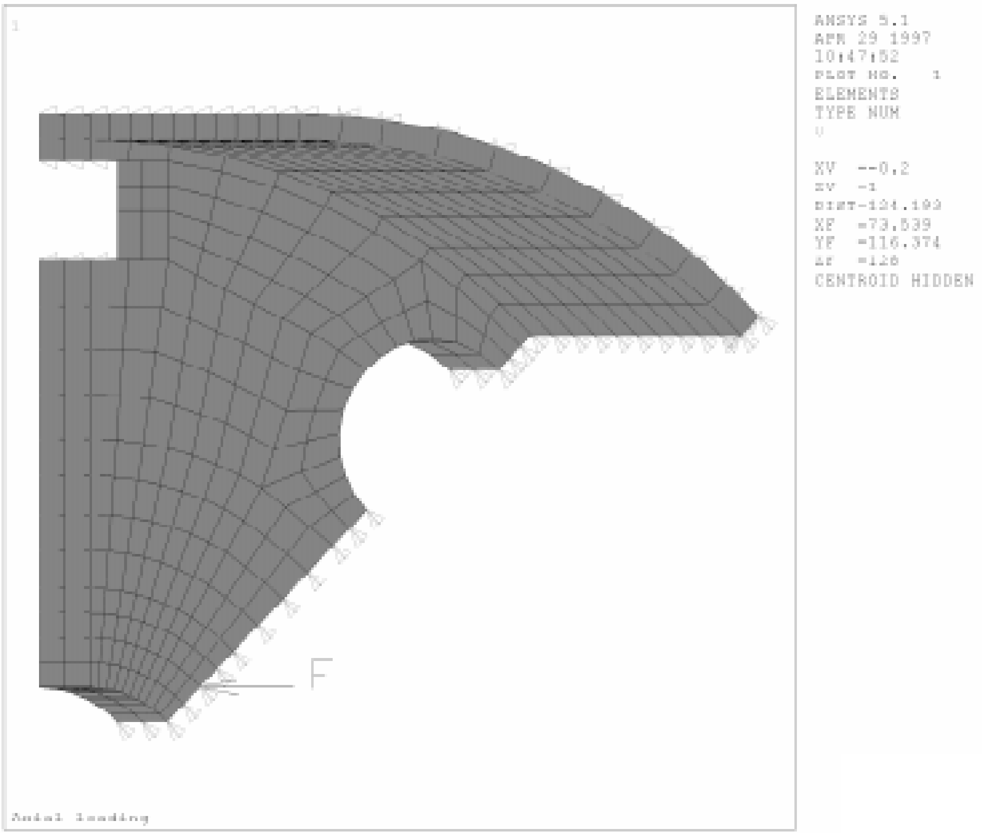

Fig. II.1.2.5-3. 3D ANSYS end plate model.

A point force equal to Lorentz load in one octant, is applied in the location near beam pipe hole corresponding to the location of the end loading screw, as it is shown in Fig. II.1.2.5-4. Results are taken at locations far enough away from this point such that local deformations due to the point load do not affect the results.

II.1.2.5.3 Lorentz Forces

The Lorentz forces acting on the coil turns are proportional to the product of current in the turn and external magnetic field. The distributions of x and y components of Lorentz force as well as total Lorentz force, calculated at a current of 1 kA in the magnet straight section, are shown in Fig. II.1.2.5-4.

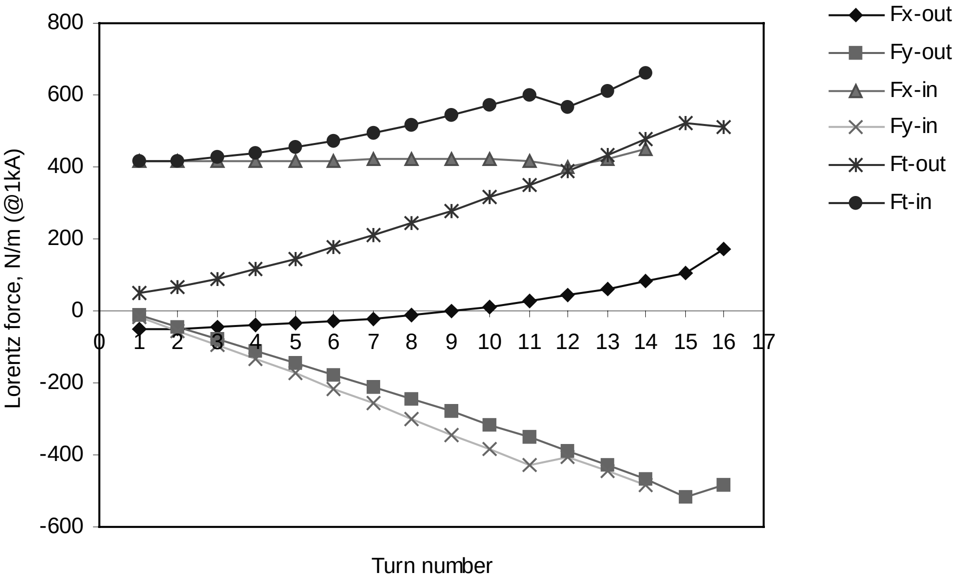

Fig. II.1.2.5-4. Distribution of Lorentz forces in HGQ cross section.

The distribution of the longitudinal Lorentz force calculated for the HGQ return end at current of 1 kA is presented in Fig. II.1.2.5-5.

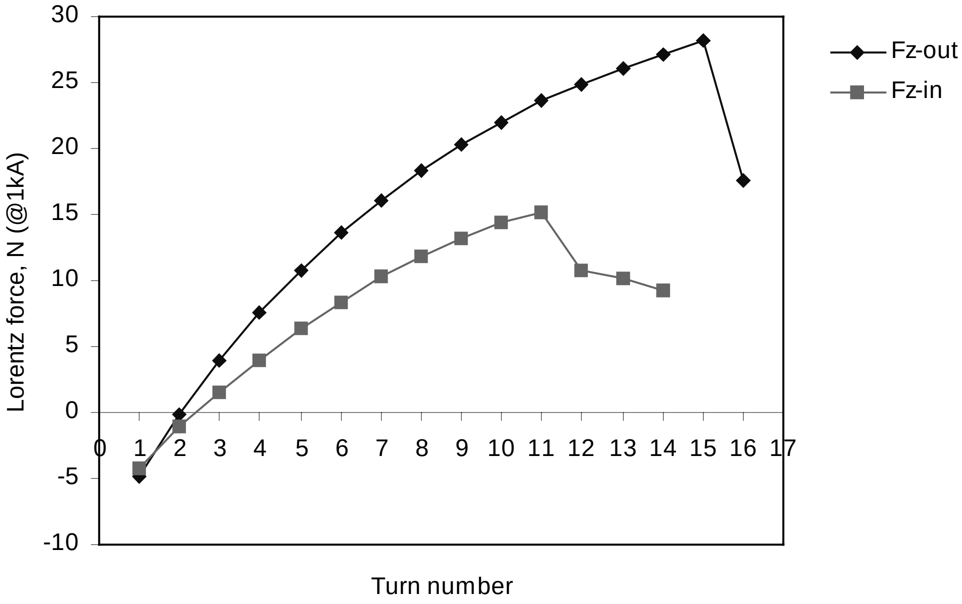

Fig. II.1.2.5-5. Distribution of the longitudinal component of Lorentz force in HGQ return end.

The distribution of the longitudinal Lorentz forces for the conductor groups at current of 14 kA per octant is summarized in Table II.1.2.5-1. The contribution of the 15-conductor group in the outer layer is dominating. The resulting longitudinal force for one octant at 14 kA current is 35.6 kN.

Table II.1.2.5-1. Longitudinal Lorentz forces in magnet ends.

Layer	*Conductor group*	*Total force, kN*
Inner	11 conductors	7.7
Inner	3 conductors	2.9
Outer	15 conductors	23.3
Outer	1 conductor	1.7

II.1.2.5.4 Material Properties

II.1.2.5.4.1 Structural materials.

Mechanical properties of the materials, which are used in the magnet, are summarized in Table II.1.2.5-2. They have been extracted from the papers [30 - 37]. Analysis of the data published has shown that the mechanical properties of the metallic materials at room and low temperatures are well known and reproducible for the different manufacturers. The uncertainty and reproducibility of the mechanical properties for the Kapton and nonmetallic compound materials are much larger.

Table II.1.2.5-2. Material mechanical properties.

Structural element	*Material*	*Thermal contraction (300-2 K), mm/m*	*Elasticity modulus, GPa*	
			warm	*cold*
Cable	Copper-NbTi composite	2.8	28	30
Wedge	Copper	3.3	120	150
Insulation	Kapton	⊥ - 10-13, ǁ - 6.0-7.5	1.5-2.5	4.5-10
End Spacer	ULTEM	6.5-7.0	7.3	8.5
Collar	Nitronic-40	3.0	190	210
Key	Bronze	3.3	120	150
Yoke	Soft iron	2.0	205	220

Skin	316L	3.0	190	210

II.1.2.5.4.2 Coil mechanical properties.

Mechanical properties of the HGQ coils, calculated based on the mechanical properties of the coil structural materials, as well as the expected azimuthal size deviation are summarized in Table II.1.2.5-3. These data are consistent with the measurement results obtained on HERA, UNK and SSC magnet coils [38 - 42].

Table II.1.2.5-3. Coil mechanical properties (expected).

	Azimuthal coil size deviation, μ m	*Azimuthal thermal contraction, mm/m*	***Azimuthal*** *elasticity modulus, GPa*	
			warm[*]	*cold*
Inner layer	±50	3.8-4.0	7 (13)	13
Outer layer	±50	4.0-4.3	11 (24)	24

*) Warm elasticity modulus shown in brackets corresponds to the coil download line.

II.1.2.5.5 Results

II.1.2.5.5.1 Coil Prestress.

Coil prestress has to be sufficient to provide the turn mechanical stability at operating temperature over the operation current range. At the same time it should not harm the cable/coil insulation at room temperature. During the HGQ prestress optimization it is also important to provide approximately uniform coil prestress in the magnet at both room and helium temperatures. The calculated nominal prestress for the HGQ inner and outer coils after assembling at room temperature as well as at helium temperature without current and with nominal current in the coil is summarized in Table II.1.2.5-4.

Table II.1.2.5-4. Nominal Coil Prestress in Pole Region

	Inner/outer coil prestress, MPa		
	Lead end (end can)	*Straight section (regular collars)*	*Return end (round collars)*
T=300 K	79/65	78/77	83/72
T=1.9 K, I=0	68/46	74/68	73/49
T=1.9 K, I=13 kA	24/23	27/35	27/27

The expected prestress variation in magnet straight section with respect to the nominal coil prestress is within ±12 MPa in the inner layer and within ±20 MPa in the outer layer. It corresponds to the essumed ±50 μm azimuthal coil size variation. The nominal coil prestress at room temperature is set by the requirement that at operating temperature and currents up to 13 kA the minimal coil prestress in pole region in both layers is not less than 15 MPa. As can be seen the maximum coil prestress at room temperature in both layers does not exceed 100 MPa, which is acceptable for the cable and coil insulation.

II.1.2.5.5.2 Collar, End Can and Key Stress.

The maximum stress in materials of the major elements of the coil support structure should be minimized to provide reliable long term magnet operation under thermal and current cycles. The stress distribution in front regular (a) and front round (b) collar for the maximum coil prestress at room temperature calculated using non-elastic material properties is shown in Fig. II.1.2.5-6. The maximum calculated stress in the end can as well as in the regular and round collar laminations are summarized in Table II.1.2.5-5.

Table II.1.2.5-5. Collar/end can maximum stress.

	Maximum stress, MPa		
	Lead end (end can)	*Straight section (regular collars)*	*Return end (round collars)*
T=300 K	130	690	690
T=1.9 K, I=0	107	650	660
T=1.9 K, I=13 kA	157	720	710

ANSYS calculations show that at room temperature the maximum stress in the collars achieves the stainless steel yield stress in small regions near key grooves. To reduce the size of these areas and to minimize the stress concentrations, the key grooves have large radii corners.. Comparison of the results of ANSYS calculation of maximum stress values in the HGQ and SSC dipole collars shows that they are on the same level. Based on that and on the real performance of the SSC dipole collars one can conclude that the existence of the stress concentration areas should not reduce the reliability of the HGQ coil support structure.

The maximum stress in the 30 mm thick aluminum end can does not exceed 135 MPa at room temperature and 160 MPa during magnet operation at currents up to 13 kA. This value is smaller than yield stress for the aluminum at both room and helium temperature.

The average stress in the keys changes from 620 MPa at room temperature to 420 MPa after cool down to 1.9 K and then to 540 MPa at the operating current 13 kA. All these values are below yield stress for key material.

a)

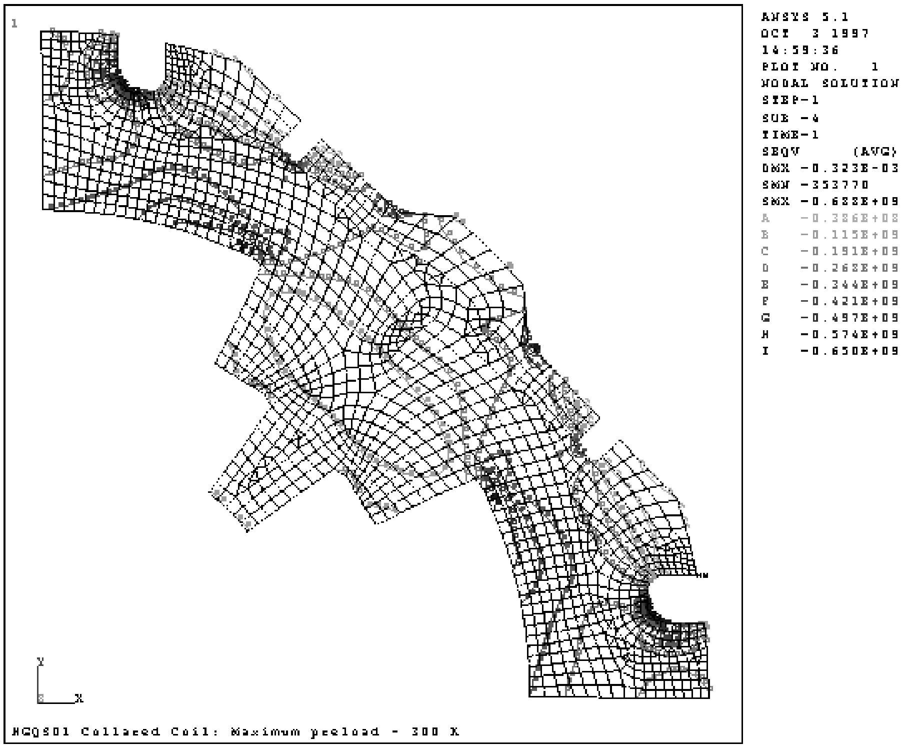

b)

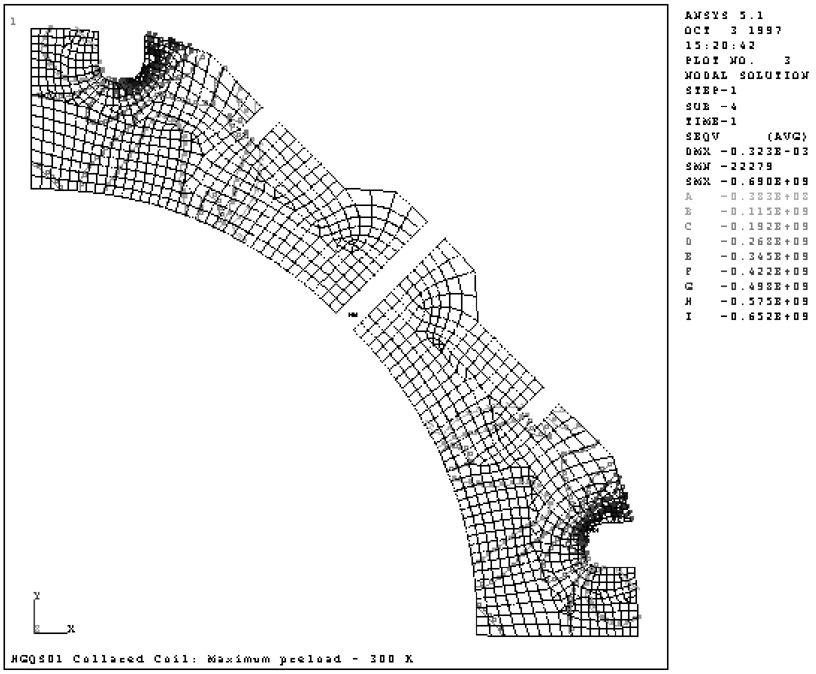

Fig. II.1.2.5-6. Stress distribution in the regular (a) and round (b) collar at maximum coil prestress at room temperature.

II.1.2.5.5.3 Cross section deflection.

Magnet cross section deformation caused by the coil prestress and Lorentz forces, affects the field quality in the bore. Turn radial displacements from the warm unstressed geometry (magnetic design) in the quadrupole straight section, calculated for the nominal coil prestress and nominal Lorentz forces at room and helium temperatures as well as at field gradient of 235 T/m are presented in Fig. II.1.2.5-7. Bore deflections at the midplane from the warm unstressed geometry (magnetic design) in the straight section and lead and return ends are summarized in Table II.1.2.5-1. At operating currents up to 13 kA (235 T/m) the radial cross section deflections from the magnetic design in the magnet body are everywhere less than 60 μm. In the end regions the magnet bore deflection is by factor of 2.5 higher.

a)

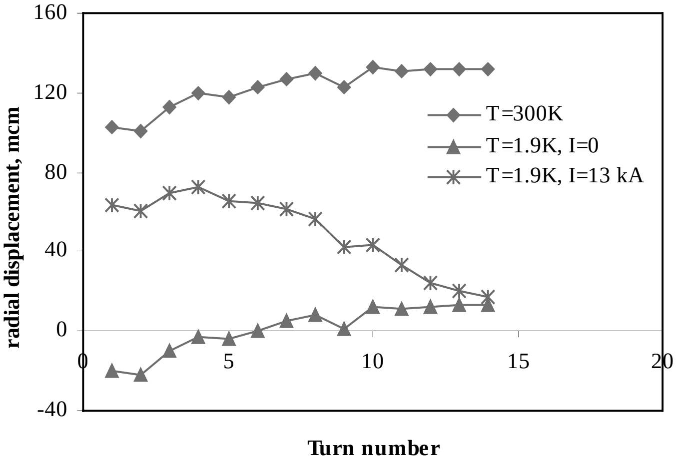

b)

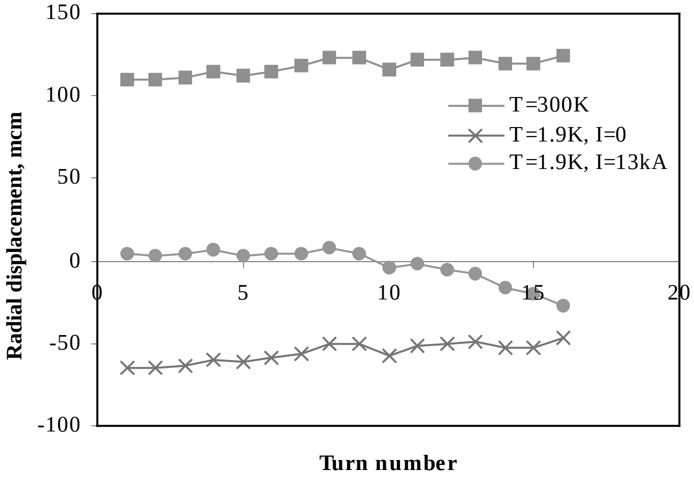

Fig. II.1.2.5-7. Turn radial displacement in the coil inner (a) and outer (b) layers.

Table II.1.2.5-6. Coil inner radius deflections at midplanes in different magnet cross sections.

	Midplane bore radial deflection, μ m		
	Lead end (end can)	*Straight section (regular collars)*	*Return end (round collars)*
T=300 K	140	100	115
T=1.9 K, I=0	-15	-20	-40
T=1.9 K, I=13 kA	145	60	95

The turn azimuthal and radial motions under Lorentz force action in the operation current range of 0 to13 kA are plotted in Fig. II.1.2.5-8. It was found that the maximum value of the azimuthal turn displacement in the above current range is less than 45 μm and the maximal radial displacement is less than 85 μm. The effect of radial and azimuthal turn displacements on the HGQ field quality was considered in Section II.1.2.4.

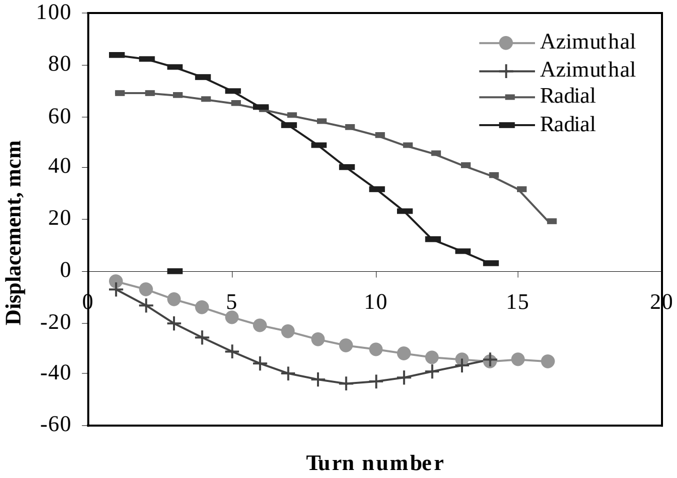

Fig. II.1.2.5-8. Azimuthal and radial turn displacement at 13 kA with respect to cold turn position in the coil.

II.1.2.5.5.4 End Plates and Skin.

The optimization of the end plate thickness includes the minimization of end plate deflection and skin elongation as well as the minimization of mechanical stresses, which occur in the area where end plates are welded to the skin. The calculated end plate maximum longitudinal deflection and maximum skin stress for the different end plate thickness at 14 kA are presented in Table II.1.2.5-7. The maximum skin stress is low enough for any of the end plate thickness considered. The skin elongation under the Lorentz forces at current of 14 kA is about 80 μm. Thus at chosen end plate thickness of 50 mm the HGQ coil end longitudinal motion does not exceed 0.5 mm.

Table II.1.2.5-7. Maximum end plate deflection and skin stress

Plate thickness, mm	*Maximum end plate longitudinal deflection, μ m*	*Maximum skin stress, MPa*
30	1382	201
40	690	127
50	409	88
60	276	65
70	205	53

II.1.2.5.6 Summary

ANSYS analysis of the HGQ mechanical structure shows that the mechanical design chosen provides the coil prestress required for the operating current range with sufficient margin, reliably restricts turn radial, azimuthal and longitudinal motion under the Lorentz force action. The maximal mechanical stresses in the major elements of coil support structure are less than the yield stress for the materials used. Existence of the small stress concentration areas in the HGQ collars should not reduce the reliability of the HGQ coil support structure.

During HGQ short model R&D stage mechanical design, structural components and materials will be experimentally studied and further optimized.

II.1.2.5.6.1 References

[30] P. Lebrun, "Cryogenic systems" (part 3 and 4), *Proceedings of CERN Accelerator School (CAS),* 1988, p.41.

[31] K.-H. Mess, P. Schmüser, "Superconducting accelerator magnets," *Proceedings of the CERN Accelerator School (CAS),* 1988, p.87.

[32] M. Davidson et al., "Measurement of the elastic modulus of Kapton perpendicular to the plane of the film at room and cryogenic temperatures," *Supercollider 4*, Plenum Press, NY, 1992, p.1039.

[33] A. Devred et al., "About the Mechanics of SSC Dipole Magnet Prototypes," *AIP Conference Proceedings, Vol. 249 (2),* 1992, p.1309.

[34] V.N. Gladky et al., "Thermal contraction of superconducting magnet materials," *Cryogenics, Vol.35, No.1,* 1995, p.67.

[35] N.I. Andreev et al., "Mechanical properties of the coil for the UNK superconducting magnets," Preprint IHEP 93-61, Protvino, 1993.

[36] J.M. Cortella et al., “Mechanical performance of full-scale prototype quadrupole magnets for the SSC,” *IEEE Trans. on Applied Superconductivity, Vol.3, No.1*, 1993, p.699.

[37] Y. Chen, “Mechanical Analysis of the DSB Cross-Section,” *SSCL-Preprint-317*, May 1993.

[38] K.-H. Mess, P. Schmüser, “Superconducting accelerator magnets,” *Proceedings of the CERN Accelerator School (CAS),* 1988, p.87.

[39] A. Devred et al., “About the Mechanics of SSC Dipole Magnet Prototypes,” *AIP Conference Proceedings, Vol. 249 (2),* 1992, p.1309.

[40] V.N. Gladky et al., “Thermal contraction of superconducting magnet materials,” *Cryogenics, Vol.35, No.1,* 1995, p.67.

[41] N.I. Andreev et al., “Mechanical properties of the coil for the UNK superconducting magnets,” Preprint IHEP 93-61, Protvino, 1993.

[42] J.M. Cortella et al., “Mechanical performance of full-scale prototype quadrupole magnets for the SSC,” *IEEE Trans. on Applied Superconductivity, Vol.3, No.1*, 1993, p.699.

II.1.2.6 Thermal Analysis

II.1.2.6.1 Introduction

The HGQ will be installed on both sides of each interaction region. A continuous heat load due to the beam-induced energy deposition will be released in magnet coils. This energy deposition varies as a function of longitudinal location, azimuth, and radius within the interaction region [43, 44]. The longitudinal distribution of the radiation induced heat deposition in LHC IR quadrupoles is shown in Fig. II.1.2.6-1. Tipical radial and azimuthal distributions of the radiation induced heat deposition for the above mentioned cross section are shown in Fig. II.1.2.6-2 and Fig. II.1.2.6-3.

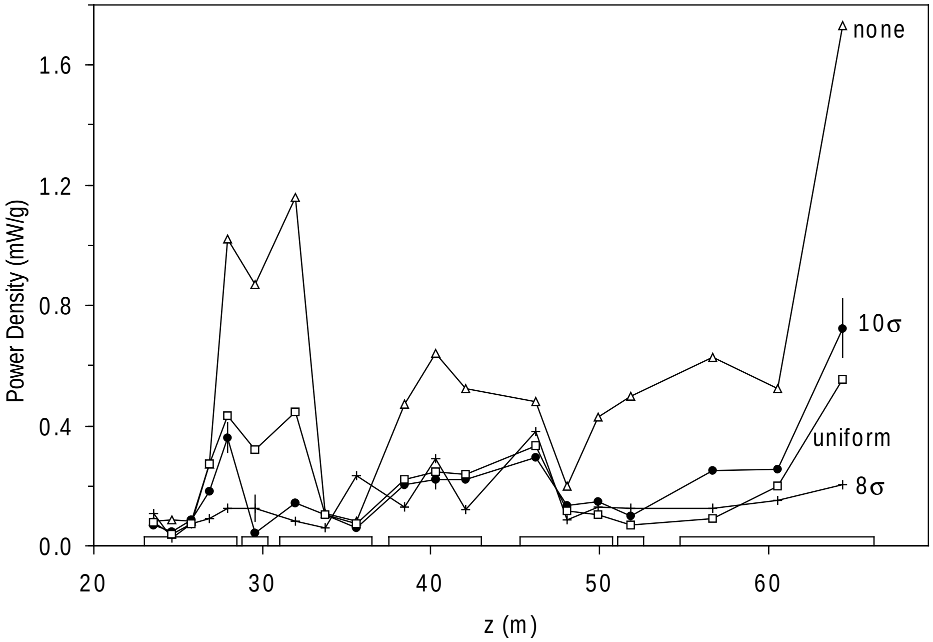

Fig. II.1.2.6-1. Peak power density vs. z for different aperture absorbers. IR layout is shown on horizontal axis.

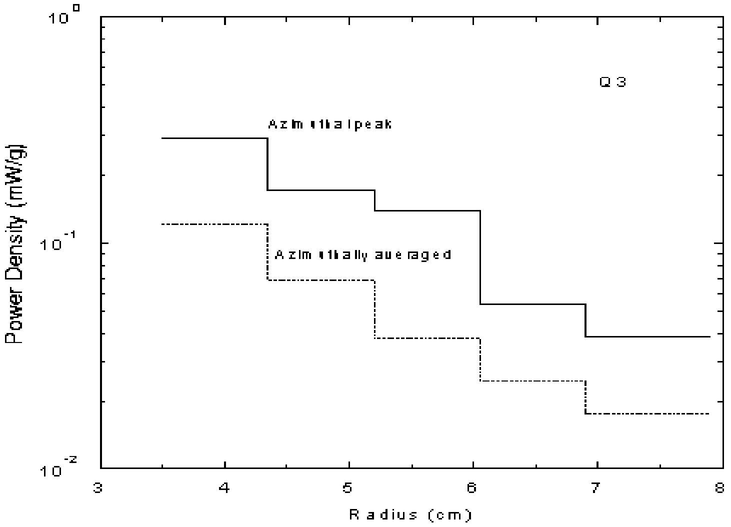

Fig. II.1.2.6-2. Radial distribution of radiation-induced heat depositions.

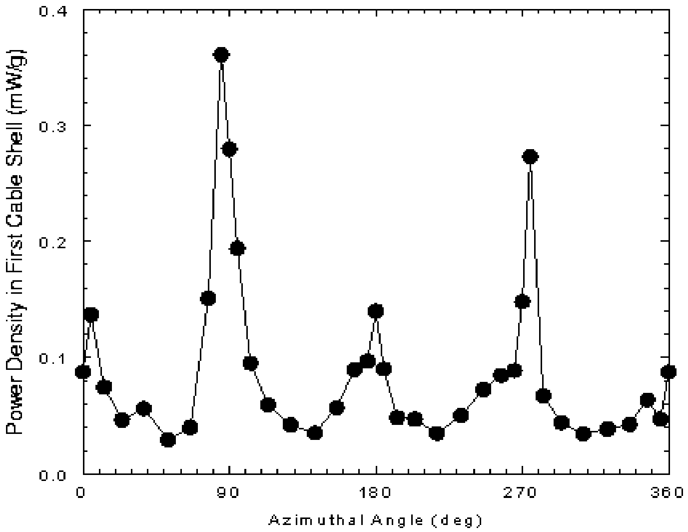

Fig. II.1.2.6-3. Azimuthal distribution of radiation-induced heat depositions.

Analysis of this distributions indicates that maximum value of the beam induced heat depositions in the inner triplet is in the region distanced from the interaction point by 32-33 m, which is located in the Q2a.

At the nominal luminosity of 10^{34} $cm^{-2}s^{-1}$ without the internal beam absorber in the magnet bore the maximum beam induced power achieves 1.2 mW/g.

The beam induced energy deposition as well as another factors (AC losses, splice heating, fluctuations of the helium temperature in cryogenic system, etc.) will cause the magnet coil temperature rise. To prevent magnet quench the cable/turn temperature everywhere in the magnet coil should be kept below the superconductor critical temperature.

This chapter describes the results of calculation of the HGQ critical temperature margin and magnet operation margin. The calculations of the temperature rise from the inner cable to the annular helium channel, then from the annular region through the laminations to the cooling holes in the iron yoke, and from the cooling holes through a heat exchanger to the saturated He II bath are also presented. The two different He II heat exchanger design and arrangement are analyzed.

II.1.2.6.2 Critical Temperature Margin

The critical temperature margin of the turns in the coil is defined as the difference between the turn critical temperature and the helium bath temperature. The turn critical temperature margin is determined by the magnet design, operating temperature, operating current, and critical parameters of the superconductor used. The turn critical temperature margin in the HGQ coil with the SSC strands is plotted in Fig. II.1.2.6-4 for the He II temperature of 1.9 K and the operating current equal to the magnet critical current.

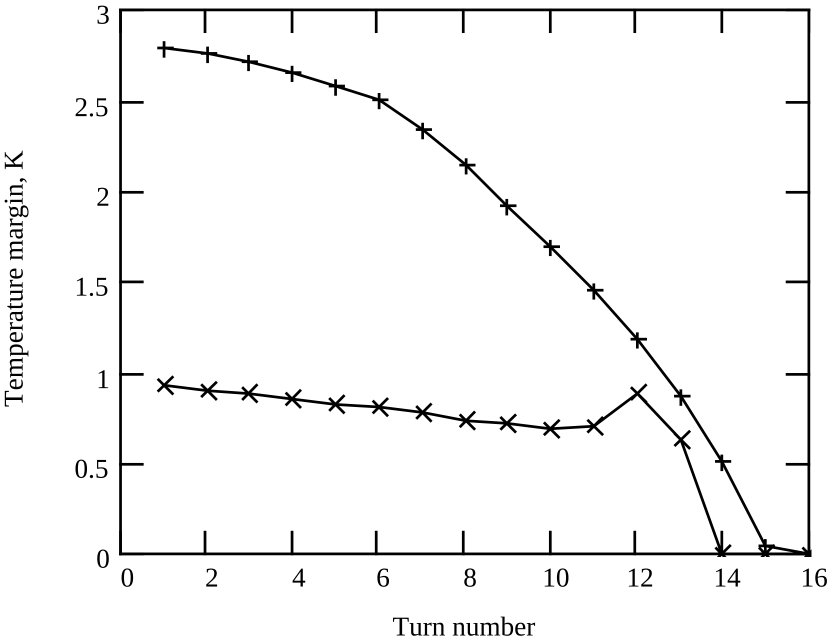

Fig. II.1.2.6-4. Temperature margin of inner and outer layer turns at I = Ic: × - inner layer; + - outer layer.

It is seen that for the above mentioned conditions all turns in the HGQ inner layer except pole turn have a critical temperature margin within 0.7-1 K. Temperature margin for the most of outer layer turns except two pole turns at the same conditions is within 0.5-2.8 K.

The effect of the magnet operating current on the turn temperature margin for the HGQ inner/outer layer pole and midplane turns at 1.9 K operation temperature is shown in Fig. II.1.2.6-5. The turn critical temperature margin is practically linearly increased when the magnet operating current is reduced with respect to the magnet critical current. The critical current margin of 10% adds about 1 K to the magnet critical temperature margin, which is determined by the inner layer pole turns. For the nominal field gradient of 200 T/m the corresponding critical current margin is 20% (nominal/critical current ratio is 0.8). In this case the critical temperature margin of the inner-layer midplane turns is about 2.4 K and of the outer-layer midplane turns is above 3.7 K. The critical temperature margin of the pole turns (magnet critical temperature margin) is about 1.9 K. At injection the critical temperature margin for all turns in the coil is practically the same and is at least 7.5 K.

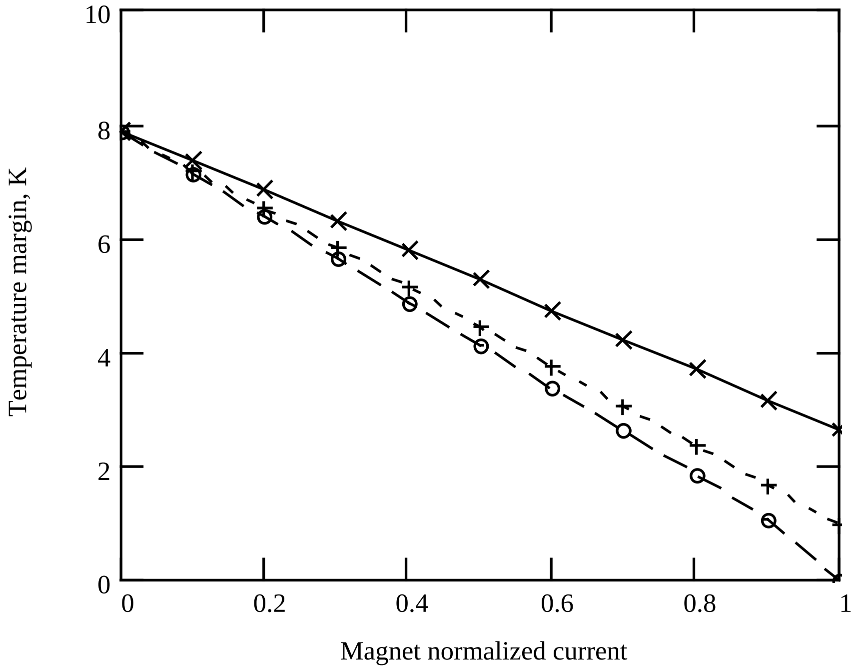

Fig. II.1.2.6-5. Turn critical temperature margin vs. normalized magnet current:
o - inner and outer layer pole turns;
+ - inner-layer midplane turns;
× - outer-layer midplane turns.

II.1.2.6.3 Magnet Operational Margin

The magnet operational margin is defined as a ratio of the turn critical temperature margin to turn temperature rise with respect to the He II bath temperature. The temperature difference between the insulated cable and surrounding He II (cable temperature rise) is determined by

$$\Delta T = \frac{q_v A}{h P_c}, \qquad (5.1)$$

where

qv - the average heating power density in the cable;

A - the cable cross sectional area;

h - the heat conductance between the cable and He II;

Pc - the cable cooling ("wet") perimeter.

The cable cooling perimeter P_c is determined by the second layer insulation wrapping scheme

$$P_c = s + P_t \cdot \left(\frac{d}{d+w} \right), \tag{5.2}$$

where

P_t - the cable total perimeter;

s – cable minor edge length;

d and w - the cooling channel width and Kapton film width, respectively.

The total thermal resistance consists of the thermal resistance through the Kapton film (cable insulation) and Kapitza thermal resistance between the Kapton film and He II. The cable is considered to be in the "dry" condition, that is, no superfluid helium exists between the bare cable and Kapton insulation. The heat conductance h, then, can be determined from

$$\frac{1}{h} = \frac{\delta}{k} + \frac{1}{h_K} \quad , \tag{5.3}$$

where

δ and k - the thickness and thermal conductivity of Kapton film, respectively;

h_K - the Kapitza thermal conductance between the Kapton film and He II.

The effect of contact thermal resistance between the Kapton film and the cable is usually included in the Kapton thermal conductivity measurement and therefore it is not included in (5.3). The typical value of Kapton thermal conductivity at 1.9 K is 0.005 W/m/K and Kapitza thermal conductance between Kapton and He II is 300 W/m^2/K.

The effective heat transfer coefficient and the cable cooling perimeter in the HGQ inner and outer layers are presented in Table II.1.2.6-1. Two cases are expected: regular turn cooling conditions with He II penetration inside inner coil into the inter-turn cooling channels and poor cooling conditions when the inter-turn cooling channels are closed for some reasons.

Table II.1.2.6-1. The effective heat transfer coefficient and cable cooling perimeter.

Coil layer	*h, W/m²/K*	*$P_{c,}$ mm*	*Case*
Inner	75	10	Regular
	53	1.5	Poor
Outer	10	2	Regular
	5	2	Poor

The calculated temperature rise for the inner and outer layer midplane turns vs. average heat energy in the cable is plotted in Fig. II.1.2.6-9. Both regular and poor turn cooling conditions are presented. The upper horizontal line shows the turn critical temperature margin at the nominal field gradient of 200 T/m. The lower horizontal line corresponds to the He II lambda-temperature (transition temperature of He II from normal to superfluid phase). In case of poor cable cooling conditions the maximum power density in the inner-layer turns must be less than 0.19 W/m and the maximum outer-layer power density must be less than 0.038 W/m. As it follows from Fig. II.1.2.6-6, the ratio of inner to outer layer heat deposition is about 2.5, and thus the above maximum outer-layer power density is achieved at the inner-layer power density of 0.095 W/m or by factor of two smaller than the maximum value for the inner layer. It means that in the case of poor cable cooling conditions the outer layer is limiting the magnet operation performance. For the regular cable cooling conditions the inner layer cable temperature can be kept below T_λ at inner-layer power density up to 0.19 W/m and the outer layer cable temperature will be below its critical value.

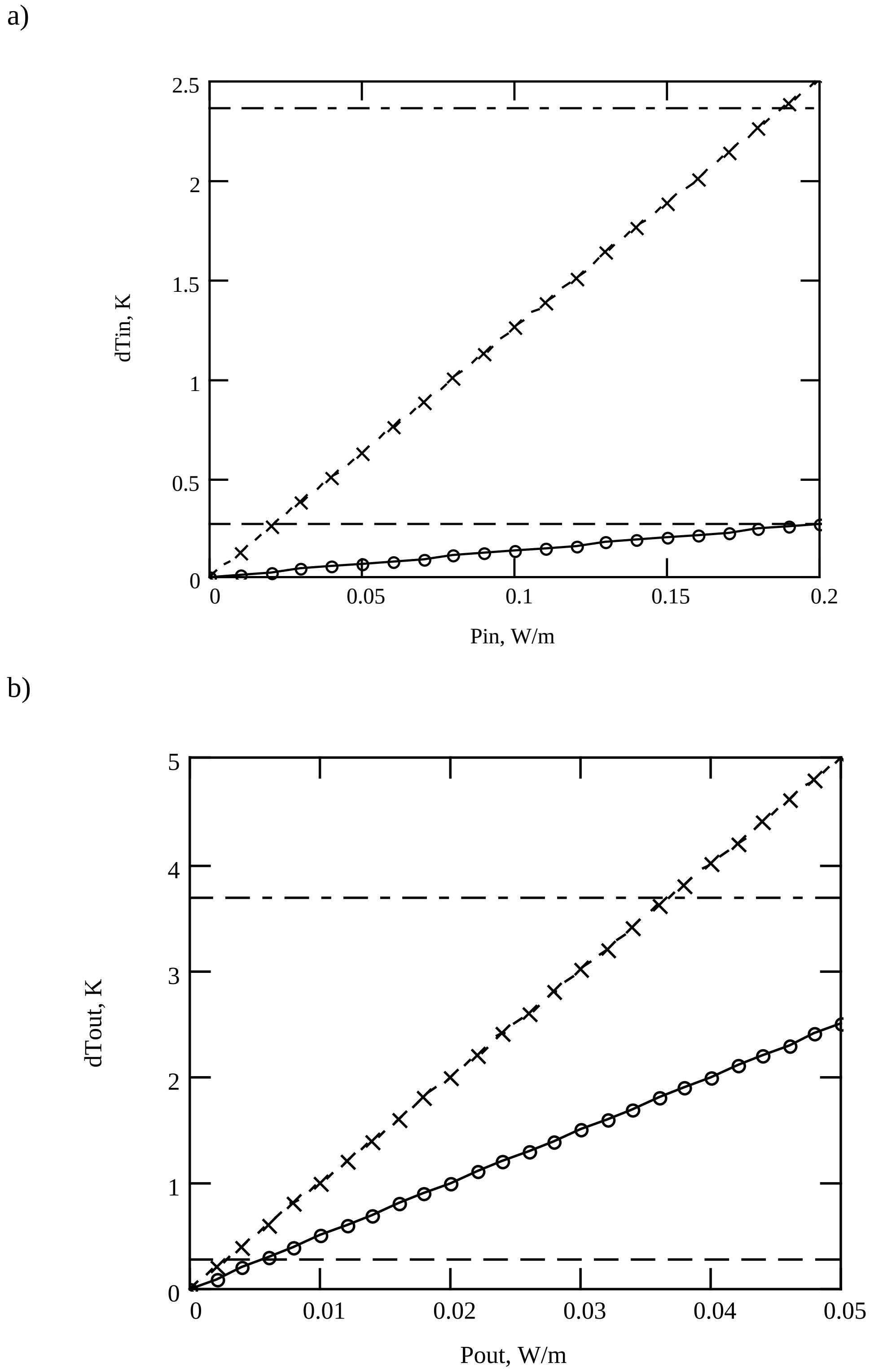

Fig. II.1.2.6-6. Inner (a) and outer (b) layer mid-plane turn temperature rise vs. average heat deposition in the inner cable:
❑ - regular turn cooling conditions; × - poor cooling conditions;
----- horizontal line corresponds to $T_c = T\lambda$;
— - — - horizontal line corresponds to turn critical temperature margin at G=200 T/m.

The reduction of beam induced energy depositions in the magnet coil can be achieved with the help of thick beam pipe/absorber [44]. The results of calculations of inner/outer layer midplane turn temperature rise and layer operational margin for different beam pipe thickness in the case of poor coil cooling conditions are summarized in Table II.1.2.6-2. In case of regular cooling conditions, the HGQ inner-layer operational margin increases by order of magnitude and the outer-layer margin increases by factor of two with respect to the data presented in Table II.1.2.6-2. As can be seen, that 4-6 mm thick beam pipe/absorber provides the operational margin of about 1.3-1.9 for HGQ even in case of poor coil cooling conditions.

Table II.1.2.6-2. Temperature rise for the inner layer cable and inner/outer layer operational margin at different beam pipe/absorber thickness.

d,	*Pmax,*	*Pin,*	*Pout,*	*Inner layer*		*Outer layer*	
mm	*mW/g*	*W/m*	*W/m*	ΔT_{cable}*, K*	$\Delta T_c\Delta T_{cable}$	ΔT_{cable}*, K*	$\Delta T_c\Delta T_{cable}$
0	1.2	0.174	0.055	2.19	1.08	5.5	0.67
2	0.8	0.116	0.037	1.46	1.62	3.7	1.0
4	0.6	0.087	0.028	1.09	2.17	2.8	1.32
6	0.45	0.058	0.019	0.73	3.25	1.9	1.94

II.1.2.6.4 Superfluid He in Small Interturn Channels

To provide the regular coil cooling conditions the HeII temperature inside the inner coil cooling channels must be kept less than T_λ. An additional temperature distribution is calculated for the heat transport in the He II cooling channel radially inward to the beam pipe region (Fig. II.1.2.6-7). The temperature profiles within the cooling channel have been calculated by using the Gorter-Mellink equation along the channel length, assuming a constant wall heat flux, q_s. The surface heat flux has been calculated based on the volumetric heat load of the midplane turn, cable cross sectional area and the cooling perimeter of the cable. The heat removal capability of He II in the cooling channel depends on the cooling channel height H and surface heat flux.

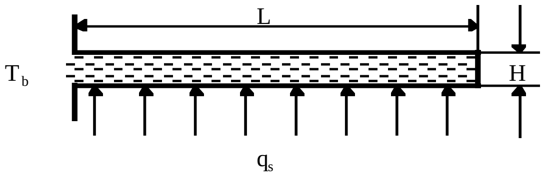

Fig. II.1.2.6-7. He II cooling channels formed by the second layer of Kapton film.

He II temperature profiles within a cooling channel with the 2 mm width and 0.025 mm height calculated for various values of surface heat flux are plotted in Fig. II.1.2.6-8. The critical surface heat flux for such channels is 13.6 mW/cm^2. This value is well above the maximum expected heat flux of about 1.8 mW/cm^2 into the interlayer channels for the HGQ inner layer midplane turns at chosen inner cable insulation scheme.

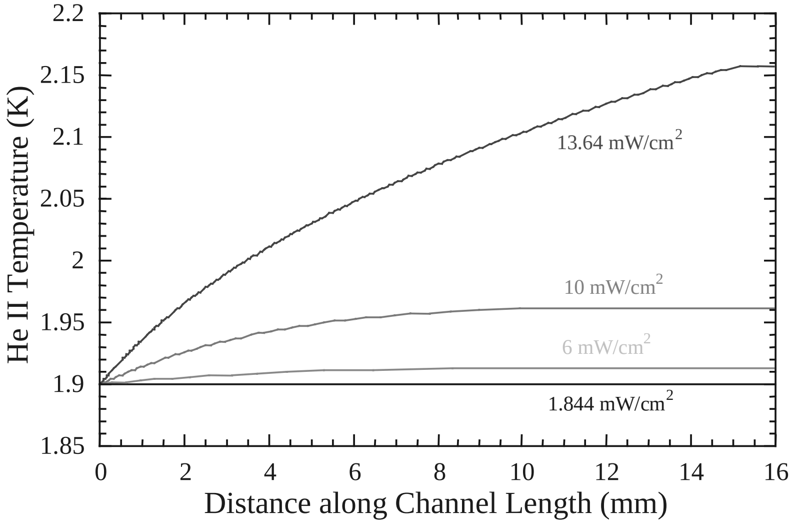

Fig. II.1.2.6-8. He II temperature profiles for various surface heat fluxes.

The effect of channel height on the temperature profiles for a heat flux of 1.8 mW/cm^2 within the He II cooling channel is shown in Fig. II.1.2.6-9. Clearly, the channel height H has to be at least 0.005 mm to keep the He II temperature within the channel below 1.95 K for the expected heat flux. The strong dependence of temperature on channel height emphasizes the importance of maintaining a minimum gap during the assembly and curing of the coil package.

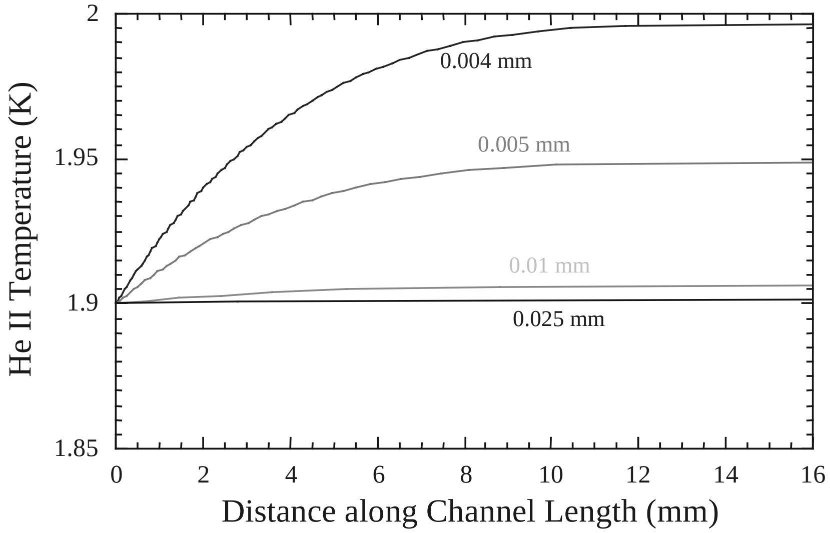

Fig. II.1.2.6-9. He II temperature profiles for varied channel heights.

II.1.2.6.5 Heat Flow Through Laminations

The temperature drop of He II from the beam pipe to the four cooling holes located in the iron yoke for various lamination packing factors has been calculated using the Gorter-Mellink equation, in a manner similar to that used for SSC interaction region quadrupoles [45]. The calculated temperature drop for the peak heat load of 5 W/m per quadrant along the magnet axis is plotted as a function of collar and yoke lamination packing factor in Fig. II.1.2.6-10.

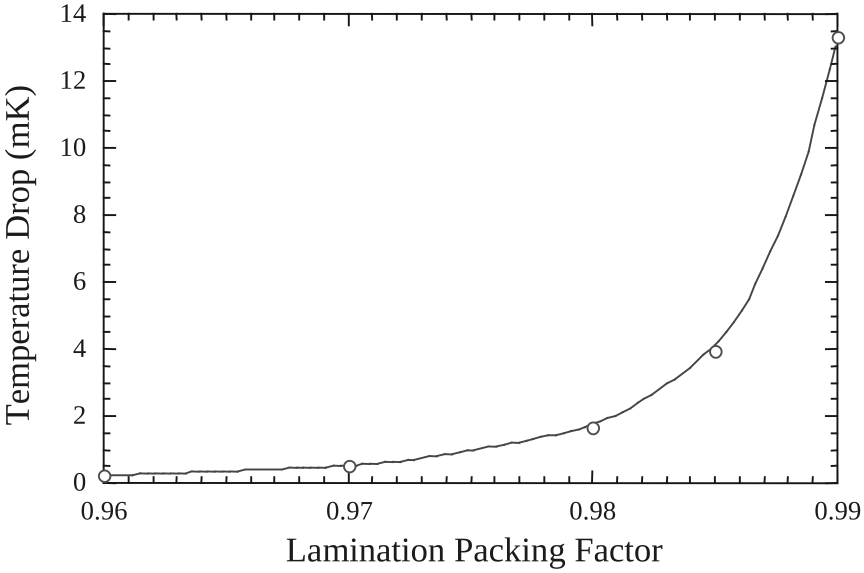

Fig. II.1.2.6-10. He II temperature drop vs. lamination packing factor.

The temperature drop within the He II is very sensitive to the gap size between the laminations as predicted by the Gorter-Mellink equation. The temperature drops in the annular channel near the beam pipe and in the collar pole area, where the special channels for He free flow are provided by the chosen collar design, are less than 0.1 mK and temperature can be considered as constant. The temperature drop from beam pipe to the coolant holes in the iron yoke can be maintained below 15 mK if a packing factor of 99% or less is achieved. Although the correlation between packing factor and average gap size between laminations is direct, individual gap sizes vary. The design iron packing factor for the HGQ is around 98%, and a small temperature drop of this size can be achieved.

II.1.2.6.6 He II Heat Exchanger

Heat exchanger transfers heat from a pressurized superfluid helium in the magnets to a saturated superfluid bath where heat is carried away by the pumped vapor. The He II heat exchanger for the LHC SC dipole magnets is a pipe placed inside the hole in the iron yoke [46]. Saturated He II flows inside the pipe and is vaporized while absorbing heat from pressurized He II surrounding the pipe. For the LHC arc dipole magnets, with an average heat load of 0.4 W/m, one heat exchanger pipe in one of the two symmetrically arranged holes in the iron yoke provides sufficient heat exchange.

For the interaction region quadrupoles at nominal beam luminosity, the average heat load is 5.3 W/m, which is 13 times higher than that of arc dipole magnets. Based on the He II heat exchanger experiment carried out at CERN [47], and using a design similar to that of the arc dipoles, four corrugated pipes are needed in the iron yoke to transport the heat from pressurized He II to saturated He II. One must carry each of these four heat exchanger pipes through interconnect between quadrupoles as well as control the saturated He II level in the four pipes.

There is an alternative to the four internal heat exchanger pipes. The heat can be carried through pressurized superfluid helium in the four holes in the magnet yoke as well as in the annular channel between magnet coil and beam pipe to the ends of the magnet and then through a larger pipe to an external heat exchanger in the same cryostat, parallel to the magnet. This heat exchanger may just be a corrugated pipe-in-pipe like what would have been in the magnet iron yoke, only a bit larger in diameter. The advantages of this system are the simplification of magnet interconnects and only one saturated liquid level to control as well as eliminating the need to place cooling holes at the same radius in the Fermilab and KEK quadrupoles and CERN multipole correctors..

Calculations were made comparing the internal and external heat exchanger arrangements. Fig. II.1.2.6-11 shows the maximum temperature rise as a function of the hole diameter in iron yoke. Three curves for the external heat exchanger arrangement are given for various heat-exchanger pipe sizes as a comparison. The total heat load per one triplet is 160 W and total triplet cryogenic length is 30 m. The saturated He II is assumed to be at 1.8 K. For the internal heat exchanger arrangement, the temperature rise includes the one caused by the pressure drop in helium vapor and the temperature difference across the heat exchanger wall. If the heat exchanger pipes are too small, the quite large temperature rise is caused by the pressure drop of helium vapor. For the external heat exchanger, the temperature rise consists of three components, one due to the vapor pressure drop, one across the heat exchanger wall and the temperature difference in the pressurized He II.

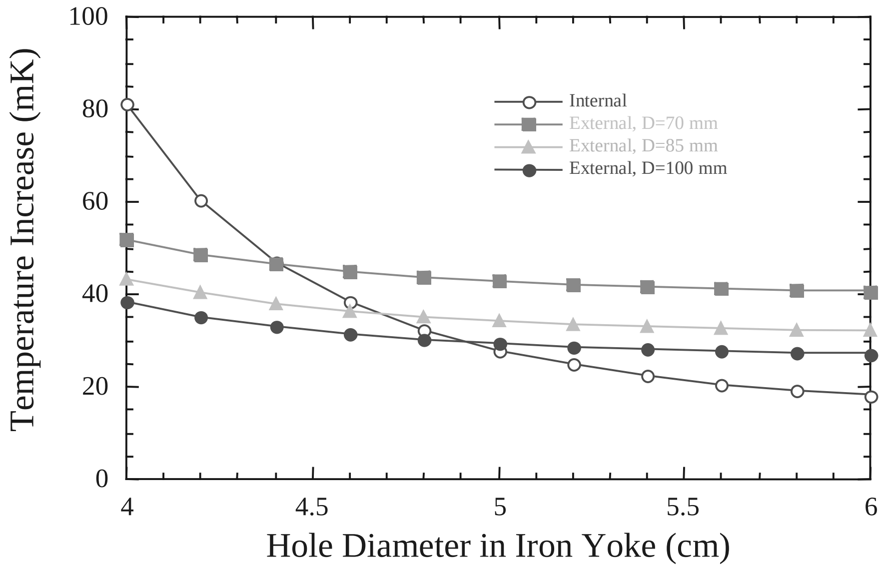

Fig. II.1.2.6-11. Temperature rise from saturated He II for various hole size in iron yoke for internal and external heat exchanger.

As can be seen from Fig. II.1.2.6-11, the external heat exchanger design is less sensitive to the hole diameter which is important for the iron yoke shape optimization. At the same time choosing the appropriate heat exchanger diameter it could be made as effective as four parallel internal heat exchangers.

II.1.2.6.7 Summary

Sufficient critical temperature margin is necessary for the compensation of the coil temperature change by the radiation-induced heating, AC losses, splice heating, mechanical disturbances, temperature fluctuations, and others. According to the calculations, for the chosen HGQ design, SSC strands and nominal field gradient200 T/m the critical temperature margin in the inner layer is 2-2.4 K and in the outer layer - 2-4 K.

The thermal analysis shows that using 2-4 mm thick beam pipe/absorber as well as the cooling channels within the inner coil insulation, in the collar structure, and maintaining a 98% packing factor in the iron laminations, the HGQ superconducting coils can be maintained below their critical temperature with sufficient margin.

The two different He II heat exchanger design and arrangement has been analyzed. The external heat exchanger may provide the means to simplify the cryogenic controls and decouple the heat exchanger design from the magnet design, with little modification to the proposed LHC cryogenic system, while maintaining an acceptable overall temperature margin.

Experimental study and optimization of the HGQ thermal performance and He II heat exchanger design will be performed in the frames of HGQ short model and Cryostat R&D stage.

II.1.2.6.7.1 References

[43] N. Mokhov & J. Strait, “Optimization of the LHC Interaction Region with Respect to Beam-Induced Energy Deposition,” presented at *the 5th European Particle Accelerator Conference,* Sitges, Spain, 10-14 June, 1996.

[44] N.V. Mokhov & J.B. Strait, “Towards the Optimal LHC Interaction Region: Beam-Induced Energy Deposition,” *Proc. of Particle Accelerator Conference (PAC’97),* Vancouver, Canada, May 1997.

[45] A.J. Mord & H.A. Snyder, “Self-Driven He II Cooling System for the Interaction Region Focusing Magnets at SSC,” *Advances in Cryogenic Engineering, vol. 39*, Plenum Press, New York, 1994, p.797.

[46] Large Hadron Collider Conceptual Design, *CERN/AC/95-05* (LHC) 1995.

[47] A. Bezaguest et al., “The Superfluid Helium Model Cryoloop for the CERN Large Hadron Collider (LHC),” *CERN AT/93-21 (CR),* LHC Notes 233.

II.1.2.7 Quench Protection

II.1.2.7.1 Introduction

HGQ will operate in severe radiation environments which may cause magnet quenches, and they have to be reliably protected during quench. The main dangers for the SC magnet during a quench are coil overheating and mechanical overstress as well as high voltage between the turns inside the magnet and between the magnet coil and ground. These factors can change the magnet operation parameters or destroy it. The magnet design and cable parameters as well as the parameters of the quench protection system should be chosen and optimized in such a way to provide a reliable magnet protection during quench.This chapter presents the results of quench protection problem analysis for the HGQ being developed at Fermilab for the LHC interaction regions.

II.1.2.7.2 Magnet and Heater Parameters

The HGQ design is described in Section II.1.2.2. It consists of four, two layer coils connected in series. Two keystoned Rutherford-type superconducting cables based on the SSC type strands are used in the quadrupole design. The main HGQ conductor and cable parameters are presented in Table II.1.2.2-1 and Table II.1.2.2-2.

The magnet inductance is 3.48 mH/m and the stored energy at the nominal current of 11.1 kA corresponding to field gradient 200 T/m is 215 kJ/m. The maximum design gradient for the SSC superconductor is about 250 T/m which is achieved at the current ~14 kA, and corresponding maximum stored energy is about 330 kJ/m.

To protect the magnet during quench, quench heaters will be used. The two-layer design allows one to put the heaters on the coil outer layers or between the inner and outer layers. Fig. II.1.2.7-1 shows the field distribution on the outer surface of inner layer and on the inner surface of outer layer where the interlayer heater is placed as well as the field distribution on the outer surface of outer layer where quench heaters are traditionally installed. Since, interlayer heaters can provide better heater efficiency, they have been chosen as a baseline. Each interlayer heater can quench one side of 10 inner layer turns and one side of 15 outer layer turns in two adjacent coils. The length of each heater is equal to double the magnet length. The number of heaters in the magnet is four (two of them are operating which quench all four quadrants and two are spare).

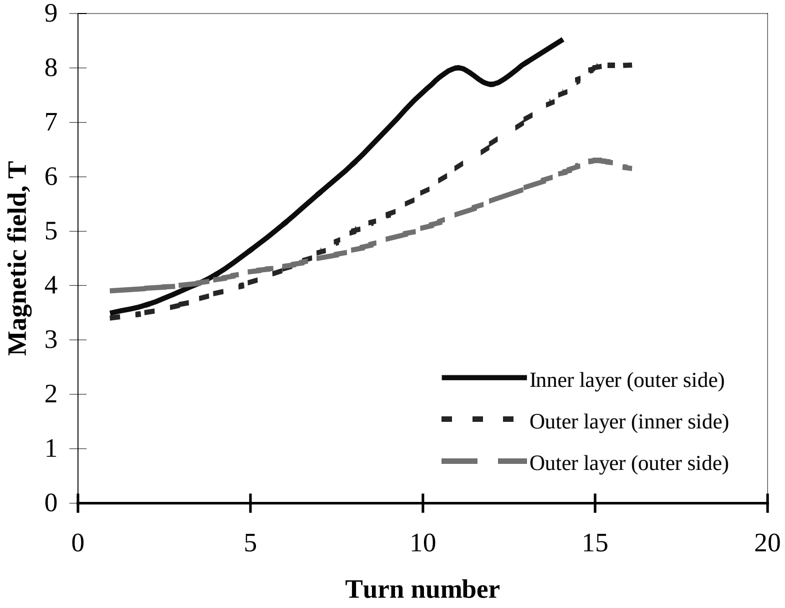

Fig. II.1.2.7-1. Field distribution in HGQ coil.

II.1.2.7.3 Coil Quench Temperature

Coil heating after a quench in adiabatic conditions is determined by the equation

$$\int_{0}^{t} I(t)^2 dt \cong N^2 \cdot S^2 \cdot \gamma \cdot \int_{Tc}^{T(t)} C(T)/\rho(T) dT \quad , \tag{6.1}$$

where

I(t) - current decay after a quench;

T(t) - coil temperature;

Tc - conductor critical temperature;

N - number of strands in the cable;

S - strand cross-section;

C(T) - strand specific heat;

ρ(T) - strand resistivity;

γ - strand mass density.

The maximum temperature T_{max} is achieved when $t \rightarrow \infty$. It is function of the quench integral (left side of (1)) and cable parameters. The relationship between T_{max} and quench integral for the quadrupole inner and outer cables is presented in Fig. II.1.2.7-2. To keep the cable temperature during quench below 400 K, as in the LHC arc dipoles [48], the quench integral has to be less than $25\cdot10^6 A^2s$ for the inner layer cable and $17\cdot10^6 A^2s$ for the outer layer one.

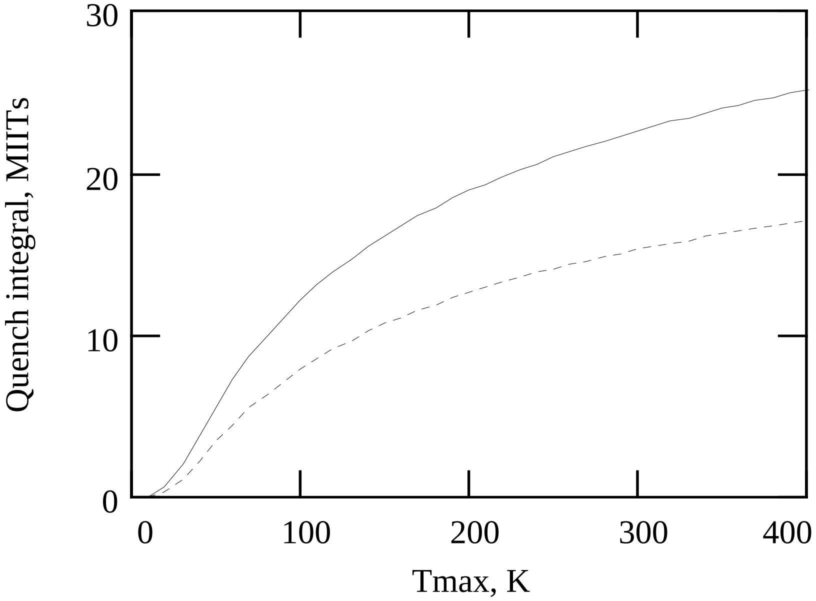

Fig. II.1.2.7-2. Relationship between the cable maximum temperature and quench integral:
——— - inner layer cable;
………. - outer layer cable.

The maximum value of the quench integral depends on the magnet current I_0, the quench detection and heater firing circuit operation time, τ_D, as well as the current decay after heater induced quench, I(t),

$$\int_0^\infty I(t)^2dt = I_0^2\cdot\tau_D + \int_{\tau_D}^\infty I^2(t)dt \quad , \qquad (6.2)$$

The dependence of the quench integral corresponding to the current decay after heater induced quench vs. magnet operating current is shown in Fig. II.1.2.7-3. The quench integral value is the same for all turns in the magnet quenched by the heaters. As follows from the data presented in Fig. II.1.2.7-4 and Fig. II.1.2.7-5, for the same current and the same quench integral, the outer layer cable is heated to a higher temperature than the inner layer one. The heater induced quench integral at the nominal current 11.1 kA equals to $8.8 \cdot 10^6 A^2 s$. The outer layer turns, quenched by heaters, are heated to the maximum temperature of 115 K and the inner layer turns are heated to 70 K.

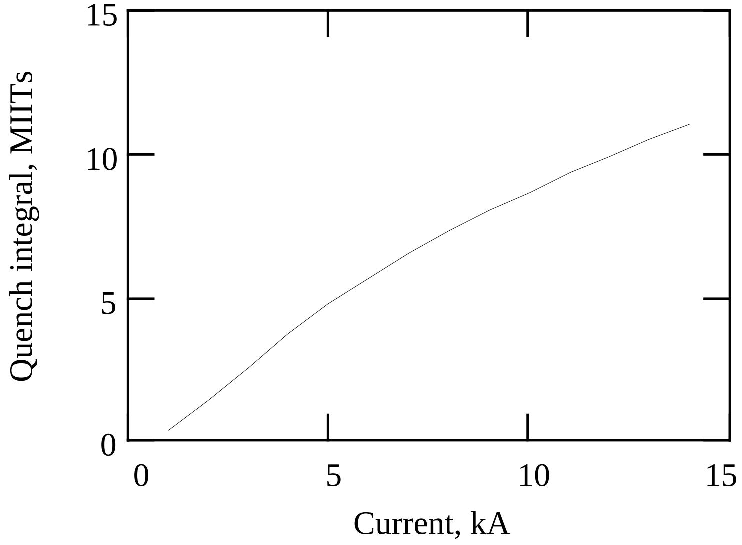

Fig. II.1.2.7-3. Dependence of the quench integral vs. magnet current.

II.1.2.7.4 Quench Detection and Circuit Operation Time

Based on the maximum quench integral budget and the value of heater induced component of the quench integral, one can determine the upper limit for the quench detection and circuit operation time (delay time). This time includes:

- Time for quench voltage to close quench detection threshold
- Time to energize heaters following detection
- Time for heat diffusion from heater to the coil and raise conductor temperature above critical value

Results of the calculations of the maximum delay time for the inner and outer cables as a function of the magnet current are presented in Fig. II.1.2.7-4. The upper limit for the quench detection and circuit operation time at nominal current of 11.1 kA is 115 ms in the case of quench in the inner layer cable and 65 ms for the quench in the outer layer cable. These limits correspond to the expected delay time for the LHC arc SC magnets [49] and can be practically realized.

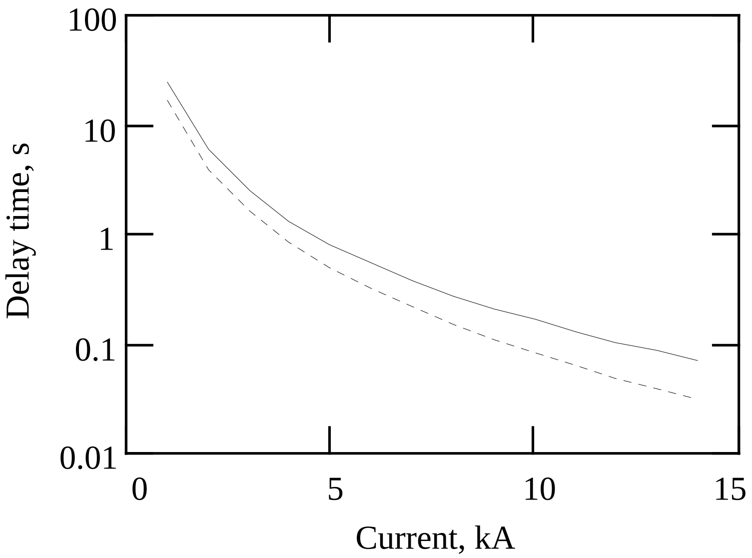

Fig. II.1.2.7-4. Dependence of the circuit operation time (delay time) vs. magnet current:
——— - inner layer cable;
………. - outer layer cable.

II.1.2.7.5 Mechanical Stress During Quench

The quenched turns in the magnet will produce a coil thermal expansion within the cold collars. As a result, the stress in the coil will increase. The stress growth is determined by the coil elasticity modulus, thermal expansion coefficient, fraction of quenched turns and their temperature. The calculated inner and outer layer mechanical stresses vs. coil temperature for chosen heater surface are shown in Fig. II.1.2.7-5. It is assumed that the thermal expansion and the elasticity modulus of the coil follow a parabolic temperature dependence.

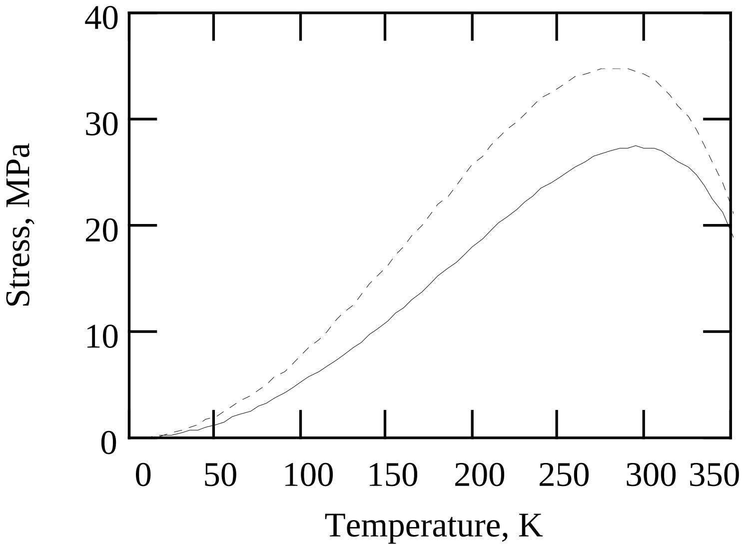

Fig. II.1.2.7-5. Mechanical stress in the layers after quench vs. maximum coil temperature:
——— - inner layer;
………. - outer layer.

A mechanical stress reaches a maximum value of ~28 MPa in the inner layer and ~35 MPa in the outer layer at a coil temperature of 250-300 K. Since the maximum temperature for most of the turns quenched by heaters is relatively small, the additional stress in the coil during a quench will be less than 10 MPa in the outer layer and less than 3 MPa in the inner one.

II.1.2.7.6 Quench Voltages

Electrical voltages are developed in the magnet during a quench. In the case when all four coils are quenched by heaters (normal operation with two heaters), the total voltage across all coils equals to zero. The coil-to-coil voltage inside the magnet in that case also equals to zero. The maximum coil-to-ground voltage, U_{cg}, is applied to the point between the inner and outer layers of each coil near magnet poles. The turn-to-turn voltage, U_{tt}, which developed in the coil during quench is a sum of the resistive, U_R, and inductive, U_L, components.

Some examples of the time dependence of the turn-to-turn and coil-to-ground voltage after a heater induced quench, computed for the current of 13 kA, are presented in Fig. II.1.2.7-6 and Fig. II.1.2.7-7. The maximum turn-to-turn voltage in the inner layer is ~10 V and in the outer one is ~25 V. The maximum coil-to-ground voltage does not exceed 200 V.

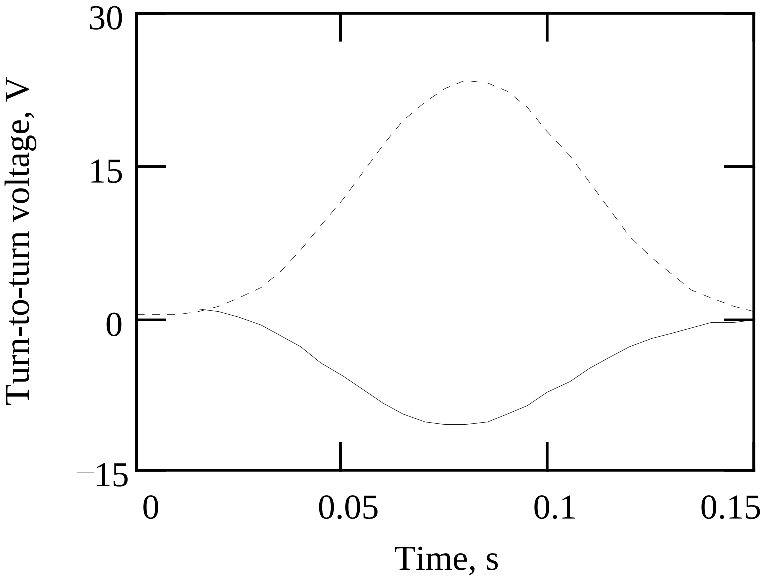

Fig. II.1.2.7-6. Time dependence of the turn-to-turn voltage after heater induced quench:
——— - inner layer cable;
------- - outer layer cable.

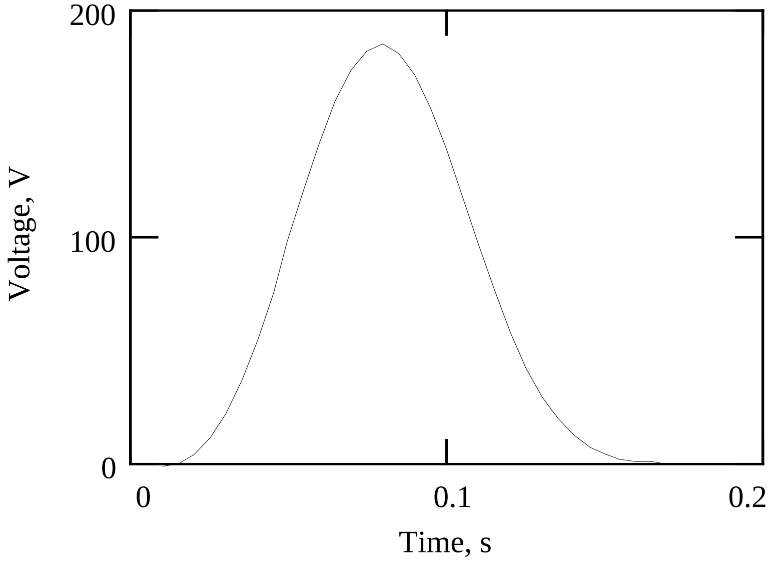

Fig. II.1.2.7-7. Time dependence of the coil-to-ground voltage during quench.

When quench is induced by only one heater, the voltage distribution depends on the heater position in the magnet. Significant coil-to-ground and coil-to-coil voltages are developed in the magnet during quench in this case. The maximum coil-to-ground voltage exceeds 1 kV and the maximum coil-to-coil voltage is 1.5-2 times higher than coil-to-ground voltage. Such high voltages can break the magnet electrical insulation and destroy the magnet. To eliminate this situation during magnet operation two set of quench heaters (operating and spare) have to be installed in each magnet.

II.1.2.7.7 Quench Pressure

The HGQ stored energy will be dumped into the coils in very short time, less than a second. The peak quench pressure depends on the stored energy and amount of liquid helium within the helium vessel.

The measurement of quench pressure during tests of the LHC dipole magnets as a function of time shows that pressure starts to rise gently between 0 and 60-80 ms and sharply afterwards. The quench relief valve starts to open 120-130 ms after the quench detection signal and reaches 90% opening within 210-250 ms. The longer the valve opening time, the higher the final pressure. A typical peak pressure is 12-14 bars if the valve opening time is 210-250 ms for a dissipated energy of 4732 kJ per 10 m long dipole magnet [50].

Fig. II.1.2.7-8 summarizes the peak quench pressure as function of stored energy per unit volume of liquid helium for the magnets cooled with He II. The data presented have been taken at CERN during tests of the 10 m long LHC dipole magnets and at Fermilab during tests of a 1.37 m long quadrupole magnet in the Vertical Magnet Test Facility (VMTF).

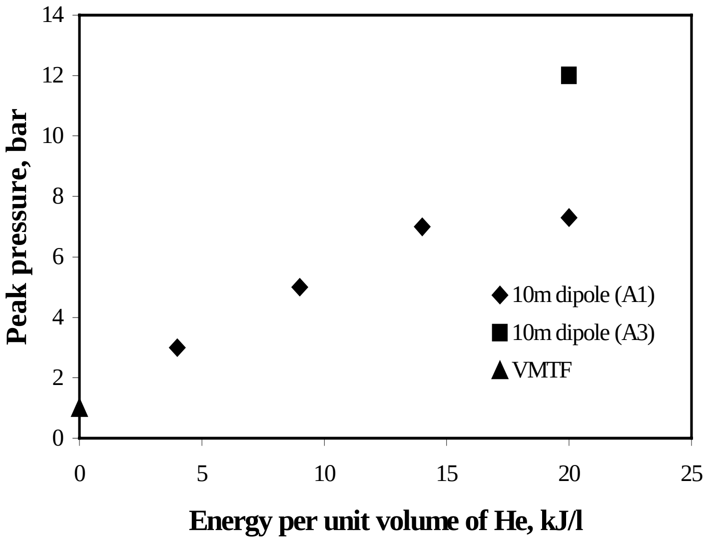

Fig. II.1.2.7-8. Peak quench pressure in the helium vessel as a function of stored energy per unit volume of He II.

The experimental data show that the peak quench pressure in cryostat during quench is proportional to the stored energy per unit volume of He II. It should be noted that even for the same designed dipole magnets, the peak quench pressure in the cryostat may vary as much as several bars as it is shown in Fig. II.1.2.7-8 for dipole magnets of A1 and A3.

The maximum stored energy in HGQ is around 330 kJ/m at maximum current of 14 kA. The calculated He II volume within the cold mass is about 20 liters. The stored energy per unit volume of He II is 16.5 kJ/l. As it follows from Fig. II.1.2.7-8, the peak quench pressure in the cryostat should be less than 12 bars. The peak quench pressure in the cryostat at nominal current of 11.1 kA will be less than 6-7 bars. For the external He II heat exchanger arrangement, an additional amount of He II will be added to the system and peak quench pressure will be reduced even further.

II.1.2.7.8 Summary

Quench protection of a HGQcan be reliably provided with two quench heaters placed between the coil inner and outer layer. Maximum values of the electrical voltages, layers temperature and stress during quench will be within safe limits close to those for the arc LHC dipoles [49]. Operation with only one heater is not recommended because of significant voltage drop between the coils inside the magnet and between the coil and ground.

The peak quench pressure in the cryostat at nominal current will be less than 6-7 bars which is within safe limit. For the external He II heat exchanger arrangement, additional amount of He II will be added to the system and quench pressure will be reduced even further.

II.1.2.7.8.1 References

[48] G. Gerin, B. Vullierme, & R. van Weelderen, “Measurement of the Thermo-Hydraulic Behavior of LHC Dipole Prototypes after Quench,” *Adv. Cryo. Eng.*, *41A*, (1996), p. 811.

[49] The LHC Study Group, “The Large Hadron Collider, Conceptual Design,” *CERN/AC/95-05*.

[50] G. Gerin, B. Vullierme, & R. van Weelderen, “Measurement of the Thermo-Hydraulic Behavior of LHC Dipole Prototypes after Quench,” *Adv. Cryo. Eng.*, *41A*, (1996), p. 811.

II.1.2.8 Conclusions

The presented analysis of the High Gradient Quadrupole design for the LHC interaction regions shows that it allows one to achieve all required parameters including the nominal field gradient and field quality, critical current and critical temperature margin, mechanical stability and quench protection. The HGQ design evolution and some additional details of the design analysis are described in the Bibliography to this Section. The experimental study and optimization of the HGQ cold mass design will be done in the frame of Short Model R&D program. Short model magnets will be tested in the newly commissioned Vertical Magnet Test Facility at Fermilab.

The major tasks to be studied in the frame of HGQ Short Model R&D program are the following:

1. Study of HGQ operation performance and margin
    - Short sample limit and training
    - Thermal performance

  - Quench protection
2. Study of HGQ field quality
   - Field harmonics in straight section
   - End field quality
   - Field quality reproducibility and tuning
3. HGQ design optimization
   - Cable and structural materials
   - External/internal splice and magnet end design
   - Quench heaters, bus-bars, lead end stabilization
   - Magnetic shims

The current HGQ short model R&D program consists of six quadrupole models with the nominal cross section and the physical length of about 2 m (1.75 m magnetic length). HGQ short model features are summarized in Table II.1.2.8-1. Different changes introduced in the magnet design with respect to its predecessor are indicated in the table by different font. The actual configuration and, perhaps, the total number of short models will be determined by the performance of practice coils, mechanical model studies and first short model test results.

In parallel with the HGQ short model R&D program the Cryostat R&D Program will be also carried out. List of major tasks for this program includes:

1. Development and fabrication a full scale model of the external heat exchanger and test it at CERN.
2. Fabrication and mechanical test a small number (2 or 3) of support posts.
3. Fabrication and test a small number of the slide mechanisms.
4. Fabrication a full scale support system and test the viability of aligning magnets after assembly.

Following the successful completion of the Short model and Cryostat R&D Programs one full-scale prototype of the Q1 will be built. The HGQ full-scale prototype development and test is an important step before the IR quadrupole production. To build and test the HGQ full-scale prototype the cryostat full-scale prototype and new Magnet Test Facility will be developed and fabricated.

Based on the results of the short model R&D program preliminary magnet specifications, which include the description of magnet major parameters and the magnet test procedure, will be prepared and coordinated with CERN. Final magnet specifications which establish the final magnet parameters, magnet certification, description of magnet storage and shipping procedure will be prepared based on the HGQ prototype test results and coordinated with CERN before the magnet production start.

Magnet production and tests are planned in FY2001-FY2004. Delivery schedule will be coordinated with the LHC interaction region installation and commissioning schedule.

IR Quadrupole project schedule is summarized in Table II.1.2.8-2.

Table II.1.2.8-1. HGQ Short Model Features.

Magnet #	*Strand/ Cable*	*Magnetic design*	*Mechanical design*	*Cable insulation*	*Quench protection*
HGQ01	**1. SSC strands.** **2. Original cable design /X-section.**	**1. Basic cross-section.** **2. Original ends.**	**1. G-10 end parts.** **2. External splices/Al end can.** **3. 50 mm end plates.**	**1.Kapton insulation (100µm).** **2. Inner cable: 4.5 mm wide outer wrap with 2 mm gap.** **3. Outer cable: butt wrap.** **4. Epoxy adhesive.**	**1. Interlayer quench heaters.**
HGQ02	1. SSC strands. 2. Original cable design /X-section.	1. Basic cross-section. ***2. Modified ends.***	**1. ULTEM end parts.** 2. External splices/ Al end can. 3. 50 mm end plates.	1. Kapton insulation (100µm). ***2. Inner cable: 9.5 mm wide outer wrap with 2 mm gap.*** 3. Butt wrapped outer layer cable. ***4.Polyimide adhesive*.**	1. Interlayer ***& outer layer*** quench heaters. **2. Spot heaters.**
HGQ03	1. SSC strands. 2. Original cable design /X-section.	1. Basic cross-section. 2. Modified ends.	1. ULTEM end parts. ***2. Internal splice/ round SS collar.*** 3. 50 mm end plates.	1. ***Variation of cable insulation thickness (Kapton 100-125µm).*** 2. Inner cable: 9.5 mm wide outer wrap with 2 mm gap. 3. Butt wrapped outer layer cable. 4.Polyimide adhesive.	***1. Optimized quench heaters (with copper).*** 2. Interlayer & outer layer quench heaters. 3. Spot heaters.

HGQ04	1. SSC strands. 2. Original cable design /X-section.	1. Basic X-section. 2. Modified ends.	1. ULTEM end parts. 2. Internal splice/ round SS collar. 3. 50 mm ***or thinner*** end plates.	1. Kapton insulation (100-125μm). 2. Inner cable: 9.5 mm wide outer wrap with 2 mm gap. 3. Butt wrapped outer layer cable. 4.Polyimide adhesive.	1. Optimized quench heaters (with copper). ***2. Optimized heater position.*** ***3. Bus-bars.*** ***4. Splice/lead Cu stabilizer.***
HGQ05	1.Final cable design.	***1. Final cross-section & end design.***	***1. Final (internal or external) splice design.*** ***2. Final end plate thickness.***	***1. Final cable insulation design and thickness.***	1.Final quench heater design. 2. Bus-bars. 3. Splice/lead Cu stabilizer.
HGQ06	1.Final cable design.	1. Final cross-section & end design.	1. Final splice design. 2. Final end plate thickness.	1. Final cable insulation design and thickness.	1. Final quench heater design. 2. Bus-bars. 3. Splice/lead Cu stabilizer.

Table II.1.2.8-2. IR Quadrupole Project Schedule

1.1 Interaction Regions					*Strait*	*FY1998*				*FY1999*				*FY2000*				*FY2001*				*FY20*		
1.1.1		IR Quadrupoles		FNAL	Zlobin	Q1	Q2	Q3	Q4	Q1	Q2	Q3	Q4	Q1	Q2	Q3	Q4	Q1	Q2	Q3	Q4	Q1	Q2	
1.1.1.1	*Tooling*				*Carson*	░	░	░	░	░	░	░	░	░	░	░	░	░	░	░	░	░	░	░
1.1.1.1.1		*R&D (2 m model) tooling*				░	░	░	░	░														
1.1.1.1.2		*Prototype tooling*						█	█	█	█	▓	▓											
1.1.1.1.3		*Cold mass production tooling*													█	█								
1.1.1.1.4		*Cryostat production tooling*													█	█	█	█	█	█	█	█	█	
1.1.1.1.5		*Infrastructure*						░	░	░	░	░	░	░	░	░	░	░	░	░	░	░	░	░
1.1.1.2	*Cold Mass*				*Nobrega*	░	░	░	░	░	░	░	░	░	░	░	░	░	░	░	░	░	░	░
1.1.1.2.1		*R&D*				░	░	░	░	░	░	░	░											
1.1.1.2.2		*2 m models*				░	░	░	░	░	░	░												
1.1.1.2.3		*Prototype*										█	█	▓	▓	▓								
1.1.1.2.4		*Q1, Q3*																█	█	█	█	█	█	█
1.1.1.2.5		*Q2a, Q2b*																						
1.1.1.3	*Cryostat*				*Nicol*	░	░	░	░	░	░	░	░	░	░	░	░	░	░	░	░	░	░	░
1.1.1.3.1		*R&D*				░	░	░	░	░	░	░	░											
1.1.1.3.2		*Prototype*												▓	▓	▓								
1.1.1.3.3		*Q1*																█	█	█	█			
1.1.1.3.4		*Q3*																				█	█	█
1.1.1.3.5		*Q2a, Q2b*																						
1.1.1.4	*Test*				*Tompkins*	░	░	░	░	░	░	░	░	░	░	░	░	░	░	░	░	░	░	░

1.1.1.4.1		*Infrastructure*				▨	▨	▨	▨	▨	▨	▨	▨	▨	▨	▨	▨	▨	▨					
1.1.1.4.2		*Test R&D models*				▨	▨	▨	▨	▨	▨	▨	▨											
1.1.1.4.3		*Test Prototype*															▩							
1.1.1.4.4		*Test FNAL quads*																		■	■	■	■	■
1.1.1.4.5		*Test KEK quads*																			■	■		
1.1.1.6	*Shipping*				*Nicol*																			

II.1.2.9 Bibliography for IR Quads

II.1.2.9.1.1 Papers:

1. R. Bossert, S.A. Gourlay, T. Heger, Y. Huang, J. Kerby, M.J. Lamm, P.J. Limon, P.O. Mazur, F. Nobrega, J.P. Ozelis, G. Sabbi, J. Strait, A.V. Zlobin, FNAL; S. Caspi, D. Dell'orco, A.D. McInturff, R.M. Scanlan, J.M. Van Oort, LBNL; R.C. Gupta, BNL, "Design of a High Gradient Quadrupole for the LHC Interaction Regions", EPAC'96 Proceedings, Barcelona, Spain, 1996.

2. R. Bossert, S. Feher, S.A. Gourlay, T. Heger, J. Kerby, M.J. Lamm, P.J. Limon, P.O. Mazur, T. Nicol, F. Nobrega, D. Orris, J.P. Ozelis, T. Peterson, P. Schlabach, J. Tompkins, A. Zlobin, *FNAL*; A. Lietzke, A.D. McInturff, R.M. Scanlan, *LBNL*, "Low Temperature Quench Performance of Fermilab Low-β Insertion Quadrupoles", EPAC'96 Proceedings, Barcelona, Spain, 1996.

4. R. Bossert, S. Feher, S.A. Gourlay, T. Heger, Y. Huang, J. Kerby, M.J. Lamm, P.J. Limon, P.O. Mazur, F. Nobrega, J.P. Ozelis, G. Sabbi, J. Strait, A.V. Zlobin, FNAL; S. Caspi, D. Dell'orco, A.D. McInturff, R.M. Scanlan, J.M. Van Oort, LBNL; R.C. Gupta, BNL, "Development of a High Gradient Quadrupole for the LHC Interaction Regions," *IEEE Transactions on Applied Superconductivity, Vol. 7, No. 2,* June 1997, p.751.

5. R.M. Scanlan, A.D. McInturff, C.E. Taylor, S. Caspi, D. Dell'orco, and H. Higley, *LBNL*; S.A. Gourlay, R. Bossert, J. Brandt, and A.V. Zlobin, *FNAL*, "Design and Fabrication of a High Aspect Ratio Cable for a High Gradient Quadrupole Magnet," *IEEE Transactions on Applied Superconductivity, Vol. 7, No. 2,* June 1997, p.936.

6. Y. Huang, J. Kerby, P.O. Mazur, T.J. Peterson and A.V. Zlobin, *FNAL*, "Thermal Design of a High Gradient Quadrupole for the LHC Interaction Regions," *IEEE Transactions on Applied Superconductivity, Vol. 7, No. 2,* June 1997, p.578.

7. A.V. Zlobin, *FNAL*, "Quench Protection of a High Gradient Quadrupole for the LHC Interaction Regions," *IEEE Transactions on Applied Superconductivity, Vol. 7, No. 2*, June 1997, p.582.

8. R. Bossert, S. Feher, S.A. Gourlay, T. Heger, J. Kerby, M.J. Lamm, P.J. Limon, P.O. Mazur, T. Nicol, F. Nobrega, D. Orris, J.P. Ozelis, T. Peterson, P. Schlabach, J. Strait, J. Tompkins, A. Zlobin, *FNAL*; A. Lietzke, A.D. McInturff, R.M. Scanlan, *LBNL,* "Tests of Fermilab Low-β Quadrupoles," *IEEE Transactions on Applied Superconductivity, Vol. 7, No. 2,* June 1997, p.598.

10. A. Lietzke, A.D. McInturff, and R.M. Scanlan, *LBNL*; R. Bossert, S. Feher, S.A. Gourlay, M.J. Lamm, P.J. Limon, F. Nobrega, J.P. Ozelis, and A.V. Zlobin, *FNAL,* "Superfluid Performance of Tevatron IR Quad Heaters," *IEEE Transactions on Applied Superconductivity, Vol. 7, No. 2,* June 1997, p.606.

11. J.P. Ozelis, P. Bause, R. Bossert, J. Dominguez, S. Feher, T. Heger, *FNAL*, "Development of Collar Lamination Strain Gauges for Coil Stress Measurements in

Superconducting Accelerator Magnets," *IEEE Transactions on Applied Superconductivity, Vol. 7, No. 2,* June 1997, p.590.

12. D.V. Mitchell, T. Heger, A. Nobrega and J.P. Ozelis, "Mechanical Studies of the Fermilab Low Beta Quadrupole Collared Coils," *IEEE Transactions on Applied Superconductivity, Vol. 7, No. 2,* June 1997, p.586.
13. T. Heger, J. Kerby, "Mechanical Analysis of a High Gradient Quadrupole for the LHC," *IEEE Transactions on Applied Superconductivity, Vol. 7, No. 2,* June 1997, p.566.
14. M.J. Lamm, J. DiMarco, E. Desavouret, S. Feher, J.D. Garvey, C. Hess, P.J. Limon, J.M. Nogiec, D.F. Orris, J. Pachnik, T. Peterson, S. Sharonov, J.B. Strait, C. Sylvester, J.W. Sim, M. Tartaglia, J.C. Tompkins, A.V. Zlobin, *FNAL*, "A New Facility to Test Superconducting Accelerator Magnets," *Proc. of Particle Accelerator Conference (PAC'97),* Vancouver, Canada, May 12-17, 1997.
15. S. Feher, R. Bossert, J. DiMarco, D. Mitchell, M.J. Lamm, P.J. Limon, P. Mazur, F. Nobrega, D. Orris, J.P. Ozelis, J.B. Strait, J.C. Tompkins, A.V. Zlobin, *FNAL*; A.D. McInturff, *LBNL*, "Quench Protection of SC Quadrupole Magnets," *Proc. of Particle Accelerator Conference (PAC'97),* Vancouver, Canada, May 12-17, 1997.
16. G. Sabbi, S.A. Gourlay, J. Kerby, M.J. Lamm, P.J. Limon, F. Nobrega, I. Novitski, J.B. Strait, A.V. Zlobin, *FNAL;* S. Caspi, R. Scanlan, *LBNL;* A. Ghosh, R. Gupta, *BNL*, "Magnetic Design of a High Gradient Quadrupole for the LHC Low-β Insertions," *Proc. of Particle Accelerator Conference (PAC'97),* Vancouver, Canada, May 12-17, 1997.
17. N.V. Mokhov and J.B. Strait, "Towards the Optimal LHC Interaction Region: Beam-Induced Energy Deposition," *Proc. of Particle Accelerator Conference (PAC'97),* Vancouver, Canada, May 12-17, 1997.
18. Y. Huang, J. Kerby, T. Nicol, and T. Peterson, "Cryogenic System and Cryostat Design for the LHC IP Quadrupole Magnets," *Proc. of CEC/ICMC'97*, Portland, OR July28-August 1, 1997.
19. G. Sabbi, J.B. Strait, A.V. Zlobin, *FNAL;* S. Caspi, *LBNL*, "Magnetic Field Analysis of the First Short Models of a High Gradient Quadrupole for the LHC Interaction Regions," *Proc. of MT-15*, Beijing, China, October 20-24, 1997.
20. Y. Huang, J. Kerby, T. Peterson, and A.V. Zlobin, "Thermal Performance Analysis of the High Gradient Quadrupole for LHC," *Proc. of MT-15*, Beijing, China, October 20-24, 1997.
21. S. Feher, R. Bossert, J. DiMarco, M.J. Lamm, P.J. Limon, F. Nobrega, D. Orris, J.P. Ozelis, J. Strait, J.C. Tompkins, A.V. Zlobin, "Study of Low-β Quadrupole Magnet with Inter-Layer Quench Protection Heaters," *Proc. of MT-15*, Beijing, China, October 20-24, 1997.
22. R. Bossert, J. Brandt, J. Carson, J. DiMarco, S. Feher, S.A. Gourlay, T. Heger, Y. Huang, J. Kerby, M.J. Lamm, P.J. Limon, P.O. Mazur, F. Nobrega, I. Novitski, D. Orris, J.P. Ozelis, T.J. Peterson, B. Robotham, G. Sabbi, P. Schlabach, J.B. Strait, M. Tartaglia, J.C. Tompkins, V. Yarba, A.V. Zlobin, *FNAL;* S. Caspi, A.D. McInturff, R.

Scanlan, *LBNL;* A. Ghosh, R. Gupta, *BNL*, “Fabrication of the First Short Model of a High Gradient Quadrupole for the LHC Interaction Regions,” *Proc. of MT-15*, Beijing, China, October 20-24, 1997.

II.1.2.9.1.2 Technical notes:

23. J. Strait, “Energy deposition studies for the LHC low-β insertions,” *TS-95-001*, 95/30/08
24. J. Strait, “Alternate LHC Low-β Inner Triplets Based on Quadrupoles of 60 - 80 mm Apertures,” *TS-95-002*, 95/22/09
25. J. Strait, “Energy deposition studies for LHC low-β insertions with different quadrupole apertures,” *TS-95-003*, 95/02/10
26. J. Strait, “Energy deposition studies for LHC low-β insertions with different quadrupole apertures – Revised,” *TS-95-004*, 95/05/10
27. A. Zlobin, J. Kerby, R. Bossert, “IRQ Cable Insulation Study Proposal,” *TS-95-005*, 95/19/10
28. S. Caspi, “A Proposed IR Quad for the LHC”, LBL SC-MAG-520 LBID-2125, October 5, 1995.A. Zlobin, “IRQ Quench Protection Analysis,” *TS-95-008*, 95/11/29
29. A. Zlobin, “Coil Porosity Study,” *TS-95-009*, 95/12/04
30. A. Zlobin , “Critical Temperature Margin of the LHC Interaction Region Quad,” *TS-96-001*, 96/01/10
31. S. Feher, J. Ozelis, A. Zlobin, “Studies of Magnet Mechanics Using Short Collared-Coil Assemblies -- Proposal,” *TS-96-002*, 96/01/17
32. T. Heger, J. Kerby, B. Wands, “HGQ Finite Element Model Verification,” *TS-96-003*, 96/02/01
33. T. Heger, J. Kerby, B. Wands, “Mechanical Analysis of High Gradient Quadrupoles for the LHC,” *TS-96-004*, 96/02/01
34. T. Heger, J. Kerby, “Comparison for 4-piece versus 2-piece Iron for HGQ Magnets,” *TS-96-006*, 96/03/05
35. A. Zlobin, S. Gourlay, “Effects of Superconductor Critical Parameters on the High Gradient Quad Performance,” *TS-96-007*, 96/03/29
36. T. Heger, J. Kerby, B. Wands, “Summary of Finite Element Analysis of LBQ Magnets (DRAFT),” *TS-96-009*, 96/06/06
37. J. Brandt, “LHC IR Quadrupole Cable Test Winding Results,” *TS-96-010*, 96/07/10
38. S. Feher, M. Lamm, A. Zlobin, “Proposal for the Fabrication and Test of RD2,” *TS-96-012*, 96/07/24
39. J. Brandt, A. Simmons, “Coil End Design for the LHC IR Quadrupole Magnet,” *TS-96-013*, 96/11/06

40. J. Brandt, “Preform and Pole Splice Design for the LHC IR Quadrupole Magnet,” *TS-96-014*, 96/11/06
41. J. Strait, “Internal Absorbers and Superconducting Dipoles in the High Luminosity IRs for the LHC,” *TS-96-016*, 96/11/15
42. J. Ozelis, “Results of Strain Gauge Measurements for Low-Beta Quadrupole Mechanical Model #4 with Additional Observations,” *TS-96-017*, 96/12/11
43. J. Ozelis, “Strain Gauge Results From LBQ RD #2 Collaring,” *TS-96-018*, 96/12/11
44. S. Caspi, K. Chow, “Normal and Skew Multipoles in the LHC Low Beta Quad – Rev.1”, LBL SC-MAG-577, February 1997.J.P. Ozelis, “Capacitance Strain Gauges - An Introduction and Modest Proposal,” *TS-96-020*, 96/12/17
45. J. DiMarco, S. Feher, M.J. Lamm, D. Orris, J.P. Ozelis, J.C. Tompkins, A.V. Zlobin, “R54002 Test Report,” *TD-97-001*, 97/01/21
46. T. Heger, “ANSYS Model of LBQ Mechanical Model #4,” *TD-97-002*, 97-02-25
47. J.P. Ozelis, “Strain Gauge Measurements of Coil Stresses During Second Collaring of LBQ Magnet RD#2,” *TD-97-003*, 97/02/20
48. I. Novitski, “HGQ Mechanical Model - Regular Collars,” *TD-97-004*, 97/2/28
49. I. Novitski, “HGQ Mechanical Model - End Can,” *TD-97-005*, 97/2/28
50. T. Heger, “Verification of the Use of Non-Linear Materials Option in ANSYS Software,” *TD-97-006*, 97/1/6
51. T. Heger, “Coil Stress Loss Due to Cooldown as a Function of Coil Modulus,” *TD-97-007*, 97/2/27
52. J. Ozelis, “Strain Gauge Results from Yoking of RD2a,” *TD-97-008*, 97/3/14
53. T. Heger, “Summary of a Finite Analysis of the HGQ Collared Coil,” *TD-97-009*, 97/03/18
54. G. Sabbi, “Calculation of the Longitudinal Lorentz Forces in the Return End of the HGQ,” *TD-97-010*, 97/03/31
55. G. Sabbi, “Load Lines and Short Sample Limits for HGQ Model #1,” *TD-97-011*, 97/04/02
56. G. Sabbi, A. Zlobin, “Expected Field Errors in the HGQ Magnet Body,” *TD-97-012*, 97/04/08
57. J. Ozelis, “Tests of Capacitance Gauges in LBQ Mechanical Model,” *TD-97-013*, 97/04/09
58. J. Ozelis, “Capacitance Strain Gauge Development at Fermilab,” *TD-97-015*, 97/04/10
59. A. Zlobin, “HGQ Coil Mechanical Properties,” *TD-97-016*, 97/04/16
60. T. Heger, “Finite Element Analysis of Full Round Collar Support of the Return End of HGQ01,” *TD-97-017*, 97/04/25

61. J. Strait, “Yoke Steel Requirements for HGQ,” *TD-97-018*, 97/05/02
62. T. Heger, “Finite Element Analysis of Full Round Collar Support for the Return End of HGQ01,” *TD-97-019*, 97/05/02
63. J. Kerby, “HGQ End Region Preload Loss with Cooldown for a Steel End Can,” *TD-97-020*, 97/05/07
64. J. Kerby, “Peak Calculated Stresses in SSC 50mm Dipole Collars,” *TD-97-021*, 97/05/07
65. J. Kerby, “Boundary Calculation for Yoking Press Load to Skin,” *TD-97-022*, 97/05/07
66. A. Zlobin, “HGQ Short Model Program,” *TD-97-023*, 97/06/16.
67. A. Zlobin, “Cable Insulation for HGQ Short Models,” *TD-97-024*, 97/06/16.
68. T. Heger, “Bullet Load Requirements and Stress Analysis of the Bullet Assembly,” *TD-97-025*, 97/06/16.
69. J. Strait, “Geometric Apertures and Internal Absorbers in the LHC Inner Triplet,” *TD-97-026*, 97/06/26.
70. S. Feher, M.J. Lamm, J.P. Ozelis, A.V. Zlobin, “HGQ Voltage Tap and Spot Heater Location (DRAFT),” *TD-97-027*, 97/06/27.
71. P. Shaw, “Strain Gauge Data Acquisition System Operations Manual,” *TD-97-030*, 97/07/10.
72. P. Shaw, “Strain Gauge Power Density Evaluation,” *TD-97-031*, 97/07/10.
73. J. Brandt, “LHC IR Quad Tooling Winding Finger Analysis,” *TD-97-032*, 97/07/17.
74. S. Gourlay, “Q2a/Q2b Interface Options,” *TD-97-033*, 97/07/28.
75. P. Shaw, “CGCAL,” *TD-97-036*, 97/08/15.
76. P. Shaw, “CGDAQ,” *TD-97-037*, 97/08/15.
77. P. Shaw, “CGDAQ2,” *TD-97-038*, 97/08/15.
78. G. Sabbi, “Magnetic Analysis of the HGQ End Regions,” *TD-97-040*, 97/09/25.
79. T. Heger, J. Ozelis, “HGQ Mechanical Model Results-Synopsis,” *TD-97-042*, 97/09/30.
80. J. Ozelis, “Fermilab/LHC High Gradient Quadrupole Procedures for Monitoring and Recording Strain Gauge Data During Magnet Keying Process,” *TD-97-044*, 97/10/02.
81. G. Sabbi, “End Field Analysis for HGQ Model S02,” *TD-97-045*, 97/10/02.
82. T. Heger, “HGQS01 Coil Size and Modulus Measurements,” *TD-97-046*, 97/10/16.
83. T. Heger, “HGQS02 HGQ Short Mechanical Model Coil Size and Modulus Measurements’, *TD-97-047*, 97/10/16.
84. I. Novitski, J. Kerby, “End Plate Thickness,” *TD-97-052*, 97/11/21.

II.1.3 (Reserved)

II.1.4 Cryogenic Feed Boxes

The LHC has four intersection or beam collision points (IR 1, 2, 5, and 8) as shown in Fig. II.1.4.2-1. Each of these points has two assemblies (left side and right side) of high gradient quadrupole magnets (Q1, Q2, and Q3) and separation dipole (D1), as shown in Fig. II.1.4.2-3. Each assembly has a cryogenic feed box that provides the cryogenic, power, vacuum, and instrumentation connections between the LHC and the magnets.

The inner triplet magnets, Q1-Q3, will be operated in pressurized superfluid helium at 1.8 K, in a manner similar to that used by CERN elsewhere in the LHC. This results in a system that is compatible in principle and practice with the cryogenics system of the LHC. The superconducting D1 dipoles at Interaction Regions 2 and 8 will be cooled with pool boiling in a bath of saturated liquid helium at 4.5 K to avoid the complications of unnecessary superfluid helium systems. At points 1 and 5 the D1 dipoles are conventional room temperature magnets.

Fig. II.1.4.2-3 shows insertion layouts for the hardware requiring the US-supplied feed boxes, taken from CERN drawing LHCLSXG_0002. Dimensions are in meters. The feed boxes are the elements labeled DFB. There are two types of feed boxes, those with a resistive D1 (at IR1 and IR5) and those with a superconducting D1 (at IR2 and IR8). Each IR has separate feed boxes for the left and right side magnets. The shaded areas indicate that the inner triplets are operated at 1.9 K and the superconducting D1 is operated at 4.5 K. The slope is also shown for each of the regions; positive slope means that the right side is higher than the left side. Slope is an important factor in the superfluid helium flow circuit since the 1.9 K feed to the magnet string must be on the high end so it can flow down the string of magnets and provide isothermal refrigeration by boiling.

Fig. II.1.4.2-5 is a CERN sketch showing the feed box as an integral part of the beamline. Figure (a) is for the case of the non-superconducting D1 where the feed box has a warm to cold beam tube transition on the D1 end. Figure (b) is for the case of a superconducting D1 where the feed box forms a bridge for the cold beam tube and the cryostat vacuum.

II.1.4.1 Requirements

II.1.4.1.1 Current Leads

The LHC inner triplets will be provided by both the US (produced at FNAL) and Japan (KEK). We assume that the KEK-produced magnets will be used in IR1 and IR2, and the US-produced triplets will be used in IR5 and IR8. The KEK triplets have an operating current of somewhat less than 8 kA, whereas the FNAL triplets have an operating current around 11 kA.

For IR 2 and IR 8, the interaction points with superconducting D1 magnets, we require the following current leads for each lead box.

Table II.1.4.1-1: The current rating and number of current leads for the superconducting D1 case.

	Current Rating	*number of pairs*
IR2 (KEK)		
Main Quadrupole	8 kA	1
Quadrupole trimming	1 kA	1
Dipole D1	6 kA	1
Dipole correctors	1 kA	4
Multipole correctors	50 A	4
IR8 (FNAL)		
Main Quadrupole	13 kA	1
Quadrupole trimming	1 kA	1
Dipole D1	6 kA	1
Corrector Magnets	1 kA	4
Corrector Magnets	50 A	4

For IR 1 and IR 5, the interaction points with resistive D1 magnets, we require the following current leads for each lead box.

Table II.1.4.1-2: The current rating and number of current leads for the resistive D1 case.

Magnet	*Current Rating*	*number of pairs*
IR1 (KEK)		
Main Quadrupole	8 kA	1
Quadrupole trimming	1 kA	1
Corrector Magnets	1 kA	4
Corrector Magnets	50 A	4
IR5 (FNAL)		
Main Quadrupole	13 kA	1
Quadrupole trimming	1 kA	1
Corrector Magnets	1 kA	4
Corrector Magnets	50 A	4

The current leads will be specified per the applicable CERN specification, such as the follow-on production specification based on IT-2441/LHC/LHC, “Technical Specification for the Fabrication and Supply of Prototype 13 kA Current Leads using High Temperature Superconductor.”

II.1.4.1.2 Preliminary Cryogenic Requirements

The following table lists the heat loads that need to be accommodated in the US-supplied interaction region equipment. We have used the ultimate heat loads in this table in order to ensure that the cryogenic valves and heat exchangers have sufficient capacity. This list is preliminary and will be updated as the design and requirements converge to the final value.

Table II.1.4.1-3: Heat load budget.

Heat Load Source	*Temperature Level*			*Mass Flow*
	50-75 K	*4.5-20 K*	*1.9 K*	
	W	*W*	*W*	*g/sec*
Half IR1, Half IR5				
Total Heat Load in Standby	250	20	20	1.6
Operational Heat Loads (Ultimate)				
Thermal Radiation	250	0	0	
Secondary Particle Heating, etc	0	0	350	
Joint Heating	0	0	10	
Beam Tube Absorber	TBD	TBD	0	TBD
HTS Current Leads (1 pr 13 kA)	0	3	0	2
Vapor-Cooled Leads (5 pr 1 kA, 4 pr 50 A)	0	0	0	0.6
Lead Chamber	0	20	0	
Total Ultimate Operational Load in half IR	250	23	360	2.6
Half IR2, Half IR8				
Total Heat Load in Standby	325	30	20	2
Operational Heat Loads (Ultimate)				
Thermal Radiation	325	0	0	
Secondary Particle Heating, etc.	0	0	100	
Joint Heating		5	10	
HTS Current Leads (1 pr 13 kA, 1 pr 6kA))		5		3
Vapor-Cooled Leads (5 pr 1 kA, 4 pr 50 A)				0.6
Lead Chamber		20		
Total Ultimate Operational Load in half IR	325	30	130	3.6

II.1.4.1.3 Diagnostic Lead Cable Requirements

The following cable counts are required to allow the magnet diagnostic and control elements to be connected to the CERN control system. The numbers are for a typical feed box that services half of the inner triplets for each interaction region.

Table II.1.4.1-4: Cable inventory for the cryofeed box.

Sensor	*type*	*size (AWG)*	*Voltage(kV)*	*number*
Beam Diagnostics				
BPM	coax(TBD)	28(TBD)	TBD	12
Quadrupole Diagnostics				
Quadrupole Voltage (Quench)	twisted pair, kapton	28	5	16
Quadrupole Quench Heaters	twisted pair, kapton	22	5	32
Temperature Sensors	4-wire	28		10
Level Sensors	4-wire	28		6
Pressure Sensors	4-wire	28		6
Corrector Magnet Taps	T.P., kapton	28	5	16
Dipole Diagnostics				
Dipole Voltage (Quench)	T.P., kapton	28	5	4
Dipole Quench Heaters	T.P., kapton	22	5	4
Temperature Sensors	4-wire	28		2
Level Sensors				0
Cryogenics Diagnostics				
Lead and Bus Voltage Taps	T.P., kapton	28	5	16
Pressure Sensors				8
Temperature Sensors	4-wire	28		4
Level Sensors	4-wire	28		2
Bath Heaters	T.P., kapton	22	5	4

II.1.4.1.4 Configuration Requirements

CERN drawing LHCLSXG_00020A (see Fig. II.1.4.2-3) establishes the linear position of the inner triplet elements, according to LHC Optics version 5. The US-supplied Feed Boxes described in this section are denoted as DFB (Distributed Feed Box) and QTSM (Cryogenic Technical Service Module) on this drawing and are located between D1 and the Corrector magnets MCBX and MCDD outboard of Q3.

The following critical dimensions for the Feed Boxes have been supplied by CERN [51]:

Height of Single Beam from Floor Level	1100 mm
Horizontal Distance of Beam from the Tunnel Axis	700 mm
Height of Cryoline	850 mm
Diameter of Cryoline	650 mm
Horizontal Distance between Beam and Cryoline	930 mm .

The Feed Boxes in each Interaction Region will be located in slightly different surroundings as described below.

IR1 - both right and left feed boxes will be located mostly in the large galleries UJ14 on the left and UJ16 on the right. The feed boxes may extend into the 9 m diameter tunnels that lead out from these galleries.

IR2 - both right and left feed boxes will be positioned in the region where the 4.4 m diameter tunnel section connects to the galleries designated as UJ24 on the left side and UJ26 on the right side, so the D1-end of each box will protrude into the 4.4 m diameter tunnel, while the other end will be in the UJ gallery where the ceiling is more than 6 m above the floor.

IR5 - the left feed box will be located mainly in a new gallery RZ54, with some extension into the 3.8 m diameter tunnel to the left. The right feed box will be located in UJ56, an existing gallery having a diameter of 13.5 m.

IR8 - the inner triplets are positioned asymmetrically with respect to the IR, so the Feed Box for the right side is located in gallery UJ86 where the ceiling is more than 5 m above the floor. The feed box for the left side is located entirely in the 4.4 m diameter tunnel to the left of UJ84. This presents the tightest space constraint for the feed boxes.

Since the feed box diameter is no larger than the magnets, the feed box creates no impediment for machine access.

It was not possible to find an economical feed box solution which did not encroach on the “space reserved for future LEP,” as defined on CERN drawing LHCLJ0000014. Several individuals at CERN advised that this zone is intended to apply in the tunnel, and not in the interaction regions, where new hardware would need to be installed for the future LEP anyway [51, 52]. Thus, the encroachment on this region was judged to be allowable.

II.1.4.1.5 Pressure Requirements

The pressurized superfluid helium piping on the high-pressure side of the pressure safety valves will have a design operating pressure of 20 atm. The normal liquid helium piping and components will have a design operating pressure of 5 atm.

II.1.4.2 Technical Description

Fig. II.1.4.2-1 shows the positions of the eight US inner triplets and their associated feed boxes with respect to the 8 LHC helium refrigerators. Because of the arrangement of the refrigerators, the feed boxes supplying cryogenic fluids to the triplets on both sides of IR8 and the right side of IR2 are at the beginning of the cryogenic sector, whereas the remaining feed boxes are at the end of the cryogenic sector. This will cause some subtle differences between the two cases of the plumbing connections for the 50 K shields, but this will not present a major problem.

II.1.4.2.1 Schematic Diagram

The schematic for the cryogenic and electrical services for the inner triplet magnets for IR2 right is shown on Fig. II.1.4.2-7. This schematic represents the features of all feed boxes, and the differences of the others can be explained and visualized rather easily. For IR2 and IR8, the lead boxes provide services to both the inner triplets (Q1,Q2, and Q3) and the superconducting dipole (D1) as shown in Fig. II.1.4.2-7. The triplets are operated in 1-atm superfluid helium, whereas the D1 is operated in a bath of liquid helium at saturated conditions. The D1 bath is connected to the lead pot helium bath, rather than being in a separate volume, for reasons of minimizing parts count and simplifying the control elements. For explanation purposes, we divide the schematic into its major components: Quadrupole Magnets, Dipole Magnet, Cryogenic Distribution Line, Valve Box, Feed Box, and Room Temperature Recovery.

II.1.4.2.1.1 Quadrupole Magnets

For IR5 and IR8, the quadrupoles will be wound and inserted into their cryostats by FNAL. These are 2-layer quadrupoles, and will require 13 kA current leads. For IR1 and IR2, the quadrupoles will be wound for CERN by KEK, and cryostatted by FNAL. These are 4-layer quadrupoles, and will require 8 kA current leads. The schematic shows the windings connected in series, with provision for differential excitation by means of the additional 1 kA current leads. The current bus leads and the quadrupole instrumentation wires are routed along the 1-atm superfluid helium duct(s), and then through the lambda plate into the normal liquid helium bath, and then finally out to the tunnel.

II.1.4.2.1.2 Dipole Magnet

The beam separation-recombination dipole D1 is superconducting for IR2 and IR8; at IR1 and IR5, it is a normal, resistive magnet. These dipoles will be provided by CERN, and the superconducting ones which mate to our feedbox require 6 kA current leads. D1 is operated in normal liquid helium, and is therefore connected directly to the liquid helium chamber in the feed box. The current bus leads and dipole instrumentation wires are routed in the duct(s) which connect D1 to the liquid helium chamber. Because of the tunnel slope, it is necessary to vent the upslope end of D1 into gas space over the liquid helium bath to prevent accumulation of vapor and magnet “dry out.”

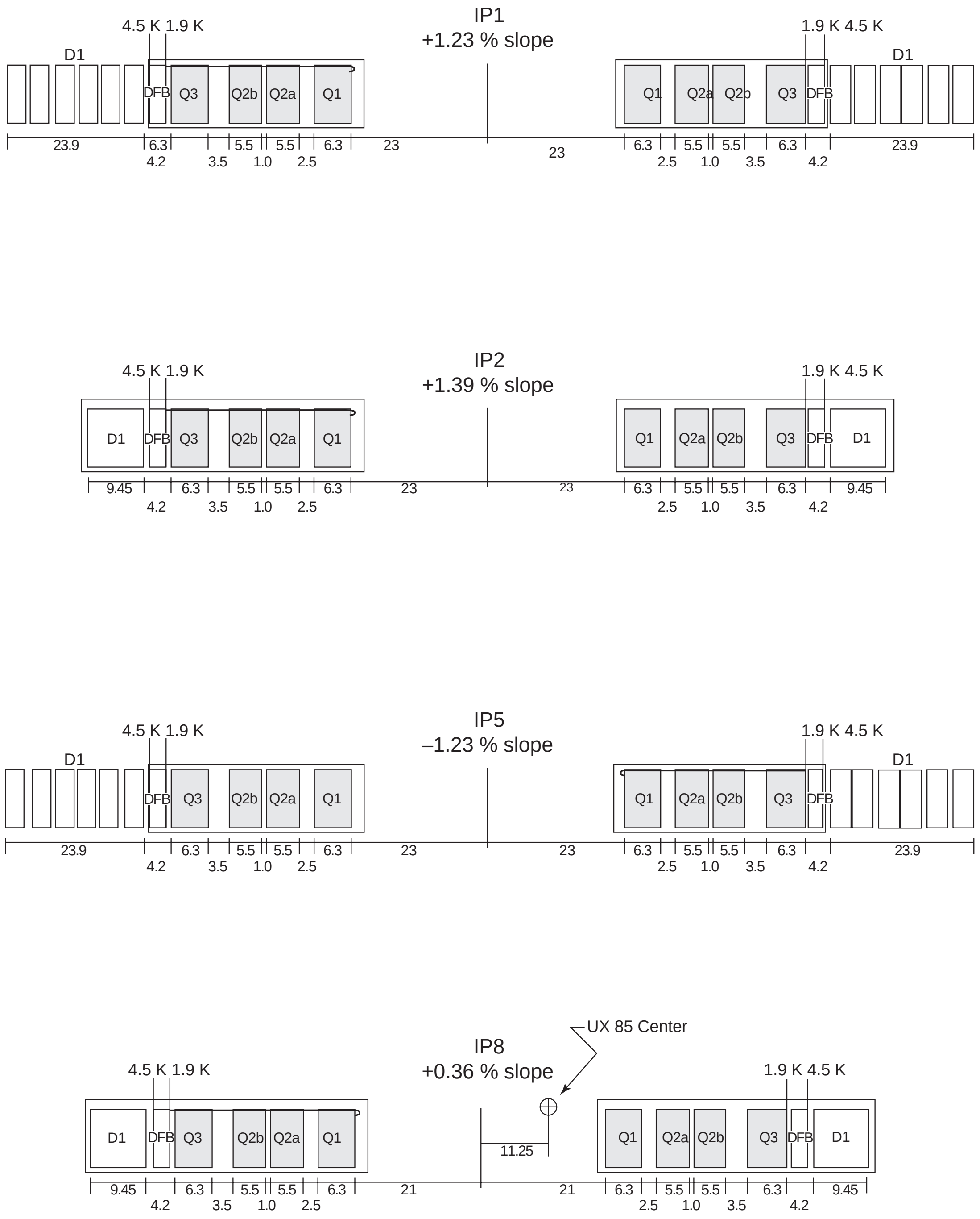

Fig. II.1.4.2-1: Location of LHC interaction points and cryoplants.

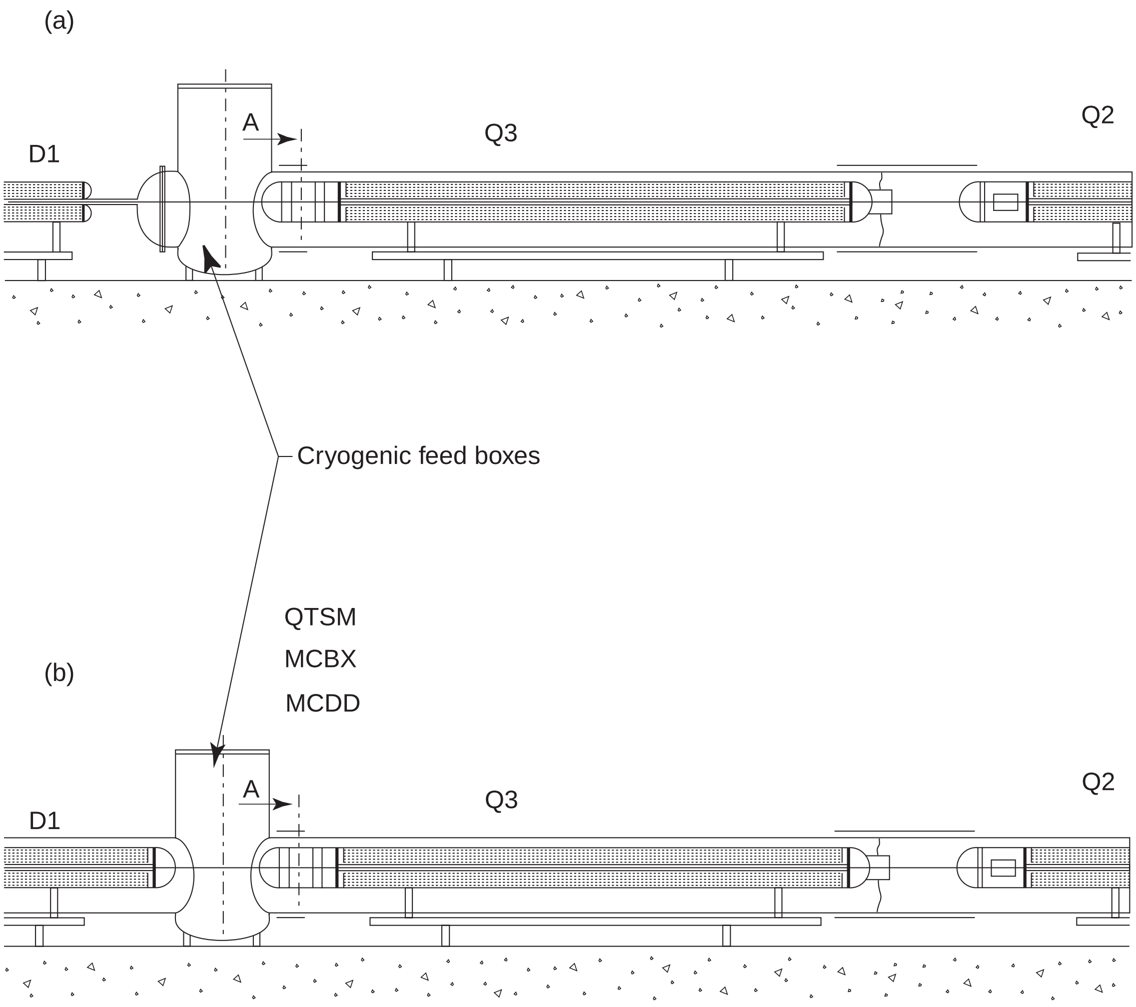

Fig. II.1.4.2-3: Insertion layout for optics version 5.

II.1.4.2.1.3 Cryogenic Distribution Line

This is a 650 mm diameter pipe located at the outside of the tunnel which contains all the cryogenic lines from the CERN helium refrigerators. The lines contained therein and their nominal conditions are:

Header B:	4 K, 16 mbar	(cold compressor inlet)
Header C:	4.6 K, 3 bar	(supply)
Header D:	20 K, 1.3 bar	(cold compressor outlet)
Header E:	50 K, 20 bar	(shield supply)
Header F:	75 K, 19 bar	(shield return)

II.1.4.2.1.4 Valve and Heat Exchanger Box

This box contains the collection of valves and heat exchanger which properly distribute and control the flow of cryogenic fluids to and from the magnets. The valve box schematic agrees with a recent CERN paper [53]. A listing of the components includes:

PSV1 - 4:	CERN-type pressure safety valve to safely vent the magnet in case of quench. Its diameter is approximately 40 mm. In addition to automatic operation as a safety device, the valve can be opened manually with an electrical signal to assist in cool down and other operations.
HX:	Heat exchanger used for precooling the 4.6 K, 3 bar helium stream to about 2.2 K at the inlet to V3.
V1 & V8:	Used for initial cooldown and liquid fill, its diameter is approximately 19 mm, with a dual trim to allow for flow control during cool down and Joule-Thompson throttling during liquid filling.
V2:	Used primarily for magnet heat exchanger cooldown, but could be used in other operational modes as well. Its diameter is approximately 19 mm.
V3:	J-T expansion valve to provide liquid for 1.9 K isothermal magnet refrigeration. It needs to supply up to 18 g/s, and has a diameter of approximately 19 mm.
V4:	Isolation valve for the HX low-pressure side. Its diameter is about 100 mm.
V5:	Inlet flow control valve for thermal shield cooling. It is controlled by the temperature of shield return gas, and has an approximate diameter of 80 mm.
V6:	Isolation valve for the thermal shield return gas. Its approximate diameter is 80 mm.
V7:	Isolation valve for the HTS current lead upper end cooling stream. Its approximate diameter is 25 mm.

V9:	J-T valve to maintain the liquid level in the lead chamber at the desired level. V9 is controlled by the liquid helium level sensing device in the lead chamber. Its diameter is approximately 25 mm.
V10:	Pressure operated check valve which returns any excess cold helium boiloff gas to the 20 K header. It prevents the lead chamber from being overpressured by the 20 K header in case of magnet quench.
V11:	A valve which allows the quadrupole string to be evacuated prior to cooldown.

The schematic Fig. II.1.4.2-3 contains a J-T heat exchanger, which is consistent with the current LHC cryogenic system design [53]. The mass flow rate through this heat exchanger is about 17 g/sec, which is considerably larger than required for the distributed heat exchangers in the main ring.

The table below summarizes the valve box component use for the four interaction points.

Table II.1.4.2-1: Valve box components for the four interaction regions.

Valve Box Component	*IR1 and IR5*	*IR2 and IR8*
V1	yes	yes
PSV1	yes	yes
V2	yes	yes
HX	yes, 18 g/sec flow rate	yes, 7/g/sec
V4	yes	yes
PSV2	yes	yes
V5	yes	yes
V6	yes	yes
V7	yes	yes
V8	no	yes
PSV3	no	yes
PSV4	no	yes
V9	yes	yes
V10	yes	yes
V11	yes	yes

II.1.4.2.1.5 Feed Box

In addition to providing the cryogenic interconnection between the CERN cryogenics system and the superconducting magnets, the feed box provides the interface to the magnet power supplies through the current leads and also provides for a section of beam tube that spans the gap between Q3 and D1. High-temperature superconducting leads are used for $I > 1$ kA, while conventional gas-cooled leads are used for $I \leq 1$ kA.

The current leads are cooled by helium vapor; in the case of the conventional style leads (1kA and less) the helium vapor is provided by boiloff gas from the liquid helium volume in the lead chamber, whereas for the remainder of the leads, the lower end (with high temperature superconductor) is cooled in the 4.2 K liquid, and the upper end is cooled with 20 K gas from Header D.

The helium chamber is equipped with a liquid helium level sensor and a 200 W electrical heater for level control if needed. An insulating plate, called the lambda plate, separates the 1.9 K, 1 atm superfluid bath from the 4.6 K liquid helium in the lead chamber. The quadrupole current bus bars and the instrumentation leads penetrate the lambda plate.

II.1.4.2.1.6 Room Temperature Recovery

A series of flow control valves are connected to the CERN room temperature recovery line to recover helium gas that is generated by heat input from the current leads and other sources in the feed box. The warm end of each current lead is equipped with a flow control valve to maintain a proper operating lead temperature by modulating the mass flow rate. The control is based on either the output of a temperature sensor or the voltage drop across the lead. The vent gas flow from the lead chamber is controlled by a valve operated by a pressure sensor. In case of excess pressure buildup, a relief valve opens and vents the gas to the CERN recovery line.

II.1.4.2.2 Feed Box Conceptual Design

A plan view of the feed box for IR8 left is shown on Fig. II.1.4.2-9; the cross-hatched areas represent the walls of the 4.4 m diameter tunnel section in which this feed box is located. We have chosen to concentrate just on the design of this box, as it will be placed in the most constricted environment. The vacuum vessel sleeves are shown slid back over the magnets, and indicate the position of the beam line, but do not show any of the cryogenic plumbing. The outer diameter of the feed box vacuum vessel is the same as the inner triplet and the D1 cryostats so the access is not impeded. The feed box is 2.2 m long and is positioned slightly closer to D1 than to Q3, since the Q3 interconnect contains more components which in turn will probably require more axial space. Q3 and D1 interconnect lengths of 600 and 400 mm, respectively, are shown.

The current leads are clustered into groups, and each group is located inside a pipe which leads through the insulating vacuum to the liquid helium chamber below. The leads are spread apart on the beam axis, which provides room for a future LEP beam line.

The cryogenic piping is contained in a single, 610 mm diameter pipe (cryoduct) which exits the feed box vacuum vessel at about the 45 deg position and connects with the CERN valve box after making a 90 degree turn towards D1. The CERN valve box is assumed to be a rectangular vertical protrusion from the Cryogenics Distribution Line which contains the long-stemmed cryogenic valves and the J-T heat exchanger.

Fig. II.1.4.2-11 is a cross section of the feed box for IR8 left, looking towards the Interaction Point from the D1 interconnect region. For clarity we do not show all of the cryogenic piping. The feed box fits inside the 4.4 m diameter tunnel with reasonable clearance, and the configuration requirements specified by CERN are satisfied, as stated in paragraph 1.1.3.1 above. The cryoduct exits the feedbox at about a 45 degree angle and extends upwards to the valve box output. The final orientation and configuration of the cryoduct will need to be approved by CERN, since CERN is responsible for providing the valve box. With the assumption of a vertical valve box, it appears that there could be interference with the tunnel, so the final design approved by CERN may be slightly different from what is shown here.

A few preliminary cryogenic interfaces to the Q3 magnet are shown in Fig. II.1.4.2-11. These interfaces include:

- thermal shield cooling pipes, located on the vacuum vessel midplane,
- magnet heat exchanger piping, located above the cold mass,
- magnet main and trim current bus bar duct located at 12 o’clock on the end dome,
- corrector magnet bus duct located at 9 o’clock on the end dome,
- quadrupole instrumentation bus duct located at 3 o’clock on the end dome, and
- beam tube centered on the cold mass.

Fig. II.1.4.2-13 is an elevation view of the feed box for IR8 left which illustrates a few more features of the conceptual design, but certain pipes and other important details such as bellows expansion joints are omitted for clarity. The design features illustrated include:

- all cryogenic plumbing connections to CERN are on the outside of the tunnel,
- the superfluid bus ducts connect to the bottom of the liquid helium reservoir,
- each superfluid duct has a vertical lambda plate,
- splice joints are sealed with a welded sleeve,
- thermal shield bridges in the interconnect regions provide continuous thermal shielding,
- the beam tube sliding joint is located at the D1 end,

- the D1 magnet leads exit the cold mass end dome at 12 o'clock, and
- the high end of D1 vents into the gas space above the liquid helium bath.

Bellows-type expansion sections will be used to allow for thermal contraction upon cooldown. The fixed point for the feed box piping will be at the cryoduct, since the piping will be supported there to the room temperature vacuum vessel. If Q3 is fixed at its midpoint, the total thermal contraction capability required of the Q3 interconnect is a minimum of 17 mm. If D1 is fixed at its midpoint, the total thermal contraction capability required of the D1 interconnect is a minimum of 21 mm. Since the beam tube spans the gap between Q3 and D1, the sliding beam tube joint must be able to accommodate 38 mm of motion.

The liquid helium chamber is a 304L stainless steel vessel with ASME-type torispherical heads. Penetrations in the bottom head are used to route the magnet and instrumentation busses into the chamber where they are either connected to current leads or instrumentation plugs in order to reach the ambient world. Penetrations in the top head are connected to chimneys which suspend the liquid helium chamber from a top plate at room temperature and also act as housings for the current leads. (The chimneys may be of a folded design to minimize heat leak.) Other penetrations in the top head serve as inlet ports for the various helium pipes.

The thermal shield is made from copper sheet, onto which stainless steel cooling tubes are brazed. Except for the materials and fabrication technique, this shield is equivalent to the magnet thermal shields, and is plumbed in series with them. The thermal shield in the cryoduct and surrounding the helium chamber will be conduction cooled by the main, actively-cooled section. In the interconnect regions, copper bridges will be used to provide a continuous thermal shield across the interconnect region. The feed box side of the bridge will be fastened to the thermal shield to provide conduction cooling and the magnet end will be allowed to slide in order to accommodate the thermal contraction.

The cryogenic pipes will be wrapped with about 20 layers of aluminized mylar (superinsulation) to minimize thermal radiation heat input to the low temperature components. The outer surface of the thermal shield will be covered with a conventional multilayer insulation blanket which consists of 20 layers of superinsulation, with Reemay separation sheets to provide thermal insulation as well as a pump-out path.

The feed box and cryoduct insulating vacuum space will be common to the magnet insulating space, with a CERN-supplied vacuum barrier on the valve box separating the feed box vacuum from the CERN vacuum. The vacuum barrier represents the physical boundary between the US-supplied equipment and the CERN cryogenic system. Vacuum sleeves will bridge the gap between magnet and feed box vacuum vessel. One of the final actions for installation will be to slide the vacuum sleeves into place and make the seal welds. A few convolutions in the sleeve may be needed to accommodate thermal expansion and contraction caused by changes in the ambient tunnel temperature.

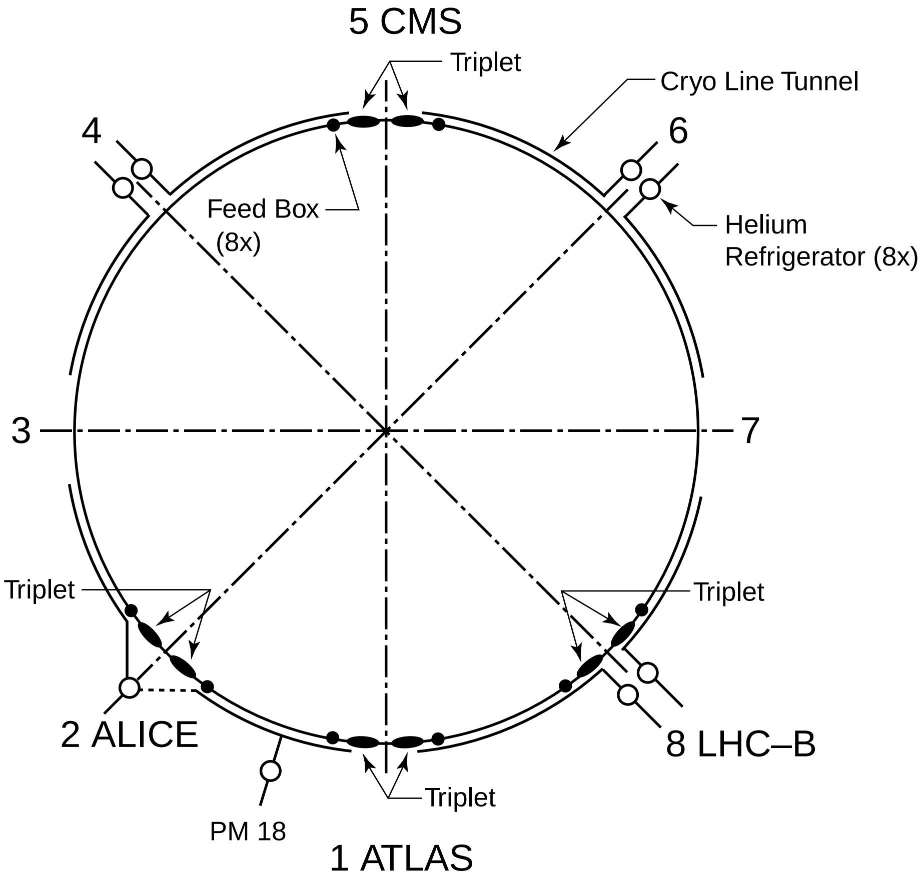

Fig. II.1.4.2-5: Sketch showing in-line lead box.

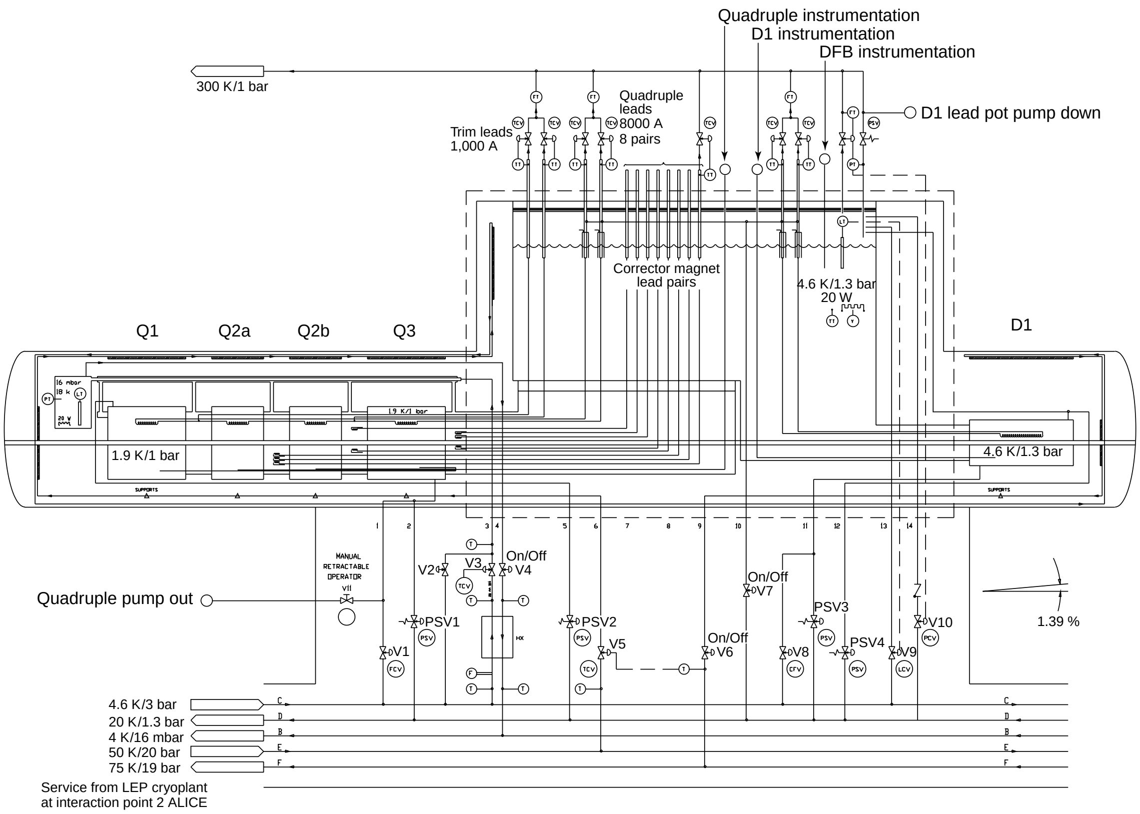

Fig. II.1.4.2-7: Schematic for IR2 right.

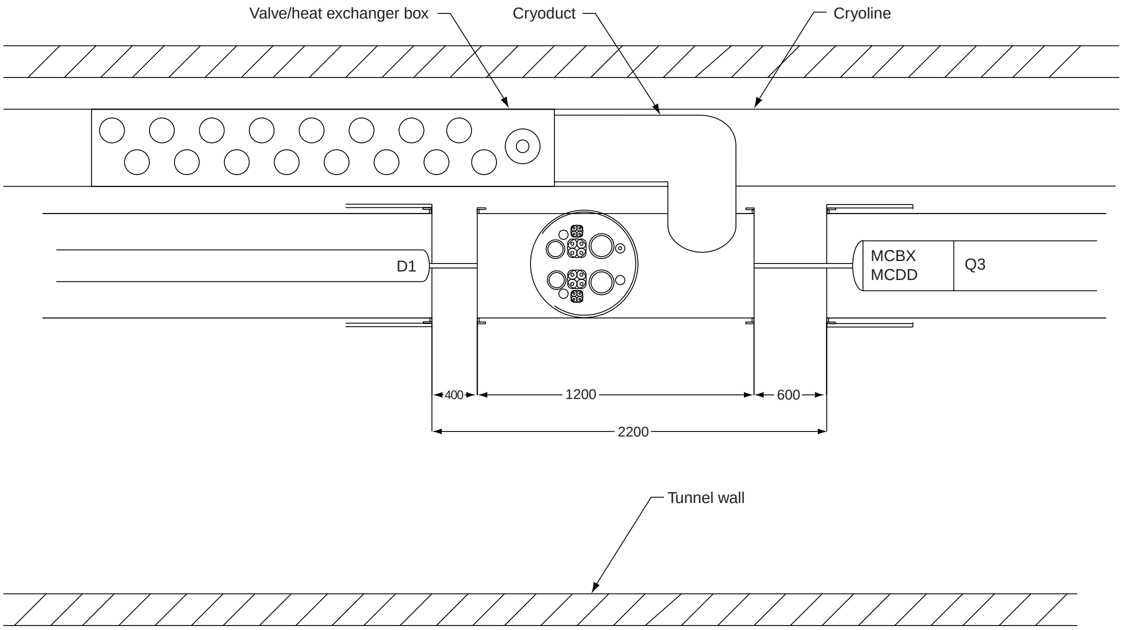

Fig. II.1.4.2-9: Plan view of IR8 left feed box installation.

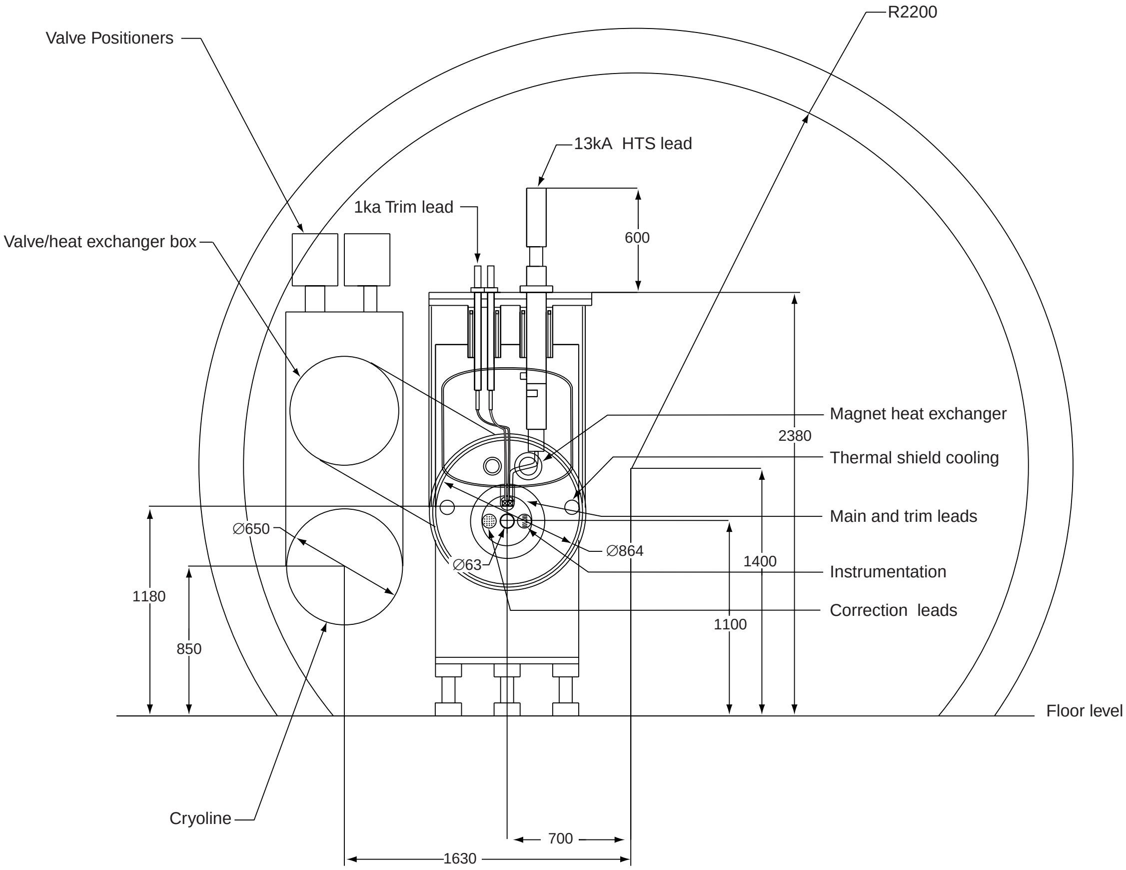

Fig. II.1.4.2-11: Cross section of IR8 feed box installation.

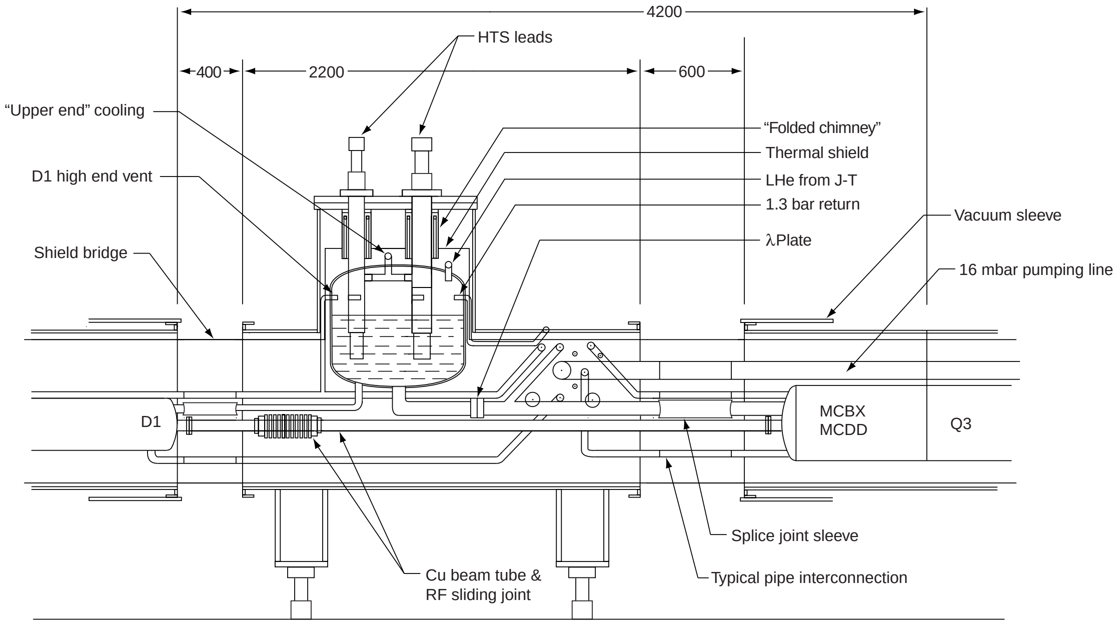

Fig. II.1.4.2-13: Elevation view of IR8 left feed box installation.

II.1.4.3 Interfaces

II.1.4.3.1 Interfaces to CERN equipment

II.1.4.3.1.1 Cryogenic piping

The interface to the CERN cryogenic system is at the CERN cryoline located generally next to the beam line. The CERN cryoline contains the cryogenic valving and J-T valve heat exchanger, all supplied by CERN according to specifications mutually agreed upon by the US and CERN. We expect that certain components, such as the J-T valve heat exchanger, will be of larger capacity than the corresponding component in the LHC arc region. The CERN cryoline will also contain the vacuum barrier which isolates the cryoline insulating vacuum from that of the US-supplied magnet system.

Table II.1.4.3-1: Pipe sizes in the cryoduct between the CERN cryoline valve box and the US lead and feed box.

Pipe ID number	*Usage*	*Diameter (mm)*
1	Quadrupole Cooldown & Fill	40
2	Quadrupole Quench Vent #1	40
3	Quadrupole He II HX Supply	25
4	He II HX Pump Line	100
5	Quadrupole Quench Vent #2	40
6	Thermal Shield Supply	80
7	4 K Intercept Supply	25
8	4 K Intercept Return	25
9	Thermal Shield Return	80
10	Upper End Lead Cooling	25
11	D1 Cooldown & Quench Vent #1	40
12	D1 Quench Vent #2	40
13	Lead Pot LHe Fill	25
14	Lead Pot Cold Vent	25

II.1.4.3.1.2 Power supplies

The interface to the CERN electrical power supplies for the main and corrector magnets is at the US-supplied current leads. The current leads will have connection areas to allow easy connection of the CERN water-cooled copper cables to the US equipment.

II.1.4.3.1.3 Room temperature helium recovery

The interface to the CERN room temperature gaseous helium recovery system will be at the component from which the room temperature helium gas is evolved, for instance the vapor-cooled leads and the liquid helium chamber. The US equipment will be shipped with capped or blanked off ports which will be removed at CERN where the CERN-supplied valves will be installed.

II.1.4.3.1.4 Diagnostic and control

The interface to the CERN diagnostic and control system will be at the US-supplied equipment. The US equipment will be fitted with electrical connectors purchased to CERN specifications and connected to the appropriate sensor element in the US-supplied hardware.

II.1.4.3.1.5 Beamline

For IR1 and IR5, the interface to the CERN beamline is at a high-vacuum isolation valve located at the end of the vacuum chamber of the lead and feed boxes. The valves and associated flanges will be supplied by CERN to ensure consistency with the rest of the machine. For Interaction Regions 2 and 8, the interface to the CERN beamline is at the beamtube flange of D1 within the D1 interconnect. Again, the flange and bellows will be supplied by CERN.

II.1.4.3.1.6 Tunnel physical

The interface to the CERN tunnel is at the US-supplied equipment, wherein the vacuum chamber will have supports with suitable adjustability to allow for installation. Since this equipment contains no elements that would affect the proton beam, there is no requirement for alignment fiducials.

II.1.4.3.1.7 Transporters

The interface to CERN transporter equipment will be at lifting points or cradle points on the US-supplied equipment, the details of which will be worked out in collaboration with CERN.

II.1.4.3.2 Interfaces to quadrupoles

The interfaces to the cryogenic lines occur at the D1 end of the cryostatted Q3 magnet. These lines include:

- 1.8 K, 16 mbar supply to the magnet heat exchanger,
- 1.8 K, 16 mbar return to the J-T heat exchanger,
- 4.5 K, 3 bar supply to magnet support heat intercepts,
- 20 K, 1 bar return from magnet support heat intercepts,
- 50 K, 20 bar supply to magnet shields and support heat intercepts,
- 50 K, 20 bar return from magnet shields and support heat intercepts,
- Quench vent line from Q1.

It is expected that these are simple pipes, so connection is made at CERN by means of an orbital tube welder without any special flanges or fittings. Pipe sizes are chosen to match those elsewhere in the LHC to allow use of the same orbital welding and cutoff tools.

The interface to the pressurized superfluid helium occurs at the D1 end of the Q3 magnet. This also provides the interface to the magnet power connections, the corrector magnet power connections, and the magnet diagnostic connections. Special sleeves and weld flanges allow the leads from the lead box to be connected to the magnet leads, to the trim bus leads, and to the corrector magnet leads. The splice (solder) blocks used in the inner triplet string can be used to make these connections. Also, the diagnostic leads from the magnet string will be connected to the box by means of electrical connectors and the surrounding superfluid-tight enclosure will be made by special sleeves and flanges which are sealed by an orbital welding machine. The connections and welds will be made by CERN upon installation.

The insulating vacuum space of the cryostatted magnet string is connected to the vacuum space of the lead and feed box by means of a weld sleeve similar to what is done in the interconnection regions of the inner triplet.

II.1.4.3.3 Interfaces to dipoles (IR2 and IR8)

The interfaces to the cryogenic lines occur at the Q3-end of the cryostatted D1 magnet. These lines include:

- Cooldown and Quench Vent #1,
- High End Gas Return and Quench Vent #2,
- 50 K, 20 bar supply to magnet shields and support heat intercepts,
- 50 K, 20 bar return from magnet shields and support heat intercepts.

It is expected that these are simple pipes, so connection is made at CERN by means of an orbital tube welder without any special flanges or fittings.

A special sleeve and weld flanges allows the leads from the lead box to be connected to the magnet leads. The diagnostic leads from the magnet will be connected to the feed box by means of electrical connectors and the surrounding liquid-tight enclosure will be made by special sleeves and flanges which are sealed by an orbital welding machine. The connections and welds will be made by CERN at the time of installation. Pipe sizes are chosen to match those elsewhere in the LHC to allow use of the same orbital welding and cutoff tools.

The insulating vacuum space of the cryostatted magnet is connected to the vacuum space of the lead and feed box by means of a weld sleeve similar to what is done in the interconnection regions of the inner triplet.

II.1.4.4 Applicable codes and standards

The pressure containing components will be designed in accordance with the US-ASME Boiler and Pressure Vessel Code for Unfired Pressure Vessels, section VIII, Division 1, and Division 2, and the applicable section of the Refrigeration Piping Code, B13.3 and B13.7. The materials and processes will be specified per the ASME Code, and the equipment will be tested per the ASME code.

The vessels will not be code stamped. Because of the nature of the final assembly work, we assume that assembly will be done at a facility such as Lawrence Berkeley National Laboratory, which is not certified by the National Board to apply the ASME code stamp. However, the work will be carried out in accordance with procedures accepted by the National Board and ASME.

The CERN Technical Inspection and Safety Commission (TIS) document TIS/DI96-39, “List and Summaries of TIS Safety Documents,” is an up-to-date reference of all safety-related codes, instructions, bulletins, etc. that have been examined for pertinent information relating to the design, material selection, and testing of the feed boxes. Examples of pertinent documents include:

- Safety Instruction TIS IS 41: “The Use of Plastic and other Non-Metallic Materials at CERN with respect to Fire Safety and Radiation Resistance”
- Safety Instruction IS 23, rev 2: “Criteria and Standard Test Methods for the Selection of Electric Cables, Wires, and Insulated Parts with respect to Fire Safety and Radiation Resistance”
- Safety Code D1: “Lifting Equipment”

II.1.4.5 Testing

As the design matures and the detailed testing procedures are formulated, this section will be revised accordingly. The preliminary test list includes:

- ☐ Pressure and leak tests on all cryogenic piping, after thermal shock to LN temperature when possible. The pressure testing will be done at a pressure equal to 125% of the design pressure. There shall be no pressure drop after a 24-hour hold period.
- ☐ Current lead tests of HTS superconductor leads. These are primarily developmental tests done before the main procurement to demonstrate that the current leads function properly on first production units. For the main procurement, certification tests will be performed by the manufacturer according to specifications and procedures which will be included in the purchase contract.
- ☐ Tests of the lambda plate operation on the component level.
- ☐ Electrical testing to verify continuity and insulation of the diagnostic cables.
- ☐ Cold testing to verify that the feed box operates properly. This can include boil-off measurements, full power testing of current leads, resistance to ground for the diagnostic cables, and vacuum in the insulating space. It will be very difficult and costly to ensure that the installed lambda plate is properly functioning in these tests, so we will rely on the component test results as verification that the lambda plates function properly.

II.1.4.5.1.1 References

[51] G. Trinquart, private communication, 18 Nov. 1997.

[52] J. Strait, private communication, 4 Aug. 1997.

[53] M. Chorowski, et al., “A Simplified Cryogenic Distribution Scheme for the Large Hadron Collider,” presented by W. Erdt at *the 1997 Cryogenic Engineering Conference*, Portland, OR. To be published in the conference proceedings.

II.1.5 IR Absorbers

At design luminosity 10^{34} $cm^{-2}sec^{-1}$ and total cross section σ_{pp} = 112 mb there are ~ 10^9 collisions per second at the high luminosity interaction points IR1 and IR5. These interactions give rise to ~ 1.25 kW of power in collision products leaving an IR in each direction. Some of this power is carried off by small angle elastic and diffraction scattering of the primary protons and stays inside the beam tube until leaving the interaction regions. However, significant fractions are carried off by particles leaving the beam tube in the interaction region - viz. neutrals, which are not deflected by magnetic field of the separation dipoles and large angle and/or off momentum charged particles. The inelastic collision power carried off by neutrals has been estimated to be 330 W leaving an IR in each direction [54]. Similarly the collision power escaping the beam tube and incident on the front face of the inner triplet quadrupoles has been estimated to be ~ 145 W and incident on the beam tube inside the inner triplet quadrupoles and first separation dipole ~ 185 W [54]. Special purpose absorbers must intercept this power to prevent quenching the inner (Q1 to Q3) and outer (Q4 to Q6) triplet quadrupoles.

This section discusses the requirements, the estimated radiation deposition and activation, and the conceptual designs for the neutral beam and front quadrupole absorbers. Absorption of the radiation incident on the inside of IR quadrupole beam tubes is described in Sec. II.1.2.6 above. Because of the high incident flux of collision products near zero degrees, the neutral absorber is a natural place for location of radiation hard ionization detectors which could provide useful information. For example providing the backgrounds from beam halo interactions and beam gas collisions are low enough these on axis ionization detectors could be used for; (1) measurement of luminosity, (2) measurement of the beam transverse dimensions at the IR and (3) feedback control of the colliding beam centers at the IR’s to maximize luminosity. A schematic layout of IR1 (IR5 is similar) for the most recent LHC lattice v5.0 is given in Figure II.1.5-1 and shows the relative positions of the quadrupoles (Q1-Q7), beam separation dipoles (D1-D2), neutral absorber (TAN) and front quadrupole absorber (TAS).

The LHC lattice in the interaction regions will continue to evolve and this will effect the precise values of the parameters of the absorbers given in the following sections - viz. their location, length, beam tube ID etc.. This evolution will be a continuation of the lattice development that has taken place during the two years the conceptual design of the absorbers has taken place. Although the precise parameters of the absorbers have changed over time, these changes have been small and the basic function and scope of the absorbers is defined well enough that changes in detail have not had a significant impact on their estimated cost.

II.1.5.1 Neutral beam absorbers

II.1.5.1.1 Radiation deposition and activation calculations for the neutral beam absorber

The TAN are located between the separation dipoles D1 and D2 and are ±148.5m from the interaction points at IR1 and IR5. A TAN’s primary function is to prevent ~ 330

W of neutral collision fragments from quenching the superconducting dipole D2 and the outer matching section quadrupoles Q4-Q7, which are in the direct path of these particles. The TANs also provide well defined physical locations for the deposition of this penetrating radiation and a location for beam diagnostic equipment. Once the primary radiation has been absorbed, the TANs become activated and require special considerations for access and handling. The size of the absorbers is determined by considerations of shielding the superconducting magnets, prompt radiation dose alongside the absorber, remanent surface activation and activation of ground water, mainly through production of tritium and radioactive isotopes of sodium. An early study of the shielding requirements and activation of these absorbers was carried out by Mokhov and Stevenson [55]. These calculations have recently been updated by Mokhov for the latest layout of LHC lattice components (LHC v5.0) [56]. Results are shown in Fig. II.1.5.1-1 to Fig. II.1.5.1-5. For these calculations, the TAN is assumed to be made of Cu out to 15 cm radius and of Fe at larger radius. The incident flux of gammas, electrons and positrons, neutrons, protons, pions and muons is shown in Fig. II.1.5.1-1. The mean energy and mean number of each of these particles that strike the TAN per pp interaction and the product of these two parameters are given in Table II.1.5.1-1.

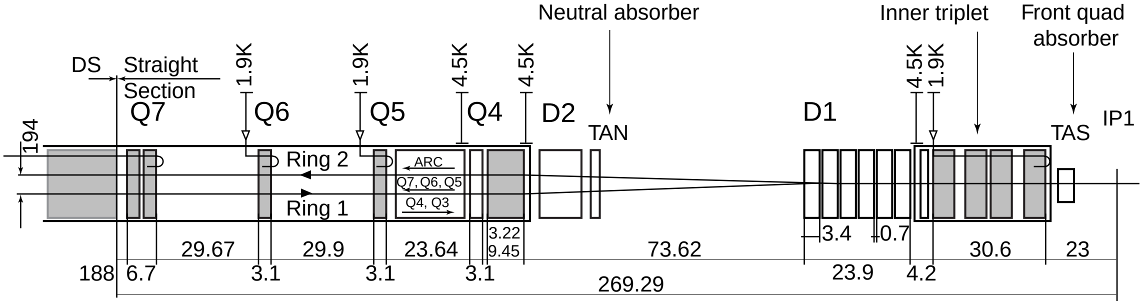

Figure II.1.5-1: Schematic layout of IR1 showing locations of the neutral absorber (TAN) and front quadrupole absorber (TAS).

Power density profiles are given as functions of axial distance in Fig. II.1.5.1-2 and as functions of radius in Fig. II.1.5.1-4. There is a peaking of the power density a few cm off the axis of the TAN due to the 200 μrad crossing angle at the IR assumed in this study. From Fig. II.1.5.1-2 the maximum power density of the shower particles occurs 22.5 cm behind the front face of the TAN and is 5 W/kg; the first of the radial profiles in Fig. II.1.5.1-4 is at this depth. From Fig. II.1.5.1-4 we see that most of the power deposition is in the Cu. If the length of absorbing Cu and Fe is assumed to be 3.0 m the maximum power density at the end of the TAN is ~ 1.5×10^{-3} W/kg. Power density limits haven’t been set for D2 or Q4-Q7 immediately behind the TAN however for Q1-Q3 a limit 0.4 W/kg is being taken so a 3 m TAN would have a large margin of safety for avoiding quenching magnets.

Activation of the TAN assuming 30 days of irradiation at design luminosity 10^{34} $\mathrm{cm}^{-2}\ \mathrm{sec}^{-1}$ and one day cool down is shown in Fig. II.1.5.1-5 as a function of axial position for various radii. Assuming an outer cylindrical surface with radius 55 cm the maximum remanent dose rate on the outer cylindrical surface is 0.5 mSv/hr. This exceeds the nominally accepted value at CERN of 0.1 mSv/hr for a person to stand alongside the absorber but is below the 1-2 mSv/hr emergency access level. The remanent dose rate could be reduced by increasing the radius of the Fe absorber; however, r = 55 cm is the presently allowed limit that has been given for the size of the TAN in the tunnel. The front surface activation is considerably higher reaching a maximum value ~ 80 mSv/hr near the axis. Assuming a 3 m absorber length the maximum activation on the back surface is 0.7 mSv/hr, which is below the emergency access limit. There is a pumping station between the TAN and D2. To allow access to this pumping station it would be desirable to further reduce the remanent dose rate to ~ 0.1-0.2 mSv/hr by increasing the length of the central part of the neutral absorber by ~ 0.5 m.

Depending upon the specific task and its duration some additional shielding and special precautions will need to be taken for people to access the region occupied by the TAN, particularly on the front surface. Looking at the contour r = 15 cm for the Cu - Fe interface one sees that the cylindrical outer surface of the Cu will reach a residual dose rate ~ 30 mSv/hr, a level for which access is not allowed. Removing the outer Fe absorber of the TAN will therefore require remote handling equipment and caskets or other precautions for storage of the pieces before re-assembly.

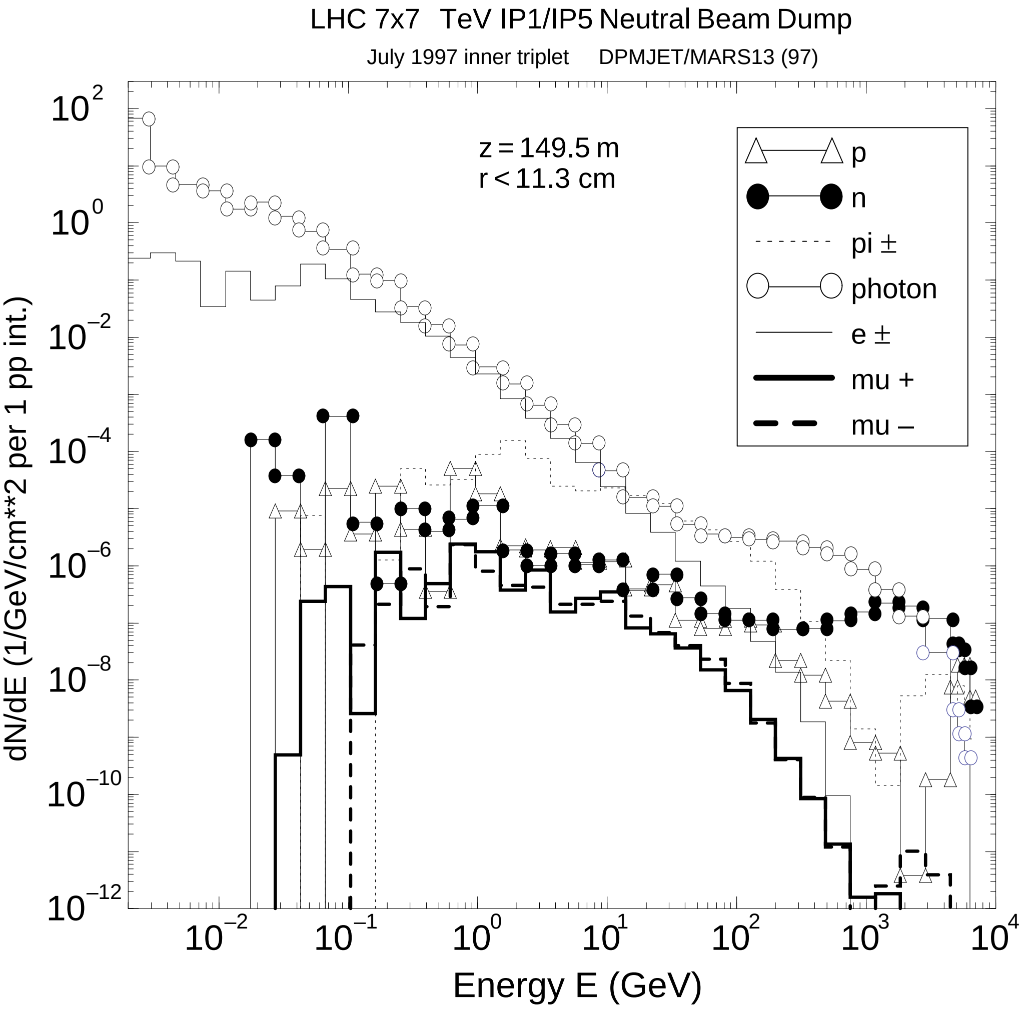

Fig. II.1.5.1-1: Particle fluxes incident on the neutral absorber (TAN) due IR interactions.

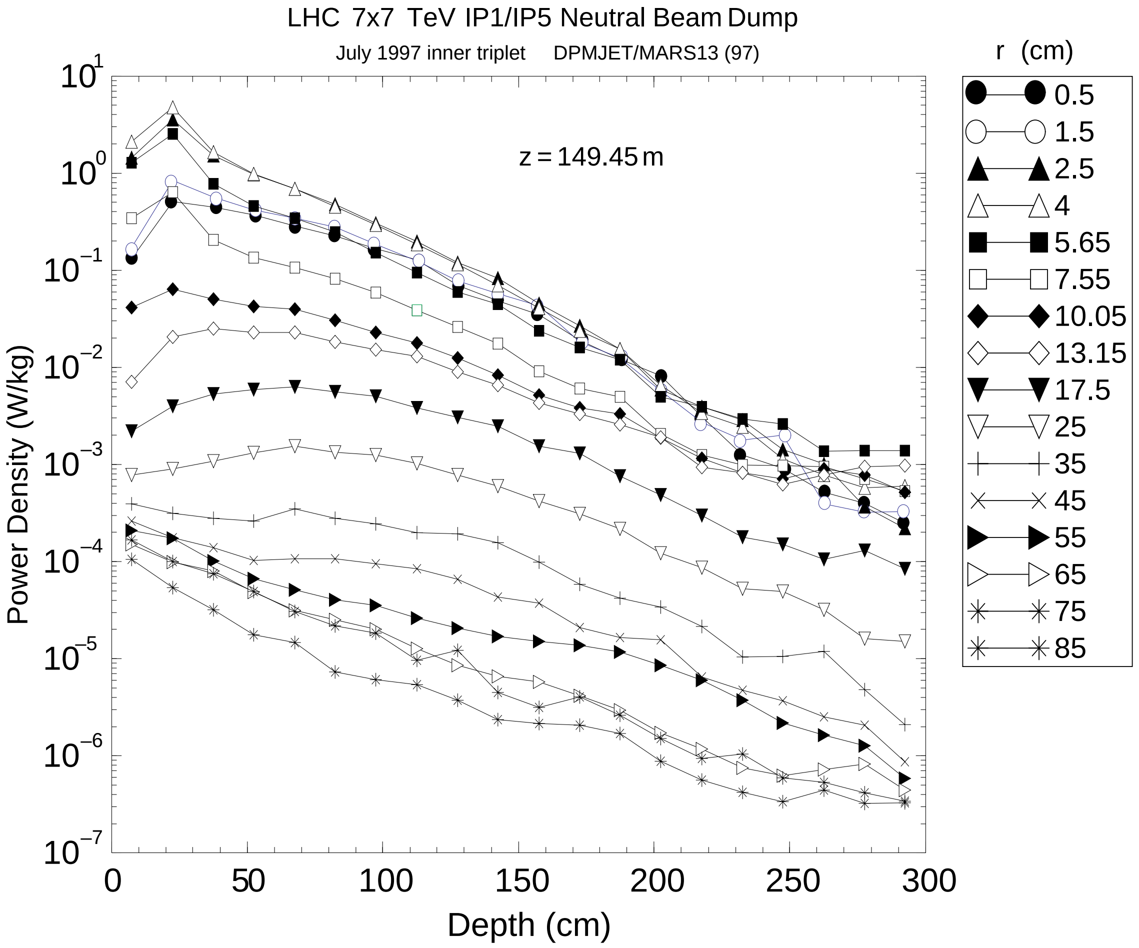

Fig. II.1.5.1-2: Power density in the neutral absorber versus axial distance averaged over azimuthal angle for several radii.

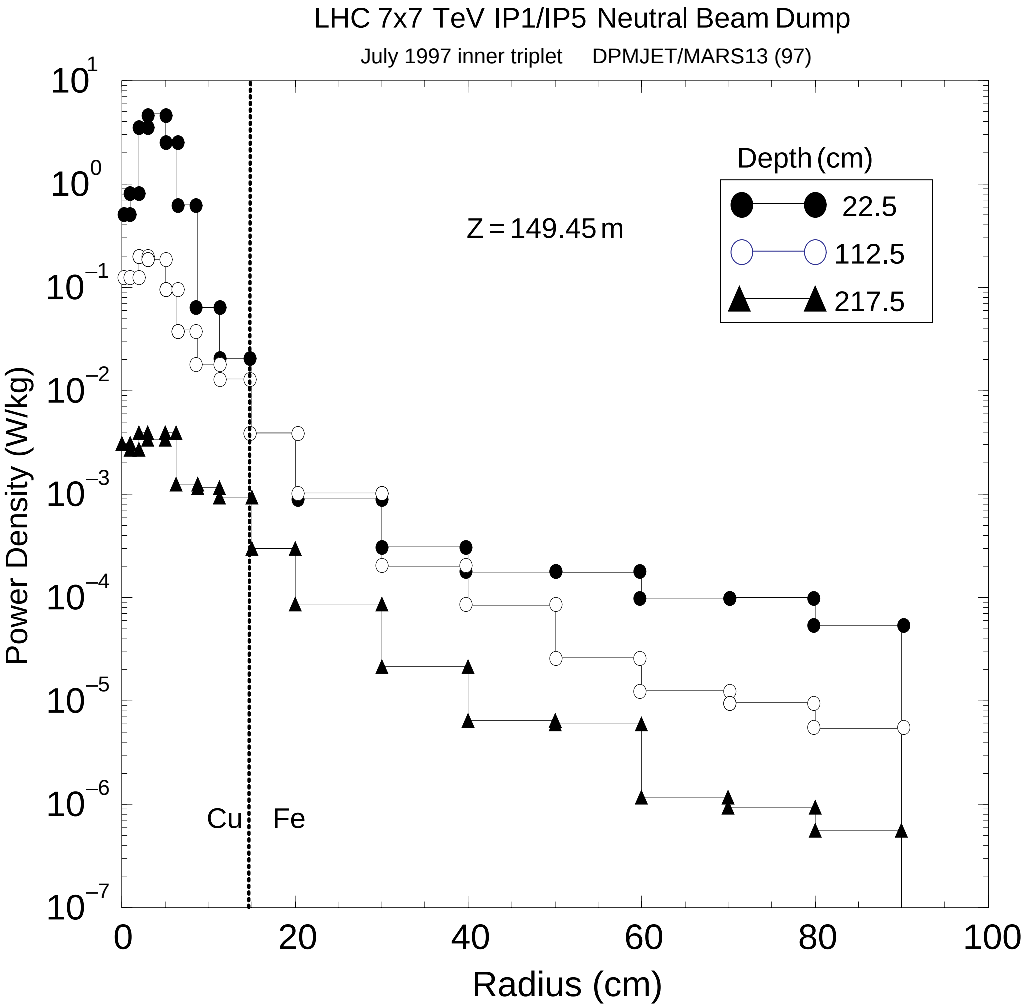

Fig. II.1.5.1-4: Power density in the neutral absorber versus radius, averaged over azimuthal angle, at three axial locations.

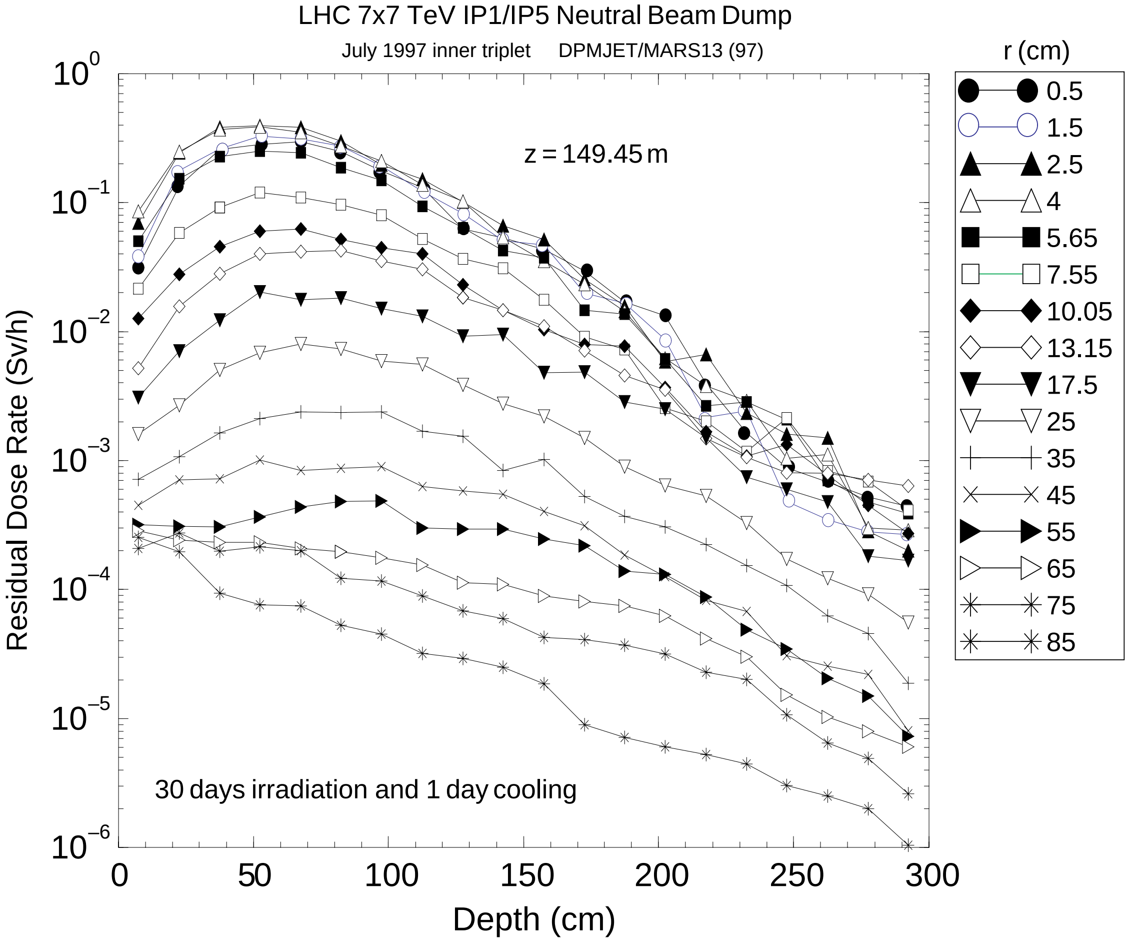

Fig. II.1.5.1-5: Residual dose rate of the neutral absorber assuming 30 days irradiation at 10^{34} $cm^{-2}sec^{-1}$ and one day cool down.

Table II.1.5.1-1: Intensity and mean energy of particles striking a neutral absorber (TAN)

Particle type	*<n> per pp interaction*	*<E>* *TeV*	*<n><E>* *TeV/pp int*
neutron	0.332	2.185	0.7254
proton	0.060	1.215	0.0729
charged pion	0.705	.125	0.0881
photon	150.8	4.88×10^{-3}	0.7359
electron/positron	12.50	0.66×10^{-3}	8.25×10^{-3}
muon	0.014	.0247	0.35×10^{-3}

II.1.5.1.2 Neutral beam absorber requirements and specifications

The requirements for the neutral absorber have been derived from considerations which include:

- intensity of incident radiation from the IR
- radiation shielding of superconducting magnets
- prompt radiation dose rate at the surface of the absorber
- remanent radiation dose rate at the surface of the absorber
- activation of ground water
- beam tube vacuum
- beam impedance
- tunnel access
- crane limits
- alignment
- installation and maintenance.

The requirements and specifications for the neutral absorber are summarized in Table II.1.5.1-3. The TAN is specified to absorb 330 W of power with a maximum temperature increase of 20^{o}C and to transmit a power density < 0.4 mW/g directly behind the absorber for protection of superconducting magnets. The material for the absorber is Cu for the inner absorber r < 15 cm, which absorbs most of the power, and Fe for the surrounding outer absorber. The maximum outside radius of the Fe absorber allowed by tunnel access is 550 mm.

Table II.1.5.1-3: Neutral absorber requirements and specifications.

Absorbed power	330 W
Transmitted power density	< 0.4 W/kg
Beam tube material	OFHC
Inner absorber material	Cu
Outer absorber material	Fe
Max. absorber outer radius	550 mm
Max. temp. increase with beam operation	20 ^{o}C
In situ beam tube bake out temp	150 ^{o}C
Distance from front flange to IR	148.5 m
Min. aperture	> $10\sigma_{x,y}$ = 12.1 mm at inj.
Beam tube radius facing IR (2 beams in one tube)	110.2 mm
Beam tube radius away from IR (2 beams in 2 tubes)	25 mm
Aperture radial tolerance	±1 mm
Max. beam tube bore taper	10^{o}
Horiz. beam separation at entrance flange	171 mm
Horiz. beam separation at exit flange	179 mm
Flange to flange length	3900 mm
Flange type	Clamped, remote assembly
Nominal beam height from tunnel floor	950 mm
Alignment tolerance	± 0.6 mm
Range of vert. and horiz. Adjustment	±10 mm
Crane lift limit	5 tonnes

The beam tube is part of the warm insertion region vacuum system and should be consistent with design specifications and practices employed for that system for vacuum and wall resistivity; OFHC Cu beam tube, in situ bakeable to 150^{o}C, ~10^{-10} Torr range for H_2 and ~ 10^{-11} Torr for the other gases CH_4, CO and CO_2 [57]. In the absence of synchrotron radiation from bending magnets, photodesorption and electron cloud effects, which are concerns elsewhere in the machine, are not a concern for the TAN beam tube. The primary gas load in the TAN beam tube will be residual outgassing. The beam tube of the TAN in Table II.1.5.1-3 is stable with respect to the ion desorption instability. For the worst case desorbed gas, CO, the safety margin is ~ 3.8 unbaked and ~ 13.1 baked for operation at design current I = 0.536 A per beam.

All apertures of the LHC including the TAS and TAN are specified to be greater than $10\sigma_{x,y}$ from the beam axis except in the beam cleaning insertion IR 3 and IR 7 where the beam scraping collimators are at $6\sigma_{x,y}$. From pg. 38 in the Yellow book [54] the aperture $n_{x,y}\sigma_{x,y}$ is related to the physical aperture $A_{x,y}$ by

$$A_{x,y}(s) = \left(n_{x,y}\sigma_{x,y}(s) + \delta_p D_{x,y}(s)\right) * k_\beta + \left(CO + \delta sep_{x,y}(s)\right) + \left(\delta_{al} + \delta_{tol}\right)$$

where we have added a subscript x,y to distinguish the two planes. The dispersion is less than 0.1 m everywhere between the outer separation dipoles D2. So with δ_p = $0.468\text{x}10^{-3}$ at injection we estimate $D_x\delta_p$<.05 mm which is negligible, so we drop it. The closed orbit, alignment and manufacturing tolerances we take the same as the Yellow book, CO = 4.0 mm,δ_{al} = 0.6 mm and δ_{tol} = 1.0 mm. The half separation between orbits $\delta sep_{x,y}$ applies in the above equation only when there are two beams in a single tube - i.e., everywhere between the TAN flanges facing the IR. For estimating the separation between the two orbits, we take a simple model. Assume no vertical separation $\delta sep_y = 0$ and for the horizontal plane assume a full crossing angle of 200 µrad at the IR. Kicks are applied at the midplanes of D1 and D2 to produce parallel orbits separated by 194 mm in Q4. The midplanes of D1 and D2 are 69.750 m and 160.050 m from the IR respectively. Then $\delta sep_{x,y}$ is given by

0 < s < 69.750 m:

$$\delta sep_x(mm) = 0.100 * s(m)$$

69.750 < s < 160.050 m:

$$\delta sep_x(mm) = 6.975 + 0.997(s - 69.750)$$

s > 160.050 m:

$$\delta sep_x(mm) = 97.0\ .$$

Assuming a distance 148.5 m from the IR to the TAN and 3900 mm TAN length, the horizontal beam separation facing the IR is 171 mm and away from the IR 179 mm. The aperture requirements are most stringent at injection when the beam dimensions are largest. For beam size we take a normalized emittance 3.75 π mm-mrad and with γ_{inj} = 479.6, an un-normalized emittance $\varepsilon = 7.82 \times 10^{-3}$ π mm-mrad. Setting $\varepsilon = \frac{\sigma^2_{x,y}}{\beta_{x,y}}$ the beam size is calculated once the beta functions are known. Beta functions at the locations of absorber flanges have been taken from MAD files for LHC v5.0 optics. For physical apertures a 110 mm beam tube radius is taken facing toward the IR with the two beams in a single tube and 25 mm radius for the two beams in separate beam tubes facing away from the IR. With these choices, the beam tube radii are continuous with the adjoining warm vacuum beam tubes. Everything has now been specified to estimate the apertures of the TAN in terms of rms beam size n_x, n_y. The minimum value obtained is 14.5, which exceeds the minimum allowed value of 10.

The angle of the taper between the beam axis and the surface of the beam tube transition between one and two tubes is specified to be no greater than 10^{o} from impedance considerations and is consistent with beam tube transitions elsewhere in the machine [57]. The flange to flange length of the neutral absorber is specified to be 3900 mm and the flanges are specified to be clamped flange type suitable for fast and possibly remote assembly due to activation. This specifies the lattice slot space needed for the TAN and defines the interface between the TAN and the rest of the LHC vacuum system. The length of actual absorber is 3000 - 3500 mm. The nominal height of the beam tube in the neutral absorber is specified to be 950 mm from the tunnel floor. The entire mass of the neutral absorber is specified to be supported with a system allowing ± 10 mm vertical and horizontal adjustment with an alignment tolerance of ±0.6 mm. For assembly and disassembly, the absorber must be assembled in the tunnel with individual sections weighing no more than 5 tonnes, set by the crane limit in the tunnel. Since the TAN will become activated, it is desirable that the handling of the TAN be as simple as possible and with a minimum number of sections each near the 5 ton limit.

II.1.5.1.3 Neutral beam absorber conceptual design

The conceptual design of the neutral absorber is shown in Fig. II.1.5.1-7 throughFig. II.1.5.1-10. Fig. II.1.5.1-7 shows a front view, a section near the back and a side view. Fig. II.1.5.1-6 shows a horizontal section through the absorber exposing the beam tube channel and separation of the beams from two beams in a single tube facing the IR to two beams in two tubes facing the arcs. Fig. II.1.5.1-6 shows the beam tube and Fig. II.1.5.1-10 is an exploded view of the components. Starting from the inside of the absorber and working to the outside, several concepts have been considered for the design of the beam tube channel.

For the presently favored concept, which is shown in Fig. II.1.5.1-6, the transition section from two beams in a single tube to two beams in two tubes is 341 mm in length and machined from a solid 300 mm x 250 mm x 375 mm block of OFHC Cu (wire

EDM). The maximum angle between the beam axes and the surfaces of the conical sections is about 10^{o}. The section of the vacuum chamber with the single tube, a 220 mm ID OFHC copper tube, is electron beam welded to a quick disconnect flange on one end and brazed to the transition section on the other end. The quick disconnect flange is a stainless steel flange into which a copper ring has been brazed. The electron beam welding is between the copper tube and the copper ring of the flange. Similarly, the two straight OFHC copper beam tubes, with 50 mm ID, are brazed to the transition section. The remaining ends are terminated with quick disconnect flanges, and the flange copper rings are electron beam welded to the copper tubes. The OD of these tubes is 70 mm so the wall is thick enough to prevent yielding during handling. The flange to flange length of the beam tube is 3900 mm. Except for 200 mm protrusions at each end the entire beam tube is inside the outer copper and iron absorber. A horizontally split copper block 300 mm x 250 mm x 2875 mm fits over the two beam tubes behind the transition section and a rectangular iron casing with outside dimensions 450 mm x 375 mm x 3500 mm fits over the entire copper assembly. The weight of the copper plus iron casing is nominally 5 ton and would be pre-assembled as a single unit before installation in the tunnel.

(a) (b)

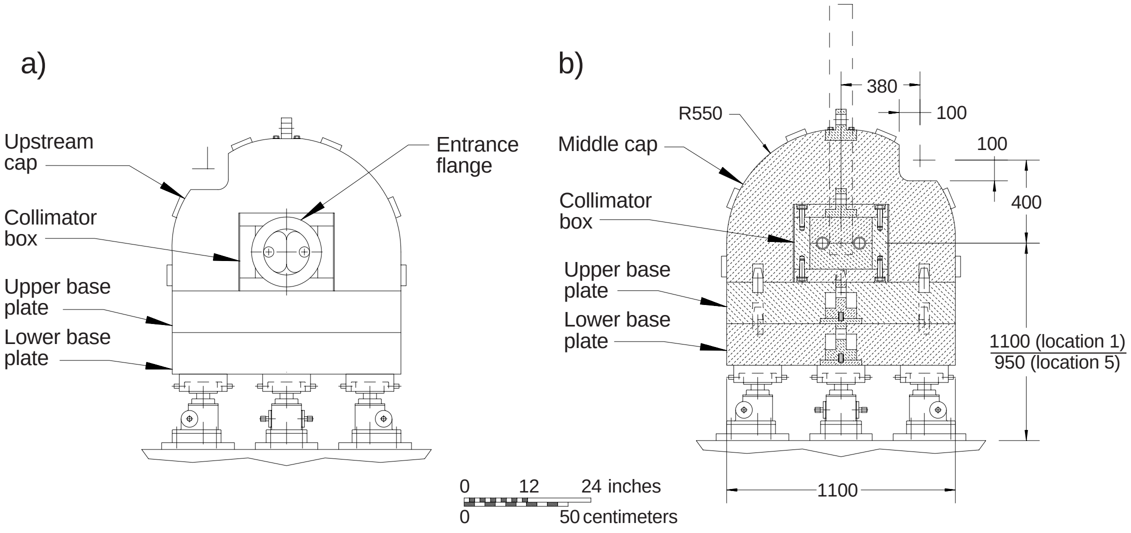

(c)

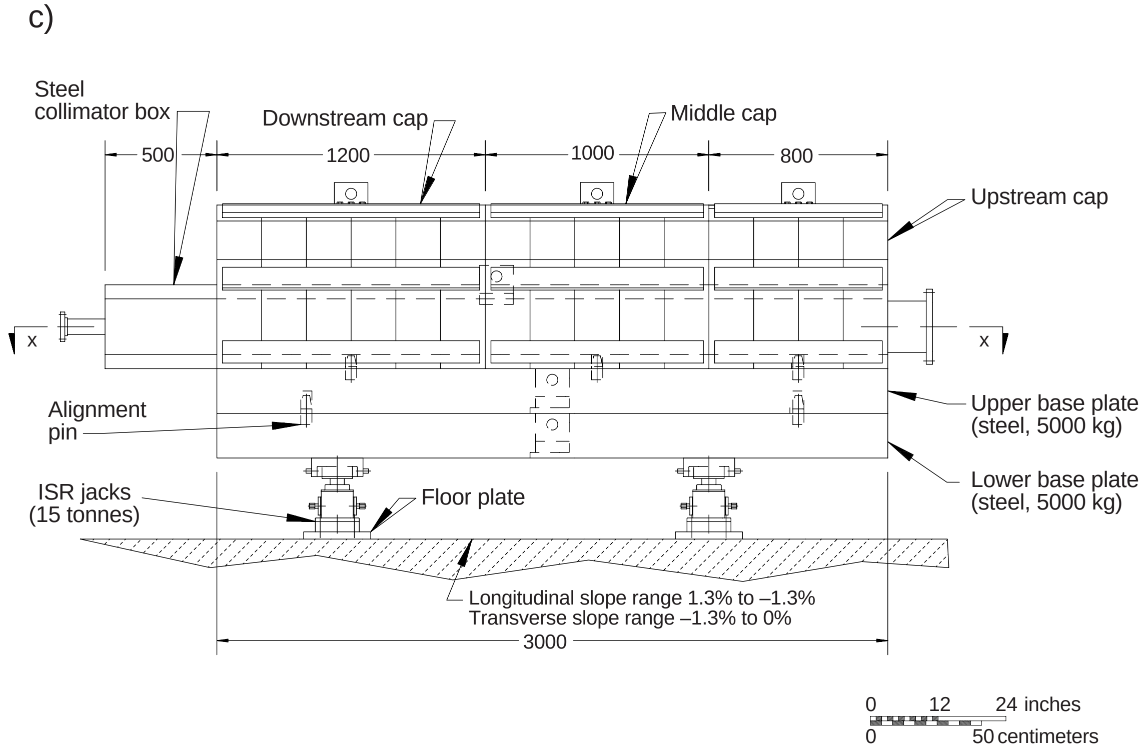

Fig. II.1.5.1-7: Front (a), back (b) and side (c) views of the neutral absorber (TAN) conceptual design.

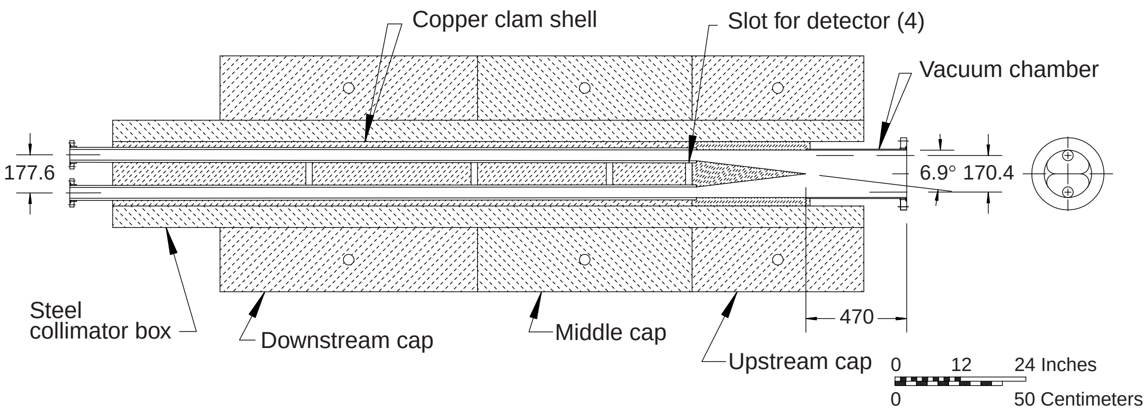

Fig. II.1.5.1-6: Horizontal section of the neutral absorber.

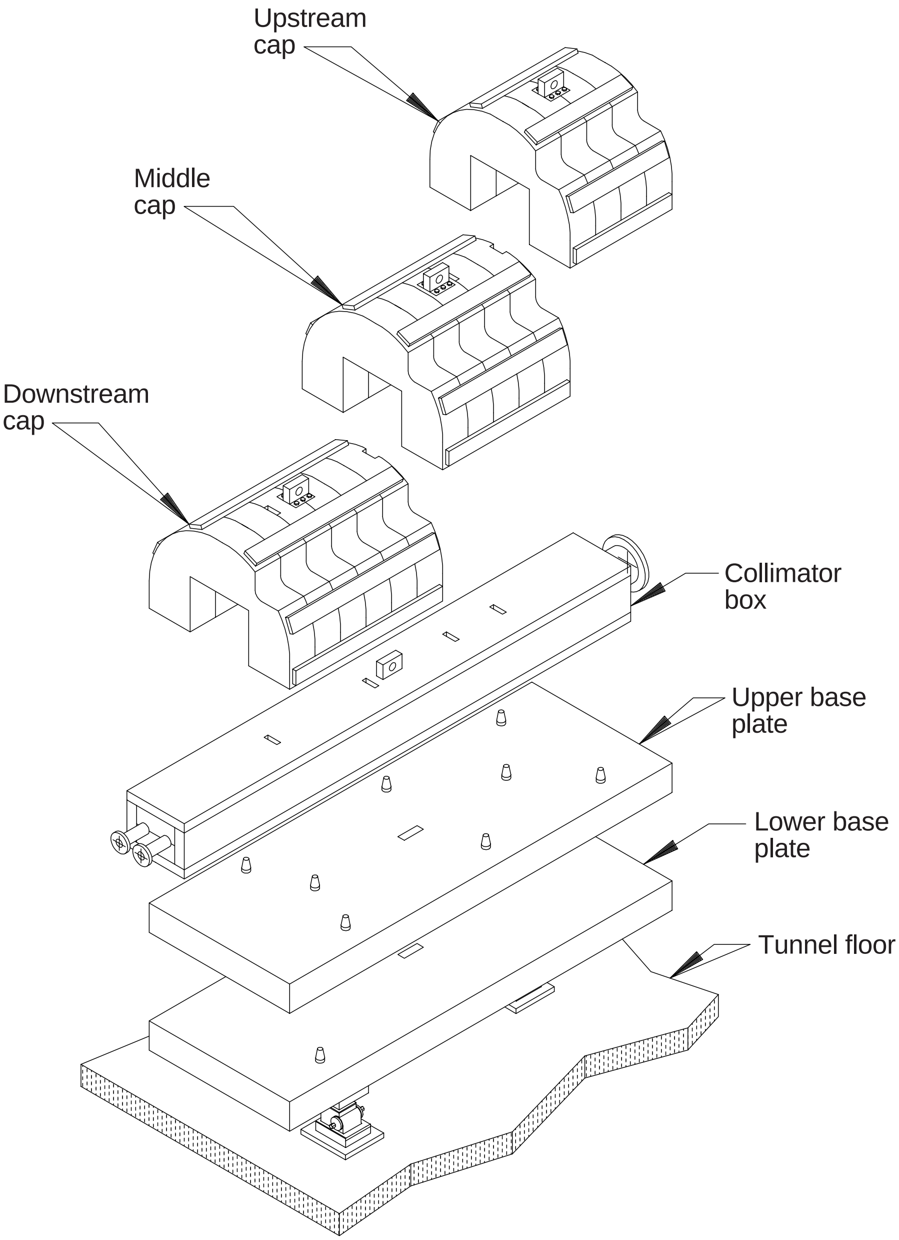

Fig. II.1.5.1-10: Exploded view of the neutral absorber.

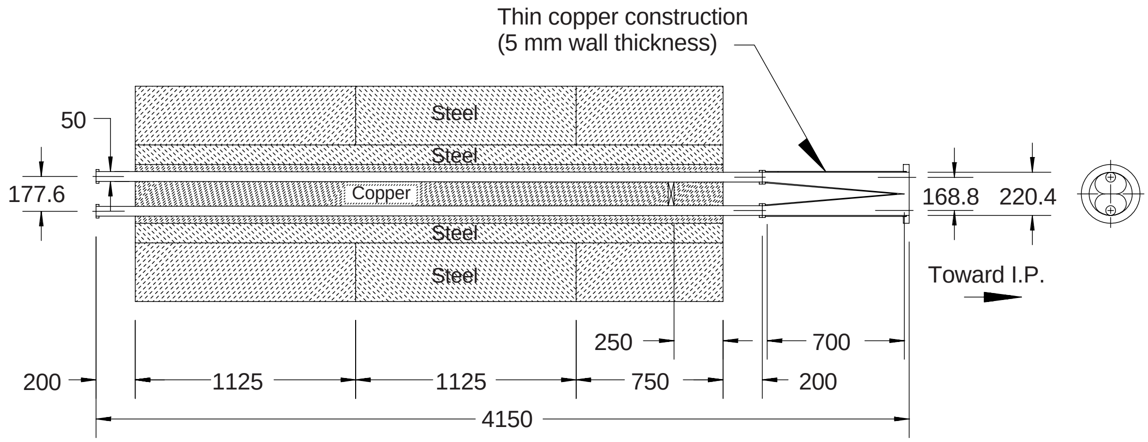

Fig. II.1.5.1-9: An alternative design for the beam tube transition section.

Another concept that has been considered for the beam tube transition is shown in Fig. II.1.5.1-9. The transition section is fabricated from thin wall copper (5 mm) and located entirely in front of the main mass of the neutral absorber. Showers initiated in the septum dividing the beam tube propagate a short distance in air and are incident normally on the front of the copper absorber. A significant disadvantage of this concept is that the transition section will become highly activated and is not shielded by the absorber mass. Fabrication from thin wall copper also seemed less straightforward than wire EDM from solid stock.

The copper plus iron box subassembly rests on a base plate made of two 200 mm x 1100 mm x 3000 mm base plates which are in turn supported on the tunnel floor by ISR magnet jacks. Each base plate weighs nominally 5 tonne. Semi-cylindrical iron caps with radius 550 mm fit over the top of the copper - iron subassembly and rest on the top base plate. The iron cap is divided into three sections each weighing nominally between 3 and 5 tonne. Altogether then, the neutral absorber is assembled in the tunnel from six approximately equal weight pieces that fall within the crane limit. Although it is not indicated in the figures, the copper - steel and steel - steel interfaces running along the beam axis would have steps to avoid shine-through.

A thermal analysis was carried out assuming 500 W is absorbed in the neutral beam absorber. Assuming ambient cooling, the absorber surface temperature rise is estimated at 12 degree C. Internal gradients of 7 degree C are estimated from the vacuum chamber to the outer absorber surface assuming that the 500 W is deposited in the first 2 m of the absorber. Thus it is expected that the vacuum chamber temperature will rise 19 degree C above the ambient tunnel temperature.

Assembly/installation of the neutral beam absorber starts with surveying the location of the floor plates followed by installation, leveling, and then grouting of the floor plates. Next comes the installation of the jacks with the necessary tie-downs. Then the lower base plate is lowered into place and engages the upper sections of the three jacks. The upper base plate is then lowered onto the lower base plate and engages the two pins mounted on the lower base plate. Then the collimator box is placed on the upper base plate, also positioned by two pins mounted in the upper base plate. Lastly, the three caps are put in place which rest on the collimator box and each is engaged to the upper base plate with two pins. The design concept has been to use a non-fastener assembly so when the unit becomes radioactive, it can be disassembled as rapidly as possible.

Alignment is accomplished with optical tooling. The relevant dimensions of the absorber vacuum chamber will be referenced to small tooling balls mounted on the vacuum chamber. This dimensional information will in turn be transferred to two Taylor-Hobson tooling ball spheres placed in tooling ball sphere cups, CERN drawing No. 8091-5203-3, that are mounted in the notches of the upstream and downstream caps and to a precision level located on the aft end of the collimator box. The alignment centerline in the notches is centered 400 mm vertically above and 380 mm transversely inward from the beam centerline, and toward the tunnel centerline. The notch is cut such that there is a 100 mm clearance around the alignment centerline. The two tooling balls will provide vertical, transverse, longitudinal, pitch and yaw position and the level provides roll position. Positioning of the absorber is accomplished with 3 jacks as shown in Fig. II.1.5.1-7. The vertical axis of the jacks are parallel to gravity and not quite perpendicular to the longitudinal axis of the absorber due to the tunnel slope. Here the 15 tonne ISR jacks, CERN drawing 232-268, have been incorporated into the design which are manually operated. The nominal jack loadings are 6.5 tonne on two jacks and 13 tonne on one jack. Available motion is ± 10 mm in the vertical, transverse and longitudinal directions. Motion sensitivity is 0.25 mm per turn vertically and 0.25 mm per turn horizontally. If greater motion is required in the vertical direction, that will be achieved by adding shims in the jack stack.

Slots have been placed in the absorber for installation of detectors to measure the flux of ionizing shower particles near the axis of the absorber and between the two beam axes. Such detectors, depending on background levels, could have a variety of uses such as fast luminosity measurement, measurement of beam size at the IR and feedback control of beam-beam separation at the IR. Section II.4.7.2 below discusses the possibility of using an Argon ionization chamber for these purposes. At low luminosity with a small probability of interaction per bunch crossing it may be possible to use a plastic scintillator for a detector.

II.1.5.2 Front absorbers for the inner triplet quadrupoles

II.1.5.2.1 Radiation deposition and activation calculations for the front quadrupole absorber

The external front absorbers (TAS) for the inner triplet quadrupoles are located in front of the Q1 quadrupoles and are ±18.4 m from IR1 and IR5. To avoid large backgrounds in the experiments due to back-scattered radiation these absorbers are imbedded in massive steel and concrete shielding which needs to be taken into account in the detailed design of the TAS. Schematics of the TAS, Q1 and the steel and concrete shielding are shown for the two large detectors in Fig. II.1.5.2-1 (ATLAS) and Fig. II.1.5.2-3 (CMS). It is necessary to design support and alignment systems for the TAS so they are an integral part of this shielding. For both detectors there are pumping stations immediately behind the TAS and between the TAS and Q1. A warm to cold transition is between the pumping station and Q1. The primary purpose of the TAS is to prevent ~ 145 W of charged and neutral collision fragments outside the beam tube [58] from quenching the inner triplet superconducting quadrupoles Q1-Q3. Calculations of maximum power density and total power deposited in the IR quadrupoles and first separation dipole have been calculated in Ref. [58] for several choices of aperture and placement of absorbers. The general conclusion of this work was that bore tube absorbers are required in addition to the front absorber in order to reduce the maximum power density to < 0.4 W/kg necessary for operation of Q1-Q3 at design gradient. The bore tube absorbers are described in the section on IR quadrupole design and not included here. Recently the radiation deposition calculations have been repeated for the current layout of the front absorber [56] and these results are given in Fig. II.1.5.2-5 through Fig. II.1.5.2-9. For these calculations, the TAS is assumed to be made of copper with outer radius 250 mm and length 1800 mm. The incident flux of gammas, electrons and positrons, neutrons, protons, pions and muons is shown in Fig. II.1.5.2-5. The mean energy and mean number of each of these particles that strike the TAS per pp interaction and the product of these two parameters are given in Table II.1.5.2-1.

Power density profiles are given as functions of axial distance in Fig. II.1.5.2-4 and of radius in Fig. II.1.5.2-6. The maximum power density is ~10 W/kg near the axis and ~15 cm behind the front of the absorber. The power density falls with increasing axial distance; at a depth 1800 mm, the power density is at most 0.2 W/kg, which is a factor of two below the 0.4 W/kg quench limit for Q1-Q3. (The 0.4 W/kg includes a safety margin of ~3). Remanent dose rates for the TAS are very high. Activation of the TAS assuming 30 days irradiation at design luminosity and one day cool down is shown in Fig. II.1.5.2-9 as a function of axial position for various radii. Assuming an outer cylindrical surface with radius 25 cm the maximum remanent dose rate on the outer cylindrical surface is ~ 17 mSv/hr, well above the emergency (1-2 mSv/hr) and routine (0.1 mSv/hr) access limits. The front surface activation is considerably higher reaching a maximum value ~ 140 mSv/hr near the axis. Assuming a 1.8 m absorber length the maximum activation on the back surface is ~ 60 mSv/hr. When the concrete and steel shielding around the TAS is removed remote handling equipment and caskets or other precautions for storage will be required.

II.1.5.2.2 Front quad absorber requirements and specifications

The requirements for the front quadrupole absorber have been derived from the same general considerations as the neutral beam absorber described in Sec. 1.1.4.1.2 with some differences. The front quad absorbers are buried in shielding cones to protect the detectors from prompt radiation. The magnitude of the prompt and remanent radiation doses coming from the TAS must be known for proper design of the shielding cones but the size of the TAS is determined primarily by considerations of protecting the magnets Q1-Q3 and not by tunnel access limits or ground water activation. The requirements and specifications for the front quadrupole absorbers are given in Table II.1.5.2-3. The TAS is specified to absorb 145 W of power with a maximum temperature increase of 20^{o}C and to transmit a power density < 0.4W/kg. The material for the absorber is Cu.

As with the TAN, the beam tube of the TAS is part of the warm insertion region vacuum system and should be consistent with design specifications and practices employed for that system for vacuum and wall resistivity: OFHC Cu beam tube, in situ bakeable to 150^{o}C, ~10^{-10} Torr range for H_2 and ~ 10^{-11} Torr for the other gases CH_4, CO and CO_2 [57]. The primary gas load in the TAS beam tube will be residual outgassing. An analysis of the pressure in the front quadrupole absorber beam tube indicates that partial pressures in the desired ranges can be achieved with a in situ vacuum baked system even if radiation from the IR causes a 50^{o}C rise in beam tube temperature and the associated increase in thermal outgassing rates [59]. This analysis is more conservative than the design presented here which should have a temperature rise less than 20^{o}C and which has better coupling to the pumps than assumed in Ref. [59]. Analysis similar to that described for the TAN indicates that ion desorption instability will not be a problem [60]. Taking account of the two beams in a single tube, I = 2x0.536 = 1.07 A), the beam tube of the TAS in Table II.1.5.2-3 is ion desorption stable. For the worst case desorbed gas, CO, the safety margin is ~ 2.6 unbaked and ~ 9 baked.

There has been and continues to be considerable discussion concerning the aperture of the TAS. On the one hand one wants a minimum aperture for protecting the quadrupoles, on the other hand the aperture must be large enough to allow beam orbit manipulation, probable injection errors etc.. The aperture analysis is similar to the TAN in Sec. 1.1.4.1.2 and the general requirement is that the aperture exceed $10\sigma_{x,y}$ after allowing for dispersion, closed orbit error, beam separation and alignment and manufacturing tolerances. Aperture tolerances are most restrictive at injection, and for the LHC v5.0 optics the minimum allowable TAS beam tube radius allowing $10\sigma_{x,y}$ is 14 mm. This has sometimes been given in the past for the radius of this beam tube however the present thinking is that the radius should start at 20 mm for initial commissioning and then be decreased to 17 mm as the machine luminosity increases. The design of the TAS should allow for a change in beam tube ID.

To reduce activation of the beam tube flanges it is desirable to increase the beam tube ID outside the absorber, keeping the taper angle between the beam axis and the beam tube surface within 10^{o} for impedance purposes. The flange to flange length is specified to be 2500 mm and the flanges should be the clamped flange type suitable for remote assembly. The actual absorber lengths 1800 mm. The nominal height of the absorber above the tunnel floor, and the range of motion are the same as for the neutral absorber. The transverse alignment and radial aperture tolerance have been reduced a factor of two to ± 0.5 mm. In the future, the aperture analysis will be updated with a new aperture algorithm and current versions of the IR optical design and crossing angle.

Table II.1.5.2-1: Intensity and mean energy of particles striking a IR front quad absorber (TAS)

Particle type	*<n> per pp interaction*	*<E>* *TeV*	*<n><E>* *TeV/pp int*
neutron	0.584	0.261	.1524
proton	0.285	0.292	.0832
charged pion	6.8	0.159	1.081
photon	8.33	0.087	0.725
muon	0.056	0.033	$1.85\mathrm{x}10^{-3}$

Table II.1.5.2-3: Requirements and specifications of the IR front quad absorbers

Absorbed power	145 W
Transmitted power density	< 0.4 W/kg
Beam tube material	OFHC
Absorber material	Cu
Max. temp. increase with beam operation	20 ^{o}C
In situ beam tube bake out temp	150 ^{o}C
Dist. from front flange to IR	±18.4 m
Min. aperture	17 mm
Beam tube radius	17- 20 mm
Aperture radial tolerance	±0.5 mm
Max. beam tube taper	10^{o}
Flange to flange length	2250 mm
Flange type	Clamped, remote assembly
Nominal beam height from tunnel floor	950 mm (1100 mm for cryobox)
Alignment tolerance	± 0.5 mm
Range of vert. and horiz. adjustment	±20 mm
Crane lift limit	5 tonnes

II.1.5.2.3 Front quad absorber conceptual design

The front quad absorber design includes a vacuum chamber, clam-shell copper absorber and an adjustable support structure as shown in Fig. II.1.5.2-9 and Fig. II.1.5.2-11. The vacuum chamber is a 2250 mm long assembly made of a 1800 mm long tube section with 10 degree flared sections attached on either end of the tube and whose ends are terminated with flanges. The tube is an OFHC extrusion with a 60 mm OD that will be machined to match the mating clam-shell. The commissioning vacuum chamber will have a 40 mm ID tube, which is to be replaced with a vacuum chamber with a 34 mm ID tube for physics operation. The flared sections which increase the bore diameter to 64 mm will be OFHC spinnings that are electron beam welded to the tube section. Flanges, nominally 150 mm OD, are to be a CERN configuration that will allow remote assembly of the vacuum connections. The flanges as presently envisioned will have a copper ring brazed to the inside diameter of the flange. The copper ring will in turn be electron beam welded to the flared section. Non-destructive testing of the joints is planned.

The basic quad absorber design configuration is based on the requirement that the quad absorber be installed with the existing ATLAS auxiliary cranes which have 5 tonnes capacity. Therefore, the basic quad absorber assembly has been designed to weigh a nominal 4 tonnes. Clam-shell construction is a two piece bolted copper alloy that clamps around the vacuum chamber. An octagonal configuration with a nominal 500 mm OD has been selected so that the absorber will be stationary when placed. The copper alloy will be a 99% alloy with the addition of either lead, tellurium, or sulfur to substantially improve the machining characteristics of the material. A lifting fixture will be bolted to the clam-shell assembly for handling. This simple construction should allow for remote disassembly if required. For remote bakeout of the vacuum chamber, cartridge heaters and thermocouples are to be built into the absorber assembly to provide a chamber bakeout temperature of 150^{o}C .

The support system is a four tube adjustable system, without moving parts at the absorber, which allows vertical, pitch, transverse and yaw positioning of the absorber. As shown in Fig. II.1.5.2-9, the quad absorber is hung from the outside of the shielding by two of the adjustable structural tubes which can provide vertical and pitch motion over a ± 20 mm range. Likewise, a similar arrangement of two structural tubes is mounted horizontally for transverse and yaw adjustment over a ± 20 mm range.

The details of the support and adjusting mechanism are shown in Fig. II.1.5.2-11. With the support plate-threaded tube assembly secured to the outer shielding and adjusted so that the threaded tube axis is positioned correctly in the transverse and longitudinal directions and the axis parallel to gravity, the structural support tube is inserted through the threaded tube and threaded into the absorber. (Note that the absorbers are at approximately 1.3 degree angles to the horizontal, so the axis of the threaded holes for the vertical structural tubes are angled 1.3 degrees longitudinally in the absorber assembly.) With the structural tube engaged, it is locked in place with the locking screw. The adjusting nut is threaded first onto the structural support tube and then into the threaded tube of the support plate-threaded tube assembly. Because the threads are different on the structural tube and the threaded tube, there is a differential lead of 1 mm per turn of the adjusting nut. With the design here, 20 turns will lift the absorber 20 mm and put it in its nominal central position. After completing the adjustment, the adjustment nut is locked with the locking nut. The horizontal adjusting system is installed in a similar way. To determine the location of the absorber, an invar rod slips through the inside of the structural tube and contacts the absorber. Near the outside end of the invar rod a threaded cap and a spring are provided so that the invar rod can be slightly preloaded after placing the rod in position. On the end of the rod is a platform for mounting a Taylor Hobson alignment sphere cup for alignment. The size of the holes in the shielding is to be minimized to least compromise the shielding.

The design shown in Fig. II.1.5.2-9 and Fig. II.1.5.2-11 is an example of how the absorber could be installed in the presently configured ATLAS shielding design. The shielding designs of both the CMS and ATLAS detectors are currently under development and since this design is quite flexible it is anticipated that the absorber design outlined here will accommodate the shielding designs that evolve for the CMS and ATLAS detectors.

Alignment of the absorber requires that the vacuum chamber be correctly aligned to the axis of the adjacent adjacent low-beta insertion quadrupole. To accomplish this goal, inside diameter measurements of the vacuum chamber are to be referenced to small tooling balls attached to the vacuum chamber flared sections. This information shall in turn be referenced to both the invar rod contact points in the absorber and to the external alignment locations on the ends of the invar rods during final assembly.

A thermal analysis shows, with 200 W of absorbed power and forced ambient air cooling, that an internal temperature gradient in the absorber of 3 ^{o}C is expected and the absorber surface - air temperature difference is 8 ^{o}C with 0.6 cubic meters per minute of air flow. Thus, it is expected that the maximum temperature of the vacuum chamber will rise 11 ^{o}C above the ambient temperature. To provide the necessary cooling, a blower and an air manifold are to be provided.

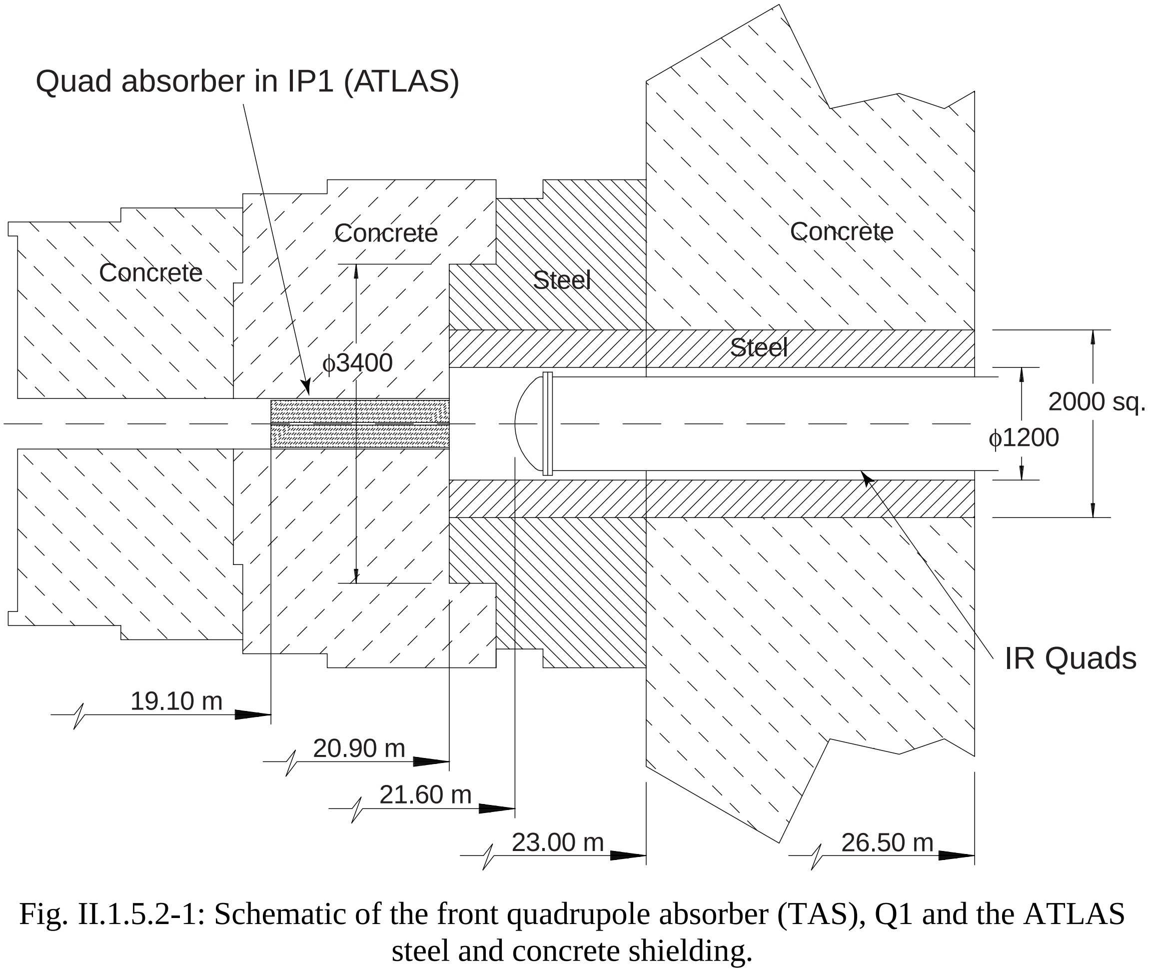

Fig. II.1.5.2-1: Schematic of the front quadrupole absorber (TAS), Q1 and the ATLAS steel and concrete shielding.

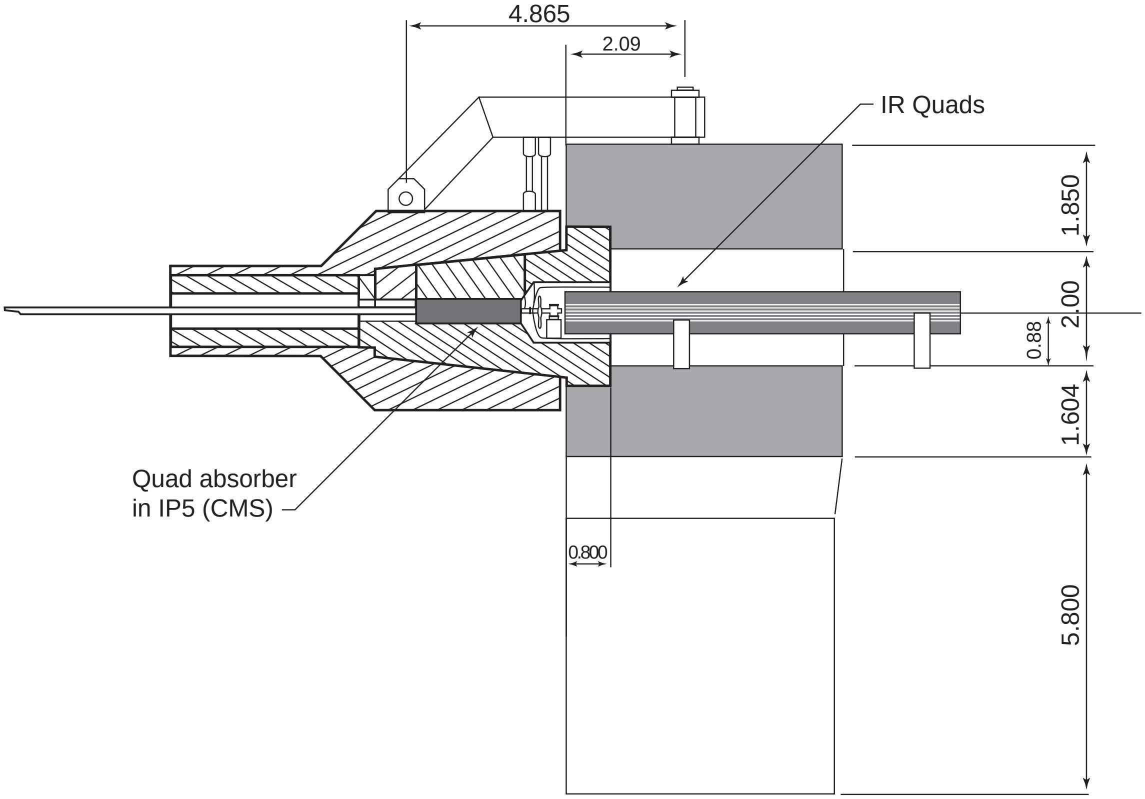

Fig. II.1.5.2-3: Schematic of the front quadrupole absorber (TAS), Q1 and the CMS steel and concrete shielding.

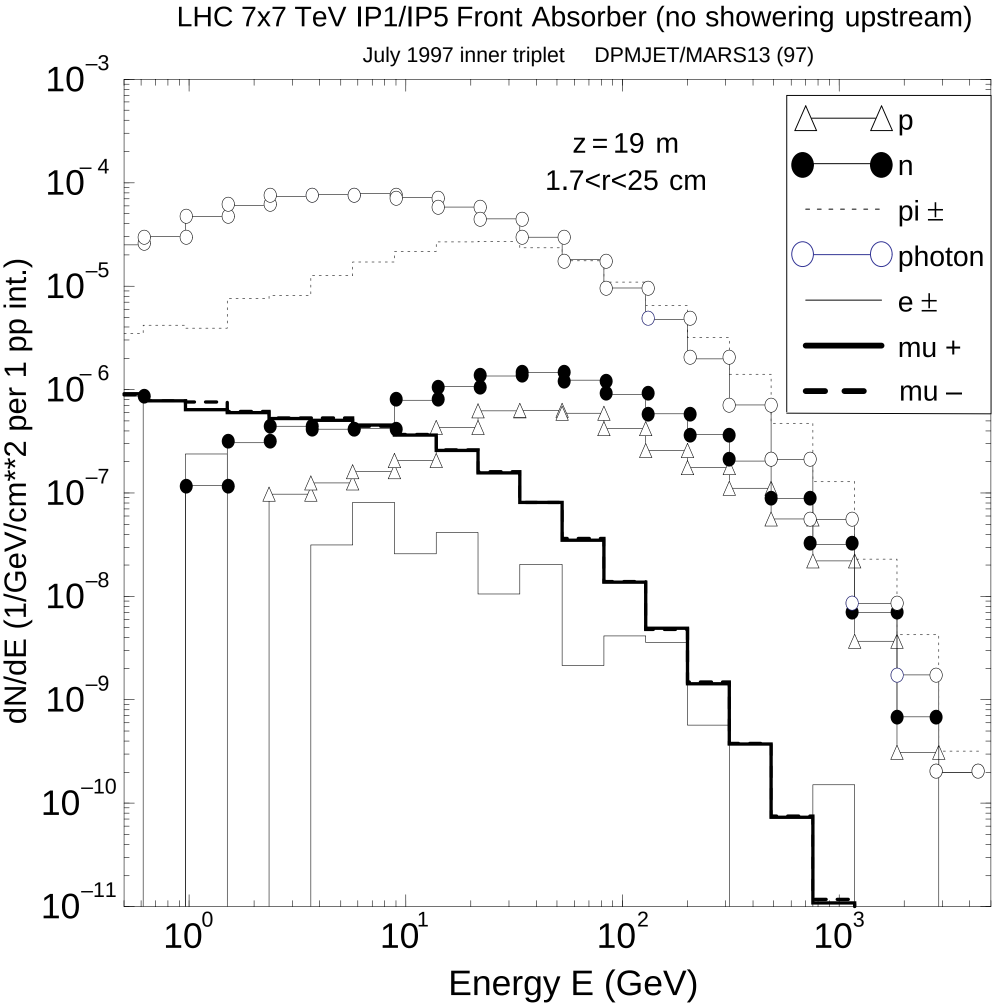

Fig. II.1.5.2-5: Particle fluxes incident on the front quad absorber (TAS) due to IR interactions.

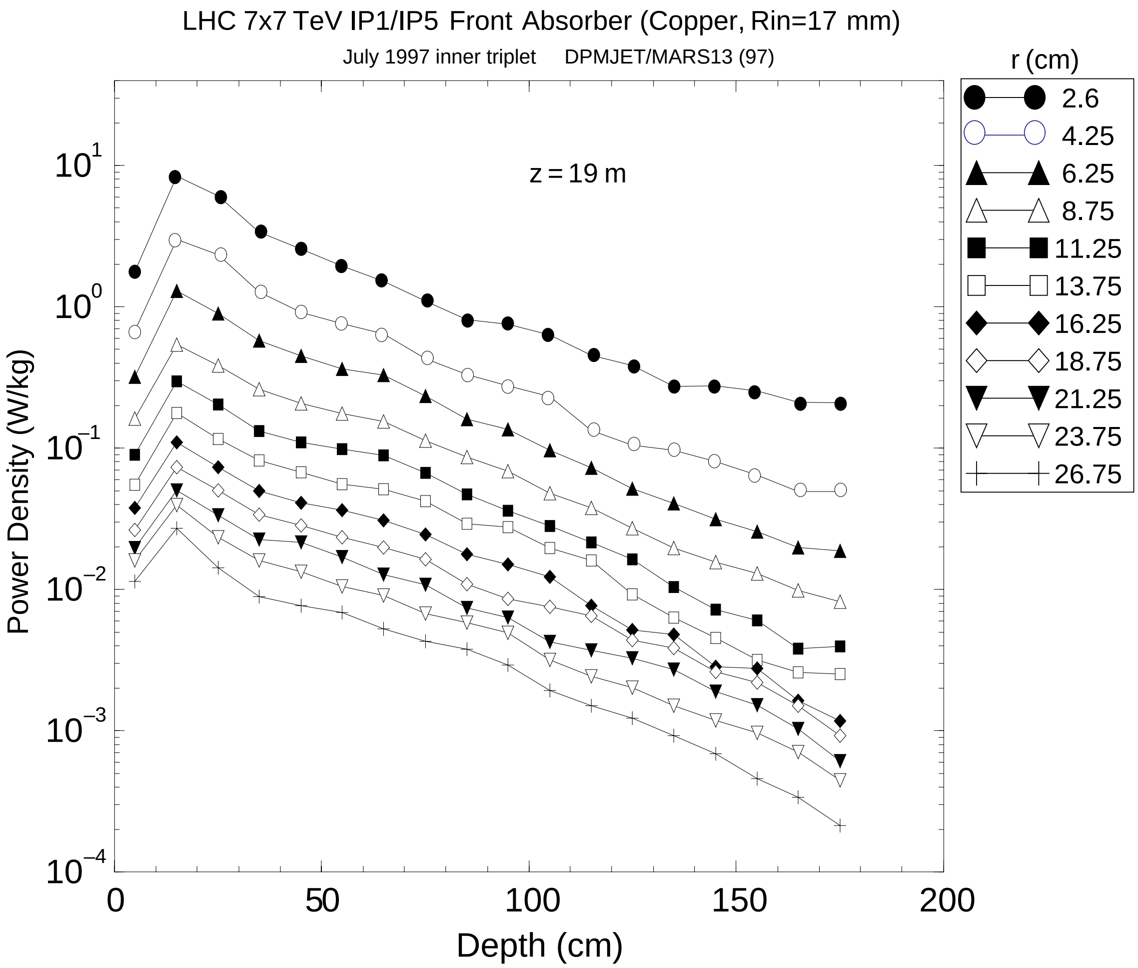

Fig. II.1.5.2-4: Power density in the front quad absorber versus axial distance averaged over azimuthal angle for several radii.

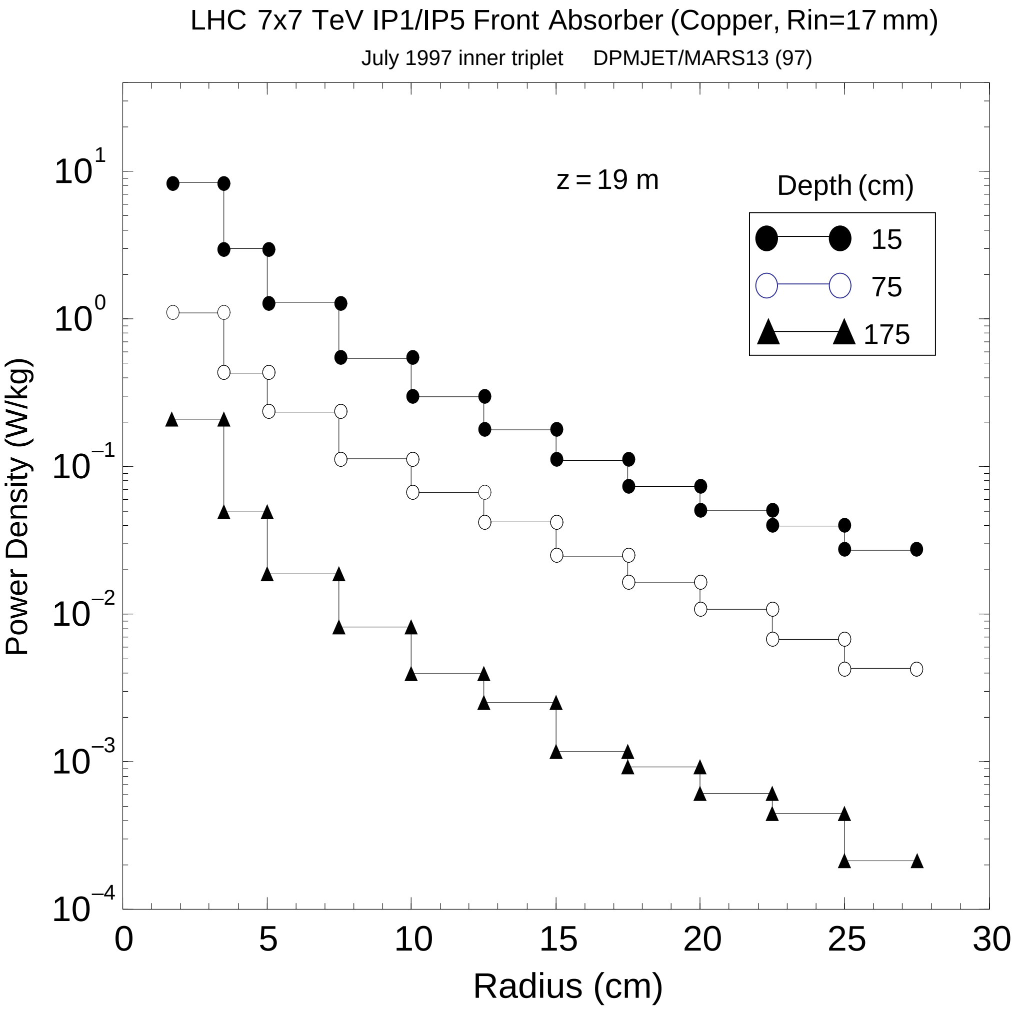

Fig. II.1.5.2-6: Power density in the front quad absorber versus radius, averaged over azimuthal angle, at three axial locations.

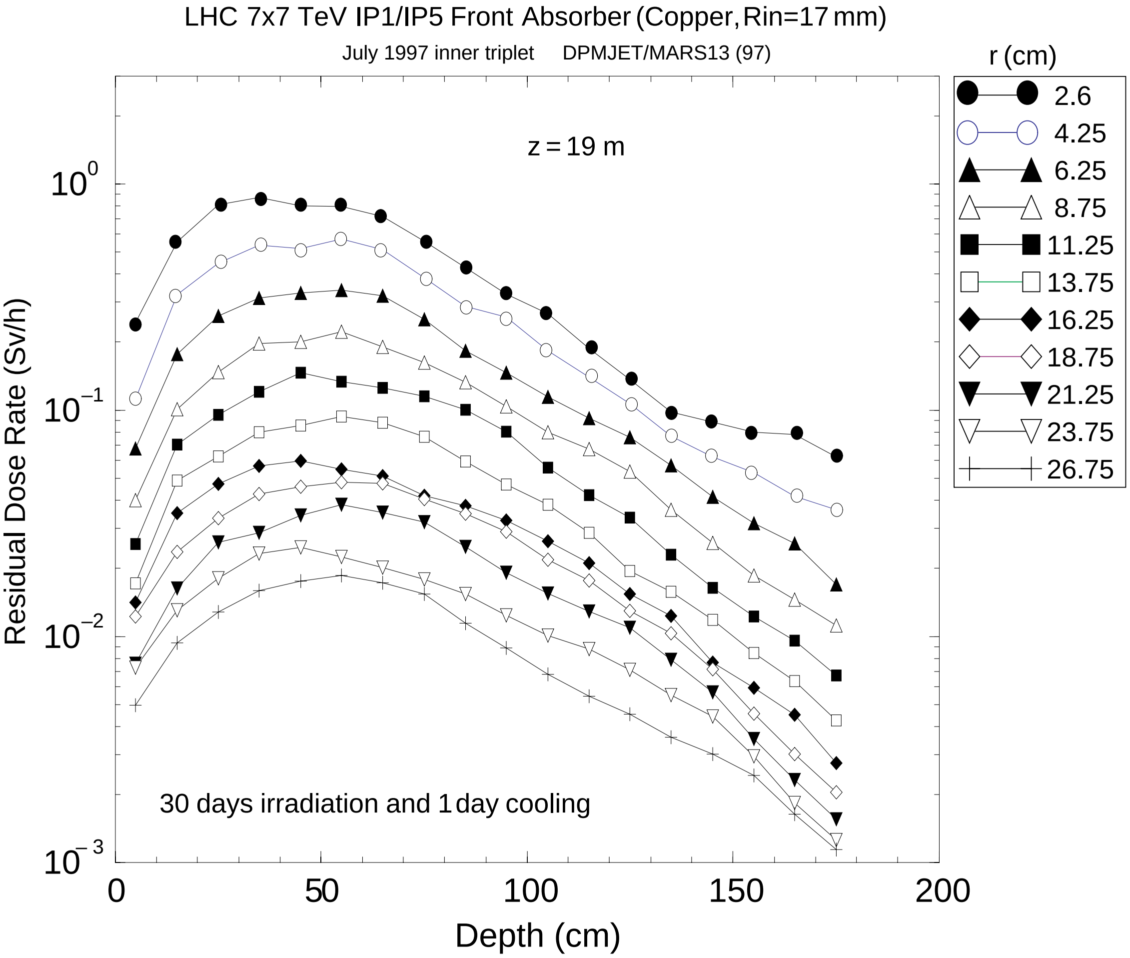

Fig. II.1.5.2-9: Activation of the front quadrupole absorber assuming 30 days irradiation at 10^{34} cm^{-2}sec^{-1} and one day cool down.

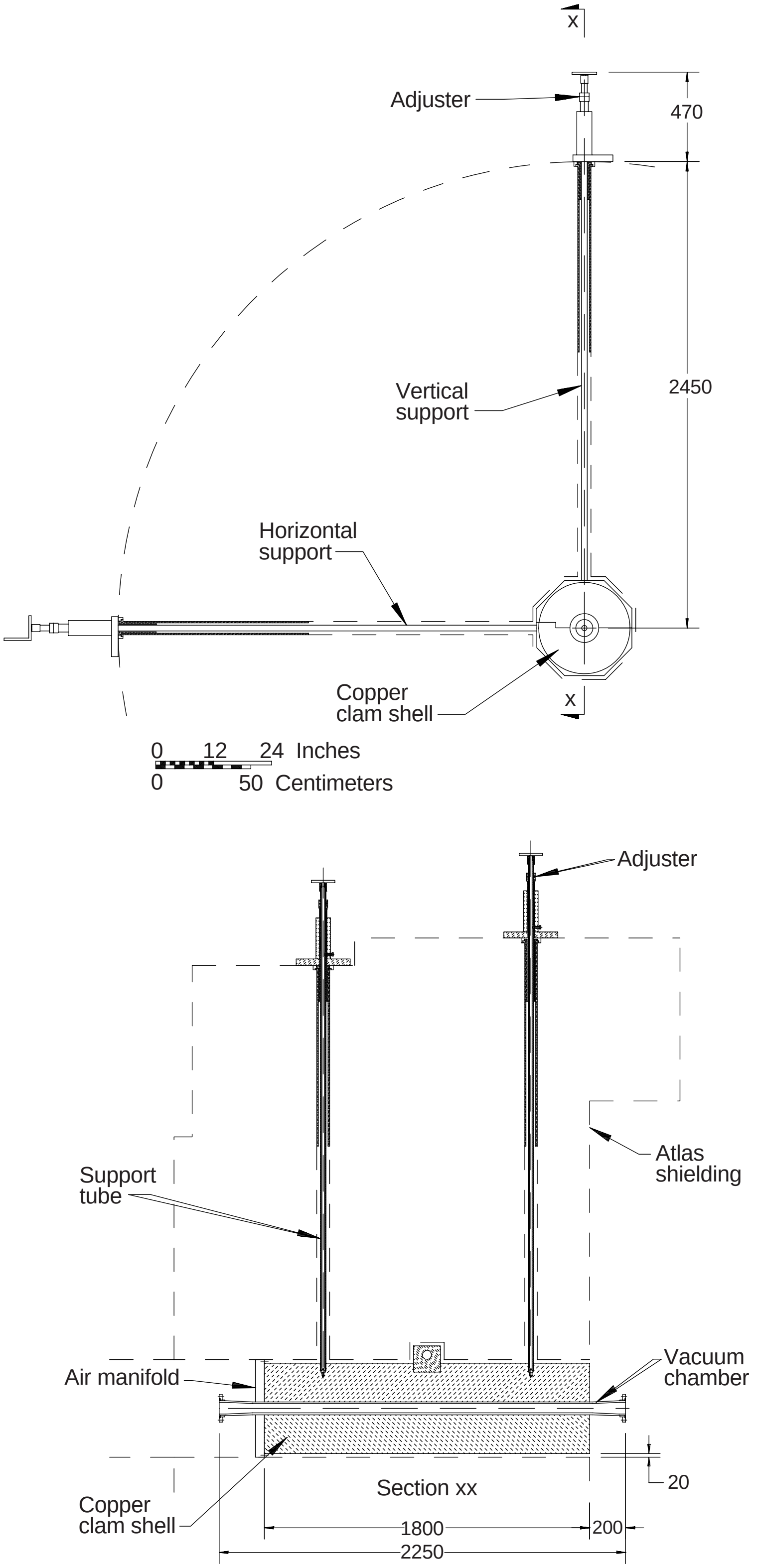

Fig. II.1.5.2-9: Front and side views of the front quadrupole absorber (TAS) and ATLAS shielding (sarcophagus).

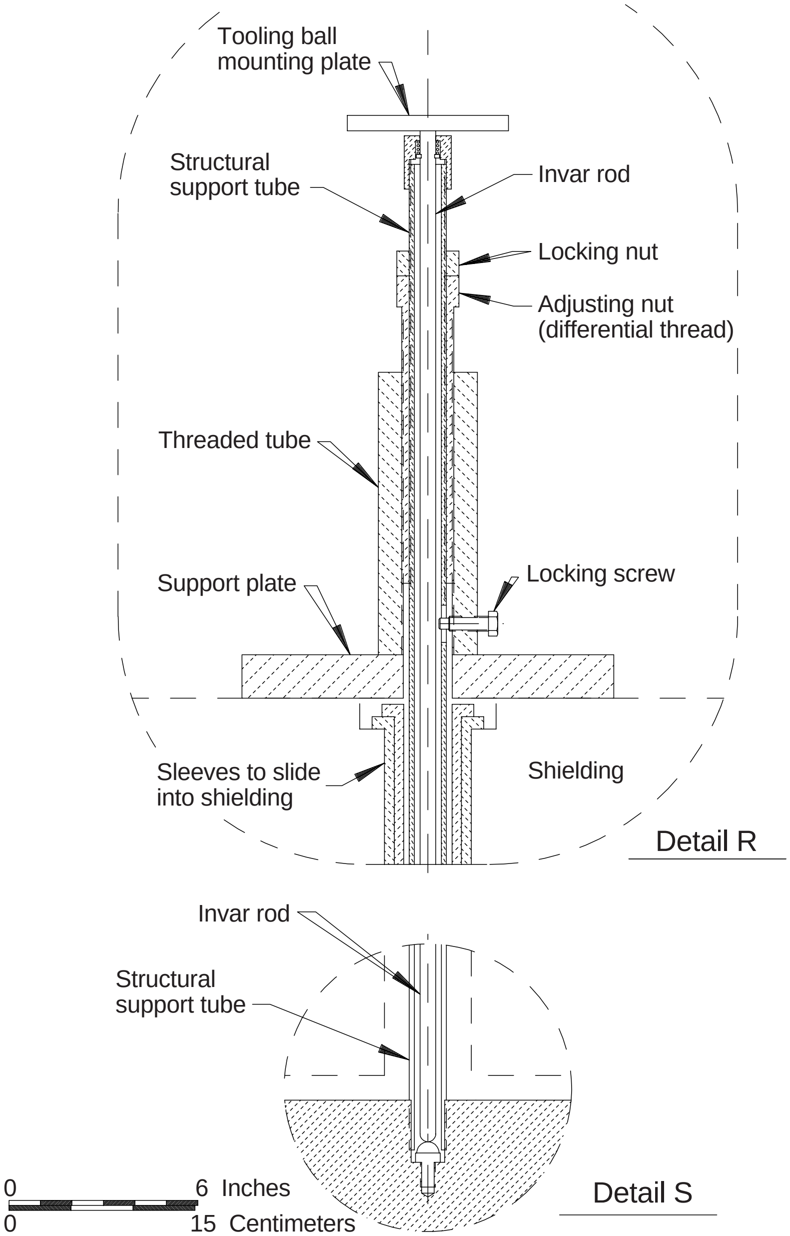

Fig. II.1.5.2-11: Details of the ends of the supporting tubes and alignment rods for the TAS.

II.1.5.2.3.1 References

[54] The LHC Study Group, The Large Hadron Collider: Conceptual Design, CERN/AC/95-05.

[55] N. Mokhov and G. Stevenson, title?, CERN/TIS-RP/IR/94-17 (Jul 1994).

[56] N. Mokhov, report in preparation.

[57] A. G. Mathewson and S. Zhang, “The LHC Warm Straights Vacuum System,” *CERN Vac. Tech. Note 95-33* (Nov 1995).

[58] N. Mokhov and J. Strait, “Optimization of the LHC Interaction Region With Respect to Beam-Induced Energy Deposition,” *Proc. of the 5th European Part. Accel. Conf., 386,* Barcelona (1996).

[59] I. Collins, A. Mathewson and S. Zhang, “The Vacuum System of the Low-β Absorbers in ATLAS and CMS,” *CERN Vac. Tech. Note 96-06* (Apr. 96).

[60] W.C. Turner, “Ion desorption stability of the beam tube in the low-β insertion absorbers of the LHC,” *LBNL CPB Tech Note 143* (Nov. 97).

II.1.6 IR Layout and Integration

II.2 RF Insertion

II.2.1 RF Region Dipoles

II.2.1.1 Introduction

The dipoles required in the RF region of the LHC have field and aperture requirements close to those of the RHIC [62] arc dipole magnets. Thus the superconducting coils developed for these magnets can be used cost-effectively in a dipole design that satisfies CERN's requirements. The required magnets will be built at BNL using tooling constructed for the RHIC program, so far as possible. RHIC magnets were built commercially but the company that built those magnets was not interested in this proposed, modest construction program. All magnets will be tested at operating temperature in the existing BNL test facility, then shipped to CERN for installation in the LHC lattice. Close coordination is required between the two laboratories to ensure that they meet all requirements for operation in the LHC.

II.2.1.2 Objectives, Specifications and Requirements

II.2.1.2.1 Overview

The dipole magnets to be built will be double aperture dipoles labeled D3a, D3b, D4a, and D4b. These magnets increase the separation of the beams of the LHC from the nominal spacing of 194 mm to 420 mm so that individual RF cavities can be installed for each beam, and then return the beams to the nominal 194 mm spacing. A drawing of this region of the LHC is shown in Fig. II.2.1.2-1.

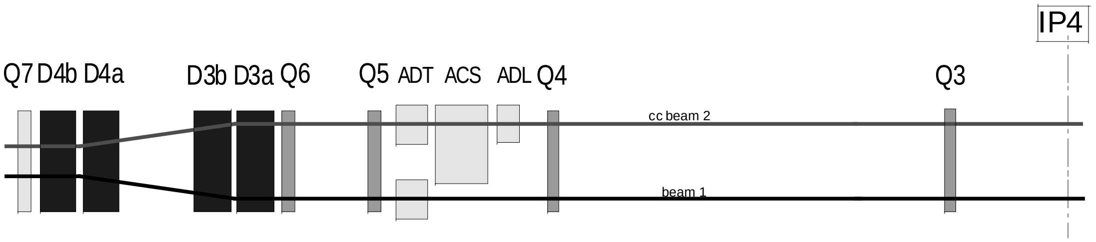

Fig. II.2.1.2-1 Geometry in the RF Region of the LHC. The nominal 194 mm separation of the beams is increased to 420 mm so that there is sufficient space for independent RF cavities for the two beams. The labels ADT, ACS, and ADL refer to components in the RF system of the machine.

The dipole magnets are designed with a common element: collared coils in which the superconducting coils are mechanically the same as those built for the RHIC arc dipole magnets [61, 62]. The RHIC dipole is a well understood magnet with good quench performance and field quality. These collared coils are assembled into yokes with common outside dimensions but with varying internal features (iron saturation control holes, aperture spacing) depending on location. The use of common outside dimensions reduces tooling cost. The yoke size has been constrained to fit into cryostats similar to those designed by CERN.

These 2-in-1 magnets have the field in each aperture in the same direction. This is different from the more usual 2-in-1 designs, such as used in the LHC arcs, where the fields are in opposite directions and the flux in one aperture returns partially through the other. With these in the same direction, the fields of the two apertures are decoupled and are like those in independent magnets, provided there is sufficient iron available to contain the flux. Judiciously placed cutouts in the yoke, where the placement is altered for each particular separation of the coil apertures, control the field asymmetries that would otherwise be generated. These cutouts are also used to give equal excitation curves for magnets with different coil aperture spacing (field quality is discussed in Section II.2.1.3.12). This latter goal is aided by again having sufficient iron on the midplane to reduce saturation effects.

The field quality expected in these magnets, given in Section II.2.1.3.12, is anticipated to be suitable for the LHC. Accelerator Physics studies planned as part of the US/CERN collaboration will confirm through tracking calculations that this field quality is adequate.

The dipole magnets to be built by BNL for the LHC are summarized in Table II.2.1.2-1.

Table II.2.1.2-1 Dipole magnets to be built by Brookhaven for the LHC.

Name	*Style*	*Coil Aperture, mm*	*Magnetic Length, m*	*Aperture Separation (cold), mm*	*Number (Spares)*
D3a	2-in-1	80	9.45	400	2(1)
D3b	2-in-1	80	9.45	382	2(1)
D4a	2-in-1	80	9.45	234	2(1)
D4b	2-in-1	80	9.45	194	2(1)

II.2.1.2.2 Dipole Cold Mass

Fig. II.2.1.2-3 shows cross-sections of the dipole cold masses. The design is based on a single-layer "cosine theta" coil, wound from a partially keystoned, 30-strand NbTi superconducting cable. The coils are collared with stainless steel collars, which are intended to constrain the full Lorentz forces when the magnet is powered. A laminated, cold steel yoke encased in a stainless steel helium-containing cylinder mechanically supports the coils. The helium vessel is also a structural part of the yoke assembly. The dipole operating field is 3.55 T. The magnets can be operated at temperatures up to 4.6 K to provide the required field; in the LHC it is planned to operate them at a lower temperature. Some general design parameters are listed in Table II.2.1.2-3. Fig. II.2.1.2-5 shows a cross section of D4a in the lead end of the magnet.

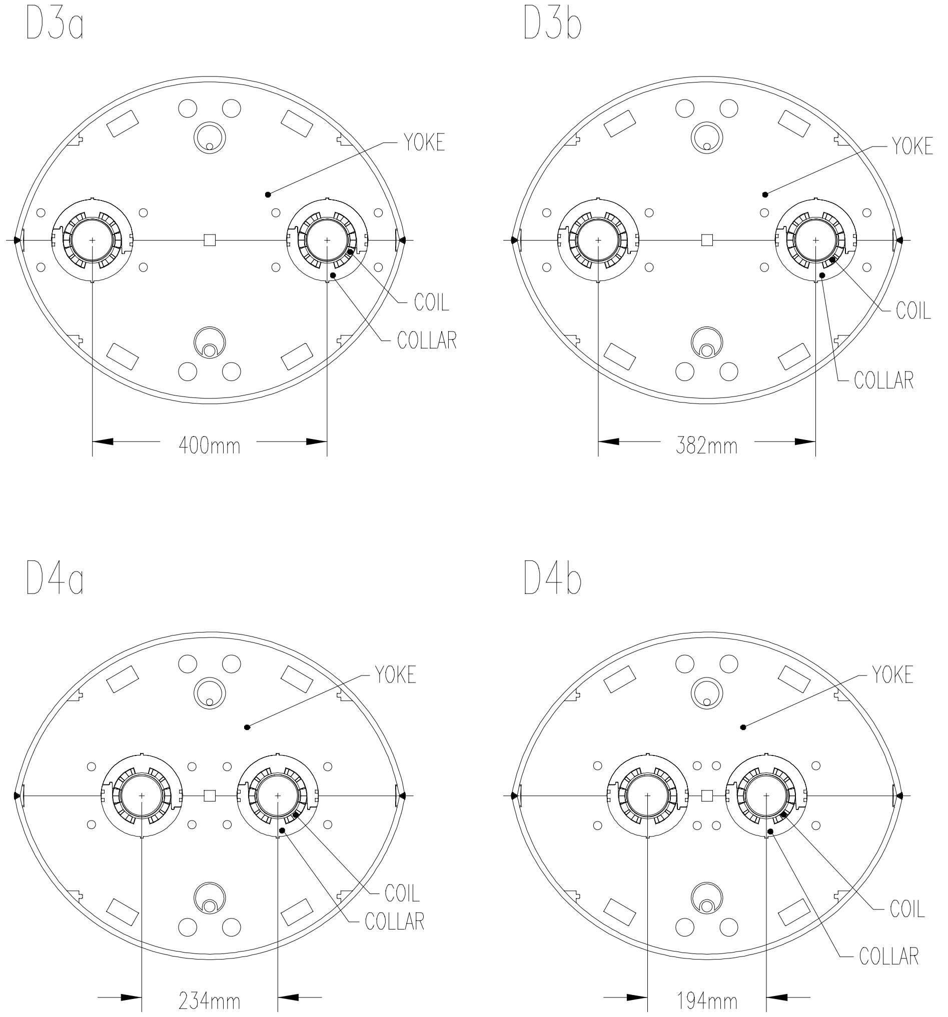

Fig. II.2.1.2-3. Dipole magnets for the RF Region. The coil apertures are 80 mm. The yokes all have the same external dimensions.

Table II.2.1.2-3. General design parameters. “Nominal” means the maximum operating point for good field quality.

Item	*Units*	*Value*
Operating field (7 TeV)	T	3.55
Nominal field	T	3.8
Nominal current	kA	6
Coil inner diameter	mm	80
Magnetic length	m	9.45
Operating temperature, max	K	4.6

II.2.1.2.3 Assembled Magnets

The cold masses are assembled into cryostats to make completed magnets, Fig. II.2.1.2-5. The cryostat consists of a cylindrical vacuum vessel, aluminum heat shield, blankets of multilayer thermal insulation, cryogenic pipes, and the magnet support system. A variety of measurements, both mechanical and electrical, will be made on the magnets during the construction process. All subassemblies must satisfy the test requirements before incorporation into a magnet. Completed magnets are tested at operating temperature, then packaged and shipped to CERN for installation into the LHC.

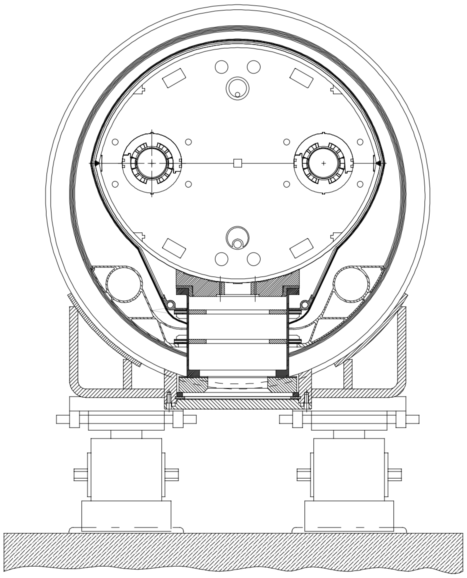

Fig. II.2.1.2-5. Magnet D3a in its CERN-style cryostat. The vertical dimensions of the coldmass are the same as those for LHC arc dipoles. The diameter of the vacuum tank is 914 mm.

II.2.1.3 Technical Description

II.2.1.3.1 Superconductor

A 30-strand (wire) superconducting cable will be used in the fabrication of all of the dipole magnets. A similar cable has been used for the RHIC arc dipole and quadrupole magnets [62].Consequently, the cable fabrication methods are well developed. The superconductor wire to be used in the cable was purchased for the SSC program and has been kept in storage since the end of that project. Its properties are similar to those of the wire used for RHIC, but with a copper to superconductor ratio of 1.8 rather than 2.25. With active quench protection in the magnets, and a sizable margin between required operating current and predicted quench current, it is anticipated that this material will give satisfactory results.

The mechanical and electrical properties of the superconducting wire to be used are summarized in Table II.2.1.3-1. Each wire consists of 4165 NbTi alloy superconducting filaments with a nominal diameter of 6 μm and a spacing of >1 μm. The exact number of filaments was chosen by the superconductor vendor based on the details of the billet design. Copper is used as the matrix between filaments, it occupies the central core of the wire, and it provides an outer covering for the wire. Copper represents about 64% of the wire cross section and is important for the cable and magnet operational stability as well as for protection against burn-out through overheating during a quench. The wire diameter of 0.648 mm was tightly controlled during final stages of manufacturing and was checked with a laser micrometer.

The wire minimum critical current is defined at a temperature of 4.22 K, an applied magnetic field of 5 T perpendicular to the wire axis and a resistivity of $1\times10^{-14}\ \Omega\cdot\text{m}$ based on the total wire cross section. This current corresponds to a minimum current density in the NbTi superconductor of 2750 A/mm^2 at 5 T. The SSC wire meets or exceeds this minimum specification. The wire critical current at 3 T will be sampled in order to monitor the effects of superconductor magnetization at low field.

Table II.2.1.3-1**.** Superconducting wire parameters.

Item	*Units*	*Value*
Mechanical		
Nominal filament diameter	μm	6
Nominal filament spacing	μm	>1
Nominal copper to superconductor ratio		(1.8±0.1):1
Number of filaments		4165±20
Wire diameter	mm	0.648±0.003
Wire twist direction		Right
Wire twist pitch	mm	13±1.5
Electrical		
Wire min. critical current at 5 T, 4.2 K	A	325
Wire maximum critical current at 3 T	A	1.6 ∗ measured I_c @ 5 T
Wire maximum R(295 K)	Ω/m	0.082
Wire minimum RRR		38

Thirty wires are fabricated into a Rutherford-type cable by first twisting them around a mandrel, then rolling them into a flat, keystoned shape with dimensions given in Table II.2.1.3-3 and Figure II.2.1.3-2. The variations of the cable dimensions, especially the cable mid-thickness, will be tightly controlled because the magnetic field quality of the magnets and the coil prestress are strongly dependent on them. The cable lay is chosen to be opposite to the wire twist and requires a cabling machine operating in a planetary mode for fabrication. The cable minimum critical current (see Table II.2.1.3-3) is defined in a similar way to that for the wire, but with the magnetic field perpendicular to the wide surface of the cable and with compensation for self-field. The cable minimum critical current can be obtained from the wire minimum critical current at 5 T times 30 (number of wires in cable) and multiplying by 0.95 (allowance for 5 % degradation in cabling). Wire piece lengths are large enough to allow all cable lengths to be produced without cold welds.

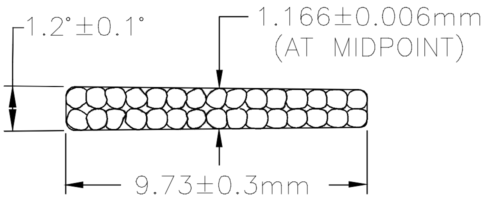

Fig. II.2.1.3-1. Cross section of the cable to be used to fabricate coils for LHC dipoles.

Table II.2.1.3-3. Superconducting cable parameters.

Item	*Units*	*Value*
Mechanical		
Number of wires in cable		30
Cable mid-thickness	mm	1.166±0.
Cable width	mm	9.73±0.0
Cable keystone angle	deg	1.2±0.1
Cable lay direction		Left
Cable lay pitch	mm	74±5
Electrical		
Cable minimum critical current at 5 T, 4.2 K	A	9260
Cable maximum R (295 K)	Ω/m	0.00287
Cable minimum RRR		38

Several differences with respect to RHIC magnets are noted. The cable interstrand resistance may differ from that in the Oxford-produced cable used in the RHIC production magnets. This will change the field distortions due to eddy currents while the magnets are ramped. In addition, the SSC wire to be used is “half hard” vs. “full hard” used in RHIC. Coils made with this wire are expected to have less post-cure shrinkage than experienced with the RHIC coils, so the coil lengths will be somewhat longer than in RHIC. These differences are not expected to compromise magnet performance in any significant way.

II.2.1.3.2 Dipole Beam Tube

The magnet includes a cold beam tube with dimensions given in Table II.2.1.3-5. It is centered inside the coils: horizontally with G-10 bumpers spaced axially at regular intervals, vertically by the collars. The gap between tube and coil defines a helium buffer space. The tube is seamless, 316 LN stainless steel and is wrapped with 25 μm Kapton with 66% overlay. This provides 75 μm of insulation, which is tested for integrity to ground at 5 kV. A beam tube liner will be installed into these magnets at CERN. Therefore, the tubes do not require copper-plating on the inside surface.

Table II.2.1.3-5. Dipole beam tube parameters.

Item	*Units*	*Value*
Outside diameter	mm	77.00 ± 0.38
Outside diameter inc. Kapton wrap	mm	77.1
Wall thickness	mm	1.96 ± 0.18
Inner diameter, nominal	mm	73
Weight, nominal	kg	38
Beam tube-coil radial gap	mm	1.5

II.2.1.3.3 Dipole Coil

The superconducting coil is assembled from two half-coils that are wound on automated machinery and then formed into a specified size in a precision molding operation. It consists of a single layer of 32 turns per half-coil arranged in four blocks with intervening, symmetric copper wedges; the sizes and positions of the wedges and pole spacers give field harmonics that are small (Section II.2.1.3.12). The four current blocks per half-coil design is identified as 9B84A. The cable is insulated with 2 double layers of the polyimide film Kapton CI. The first double layer has polyimide adhesive on the outer side of the film; the second has it on both sides. This all-polyimide insulating system requires a brief exposure to a temperature of 217 °C to set; an appropriate curing cycle was developed and extensively used in the RHIC program with excellent results. The coil ends have been designed to simplify construction and to reduce harmonic content. The number of spacer parts, machined from Ultem, in the two ends of each half-coil totals 27: 17 turn spacers, 2 end saddles, and 8 wedge tips. The coil design parameters are given in Table II.2.1.3-9 and -II.2.1.3-4.

The coil length given is that of RHIC production coils. As mentioned earlier, the superconductor wire in those coils was “full-hard”, whereas the SSC surplus wire to be used in these coils is “half hard”. This means that it was annealed after wire draw-down. Coils have a tendency to shrink and develop considerable tension during the curing process, so that they become shorter upon removal from the curing mandrel. This is due to tension in the superconducting filaments within the wire, which is developed during wire manufacturing in the draw-down steps, and which is released as the copper anneals during curing. Those that have been made with annealed wire demonstrate less shortening, so the length of these coils for the LHC magnets in expected to be somewhat longer (several millimeters) than given in Table II.2.1.3-5.

Table II.2.1.3-9. Dipole coil design parameters.

Item	*Units*	*Value*
Inner diameter	mm	80
Outer diameter	mm	100
Length, overall	m	9.646
Length, coil straight section	m	9.266
Cable length per half-coil	m	610
Cable mass per half-coil, bare	kg	50
Cable mid-thickness with insulation, under compression	mm	1.352
Dielectric strength: current to ground @ 5 kV	μA	<200
Coil-collar insulating Kapton thickness, inc. quench resistor	mm	0.64
Midplane Kapton thickness	mm	0.10
Cable wrap material thickness, Kapton CI	μm	25
Pole angle	deg	73.18
Number of turns per half-coil		
1st block (pole)		4
2nd block		8
3rd block		11
4th block (midplane)		9

Table II.2.1.3-7. Coil wedge parameters.

Wedge	*Angle, deg*	*Inner edge thickness, mm*	*Radial width, mm*
1 (pole)	16.68	7.12	9.70
2	9.83	3.09	9.70
3 (midplane)	8.10	0.39	9.65

II.2.1.3.4 Collars

In the 2-in-1 magnets, collars apply mechanical prestress to the coil and separate the coil from the steel yoke, resulting in reduced saturation effects at high field. In addition, they key the coil to the yoke laminations so that precise alignment of the magnetic field can be set and maintained. The collars are punched from high-manganese stainless steel. This material was used with good results in the SSC program and features high strength, low permeability, and a low thermal coefficient of expansion well matched to that of the iron yoke. The collars are placed around the coil in packs that are ~150 mm long. Sheets of insulating Kapton and quench protection heaters are first placed around the coil, and mid-plane caps of Kapton between coil halves. A press (existing) compresses the collars around the coil. They are held together with phosphor-bronze keys inserted in keyways in the outer surface. The nominal design preload in the coil is 69 MPa at room temperature. This reduces to no less than 33 MPa at cryogenic temperature.

Finite element calculations [63] using ANSYS have established the collar width (the width of the material on the midplane) of 20 mm in the straight section of the magnet. With a coil compression of 84 MPa, the vertical elongation of the collared coil radius is 75 µm, an acceptable value that allows straightforward assembly of the yoke around the collared coil. The Lorentz force at full field results in collar deflections outward in the horizontal direction. After 50-100 µm of radial movement (depending on the actual clearance, nominally line-to-line, between collared coil and yoke inner diameter), the yoke restrains the collared coil and further motion is not possible. Small elastic motions such as these are acceptable and do not compromise quench performance.

In the lead end of the magnet, it is necessary to bring the lead from the pole turn of the coil to the outside over the top of the coil. This is done with a spacer incorporating a path for the cable to follow. Enlarged collars are designed to fit over this spacer. To avoid potentially inadequate support of the coil at the pole in the critical end turn-around, the collars' width is increased from 20 mm to 25 mm. This design results in an enlarged cutout in the yoke, which also has the desired effect of reducing the peak field in the ends. The same yoke cutout is implemented at the return end to maintain symmetry between the ends of the magnet and to reduce the peak field there as well.

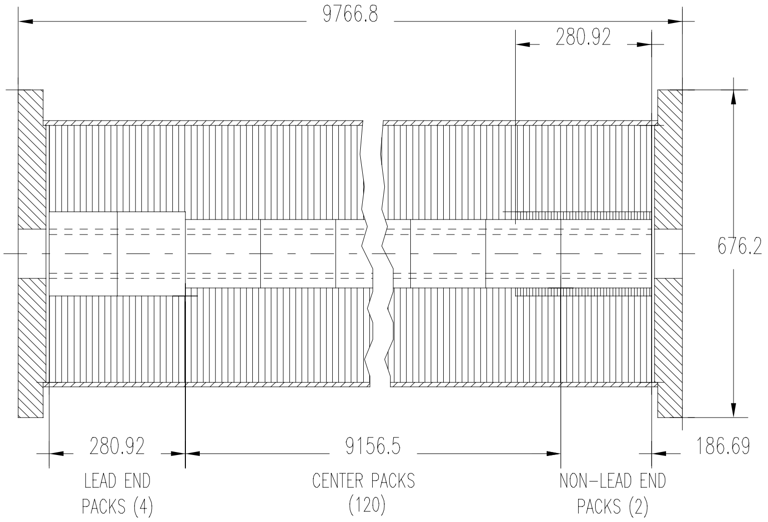

Fig. II.2.1.3-3. A longitudinal section through one of the apertures of the 2-in-1 magnet. The two sets of dashed lines near the center indicate the coil, which has an ID of 80 mm and an OD of 101.6 mm. The collars, shown unshaded around the coil, have ODs of 141.6 mm and 173.7 mm in the center and in the lead end respectively. The end plates, which are round and have a machined shoulder to accept the oval yoke/shell cross section, are shown as they appear at the center of the magnet, not at the coil position.

With a width of 25 mm, the radial vertical distortion of the end collar is 150 μm under a collaring load of 84 MPa [64] , still an acceptable amount to assemble the collared coil into the yoke. For most of the end, the modulus of the coil is insufficient to maintain so high a compressive load, so the 150 μm distortion occurs over only a short section of the coil near the pole turn-around.

Fig. II.2.1.3-3 shows a drawing of the radial construction of the magnet along its length including its two ends. A view of a half-coil including the design for the exit of the lead from the coil pole turn to the outside is shown in Fig. II.2.1.3-4. The turn is first deflected to the center of the pole, then is ramped up to clear the end turns as it exits the magnets. Parts that fit the geometry and that can be compressed by the collars are used to ensure that the large Lorentz forces exerted on this lead are well constrained. The geometry is difficult because the locations of all parts move as the collars are squeezed onto the coil, yet the parts must fit with good precision in the assembled magnet if the conductor is to be free of Lorentz motion.

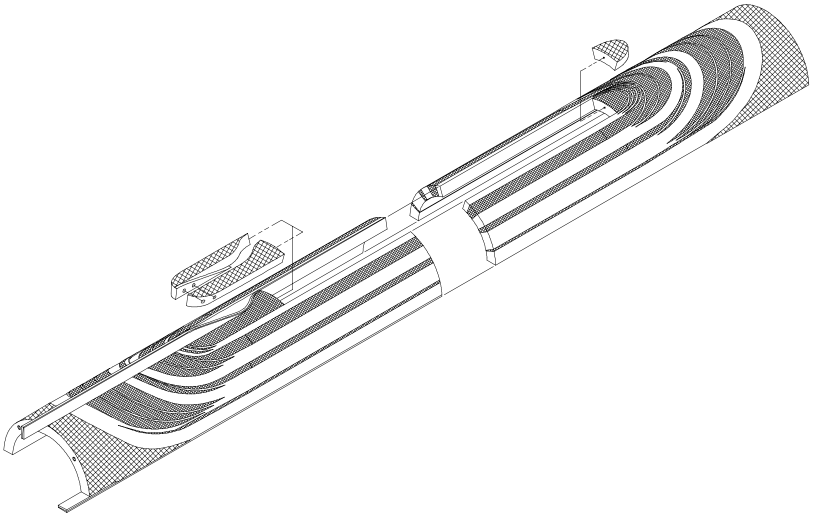

Fig. II.2.1.3-4. A half-coil showing the leads entering and exiting the coil. The parts guiding the lead from the pole turn to the outside of the coil are especially critical for good performance.

II.2.1.3.5 Dipole Yoke and Helium Containment

The yoke is optimized to minimize the current dependence of multipoles at high fields. To reduce cross-talk induced harmonics (such as a normal quadrupole term in the dipole), the yoke is made wide enough to contain the flux lines at the maximum design field. Since more iron is required at the midplane, the oblate shape is adopted. This is done by vertically offsetting the center-of-curvature of the half-yoke from the magnet center. The horizontal size is determined by the goal of reducing the cross talk at the maximum design field for magnets having the maximum aperture separation.

The vertical size is made equal to the LHC dipole yoke outer diameter so that some of its cryostat's hardware can be used. In the present design the yoke outer diameter is 670 mm and, after offsetting the center-of-curvature, the two half-yoke centers, above and below the midplane, are separated by 120 mm. This matches the vertical size of LHC dipoles, which have an outer diameter of 550 mm.

The high field current dependence due to iron saturation is minimized by optimizing the size and location of the saturation control holes or cutouts. In the optimized solution, the computed change in the saturation-induced harmonics (allowed and non-allowed) is within one unit (@ 25 mm radius) in all the dipoles. The saturation is controlled by four, 15 mm radius holes symmetrically located at a radius of 100 mm from the center of each aperture. The optimized angular location depends on the separation between the two apertures and is respectively 28^o, 28^o, 30^o, 31^o in the first quadrant of dipoles D3a, D3b, D4a and D4b.

The yoke laminations are punched from 1.5 mm thickness, low-carbon steel sheet. The specified rms tolerance for the magnetic field integrated over the length of the dipoles requires that the weight of steel in the yoke be controlled to within 0.07%; to achieve this, the laminations that make up the yoke are weighed and adjusted to this tolerance.

For assembly, the bottom yoke laminations are set up on rails to provide alignment, the two collared coils are placed into the laminations, and the top yoke laminations are placed over the assembly. Stainless steel shells, 9.5 mm thick (designed to meet pressure vessel code), are positioned around the yoke while the yoke is supported through holes in the bottom shell. This support fixture maintains alignment in the subsequent welding operations. The shells are welded along the horizontal midplane to stainless steel weld-backing strips fabricated to the required shape (written assembly procedures give the actual sequence of steps required). This welding operation closes the structure and forms a high-pressure (2.1 MPa) helium containment vessel. The shrinkage of the weld compresses the steel yoke and ensures that any residual gap on the yoke midplane is closed. Further compression is provided at operating temperature due to the differential contraction of the stainless steel shell relative to the steel yoke.

Following the longitudinal welding of the shell, round end plates with a machined, oval shoulder are welded to the shell at each end of the magnet. Set screws that press shaped, stainless steel bars against the ends of the coil are installed in the end plates. They serve to restrain the axial Lorentz forces. The magnitude of these forces determines the thickness of the end plates; the goal, as specified for the RHIC magnets, is typically to prevent deflections in the plate of more than 0.25 mm.

Additional operations on the cold mass include the welding of closure plates over the alignment holes in the shell and the attachment of cradles to support the cold mass on posts in the cryostat. After completion of electrical interconnect work at the ends of the magnets, round end bells including bellows are welded to the end plates to close the helium volume and to make the transition to the neighboring magnet or cryo-module.

Some yoke design parameters are listed in Table II.2.1.3-8. For comparison, the RHIC dipole parameters (operating field is 3.4 T) are also listed.

Table II.2.1.3-8. Dipole yoke and yoke containment design parameters.

Item	*Units*	*Value*	
		1-in-1	*2-in-1*
Aperture for collared coil	mm	119.4	141.6
Yoke horizontal size	mm	266.7	657
Yoke vertical size	mm	266.7	550
Lamination length	m	9.64	9.64
Length inc. end plates	m	9.73	9.78
Weight of steel	kg	2,757	16,700
Shell, wall thickness	mm	4.9	9.5
Shell, weight	kg	306	1340
End plate, thickness	mm	31.8	57.2
End plate, weight	kg	18	90
Cold mass weight	kg	3,607	19,200

II.2.1.3.6 Electrical Connections and Quench Protection

The bus conductor for each magnet and its neighbors is placed inside an insulating conduit that is then installed as a completed package into the bus slots at the bottom of the yoke. The electrical connections between bus conductors and magnet leads are at the ends of the magnets, within the volume contained by the stainless steel helium containment vessel and end bellows. The end volume also contains the thermal expansion joints for the bus conductors. The magnet buses are expected to follow the CERN designs when they become available but the expansion loops and interconnects will follow BNL designs as developed for RHIC. No magnet warm-up heaters to accelerate the occasional warm-up of the cold mass are planned; warm gas only is used for warm-up in the LHC. Quench protection heaters are installed between the collars and coils for the full length of the magnet at the time of coil assembly for collaring. The basic heater design was developed and extensively tested by BNL in the SSC program. In operation, the magnets in each half IR will be connected in series and the quench protection system will, when triggered, fire the heaters in all the magnets (8 apertures).

Until measurements are made on a prototype magnet, it is not possible to predict exactly the temperature that will be reached in a coil during a quench. The active quench protection system being planned for these dipoles will result in much lower peak quench temperatures than is the case in the similar RHIC dipoles, which are protected with diodes only, even though the conductor in these magnets will contain less copper. In the RHIC program, measurements were made of $\int I^2 dt$ (10^6 A^2 sec or MIITS) versus temperature for a preliminary version of a RHIC dipole. This enabled calibration of a model used for predicting the quench margins in the final version of the RHIC dipole. Final estimates of worst case $\int I^2 dt$ values in RHIC magnets for conductor with a copper-to-superconductor ratio (Cu:SC) of 2.25:1 and a single quench protection diode for each magnet gave a value of about 12.4 MIITS, compared with an estimated cable damage level of 13.8 MIITS. This converts to a temperature margin of about 250 K before the damage temperature of 835 K is reached.

II.2.1.3.7 Dipole Cryostats

The cryostats for D3 and D4 will be the same as those for the main LHC dipoles [65] wherever possible. The lengths will be different (shorter), the support points for the cold mass will be adjusted, and the support cradles will be designed to accommodate the 2-in-1 yoke, but the diameter of the vacuum tank, the support posts [66], and the heat shield support extrusions will be the same. A drawing of a 2-in-1 magnet in its cryostat is shown in Fig. II.2.1.2-5.

II.2.1.3.8 Magnet Cooling

The RF Region dipoles will operate in liquid helium at 4.5 K. Schematic drawings of a part of the cryogenic system for supplying helium is shown in Fig. II.2.1.3-6.

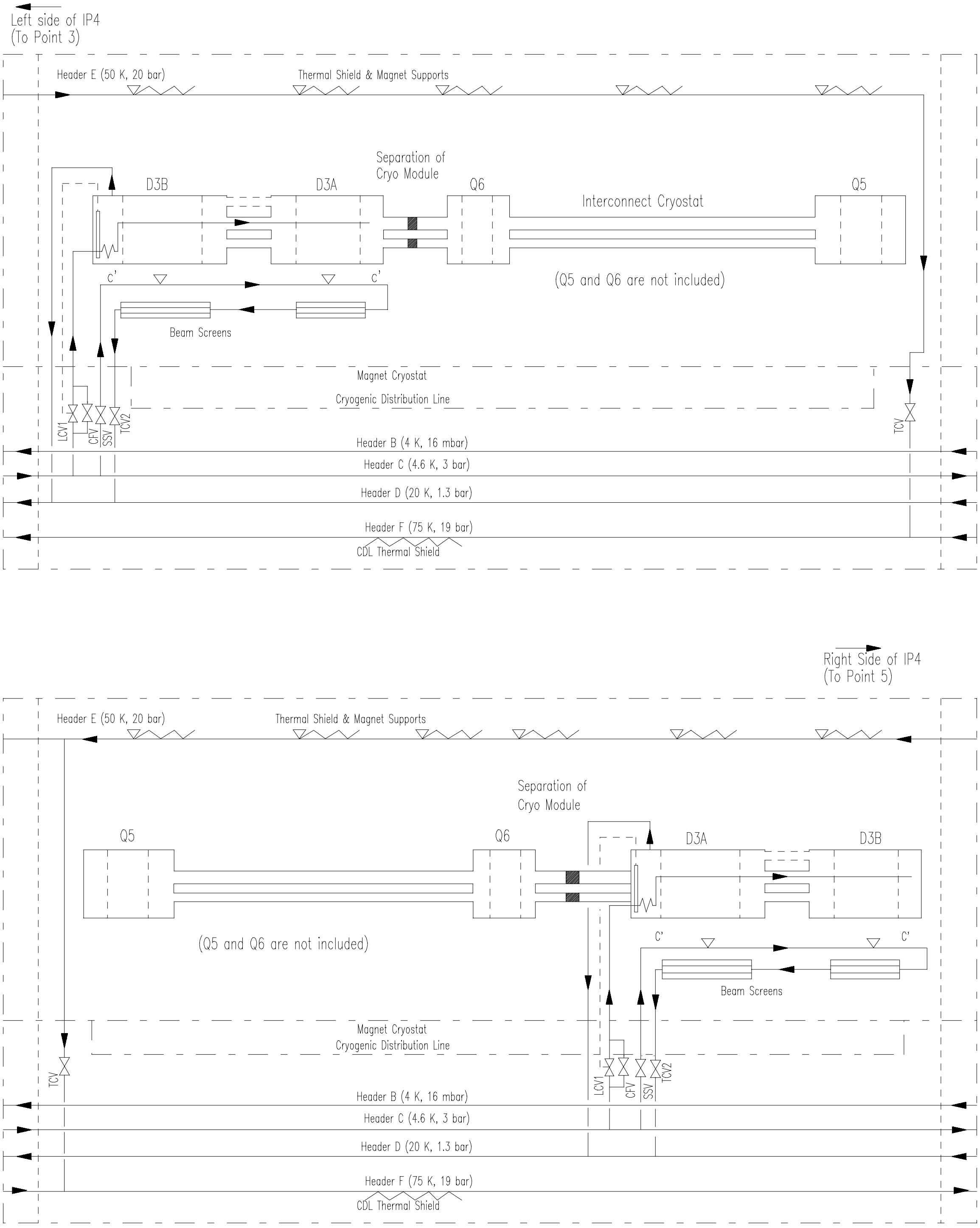

Fig. II.2.1.3-6. Schematic drawings of the cryogenic system to furnish liquid helium for the IR4 magnets. In this region, the tunnel slopes downward to the right and the helium must be brought in at the high elevation end of the magnet string.

There are a number of design features that must be observed in a system of this type, including the following:

- Connect the cryo loop to the distribution system at the high elevation end.
- Use the 4.6 K line to transfer liquid helium to the low elevation end.
- Allow helium vapor to return to the high elevation end through the helium containment of the magnet, mostly through the two upper helium passages.
- Use the lower bus openings in the magnet for the superconducting bus.
- Make provision to vent each magnet in order to avoid trapped vapor.
- Introduce a small heat exchanger in the end volume of the first magnet of the cryo loop.
- Use a level gauge in the end volume to control helium flow and keep magnet coil and bus in the liquid region.
- Keep the C'-C' line, the E line, the cooldown lines and relief valves the same as the 1.8 K cooling in the regular LHC arc magnets.

II.2.1.3.9 Transfer Function, Quench Field, Inductance, and Stored Energy

A plot of the expected field vs. current in the dipole magnets is shown in

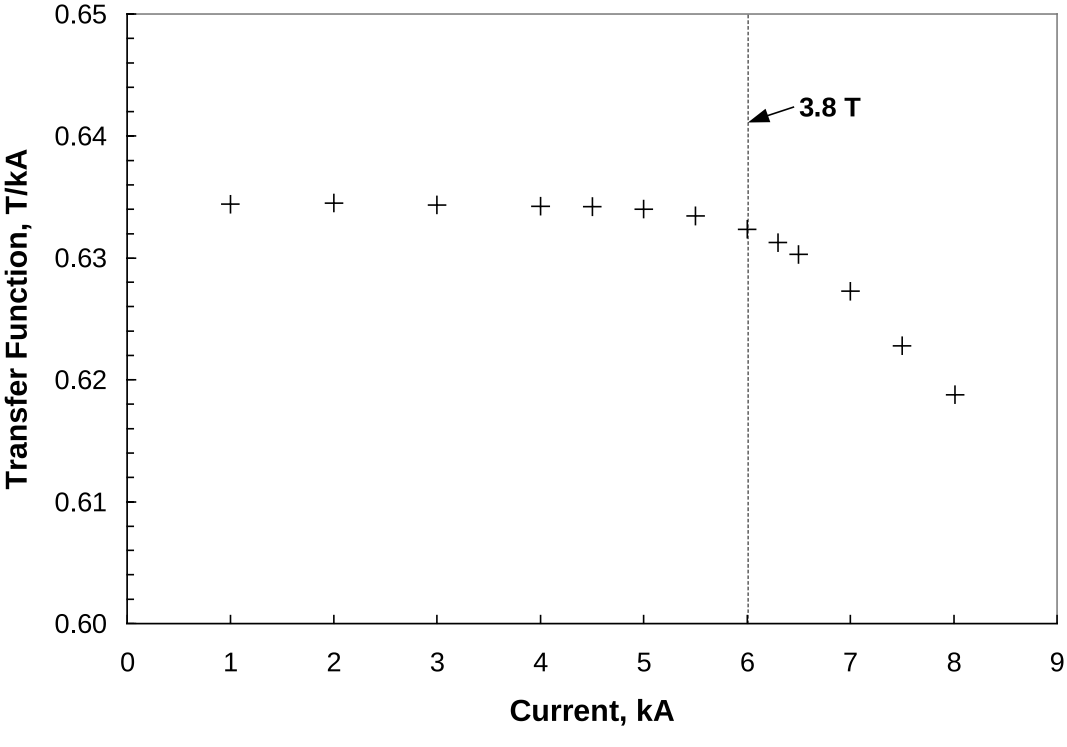

Fig. II.2.1.3-8. The calculation is for the magnet D3b, though the transfer function is expected to be the same for the other magnets. This calculation will be refined when the exact configuration of the cutouts in the yoke is finalized. The calculation is for a temperature of 4.3 K and cable with a copper to superconductor ratio of 1.8. The field is 2.537 T at 4 kA (0.634 T/kA). The quench field is expected to be 4.96 T at a current of 8014 A, assuming conductor with a short sample limit of 2750 A/mm^2 at 5 T, 4.2 K. The current density in the copper at the quench point is 1261 A/mm^2. The inductance of each aperture is 28 mH and the stored energy in each aperture at 3.8 T is 387 kJ.

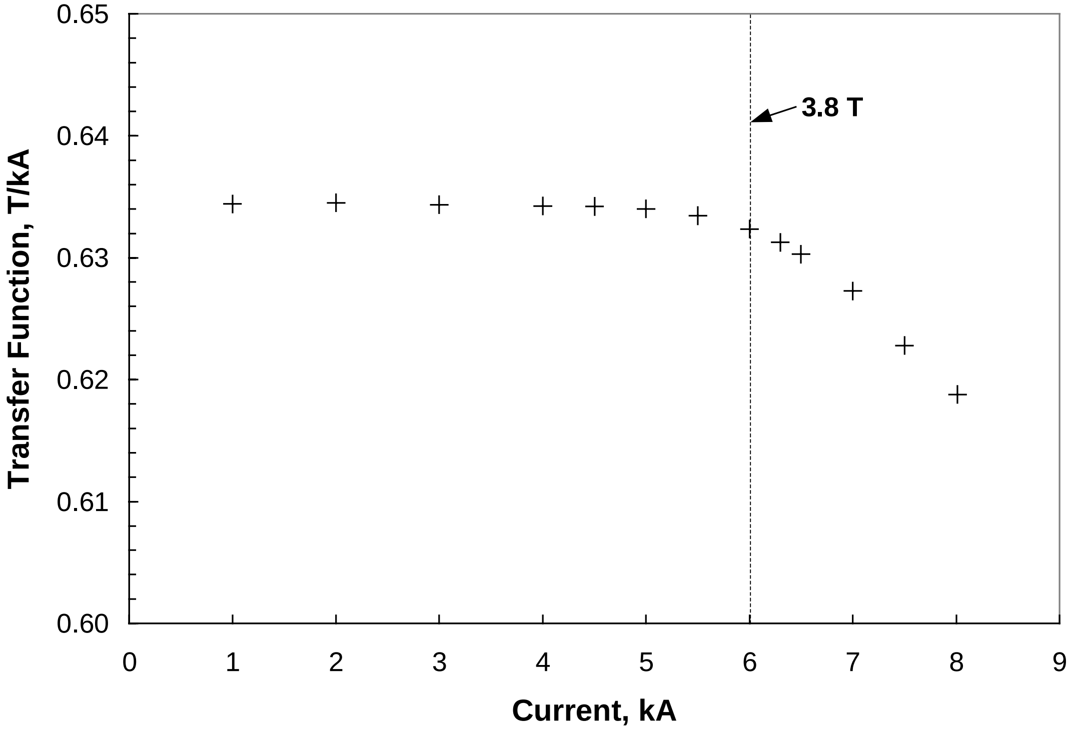

Fig. II.2.1.3-8. Transfer function for dipole magnet D3b.

II.2.1.3.10 Magnetic Field Quality - Measurements

Warm magnetic measurements to determine field multipoles will be made when magnet construction has been completed, including all welding and installation into the cryostat. This will allow detection of errors in magnet construction that may not have been detected in the earlier construction testing. Except for small systematic offsets in the lower allowed multipoles, warm field measurements have been shown to be closely related to the field multipoles measured when the magnet is cold. The data will be examined for conformance to expected field quality. This includes the dipole field angle orientation, the integral of the magnet's dipole field, the multipole content of the field, and the variations of the field parameters along the length of the magnet. Just as for the RHIC dipoles, it is anticipated that all magnets properly built to print will easily pass the field quality test, and that only a magnet with construction deficiencies will fail to pass the test. Following the warm tests, cold testing will be done on each magnet in

Brookhaven's Horizontal Test Facility to check quench performance and to verify field quality. As in the case of RHIC magnets, on which the design of these dipoles is based, a reference radius of 25 mm is used for all harmonics measurements.

The MOLE measuring system [67] developed at BNL and used for RHIC field measurements will be used for the LHC magnets. Integral fields will be measured with the stationary integral coil system [68] used for RHIC magnets.

II.2.1.3.11 Magnetic Field Quality – Measurement Errors

The extensive measuring program carried out for RHIC magnets has given data that can be analyzed for systematic and random measurement errors. Such an analysis has been carried out, including also an analysis of errors in the and calibration of the measuring coils. The analysis has been summarized in a series of tables and plots [69]. Table II.2.1.3-10 is excerpted from the report. These errors apply to the measurement system used for the RHIC measurements, which will be used for these magnets, and will be different for other measuring systems. They are, however, a good benchmark for the accuracy that can be achieved in a carefully built and calibrated system.

Table II.2.1.3-10**.** Estimated measurement errors. δ is the maximum error due to measuring coil construction/calibration, given as a percent of the value of the harmonic. $\sigma(b_n)$ and $\sigma(a_n)$ are the random errors in the measurements. $\Delta(b_n)$ and $\Delta(a_n)$ are the suggested values for the total measurement errors for magnets with small harmonics as in the RHIC dipoles. These include also some variations due to magnet changes after quench and/or thermal cycles as seen in the RHIC magnets. They are obtained by rounding the sum of the effects upward and by specifying minimum values for several of the harmonics. Note: sextupole is n=3, σ and Δ in units (parts $*$ 10^{-4} of the central field), reference radius=25 mm.

n	δ*,%*	σ *(b_n), units*	Δ *(b_n), units*	σ *(a_n), units*	Δ *(a_n), units*
2	0.48	0.061	0.10	0.043	0.50
3	0.78	0.033	0.50	0.015	0.05
4	1.08	0.012	0.05	0.010	0.10
5	1.38	0.004	0.10	0.005	0.02
6	1.68	0.003	0.02	0.004	0.05
7	1.98	0.002	0.02	0.002	0.02
8	2.28	0.001	0.02	0.002	0.02
9	2.59	0.001	0.02	0.001	0.02
10	2.89	0.001	0.02	0.001	0.02
11	3.19	0.001	0.05	0.001	0.02

II.2.1.3.12 Magnetic Field Quality – Expected Values

The magnets are designed to have harmonics that are small. Thus, the geometric multipoles (harmonics) are expected to be zero. At low fields, persistent currents in the superconductor will generate allowed multipoles such as sextupole (b_3) and small decapole (b_5) components[1]. These are shown in

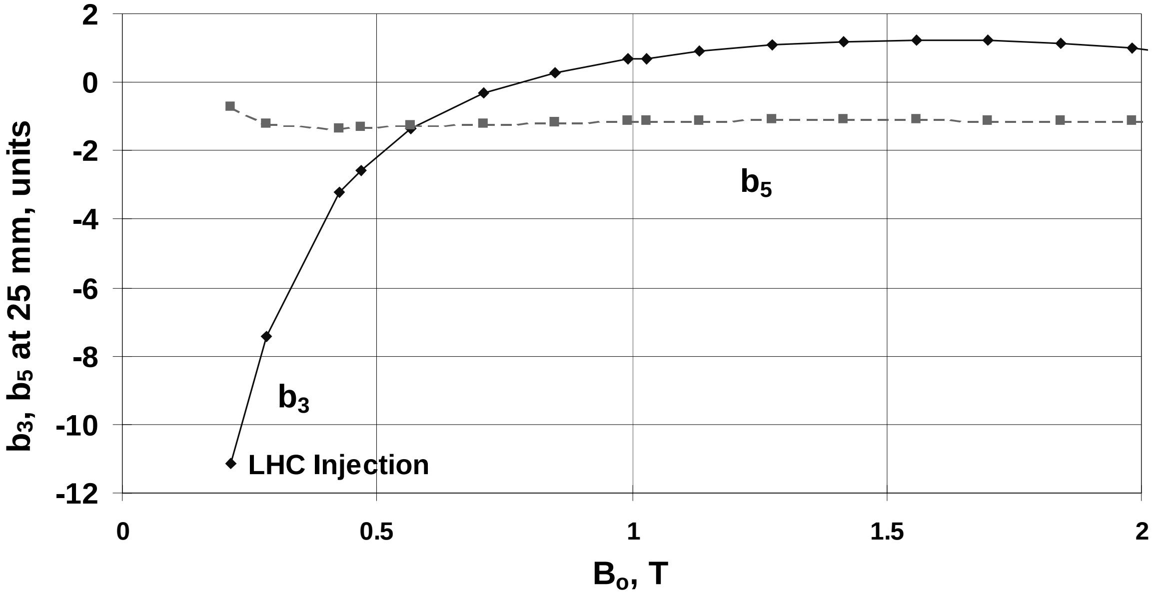

Fig. II.2.1.3-10. At high fields, some harmonics will be induced by the saturation of the iron yoke, as shown in

---

[1] Table II.2.1.3-15 shows that b_4, b_9, and b_{11} are also generated by persistent currents with values larger than b_5.

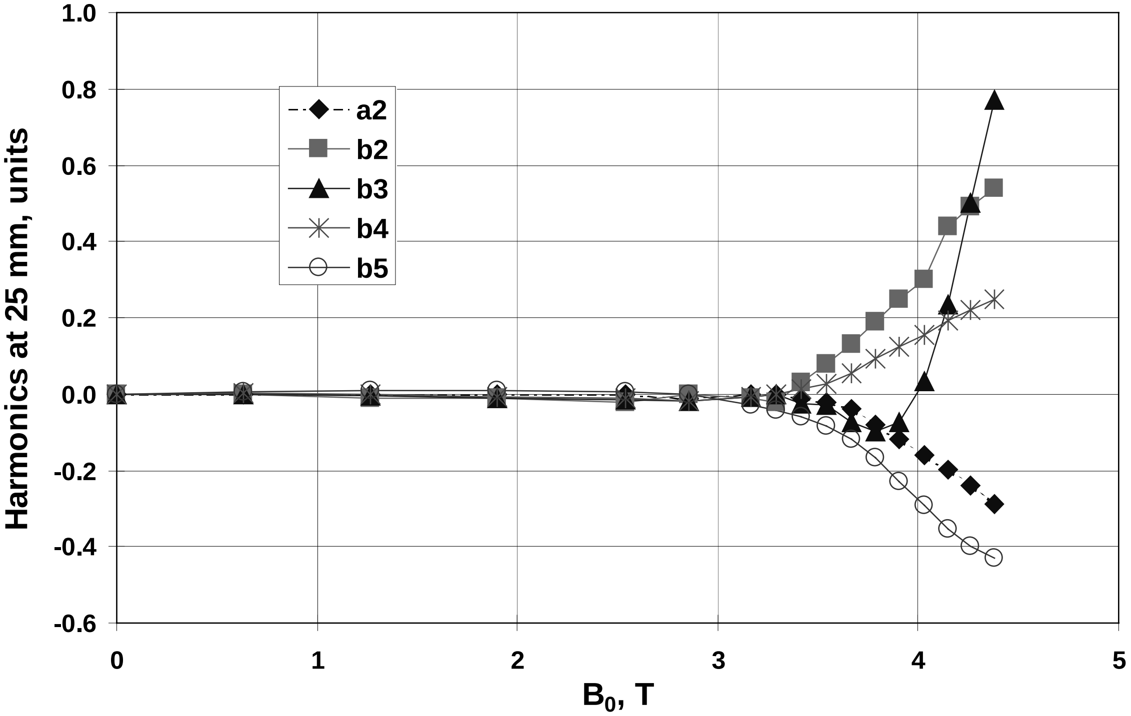

Fig. II.2.1.3-12.

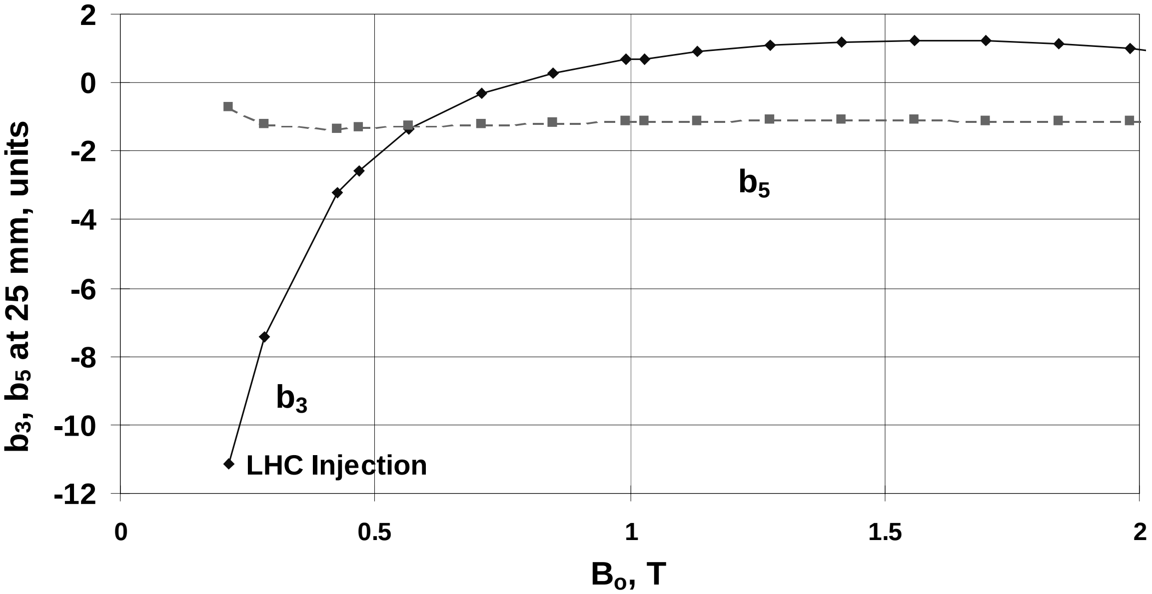

Fig. II.2.1.3-10. The measured dependence of the sextupole and the decapole harmonics on field during up-ramp in the 80 mm aperture RHIC arc dipole DRG107. At low fields, the value of the sextupole harmonic (b_3) is dominated by the persistent currents.

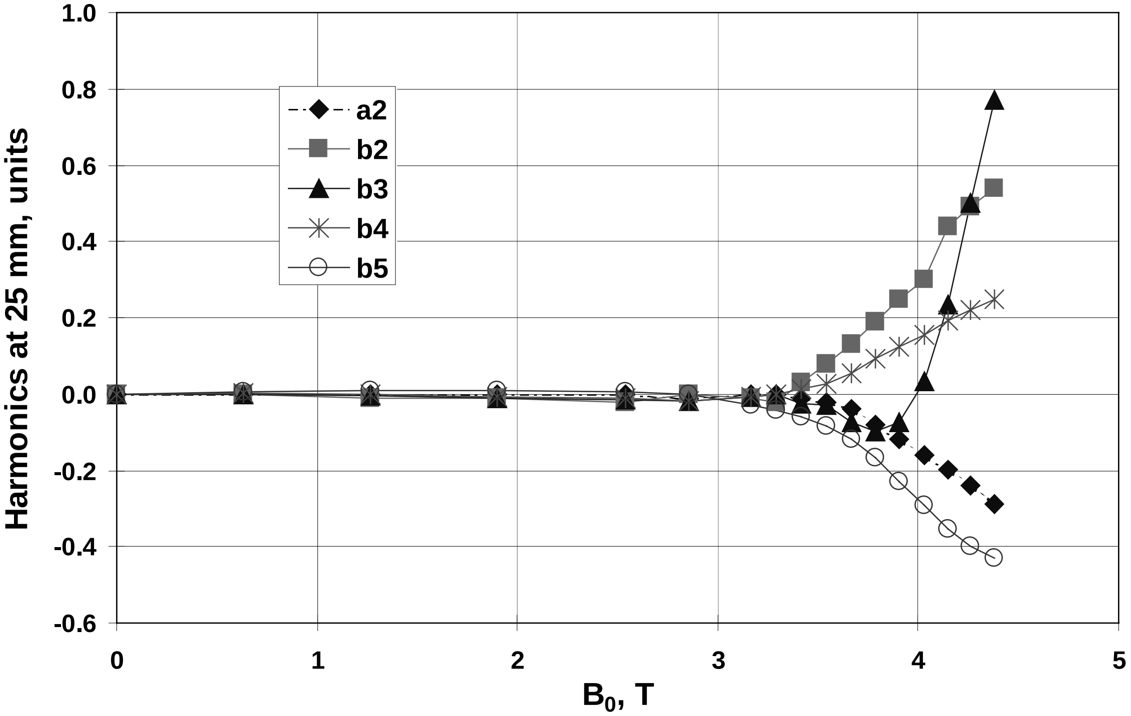

Fig. II.2.1.3-12. The computed current dependence of the field harmonics in the right aperture of dipole D3a. The maximum design field in the magnets in 3.8 T. b_3 is the normal sextupole component.

II.2.1.3.13 Magnetic Field Quality – Expected Errors

Field integral and field angle errors in the 2-in-1 dipoles, based on RHIC magnets [61, 62], are given in Table II.2.1.3-12.

Table II.2.1.3-13. Estimated errors on integral field and field angle.

Item	*Value*
Integral field, magnet-to-magnet variation, rms	$5*10^{-4}$
Single magnet, mean dipole angle, α	±3 mrad
Single magnet, variation (twist) of dipole angle Δα from mean, rms	2 mrad
Mean angle between apertures, rms	2 mrad

The measured harmonics in the magnets may be non-zero due to design and construction errors. The estimated integral values of field harmonics and their errors [70] are given in Table II.2.1.3-14. The saturation-induced harmonics in all magnets are sufficiently small for $B \leq B_{nom}$ ($B_{nom} = 3.8$ T) that they are included in the uncertainty in the mean. This permits a single table of expected harmonics. The estimated values of persistent current-induced allowed harmonics around injection (~0.3 kA or ~0.2 T) are given in parentheses.

Table II.2.1.3-15. Estimated field errors in the LHC RF Region dipoles. b_n and a_n are the expected means of the normal and skew terms due to geometry. $\delta(b_n)$ and $\delta(a_n)$ are the combination of (i) the uncertainty in the mean and (ii) the saturation induced harmonics. $\sigma(b_n)$ and $\sigma(a_n)$ are the expected random variations. The expected deviations from zero (given in parentheses) are the largest at injection and are due to persistent currents. Other values are given for moderate to high fields. Note: sextupole is n=3, ref. radius = 25 mm.

n	b_n, *units*	$\delta(b_n)$, *units*	$\sigma(b_n)$, *units*	a_n, *units*	$\delta(a_n)$, *units*	$\sigma(a_n)$, *units*
2	0	0.5	0.4	0	0.5	1.6
3	0(-9)	2(4)	2(3)	-1.1	0.2	0.2
4	0	0.2	0.1	0	0.2	0.5
5	0(0)	0.6(0.9)	0.6(0.7)	0.2	0.05	0.1
6	0	0.03	0.04	0	0.1	0.2
7	0.1(-0.4)	0.1(0.2)	0.1(0.15)	-0.1	0.03	0.03
8	0	0.01	0.01	0	0.03	0.05
9	0.05(0.3)	0.03(0.1)	0.02	0.02	0.01	0.01
10	0	0.01	0.02	0.04	0.02	0.01
11	-0.5(-0.6)	0.02(0.1)	0.02	-0.01	0.01	0.01

It is anticipated that the field errors in the magnets (which are based on the already excellent RHIC field quality) may be somewhat smaller than given here because the replacement of RX630 phenolic spacers with punched stainless steel collars will result in smaller dimensional variations. Nevertheless, techniques for adjusting the field harmonics by small amounts have been developed in recent years [71]. These include coil size adjustment during cure, adjustment of coil midplane and pole shims, and coil wedge thickness adjustment. Changes can be made if field measurements on the first one or several magnets indicate, through tracking studies, that such adjustment would be appropriate. These techniques will be available for use on the magnets as needed.

The non-zero values of geometric a_3, a_5, etc. are primarily from the harmonics in the lead end, as measured in the RHIC arc dipoles. In a single layer coil design such as used in these dipoles, there are leads carrying the current into and out of the coil that cannot be paired at every point. These leads, particularly the lead at the pole, produce a low level of skew harmonics in the lead end field. In addition, some normal allowed harmonics are generated in the ends of a single layer coil because it is not possible to completely balance the opposite multipoles generated by current turns near the midplane vs. current turns near the pole in the end region of the magnet.

II.2.1.3.14 Magnet Shipping

Once construction and testing of the magnets is complete, they will be shipped to CERN for installation into the LHC. To prepare them for transit, support posts and restraining frames will be installed to protect the cold mass support posts from damage. The magnets will be sealed and filled with dry nitrogen so that moisture cannot penetrate the cryostat or cold mass. Each magnet will be mounted on a shock-absorbing frame and then placed into a standard 40-foot-long shipping container. This container will be transported by truck to a shipping terminal, then by ocean freight to a terminal in Europe, then by truck to CERN. The frames will be returned to the US for reuse. The production rate is low enough that only two such frames are necessary for this program.

II.2.1.3.15 Installation at CERN

CERN personnel will install the magnets into the LHC lattice. They must be placed on stands supplied by CERN, and surveyed into place. The beam tube liner must be installed, internal wiring and plumbing connections must be made, the several volumes welded shut, and various leak checks and pressure checks carried out. CERN test apparatus will be required to verify that the magnets have survived the trip and are behaving up to specification. At this stage, the magnets become the responsibility of CERN as that laboratory brings the LHC into operation.

II.2.1.4 R&D Program

Because the superconducting coils planned for these magnets are the same as those used in the RHIC dipole magnets, the required R&D program is reduced in scope from that normally required to develop a new design of superconducting magnet. Two short 2-in-1 models, each ~ 3 m long, will be built and tested in vertical dewars, with the following goals:

1. Qualify tooling and construction techniques.
2. Confirm the proper fit of all mechanical components.
3. Monitor the coil prestress at room temperature and at cryogenic temperature using strain gauges.
4. Check quench performance and field margin.
5. Measure magnetic field for possible iteration of coil design to achieve the desired field uniformity.

6. Check performance of quench protection heaters.
7. Measure temperature rise in coil for quenches at various current levels using a system of voltage taps and spot heaters.

II.2.1.5 Production Plan and Schedule

Magnet production will take place at BNL in the buildings and facilities currently being used for RHIC magnet production, which is scheduled to end in 1998. These facilities will be reconfigured to build spare RHIC magnets as required, and the LHC magnet production will share the space and manpower assigned to that work. The LHC production has been planned as late as possible to meet CERN schedules. This was done to flatten the spending profile in the US accelerator program. The work could be moved earlier, and accelerated, if funding were to become available sooner. The schedule for RF dipole production is shown in Figure II.2.1.5-1.

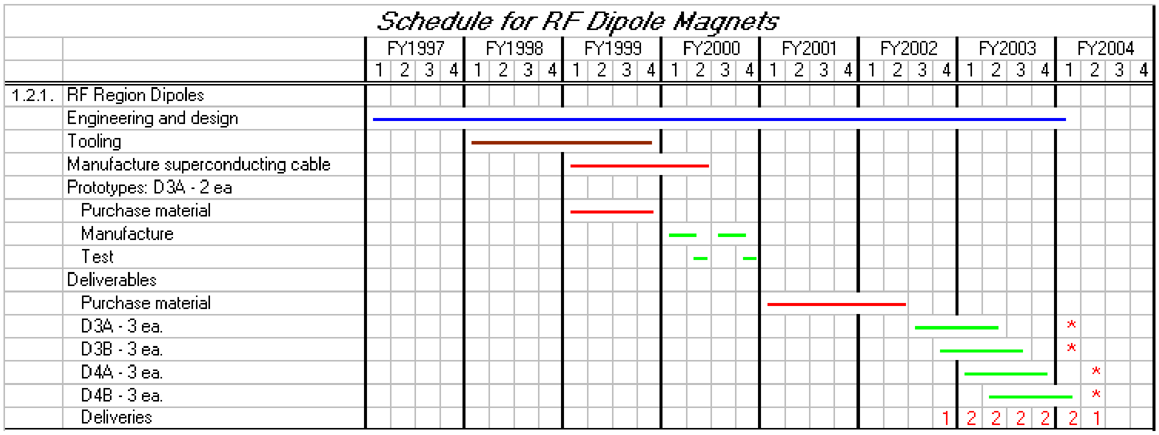

Fig. II.2.1.5-2. Schedule for building the RF dipoles, including the prototype R&D program. The stars in FY2004 represent the planned installation date into the LHC lattice.

II.2.1.5.1.1 References

[61] E. Willen, Superconducting Magnets, BNL 64183.

[62] RHIC Design Manual, Brookhaven National Laboratory.

[63] R. Alforque, LHC Magnet Central Collar, http://dekooning.cad.bnl.gov/design_safety/notes, Number 9.

[64] R. Alforque, LHC Magnet End Collar, Rev.1, http://dekooning.cad.bnl.gov/design_safety/notes, Number 12.

[65] J.C. Brunet, V. Parma, G. Pe∧n, A. Poncet, P. Rohmig, B. Skoczen, L.R. Williams, Design of the Second Series 15 m LHC Prototype Dipole Magnet Cryostats, LHC Project Report 133.

[66] M. Mathieu, T. Renaglia, C. Disdier, Supporting System for the LHC Cold Mass, LHC Project Report 139.

[67] G. Ganetis, J. Herrera, R. Hogue, J. Skaritka, P. Wanderer, E. Willen, Field Measuring Probe for SSC Magnets, Proc. 1987 PAC, Washington, DC, March, 1987.

[68] A. Jain, Field Quality Measurements in RHIC Dipoles, Proc. 9th Int. Mag. Meas. Workshop, Vol. 1, Saclay, June 19-22, 1995.

[69] A. Jain, Estimation of Errors in the Measurement of Harmonics in RHIC Arc Dipoles, Magnet Group Note 570, Brookhaven, November 18, 1997.

[70] R. Gupta, R. Alforque, M. Anerella, E. Kelly, S. Plate, C. Rufer, P. Wanderer, E. Willen, KC Wu, Coldmass for LHC Dipole Insertion Magnets, Submitted to MT15, Beijing, October 1997.

[71] R. Gupta, Estimating and Adjusting Field Quality in Superconducting Accelerator Magnets, Proceedings of the LHC Collective Effects Workshop, Montreux, 1995, published in Particle Accelerators, **55**, [375-385]/129-139, 1996, and BNL Report 62952.

II.3 Superconducting Wire and Cable

II.3.1 Superconducting Wire and Cable Testing.

II.3.1.1 Overview

This chapter deals with the testing and evaluation of the superconducting cables and wires that are used in the main LHC dipoles and quadrupoles. It is expected that for the entire duration of the superconductor cable procurement by CERN for the LHC project, BNL will provide the resources to verify the superconducting properties of the cables. Collaboration in this area began in 1995 and is scheduled to be completed in the calendar year 2004.

During this period the cable test facility at BNL will be used to measure the critical current, Ic,of LHC dipole and quadrupole cable samples in accordance with the cable specification requirements. The standard tests on production cables will be at 4.2K. However, approximately 10% of the cable samples will be tested in superfluid helium at 1.9K to determine the consistency of the ΔH shift of the Ic-H curve from 4.2K to 1.9K. In addition, critical currents of an equivalent number of wire samples will be conducted at 4.2K in the field range of 6-8T.

It is anticipated that the production phase of the conductor procurement will commence during calendar year 1999. Pre-selection of the strand and cable manufacturers as well as R&D on conductor will continue through 1998.

Table II.3.1.1-1 lists the main characteristics of the LHC dipole Cables 1 and 2.[1] Note that some of the values in this table are modified from previous specifications.

---

[1] Conductor specification LHC-MMS/97-152 and LHC-MMS/97-153 (July'97)

Table II.3.1.1-1. Characteristics of LHC dipole Cables 1 and 2.

	Cable 1	Cable 2
Cable Width	-0.02 15.1 mm +0	-0.02 15.1 mm +0
Cable mid-thickness at 50 MPa	1.90 ± 0.006mm	1.48 ± 0.006mm
Keystone angle	1.25 ± 0.05 degrees	0.90 ± 0.05 degrees
Cable thin edge thickness	1.736 ± 0.006mm	1.362 ± 0.006mm
Cable thick edge thickness	2.064 ± 0.006mm	1.598 ± 0.006mm
Cable edge radius	≥0.30mm	≥0.30mm
Cable transposition pitch	115 ± 5mm	100 ± 5mm
Number of superconducting strands	28	36
Minimum critical current at 1.9 K, with afield normal to broad face.	13750 A at 10 T	12960A at 9 T
Minimum critical current at 4.222 K, with a field normal to broad face	14140 A at 7 T	13236 A at 6 T
Minimum critical current at 1.9K of extracted strand	491 A at 10T	360 A at 9 T
Residual resistance ratio	≥70	≥70
Cable transposition direction	left-handed screw thread	left-handed screw thread
Minimum unit length *	460m	750m

*The minimum unit length is defined as the minimum continuous length of cable without a cold weld in any of the strands. This is determined by the cable length required to wind an inner or outer dipole coil.

In the near term, testing at BNL will include the following:

a). critical current measurements of cable and strand samples at 4.2 K to monitor pre-selection manufacture of LHC inner and outer cables as and when required by CERN.

b). R & D work on stability tests of LHC prototype cables and strands selected by CERN. Prior to '97 such measurements have been done at 4.2 K for the cables. More recently these tests have also been made in atmospheric pressure 1.9 K superfluid helium. Strand stability measurements are being made at 4.2 and 1.9 K to study the effect of strand coatings and other variations in conductor parameters.

II.3.1.2 Scope of work

Electrical tests of cable samples during the production of cables needs to be done in a timely manner for early detection of problems during cable manufacture. Hence the schedule of tests as well as the frequency of these tests are set by the the production timetable. Experience in such testing was gained during cable fabrication for the HERA dipole magnets at DESY [72] and more recently during the cable manufacture for RHIC dipoles [73]. However, for LHC the number of such tests is an order of magnitude greater than either of the previous projects and hence requires significant upgrade to the existing test facility as described in the subsequent sections.

II.3.1.2.1 Schedule of Testing

Cable production for the 'pre-series' dipole magnets is scheduled to begin in '99, with the bulk of the manufacture to take place during the years 2000 to '04. The schedule for testing has been based on the preliminary production schedule[4] shown in Table II.3.1.2-1. The number of cable samples has been calculated on the basis of one test per cabling run, where one cabling run has 4 unit lengths of conductor. Hence one cable test will represent either 1840m of Cable 1 or 3120m of Cable 2. Table II.3.1.2-1 shows the expected number of cable samples to be tested in a given year. All of these will be tested at 4.2 K, and ~ 10% will also be tested at 1.9 K.

II.3.1.2.2 Frequency of Testing.

Using the schedule of cable production, Table II.3.1.2-3 enumerates the number of tests that are to be performed in a particular year and the total number of tests to be performed. If the number of tests actually required exceeds the totals shown in Table II.3.1.2-3, CERN has agreed that they will perform the additional tests in their facilities.

For cables, the highest frequency of testing will be in the latter part of the production, with the number of tests exceeding 800 per year. To meet this frequency of tests, it would require that the tests be conducted at the rate of 16-20 per week. Since typically, 4 samples are tested in one cooldown, cable tests have to be conducted almost daily for a period of four years. This necessitates the use of a *minimum* of two dewar systems equipped with similar dipole magnets, such that they can be alternately warmed-up and cooled down to meet the testing schedule. Three test stations are now planned to meet the LHC test schedule at its peak testing rate.

---

[4] Based on schedule that was given by D.Leroy 5-15-97

Table II.3.1.2-1. Cable testing schedule.

Dates	*Quantities of Cables*		*Measurements*		
	Cable 1 km	Cable 2 km	Cable 1 # samples	Cable 2 # samples	Total # samples
FY 1999	45	75	100	100	200
FY 2000	184	380	100	129	229
FY 2001	404	822	220	278	498
FY 2002	585	1223	318	418	736
FY 2003	585	1223	318	418	736
FY 2004	585	992	318	318	636
Total	2388	4715	1374	1661	3035
100% tested at 4.2K					3035 Unit Test
10% cables tested at 1.9K					304 Unit Test

Strand electrical testing will be handled by one dewar system ,where either eight Cable1 or four Cable 2 strands are tested in a single day. In these tests the solenoid magnet is kept cold during changing of sample holders.

Magnetization tests for a very limited set of strands will be conducted using the SQUID magnetometer which is available at the Metallurgy Department at BNL.

Table II.3.1.2-3. Yearly schedule of superconducting wire and cable testing.

Superconductor Testing	Total	FY97	FY98	FY99	FY00	FY01	FY02	FY03	FY04
A): Wire Tests									
Number	3900	300	300	300	600	600	600	600	600
B): Cable Tests									
Number @ 4.2K	3435	100	300	200	229	498	736	736	636
Number @ 1.9K	304			20	23	50	73	74	64
C): Strand Magnetization									
Number	300	30	30	40	40	40	40	40	40

II.3.1.3 Facility Upgrade

The requirements for testing LHC cables are quite different from any earlier conductors in several respects: a) need for 1.9 K, one atmosphere superfluid helium test, b) requirement of sample current capability in the range of 15-20 kA, c) ability to sustain a high testing rate for several years. With this in mind several improvements to the test facility were initiated in FY‘96 namely 1) construction of a 1.9 K cryostat system with a lambda-plate, 2) fabrication of a special sample holder for testing cables at 1.9 K with 20 kA capability, and, 3) data acquisition of the V-I curve under current ramp condition. These have since been completed and are in operation. The other upgrades that are in execution or planned are the following : 1) additional dipole test magnets and test cryostats, 2) re-configuration of existing power supplies to deliver 25 kA for the sample current, and 8 kA for the magnet, and the associated bus-work to switch to the three cryostats systems, 3) cryogenic and controls upgrade to (a) facilitate the use of two separate helium refrigerators to fill the existing storage dewars that service the test cryostats, such that either refrigerator can be used to supply helium when the other is off-line due to maintenance or mechanical problems and (b) to semi-automate certain cryogenic operations like warm-up and cooldown of the test cryostats and cryogenic distribution among the cryostats, and c) improve controls and systems for power supply operation, safety protocol, and data acquisition .

II.3.1.3.1 1.9 K superfluid operation

As part of a collaboration between CERN and BNL, a test facility was established at BNL to evaluate superconducting cables at 1.9 K and atmospheric pressure for the LHC. This facility was constructed using some existing components modified for operation at 1.9 K and some components supplied by CERN based on the designs incorporated in the low temperature test facilities in operation at CERN.

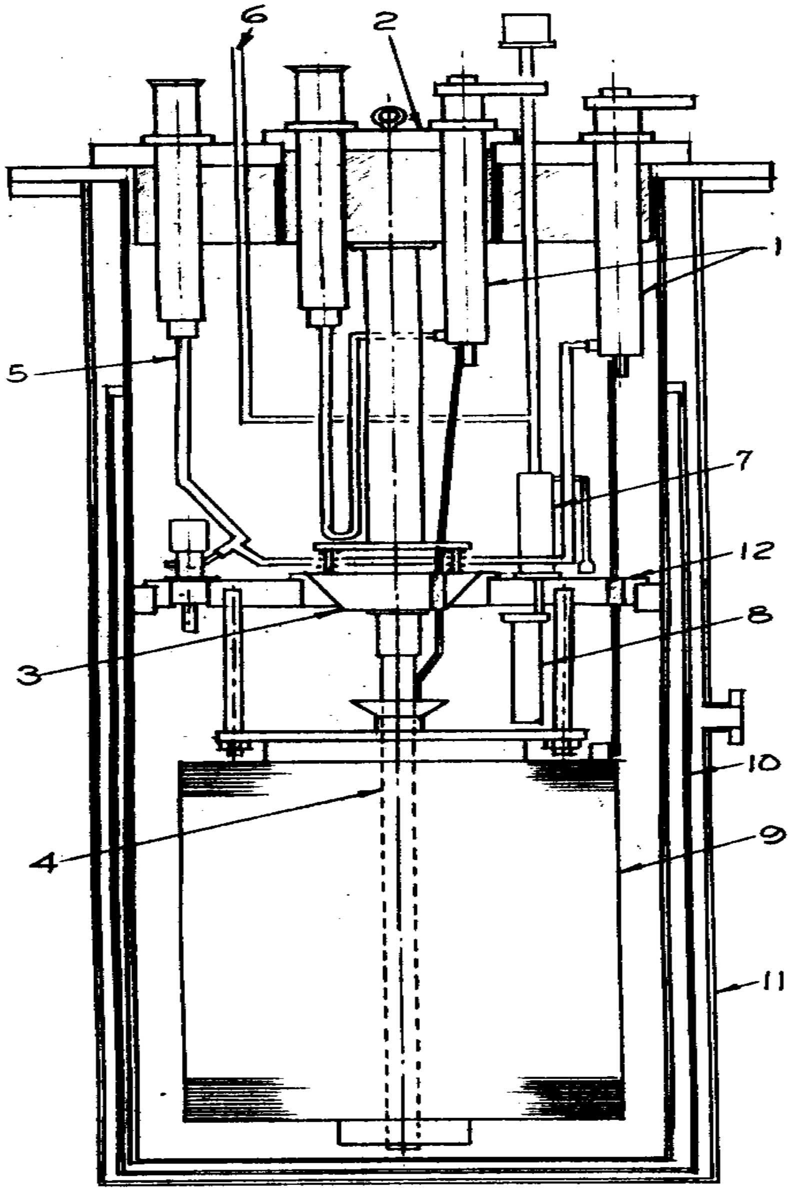

Fig. II.3.1.3-1. Vertical cryostat: (1) Liquid injection leads, (2) Sample holder, (3) Sample holder G-10 plug, (4) Conductor samples, (5) Fill line, (6) Pump line, (7) Upper counterflow heat exchanger, (8) J-T valve and lower heat exchanger, (9) Test magnet, (10) 10K shield, (11) Vacuum vessel, (12) Lambda plate.

The conductor test facility has several major components: 1) a helium cryostat modified to be capable of operation over a range of temperatures, 2) a large pump station, 3) a superconducting magnet in whose bore superconducting cable samples are positioned, 4) conductor sample holders, 5) power supplies for the magnet and the conductor samples and 6) instrumentation for the cryostat and superconducting magnet.

An existing helium cryostat, shown in Fig. II.3.1.3-1, was modified by the addition of a ring to support a 6.35 cm thick G-10 Lambda plate which separates the 1.9 K volume in the cryostat from the 4.5 K volume above it. A copper thermal shield supported by a ring welded to the helium vessel above the Lambda plate encloses the low temperature volume below the plate and about half of the volume above it. The average temperature of the shield is calculated to be about 10 K. Superinsulation is placed between the helium vessel and the shield and between the shield and the vacuum vessel. The heat load on the 1.9 K helium volume is estimated to be less than 10 watts.

Helium is supplied to the cryostat from two 3780 liter storage dewars connected to a 170 liter/hr (700W) liquifier/refrigerator. Since there is some interest in pumping the entire helium volume to below atmospheric pressure for some tests, the power leads for both the test magnet and the conductor samples, which are placed inside the bore of the magnet, are cooled by injecting helium from the supply transfer line directly into the bottom of the leads. The lead flows are manually controlled at this time but are being programmed to respond to current changes in the several leads.

The pump system is a two stage system assembled by Nash-Kinema, Inc. The first stage is a plugged rotor booster driven by a 74.6 kW (100 HP) three phase motor. The second stage is a NASH liquid ring pump, also driven by a 74.6 kW motor. Control of the suction pressure is achieved by the use of a bypass valve to control spoiling of the inlet gas flow. All active components are under computer control using a GE Programmable Logic Controller. The PLC actively controls the inlet pressure and monitors operating parameters critical to the functioning of the system. Should any operating parameters fall outside normal limits, the system is shutdown to minimize damage to any component.

Once the helium level is established in the cryostat, these pumps are turned on, which pump on the helium in a three cylinder heat exchanger, supplied by CERN, mounted just below the Lambda plate as shown in Fig. II.3.1.3-1. Liquid helium drawn through a small tube from just above the Lambda plate passes through a vacuum insulated heat exchanger above the plate where it is cooled by exchanging with the helium being pumped. The helium then passes through a J-T valve into the lower heat exchanger, and back through the upper heat exchanger to the pumps and recovery. Details of the 1.8 K cryogenic operations can be found in Ref. [74].

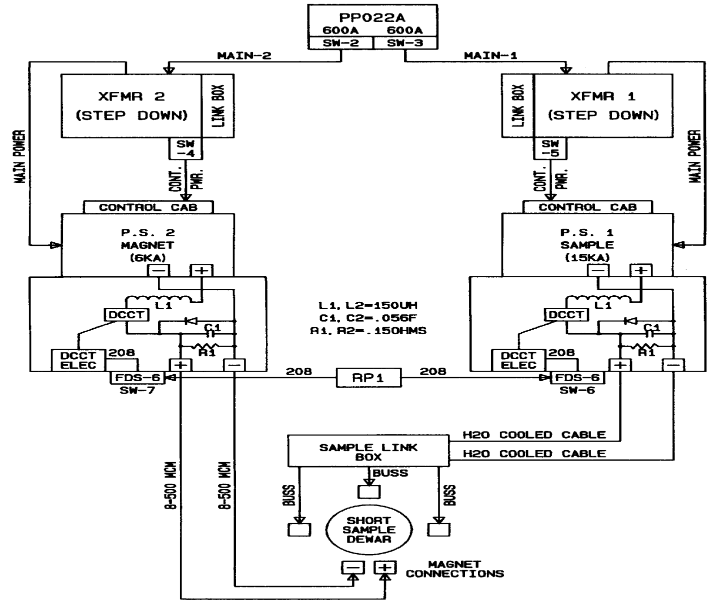

Fig. II.3.1.3-2. Present Power Supply configuration.

II.3.1.3.2 Power Supply Re-configuration

The current power supply system to the cable test cryostat consists of two Rapid Electric Co. air-cooled supplies. The supplies are SCR controlled and each is capable of producing 15 kA DC at 24 volts. One power supply delivers current to the magnet (PS2) and the other (PS1), to the conductor samples. The magnet power supply has been derated and operates at only 6 kA, while the supply for the cable samples is capable of supplying its full rated current of 15 kA.

To increase the cable current to 25kA, the two 15kA supplies are being configured to be energized in parallel. The test magnets which only require a maximum current of 5kA will be fed from another 8 kA 12 V supply. A PC-based control and monitoring system is being implemented to match the needs of the test sequence.

II.3.1.3.3 Dipole Magnet and Test Cryostats

The cable samples are measured in the central field of a 4-layer dipole magnet, which has been in use since 1989. The magnet has a clear bore of 75 mm and an effective magnetic field length of 76 cm of which 61 cm is uniform to 0.1 % longitudinally along the axis. It is capable of generating a magnetic field intensity of 7.5 T with a current of 3400 A at 4.5 K and 10 T with a current of 4900 A at 1.9 K. The iron yokes were adapted from parts originally made for the CBA project at BNL and uses cable identical to the inner and outer cables of the SSC 4 cm magnets. A thermally activated superconducting switch is installed across the magnet so that it can be operated in the persistent mode. Details of the construction can be found in Ref. [75].

Although this magnet reached the design field of 7.8 T at 4.5 K, it has shown considerable training at 1.9 K. The highest field reached so far has been ~ 9.0 T, however on a routine basis the field is set at 8.7 T for cable measurements.

Although two cryostats are a minimum requirement, it is prudent to have a third identical system to offset additional testing demands as well as serving as a back-up system. For these additional test cryostats that are required for production cable testing, two magnets similar in design to the existing dipole are being constructed. Since the old SSC 4cm cables are not readily available, the two inner coils of the new magnets are being fabricated using SSC 5cm inner cables which are available from SSC surplus inventory. For the outer two layers, RHIC dipole cables are being used. These are geometrically similar to the old SSC 4cm outer cable, except that RHIC conductors have a higher Cu/Sc ratio of 2.25 as compared to 1.8. Because the old coil fabrication tooling is being used with the present cables which are wider than the old SSC 4cm cables, the clear bore of these new magnets will be 68 mm. Sample holders are being modified to fit inside this reduced aperture. The additional test cryostats are being designed to operate only in ~ 4.3 K pool-boiling Helium I.

II.3.1.3.4 Cryogenic and Systems Control Upgrade

The upgrade of the cryogenic system to support the LHC conductor test program includes the installation of helium transfer lines together with a wet expander and J-T valve in parallel to liquefy helium from a second refrigerator/liquifier into the existing storage dewars. The system operates with either the wet expander or the J-T valve on-line. This upgrade helps to ensure continuity in the production of liquid helium by having one of the liquifiers in operation while the other liquifier serves as a back-up machine to be used when the operating liquifier is shut down for maintenance or repairs. Each of the two liquifiers has sufficient liquefaction capacity to support the LHC conductor test program on its own.

The upgrade of the cryogenic system will also include modifications and additions to the transfer lines such that each of the two storage dewars may be filled by either of the two liquifiers and each of the three test cryostats may be filled from either of the two storage dewars.

Additional valves and controls will be added to semi-automate several of the sequential operations associated with the use of the vertical test cryostats and to control simultaneously different operation in each of the three cryostats. These operations would include, for example, the initial pump and purge of the cryostats after installation of conductor samples, cooldown of the cryostat either by initial heat exchange of helium gas with liquid nitrogen followed by a continuing cooldown and fill with liquid helium or by direct cooldown and fill with liquid helium, maintenance of the liquid helium level in the cryostat during conductor tests, control of the helium flow to cool power leads, venting of the helium to another test cryostat or to gas recovery when tests are completed, and warmups of the cryostat.

II.3.1.4 Strand Test Procedure

II.3.1.4.1 Wire Critical Current Determination

II.3.1.4.1.1 General Outline: Definition of Critical Current

The V-I curve is determined as a function of increasing current until an irreversible transition or quench occurs. This measurement is normally carried out in the specified external field (6 T - 8 T) applied normal to the wire axis, and in a temperature bath of liquid helium at 4.2 K. No correction is made for self-field effects. For currents less than the quench current the V-I curve is reversible. The critical current, I_c, is defined as that at which the resistance per unit length, R, is:

$$R = 10^{-14} /(\pi d^2/4), \text{ ohms/m}$$

where d is the wire diameter in meters. The effective resistivity of the wire is 10^{-14} ohm · m at the critical current.

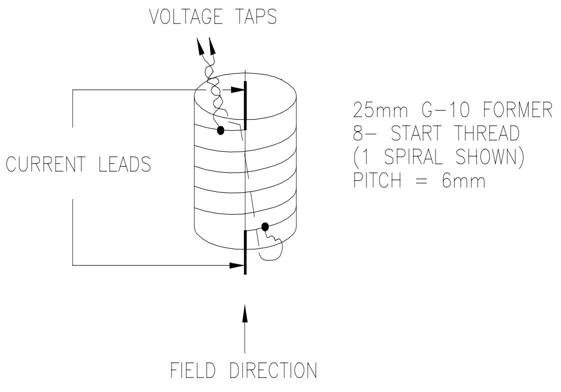

SAMPLE MOUNTING ARRANGEMENT

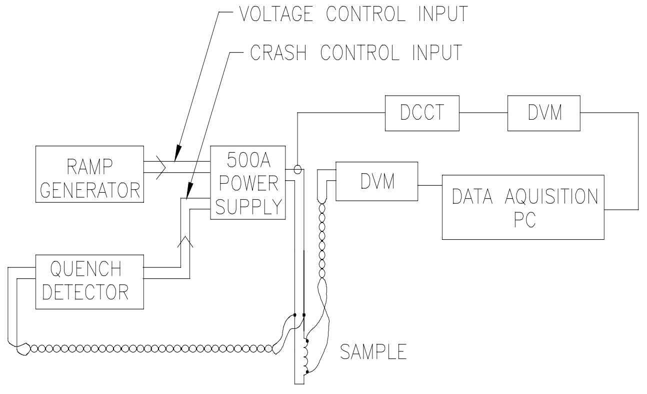

SCHEMATIC OF ELECTRICAL MEASUREMENT APPARATUS

Fig. II.3.1.4-1. Schematic of the Strand Electrical Measurement

II.3.1.4.2 Sample Mounting

The sample wire is most conveniently mounted on a cylindrical grooved form which is made of G-10, and which fits into a solenoid magnet. The monofilar arrangement, Fig. II.3.1.4-1, is used; this lends itself to multiple sample mounting if desired. Voltage taps are arranged as shown. Adequate tension is used during the wire mounting in the groove to prevent wire motion and hence training.

The V-I curve may be taken either point-by-point (current constant for each measurement) or continuously if induced signals due to ramping are not too large or noisy. When the V-I curve is determined by the latter procedure, care is taken to ensure that there is no rate effect for the ramp rate used. Typically, the current is supplied by a stable, well-filtered power supply. The current is measured to a precision of ± 0.5%. Electronic circuitry for quench protection is used to protect the sample during a quench.

The Quality Index (n) is estimated using the equation $\rho = \text{constant} \times I^n$. Data points corresponding to ρ-values less than 10^{-14} ohm-m will usually be less accurate than those for which ρ is greater than this value. Above 10^{-13} ohm-m resistive heating may cause the observed voltage values to be too large. Hence, in fitting a straight line to the log-log plot of the data, the region corresponding to $10^{-14} \le \rho \le 10^{-13}$ ohm-m is emphasized.

II.3.1.4.2.1 Magnetic Field

The external field is applied by means of a 8 T superconducting solenoid. The field is uniform over the sample reference length to ± 0.5%. The direction between field and wire axis is $90^o \pm 6^o$ everywhere. This range of angles corresponds to an estimated variation in I_c of <0.5%.

II.3.1.4.2.2 Bath Temperature Correction

The specification temperature is 4.22 K, that of boiling helium at standard atmospheric pressure. The bath temperature is recorded with the aid of cryogenic thermometry with a precision of ± 0.002K (2 mK). A "linear T" type of correction is applied for temperatures different from 4.22 K:

$$\frac{I_c}{I_t} = \frac{T_c - 4.22}{T_c - T}$$

$$T_c(B) = 9.2\left[1 - \frac{B}{14.5}\right]^{0.59}$$

where $T_c(B)$ is the transition temperature at the specified magnetic field. I_t is the current measured at temperature T, and I_c is the critical current at the specification temperature.

II.3.1.4.2.3 Wire R(293) and RRR Determination

The same test set-up is used to measure the wire resistance at room temperature and at low temperatures. The resistance per meter is determined at room temperature (293 K) and just above the superconductor transition temperature ($T_c \sim 9.5$ K). These quantities are designated

R(293) and R(10), respectively, and are measured with an accuracy of 0.5%. The ratio R(293)/R(10) is defined to be the residual resistance ratio, RRR.

R(293) is determined chiefly by the copper matrix. For a given wire diameter it provides a measure of the copper-to-non-copper volume ratio. R(10) is determined chiefly by the residual resistance of the copper matrix and R(293). The ratio RRR provides a measure of the electronic purity of the copper matrix.

Currents in the range 0.1 to 1.0 A for the R(293) determination and 1 to 10 A for the R(10) determination are provided by a well regulated and filtered DC power supply. The current is measured by means of a shunt of 0.25% accuracy thermometer of sensitivity 0.1^{o}C is conveniently used for this purpose as an uncertainty of 1^{o}C is not accurate enough to determine the copper-to-superconductor ratio to ±0.01. Since the measurements are made at room temperature the differences from 293 K necessitate a temperature correction. Designating the observed resistance as R_m and the ambient temperature as t(^{o}C), the resistance at the reference temperature of 293 K is calculated as follows:

$$R(293) = R_m/[1 + 0.0039 (t - 20)]$$

The effect of the Nb-Ti is negligible for the purpose of this correction.

II.3.1.4.2.4 Cu/Sc Ratio Calculation

The copper: superconductor volume ratio (x) is calculated from R(293) and RRR by means of the formula

$$x = \frac{1 - R(293)\, A / \rho_s}{R(293)\, A / \rho_{Cu} - 1}$$

where R(293) = resistance of the strand at 293K in ohms/m

ρ_{Cu} = resistivity of the copper at 295K, in ohm · m

$= r_i \dfrac{RRR}{(RRR - 1)}$

r_i = resistivity of pure copper at 293K

$= 1.682 \times 10^{-8}$ ohm · m

ρ_s = resistivity of Nb-Ti at 295K

$= 60 \times 10^{-8}$ ohm · m

and A = wire cross section area in m^2

$= \pi d^2/4$ (d = wire diameter in m)

II.3.1.5 Cable Test Procedure

II.3.1.5.1 Cable Critical Current Determination

II.3.1.5.1.1 Introduction

The sections which follow describe the test method used at BNL to determine transport critical currents of meter long cable samples. The measurement of critical currents of order 10^4 A is more difficult than the corresponding measurement for a wire carrying several hundred amps for a number of reasons. Large power supplies are required and sensitive voltage measurements must be made in the presence of much noise. Forces on the samples are large and care is required to restrain mechanical motion. Finally, self-field effects are large and must be carefully corrected. This section describes the methods and procedures which have been developed at BNL over a number of years. These procedures have proven suitable for production testing.

The critical current of a cable, I_c, is somewhat less than the sum of the individual wire values as there is invariably some degradation during the fabrication of the cable. This is expressed as follows:

$$D = 1 - (I_c/\Sigma\, I_{cw})$$

where $\Sigma\, I_{cw}$ = sum of the Ic's of the wires in the cable. An allowance for degradation, in modern practice, is $D < 0.05$ (=5%).

The critical current is a function of temperature, T, and magnetic field, B. It is generally necessary to convert (or "correct") short sample test results obtained at particular values of T and B, to values corresponding to a standard temperature and field. The steps in this conversion are as follows:

a) Obtain raw data for several applied fields: I_t, critical current at bath temperature, T, and applied field, B_a.

b) Calculate the peak field, B: the sum of the applied field and the self field, due to the measurement current.

c) Convert I_t at field B to I_c , the value corresponding to reference temperature T_{ref}.

d) Plot I_c vs. B and calculate I_c at the reference field from a linear fit to the data.

The calculations used in the above steps are described in detail below. The I_c vs. B short sample curve may be combined with the load line of the magnet to obtain a prediction of its expected performance.

II.3.1.5.2 Definition of Critical Current

Accelerator magnet cables are designed to carry currents of 1-15 kA in fields of order 6-7 T, at 4.2 K. The voltage drop under these conditions is not zero; typically it is a few microvolts per meter. The variation of voltage with current can be measured in a range corresponding to about 0.5 μV/m to 50 μV/m. Smaller voltages are difficult to measure. At the high end, the V-I curve is unstable and an irreversible quench occurs. For currents less than the quench current, the V-I curve is reversible. The critical current is a property of the reversible portion of the V-I curve. It is defined as that current for which

$$V/I = 10^{-14}/(N\pi d^2/4)$$

where V = voltage drop per m, I = current in amps N = no. of wires in cable d = wire diameter in m. The shape of the V-I curve is of the form $V = \text{constant} \times I^{n+1}$. (Note that n is defined from the equation $\rho = \text{constant} \times I^n$). The quantity n is routinely measured as required by the specifications. Large n-values are indicative of uniform filaments. The n-value is, therefore, a useful diagnostic for monolithic conductors and individual wires, although less so for cables. Usually low n-values is associated with conductor damage due to cabling. It is sometimes required that n exceed a specified value for some types of conductor.

The quench current is dependent on T and B in a somewhat similar way as the critical current. Unlike the critical current, however, it is also dependent on several external factors: insulation, ramp rate, mechanical security. These affect the characteristic feature of quench current behavior, viz., training. This is the increase in quench current upon successive applications of current until, except in pathological cases, a limiting or plateau value is reached. This value is referred to as I_q. Temperature and field corrections are not generally made for I_q.

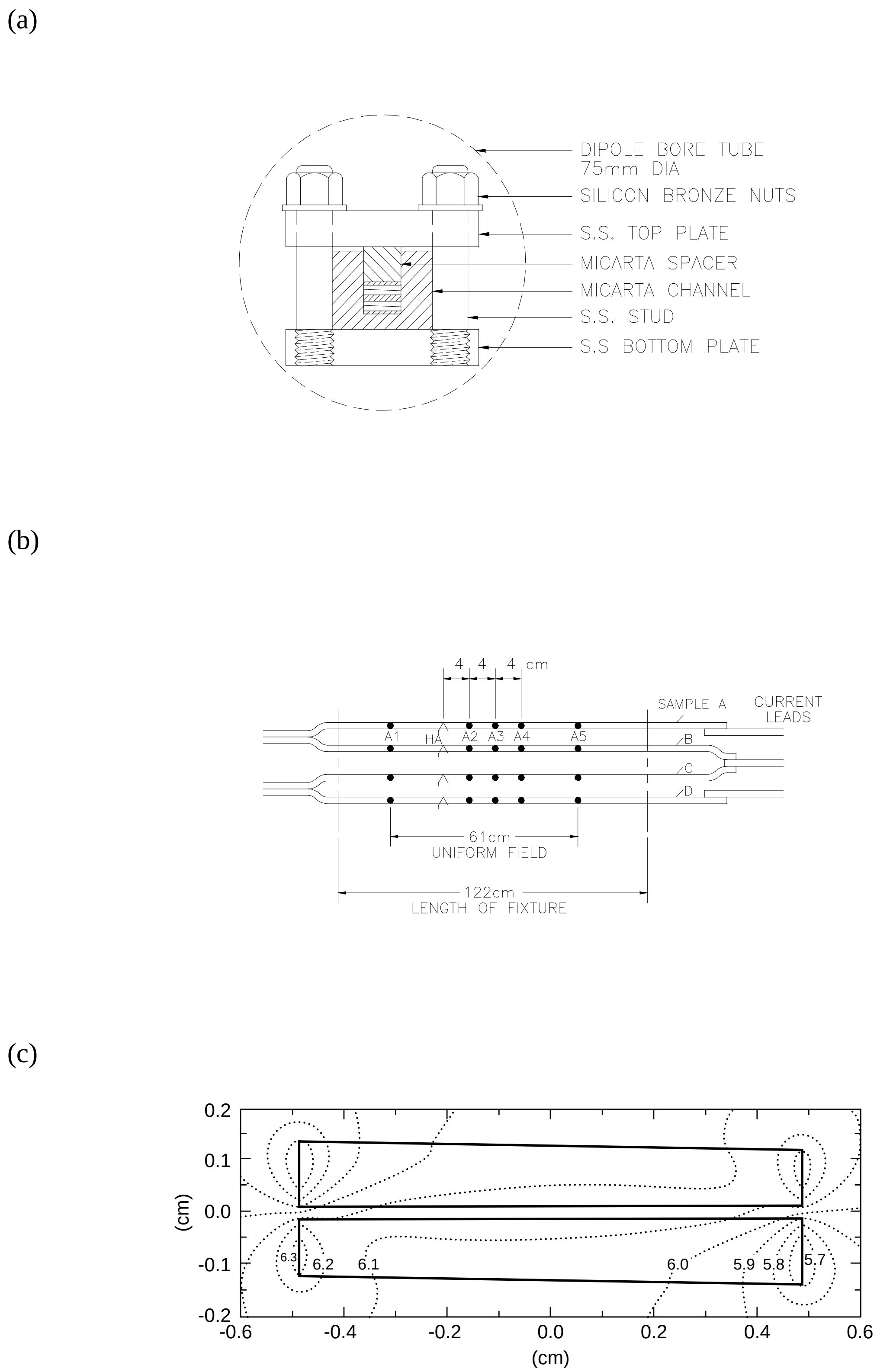

Fig. II.3.1.5-1. (a) Mechanical assembly of 2 pairs of cable. (b) Electrical Wiring Schematic. (c) Contours of constant field magnitude for perpendicular applied field of 6T and current of 10kA. The peak field of 6.4T occurs at the thin edge of the cable.

The number of training quenches is minimized in short sample testing by using bare cable samples and by strong mechanical clamping as discussed below. I_q is generally greater than I_t and, as it provides a measure of the ultimate current carrying capability of the cable, it is routinely recorded. If I_q is less than I_t, the latter may be determined by extrapolation provided there is enough of the V-I curve to permit this. However, in this event I_t is of academic interest only as it cannot be attained in practice.

II.3.1.5.3 Sample Mounting

The samples are mounted in a compression fixture which is illustrated in Fig. II.3.1.5-1. The usual test arrangement involves four bare cable samples. As these are keystoned, (i.e., they are trapezoidal in cross-section), care is taken to alternate thick and thin edges so that pairs of conductors present parallel surfaces to the clamping faces. As indicated in Fig. II.3.1.5-1 there are a series of separators: 0.76 mm. thick G-10 strips which carry electrical instrumentation described below, and 0.25 mm. thick Mylar strips which insulate adjacent samples of the upper and lower cable pairs.

Compression is applied by tightening 9.53 mm (3/8 in.) bolts. These run along each side at 38 mm intervals. A torque of 53 N-m (240 inch-pounds) is used to tighten the bolts. This produces a clamping pressure of 54± 7 MPa for the 15 mm wide LHC cables at room temperature. The pressure has been found to increase slightly at low temperature. With this method training behavior is limited to a few quenches.

The sample compression fixture is supported together with the sample leads from a room temperature flange, which may be rotated. The standard configuration for quality control testing is the perpendicular one, i.e., the applied dipole field is perpendicular to the sample faces. In this configuration, a strong twist about a vertical axis is generated by a bifilar sample for currents above a few kiloamps in fields above several Tesla. Rotation of the sample fixture relative to the magnet is prevented by means of a locating key on the fixture and a slotted plate at the bottom of the magnet.

Fig. II.3.1.5-1 shows schematically how the cables are connected to each other and to the gas cooled leads. The connections are made using ordinary soft solder over a 15 cm. length. A typical joint resistance is about 10^{-9} ohm. The samples are excited in pairs, either A-B, or C-D.

II.3.1.5.4 Electrical Instrumentation

Primary instrumentation consists of the following:

- Five voltage taps and thin foil heater element for each sample.
- These are contained on the G-10 strips shown in Fig. II.3.1.5-1. The voltage taps work by the pressure contact of a copper wire across the width of the sample; the leads run out through a fine groove in the G-10. The heater element is a strip of stainless steel foil, 0.013 mm. thick x 3 mm. x 6 mm,
- which is located in a shallow well formed in the G-10 strip.
- Hazemeyer DCCT secondary current standard.
- Digital voltmeters, 6-1/2 digit, 0.1 μV sensitivity.

- Nicolet 12 bit, 4 channel digital oscilloscope.
- Two calibrated carbon resistor thermometers, located at each end of the magnet.
- Isolation preamplifiers, 1 mV noise level.
- Secondary instrumentation consists of the following:
- Quench current protection circuits for the magnet, the gas-cooled leads, and the samples.
- DC power supplies for persistent switch, and sample heater element.
- Pulse power supply for sample heater element.

II.3.1.5.5 Measurement Procedure

The cable samples are energized in pairs, either A-B or C-D in Fig. II.3.1.5-1, and the V-I curves are determined simultaneously for each member of the bifilar pair. In the event that one member has a low I_q its partner may not be measurable in the set-up. The latter must be tested at another time with a partner having a comparable I_q - another piece of the same cable, for example. In situations like the preceding, a minimum of two and perhaps three of the cable samples can be measured. In quality control tests of production cables, the match between samples is close enough that I_c's can usually be determined for all four samples. In the rest of this section we shall describe the procedure for testing one cable only, it being understood that a pair of samples, or all four, are under simultaneous test.

The measurements are made with the helium bath level above the upper sample and well above the top of the dipole magnet. The magnet field is set to a desired value and locked in with the persistent switch. The standard arrangement is such that the field is oriented perpendicular to the cable face.

The relative direction of the current flow and of the magnet field is very important for reasons which will be discussed below. Therefore, the polarity of the power supply connections is carefully checked. Before the V-I curve is measured the sample is trained. This is done by ramping the current until a quench occurs. For relatively high Cu/SC ratio cables, as in the RHIC design, one quench is usually sufficient to reach the plateau value of I_q.

In the past a point-by-point method was employed to measure the V-I curve. For LHC testing voltage-current readings are taken with a current ramp of ~200A/s. The most important feature of this method is that a very high degree of filtering of noise voltage can be achieved by the following technique. The noise is mostly in the form of harmonics of the line frequency. By integrating the voltage signal for an integer number of cycles, this harmonic noise is filtered to a very low value. In practice, the integration is over 10 cycles, and AC peak-to-peak voltages of order 10^{-3} volts are reduced to an effective uncertainty in any DC reading of 10^{-7} volts. I_q is determined while ramping by means of a peak-reading DVM. I_q is determined by one sample of the pair being measured; this value is a lower limit of I_q for the other sample. By observing the quench on a digital oscilloscope one can determine in which sample the quench originates. It is usually the one with the lower I_t value.

The V-I data are converted to log ρ - log I data and fitted by a straight line. This gives the 10^{-14} ohm · m current and the n-value (the slope of the log-log plot). The following data are the result of the measurement: B_a, T, I_t, I_q, n, where B_a is the applied field, and I_q is the quench current or a lower limit of it. This procedure is repeated for each of the four cables at several fields in the vicinity of the specification field.

II.3.1.5.6 Temperature Calculation

Calculations of the critical currents at temperatures other than that at which I_t is measured are made using the same procedure outlined in the procedure for wires. The only difference being that the field B is not just the applied field but that which takes into account the field produced by the cables as explained below.

II.3.1.5.7 Magnetic Field Correction

The magnetic field is the sum of the applied field produced by the dipole magnet and the self-field produced by the measuring current. The latter produces a substantial correction. However, since the self-field is spatially non-uniform and depends upon the geometrical details of the bifilar sample, its effect on the V-I curve is difficult to calculate precisely. Experience has shown [76] that the following assumptions give results which are self-consistent for a wide variety of geometry and which give reliable predictions of magnet behavior.

a)The critical current of the sample is determined by the peak magnetic field. This depends, of course, on the orientation of the applied field and the direction of the sample current. This important point will be discussed further in the next section.

b)The sample current is distributed uniformly over, and normal to, the area of the trapezoid which encloses the cable cross-section.

c)The geometry is accurately reproducible; this is a matter of care in assembly, as discussed above.

With the dipole field perpendicular to the wide face of the sample, the peak field occurs at a point on the surface of the sample where the self-field and the applied field are very nearly parallel; that is, they are simply additive. For the standard test configuration, therefore, the self-field correction can be written:

$$B = B_{peak} = B_a + c \times I$$

where B_a = dipole field and c = geometric constant. Below is given the value of c for LHC cable, for B_a perpendicular to the sample, and for the standard BNL test geometry in which the bifilar samples are separated by 0.25 mm

Self-field constant, c, gauss/amp, for LHC Cable1: 0.249

Self-field constant, c, gauss/amp, for LHC Cable2: 0.255

II.3.1.5.8 Critical Current of the Thin Edge:

The thin edge of a keystone-shaped cable is of special interest for two reasons. First, it forms the inner surface of a dipole (or quadrupole) magnet coil, and the maximum value of the field occurs there. Second, this part of the cable experiences the most deformation during fabrication, and possibly the most degradation. The bifilar sample test arrangement with applied field perpendicular has the characteristic feature that the peak fields occur at diagonally opposite points, at the two thin edges (c.f. Fig. II.3.1.5-1). Experience has shown that when the current is reversed, so that the peak field points are along the thicker edges, a higher critical current is measured (even though the calculated peak field is slightly higher in this case). This is due to the smaller degree of degradation along this edge. In practice, the quality control test determines the critical current for the thin edge; i.e. the field and current direction are oriented as in Fig. II.3.1.5-1.

II.3.1.5.9 Data Averaging Using I-B Graph

The critical currents are plotted on a graph of I vs. B and I_c is obtained from an interpolation to the specification field.

The degradation of the cable, as mentioned before, is $D = 1 - (I_c/\Sigma\, I_{cw})$. In practice, a few wires may be measured and $\Sigma\, I_{cw}$ estimated from this sample, but in cases where questions arise as to whether D meets a specification, it is necessary to determine I_{cw} for all the wires in the Cable Map.

We have ignored the fact that the critical current of a wire is also subject to a self-field effect. However, it has become general practice <u>not</u> to take account of this correction, notably in discussions of J_c in the literature. For cables it is not acceptable to ignore self-field corrections for the reasons given previously: sensitivity of measurements to sample configuration and comparison of data with magnet performance. As a result of this convention, the specified degradation is lower than the true degradation, which would take account of wire self-field effect and lead to a larger value of $\Sigma\, I_{cw}$.

II.3.1.5.10 Cable R(293) and RRR Determination

As in the case of wires, the cable resistance at 293 K and that at 10 K is determined using the same set-up used for Ic determination. The residual resistance ratio, RRR, is defined to be R(293)/R(10). R(293) is measured with an accuracy of 0.5%; R(10) is measured with an accuracy of 2%.

The quantity RRR provides a measure of the state of anneal of the copper matrix. It may be used to check that a cable has been given a post-cabling heat treatment in order to facilitate coil winding, if this has been specified. Such cables have RRR values over 100, whereas, typically, cables have values around 70, if the wire has had a final anneal, and 35 if it has not been annealed after the final drawing stages.

The room temperature measurement is made using a DC current of 1 A, and voltage contacts 61 cm apart (see Fig. II.3.1.5-1). A thermocouple device of 0.1^0C accuracy is used to determine the ambient temperature. Normally occurring room temperature variations produce significant variations in the measured resistance. Designating this resistance as R_m and the ambient temperature as t(^{0}C), the resistance at the reference temperature of 293 K is calculated as follows:

$$R(293) = R_m/[1 + 0.0039\,(t - 20)]$$

The effect of the Nb-Ti is negligible for the purpose of this correction.

The low temperature measurement is a dynamic one, made by inducing a superconducting-normal state quench while the cable is carrying current. Referring to Fig. II.3.1.5-1, a quench is triggered in Cable A, for example, by means of heater HA. The resulting waveform observed at nearby voltage taps, A2-A3 or A3-A4, consists of three parts: a superconducting state baseline voltage, a linear ramp voltage corresponding to the passage of the superconducting-normal interface between the voltage taps, and a slowly increasing signal characteristic of the normal state resistance. The latter increases in time due to normal state heating. However, at first the voltage is almost constant due to the residual resistance characteristic of the copper. Thus, there is a kink in the voltage waveform at the beginning and at the end of the linear ramp portion. The voltage difference between these two points equals the current times the residual resistance of the section of cable between the voltage taps. The resistance per centimeter is determined for two pairs of taps (A2-A3 and A3-A4 in the above illustration) and averaged. The taps are relatively close to the heater in order to minimize the effect of current fall-off which results from the increase of normal state resistance as the quench propagates. The usual specification is for zero magnetic field. However, the above measurement may be made in an external field, in order to determine the magnetoresistance effect. Routinely only the resistance in zero field is measured.

II.3.1.6 Copper/Superconductor Ratio

The copper/superconductor ratio of the cable is determined in nearly the same manner as for the wire; The same formulas are used but with two exceptions:

a) The area is that of all the wires, viz., $N\pi d^2/4$.

b) The spiral path of the wires necessitates applying a length correction to the measured value of R(293). For LHC cables R(293) is replaced by 1.045 × R(293) in the formula .

The resistance determination of Cu/SC for cables is routinely done in the BNL short sample test procedure and serves as an accurate check on the wire data. Cable and wire Cu/SC values agree to better than 2% in well-behaved cases, i.e. those in which there have been no errors in the strands used for cabling. This determination is, therefore, an important quality control check. An example of a cable test report is given below:

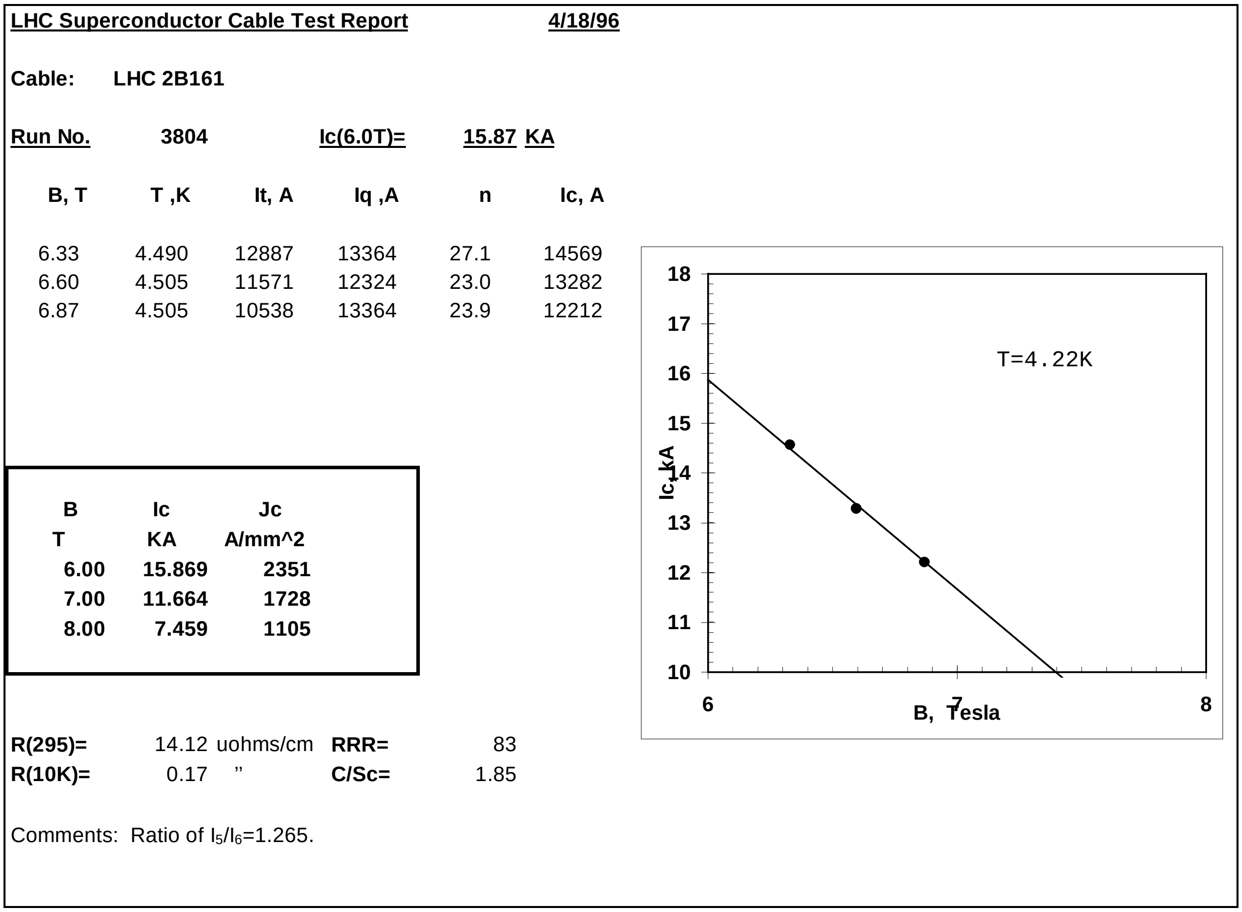

LHC Superconductor Cable Test Report **4/18/96**

Cable: **LHC 2B161**

Run No. **3804** **Ic(6.0T)=** **15.87** **KA**

B, T	**T ,K**	**It, A**	**Iq ,A**	**n**	**Ic, A**
6.33	4.490	12887	13364	27.1	14569
6.60	4.505	11571	12324	23.0	13282
6.87	4.505	10538	13364	23.9	12212

B **T**	**Ic** **KA**	**Jc** **A/mm^2**
6.00	**15.869**	**2351**
7.00	**11.664**	**1728**
8.00	**7.459**	**1105**

R(295)=	14.12	uohms/cm	**RRR=**	83
R(10K)=	0.17	”	**C/Sc=**	1.85

Comments: Ratio of I_5/I_6=1.265.

Fig. II.3.1.6-1. an example of a superconductor cable test report.

II.3.1.7 Strand and Cable R&D

Two years ago, a collaboration work with CERN was begun to examine the intrinsic stability of cables [77]. stability is defined in terms of the minimum quench energy MQE of the cable, i.e. that energy input, of short duration applied to a small section of one wire in the cable, which is just sufficient to quench the sample. In the past attempts to measure MQE by using resistive heaters which are insulated from the strand have always yielded a high value since the thermal time constant of the heater-wire system is usually large and not well controlled. More recently ,a technique of using graphite paste heaters attached directly on the strand have proven to be effective in reducing the time constant and have yielded MQE values for single strands that are of the same order as theoretical calculations. We have successfully used this technique to measure the MQE of LHC single wires and insulated cables.

MQE tests on several LHC cables are being made to study the following:

1. Effect of cable compaction on the stability at 4.2 K and 1.9 K. This series of cables were manufactured at LBL.
2. Effect of different ‘porous metal’ filling of cored cables on the stability of such cables in 1.9 K superfluid helium.

3. Effect of different surface coatings on the strands. This primarily has implications in understanding the interplay of inter-strand resistance and stability.

Results to date show that the level of compaction of the cable has a significant effect on the stability of the cable to transient heat input both at 4.4 K and in superfluid helium at 1.9 K. The low compaction cable has a larger internal void space for trapped helium which helps in raising the MQE of such cables. However, the choice of compaction has to be balanced with the need to have a mechanically good cable with tight dimensional control. This has prompted CERN to change the cable dimension to decrease the compaction from 91.2 to 89.9 %.

Research on cored cables was motivated by the need to look for alternate cable designs that would reduce the eddy-current effect in LHC dipoles. Putting a resistive core into the center of a Rutherford cable increases resistance between the strands in the crossover direction, which greatly reduces the coupling currents, even when the adjacent turns remains small [78]. This allows one to improve stability by soldering strands together or using porous metal, without incurring a penalty for increased coupling. Preliminary results indicate that although the eddy current coupling is reduced, this comes at the expense of reduced stability at 1.9 K, even when adjacent strands are soldered with a porous metal solder.

The recent specification for LHC cables made from AgSn coated strands calls for a post-cabling anneal at 190 C for several hours. Studies at CERN have shown that this treatment increases the inter-strand resistance from a few μ-ohms to few tens of μ-ohms . This is being done to reduce the effects of eddy-current coupling on the harmonics of the magnet. The effect of this heat-treatment on the stability of the cables are being studied.

In addition to the cable tests, MQE measurements are also being done on a series of strands to understand whether the stability of such strands depend on any of the following :

1. NbTi alloy source
2. Different strand designs like whether the strand is single or double-stacked.
3. Difference in processing parameters that is employed by different wire manufacturers.

Results to date indicate that the stability of the strands as gauged by MQE measurements do not show any appreciable difference based on the source of the alloy and the processing of the wires. However, critical current measurements as a function of temperature show that the billet design does influence the relative stability of these strands. Further work is being done to understand this dependence.

II.3.1.8 Summary

The preceding sections describe the resources that will be available for testing and evaluation of the superconducting cables and wires for the LHC magnets. The facility upgrade will be completed by the end of 1999, in time to be ready for the cable production testing. It is expected that this collaboration will be successfully completed in the year 2004.

II.3.2 Superconducting cable R&D at LBNL

As a result of a sustained program to develop high performance superconducting cable for the SSC, the U.S. possesses some unique experience and measurement equipment that is valuable to the LHC project as they begin their efforts to scale-up the production of cable for the LHC magnets. Although the SSC project was terminated, the cabling expertise and much of the specialized measurement equipment resides at LBNL. In addition, the Superconducting Magnet Program at LBNL has continued to develop cabling technology and instrumentation that can benefit the LHC project. The new cabling technology includes the introduction of cores to reduce interstrand coupling and the implementation of eddy current inspection for cable defects.

Several outstanding issues remain for the LHC dipole cable. These include (1) control of the interstrand resistance, (2) choice of lubricant for the cabling process, (3) development of in-line cable defect detection, and (4) control of the cable dimensions to close tolerances.

II.3.2.1 Dipole Cable Interstrand Resistance

The interstrand resistance can be as low as a few microOhms per unit pitch length for cables made from bare Cu or stabrite coated strands. For a wide cable such as the LHC dipole cable and at relatively fast ramp rates, eddy currents become a significant problem, both from the field homogeneity standpoint and also eddy current heating of the cable. The interstrand resistance must be increased to greater than about 20 microOhms per unit pitch length for the LHC dipole cables; several methods are being explored in order to produce a high and reproducible interstrand resistance. The LBNL cabling facility offers a unique capability to address the possible solutions–we can investigate the options objectively, without the competitive pressures that are present in the production cabling facilities.

Work on this task was begun in FY96, and the task is approximately 50 % complete. A total of 10 cables with different parameters have been delivered to CERN for evaluation and testing. These include cables with stainless steel cores, cables with different coatings on the strands, and cables with varying amounts of compaction. Measurement of interstrand resistance indicates that a stainless steel core can provide the required interstrand resistance in a reliable, reproducible manner (Fig. II.3.2.3-1). At present, we are fabricating enough inner and outer cable with stainless steel cores to make a 1-m model for testing at CERN [79].

II.3.2.2 Cable Measurement Support

Over 6000 km of cable will be manufactured for the LHC project. This cable must be manufactured to exacting dimensional tolerances e.g., cable mid-thickness controlled to +/- 6 microns**.** Special cable measuring machines (CMM, Fig. II.3.2.3-3) were developed for the SSC project, and these machines have been held in storage in anticipation of a collaboration agreement between the U.S. and CERN on the LHC. The machines have been modified to accept the wider LHC cables and to measure the cables at higher clamping pressures. A new version of the control and data acquisition software has been prepared, installed, and debugged [80]. A total of five CMMs, four from the SSC close-out and one new machine, will be delivered to CERN for use in their cable quality control program. As of the writing of this report, the four existing machines have been delivered to CERN and are awaiting commissioning. A contract for construction of the new machine has been let, and delivery is planned for late 1998. LBNL personnel will make several trips to CERN to activate these machines and to train CERN personnel on the use and maintenance of these machines.

In addition to the dimensional inspections, the cable must be inspected for defects such as broken strands, cold welds, crossovers, or sharp edges. At present, the cable is inspected visually by an operator–this is not feasible for the large quantity of cable needed for the LHC. An eddy current flaw detection system was under development in the U.S. at the time of the cancellation of the SSC project. This system is being completed and a prototype system will be evaluated on the cabling facility at LBNL [81]. After its performance is optimized, a production unit will be delivered to CERN for use in cable inspection. If this system proves satisfactory, CERN anticipates ordering 6 additional systems for use on the LHC cabling and cable inspection lines.

II.3.2.3 Cable Manufacturing Support

In order to verify the specification limits for the LHC cables, a series of cables must be made and tested with parameters at the chosen specification limits [82]. This series of cables will be fabricated at the LBNL cabling facility in order to do an independent evaluation of the specification limits.

The cable interstrand resistance is sensitive to many parameters which must be controlled during cable manufacture; among these is the lubricant used in cabling. LBNL will assist CERN in the evaluation and selection of a lubricant that can be used on all cables manufactured for the LHC project.

A powered Turkshead was used to manufacture most of the cable for the SSC project, and has been used effectively at LBNL to make wide cables such as those required for LHC. One of the powered Turksheads used for manufacture of SSC cable (and now in storage at LBNL) will be provided to CERN so that they can assess the differences in cables made with powered vs. non-powered Turkshead forming.

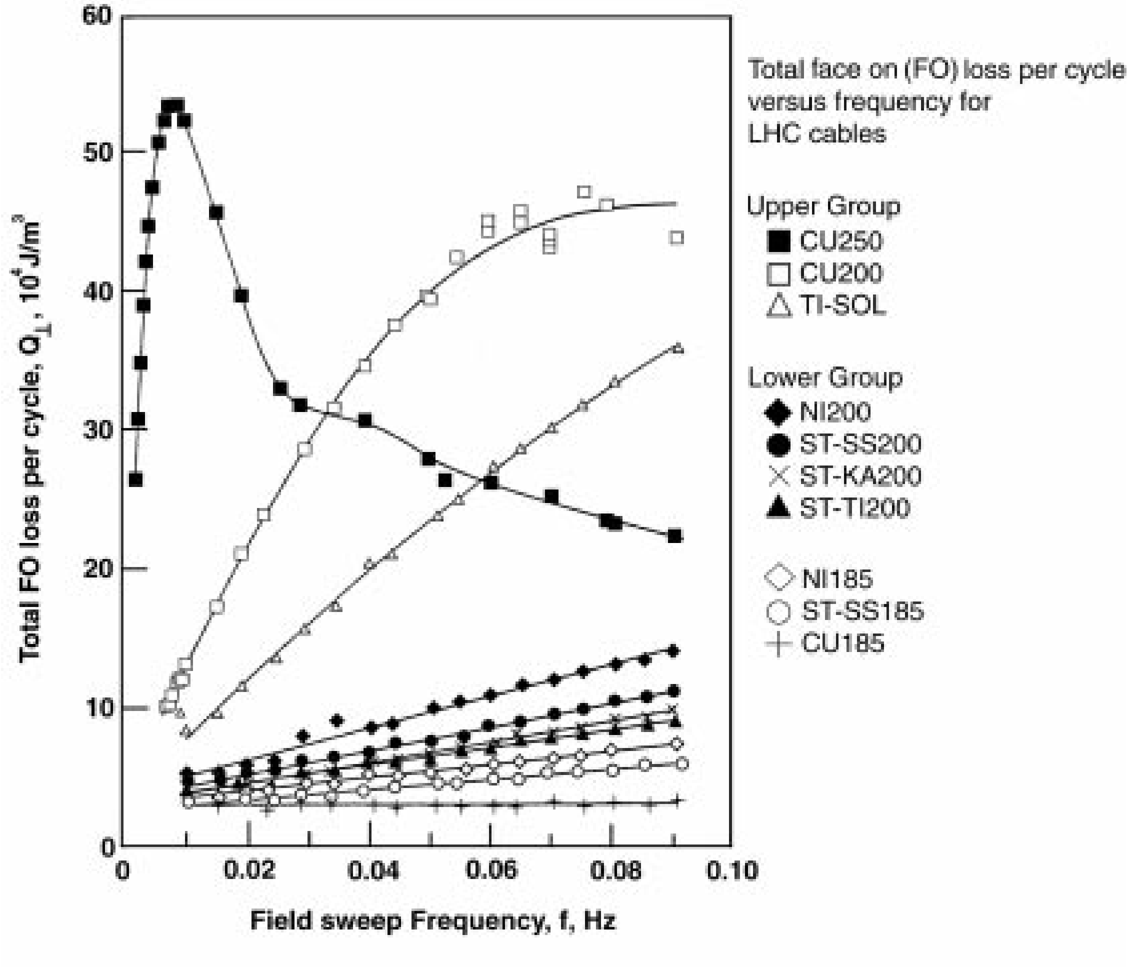

Fig. II.3.2.3-1. Calorimetric measurements of the effect of Ni and Stabrite coatings and resistive cores on AC loss in accelerator cables under fixed pressure.

Fig. II.3.2.3-3. Photograph of a LBNL cable measuring machine (CMM).

II.3.2.3.1.1 References

[79] J.D. Adams et al., “Rutherford Cables with Anisotropic Transverse Resistance,” *IEEE Transactions on Applied Superconductivity, Vol. 7, No. 2*, June 1997.

[80] R. Hannaford, “Cable Measuring Engine Operation Procedures,” *LBNL-40565, SC-MAG 597*, July 1997.

[81] Proposal for a smart EDDY On-line Inspection System Development Program, SE Systems Inc., Jan. 1997.

[82] CERN Cable Specification, IT-2422/LHC.

II.4 Accelerator Physics

II.4.1 Introduction

The overall objective of the Accelerator Physics program is *to support CERN in the construction of the LHC*. This naturally translates into a scope with two categories of task: *core* and *non-core*.

Core tasks are essential to the successful completion of the US-LHC Accelerator Project. For the most part the core activities support the quality assurance of physical deliverables – cryostated magnets and neutral absorber ionization chambers. For example, those tasks that involve evaluating expected and measured magnetic field harmonics are core activities.

Non-core tasks, upon their successful completion, significantly enhance the performance of the LHC. These tasks often take advantage of unique US capabilities to perform Accelerator Physics (AP) calculations or measurements. One example is the use of an existing software infrastructure to perform electron cloud effect simulations. Another example is making beam based performance measurements (such as ground motion studies) in existing superconducting hadron colliders - the Tevatron and RHIC.

A small number of issues do not fall neatly into either of these categories, but overflow into areas of joint interest to US labs and to CERN. For example, in order to have close collaboration among the US labs and CERN, it is necessary to develop and maintain a smooth data flow infrastructure. Although this issue is specifically identified and addressed as a topic in the section “Software maintenance and development”, below, it also naturally crops up in other sections of this chapter. It should also be recognized that other AP topics may well arise in the lifetime of the project, and will be handled appropriately.

For better or worse, this chapter is divided into two major sections: *Design Issues* and *Beam Physics Issues*. The former mainly covers core topics (supporting physical deliverables) while the latter mainly describes non-core activities (invoking unique US capabilities and resources). *Design Issues* need to be jointly addressed by magnet builders and accelerator physicists, in step with the magnet development and construction schedule. *Beam Physics Issues* are less directly related to physical deliverables, but are also important in optimizing LHC performance.

While all of the AP activities *support CERN in the construction of the LHC*, many of them do so by advancing the state-of-the-art of our understanding of current and future large hadron colliders. In this way the AP community in the US benefits directly from the US-LHC Accelerator Project.

Accelerator physics information can be found on the World Wide Web. The main US-LHC home page, http://www-td.fnal.gov/LHC/USLHC.html has connections to local laboratory web sites at BNL, FNAL, and LBNL.

II.4.1.1 Major milestones and mini-workshops

The accelerator physics program supports all phases of magnet design and construction, cold mass and cryostat assembly, and tunnel installation. For this support to be effective, the accelerator physicists must work in close collaboration with US magnet builders, and with CERN. Major technical milestones will be established and met, in coordination with the magnet builders. In approximate chronological sequence, and emphasizing those magnets that will be installed at high β locations, the milestones include:

(1) Final design and implementation of the High Gradient Quadrupole body cross-section and end geometry. This potentially includes lead end redesign, body-end compensation, and body shims.

(2) Final design of the inner triplet compensation and correction scheme. This potentially includes the use of tuning shims, optimization of corrector layers and layout, and accelerator tuning algorithms.

(3) Decision of whether or not to split the inner triplet cryostat into two pieces. Evaluate the direct and indirect effects on luminosity performance.

(4) Final design and implementation of surveying and alignment measurements and procedures, during cryostat assembly and installation.

(5) Full implementation of data flow in support of field harmonic and alignment quality assurance, optimized installation, and standard accelerator model exchange.

A timeline including these and other milestones is being established in discussions with the magnet builders.

Mini-workshops are one way to support milestone decisions. They also have a crucial role to play in establishing effective personal communications between the US labs and CERN. Several mini-workshops have already occurred, or are in the planning stages:

October 97	FNAL	High Gradient Quadrupole (HGQ) workshop
February 98	BNL	UAL/LHC software modeling
June 98	BNL	Database / data flow
October 98	FNAL	HGQ body cross section and ends
1999		Integrated compensation and correction
1999		Alignment

These workshops need to be limited in attendance to relevant experts from the US labs and at CERN, in order to permit efficient consensus planning and decision making. They will be held once every four months or so, rotating among the US labs.

II.4.1.2 Superconducting magnets

LHC performance depends directly on achieving the highest possible magnetic field quality and alignment accuracy in the US-LHC project magnets.

Collisions occur in the LHC at Interaction Points (IPs) 1, 2, 5 and 8 [83]. At these IRs both counter-circulating beams share the same inner triplet quadrupoles (Q1, Q2A, Q2B, and Q3) and common dipoles (D1). The sensitivity to field quality and alignment errors is greatest in these magnets, because the β values there are very large, in inverse proportion to small β* values at the collision point. The optical sensitivity also depends strongly on Φ, the *total* crossing angle. The beams do not cross at the other interaction regions, which serve other purposes. For example, the beams are further separated at IR4 to make space for the RF cavities. Beam cleaning occurs at IR 3 and IR7, and the beam abort is at IR6.

Table II.4.1.2-1 shows the values for β* and Φ at the 4 collision IPs in the nominal storage optics (lattice version 5.0) [83, 84, 85]. This table also shows optional values currently under investigation. Table II.4.1.2-3 lists maximum beam sizes, separations, and other parameters at these interaction regions for both injection and collision conditions [83, 86]. The primary low β* interaction points are IP1 and IP5. Although the optical layout at IR2 and IR8 is almost identical to that at IR1 and IR5, the nominal β* values at these locations are much larger. In principle, although not in current planning, IR2 and IR8 could also be upgraded to operate with β* values as low as 0.5 m.

Table II.4.1.2-1. Nominal and provisional optional collision parameters in LHC lattice version 5.0.

	IP	*nominal*	*optional*
β* [m]	1	0.5	down to 0.25 m possible
	2	250	50 m to 250 m in p operation 0.5 m possible in ion operation
	5	0.5	down to 0.25 m possible
	8	33	
Φ [μr]	1	200	up to 300 μr possible
	2	200	
	5	200	up to 300 μr possible
	8	200	

Table II.4.1.2-3. Nominal injection and collision parameters at IP1 and IP5. The maximum *total* beam separation $\Delta_{sep}(\max)$ occurs in the triplet.

Quantity	*Unit*	*Injection*	*Collision*
Energy, E	TeV	0.45	7
β^*	m	> 18	0.5
$\beta(\max)$	m	~ 200	4700
Φ	μr	350	200
RMS norm. emittance, ε	μm·rad	3.75	3.75
$\sigma(\max)$	mm	1.3	1.5
$\sigma(\text{arc})$	mm	1.2	0.3
$\Delta_{sep}(\max)$	mm	16.6	9.4
$8\sigma(\max) + \Delta_{sep}(\max)/2$	mm	18.3	16.7

Fermilab is building the High Gradient Quadrupole (HGQ) cold masses for IR5 and one of IR2 and IR8, and KEK is building inner triple quad cold masses for IR1 and one of IR8 and IR2. The US is assembling these cold masses together with CERN-supplied correction coils and instrumentation into complete, integrated, cryostated packages. Brookhaven is supplying separation dipoles (D3A, D3B, D4A, and D4B) for the RF interaction region, IR4.

Next to the superconducting inner triplet at IR1 and IR5, and still in a region of very high β, are *warm* beam splitting D1 dipoles. These dipoles will be built at CERN from iron, in order to ameliorate quenching problems. The superconducting D1 dipoles at IR2 and IR8 may be built at BNL, based on the RHIC arc dipole magnets. Wherever they are built, and whether they are warm or cold, it is important to include all D1 magnets in models used to evaluate the low β^* performance of an IR, since the dynamical performance is as sensitive to field errors in these magnets as in the inner triplet quadrupoles.

II.4.1.3 Acknowledgements

Many authors contributed to this chapter. Grateful acknowledgements go to W. Chou, J. Corlett, A. Drozhdin, S. Feher, M. Furman, D. Herrup, J. Holt, C. Johnstone, F. Meot, N. Mokhov, J. Peterson, F. Pilat, V. Ptitsin, D. Ritson, G. Sabbi, V. Shiltsev, J. Strait, S. Tepikian, G. Trahern, W. Turner, W. Wan, J. Wei, and A. Zlobin.

II.4.2 Design Issues

The *Design Issues* section covers topics that support physical deliverables, mainly cryostated magnets, which are being jointly addressed by accelerator physicists and magnet builders.

The first sub-section, *Dynamics analysis and simulation*, describes the standard data and calculation tools that are used to evaluate most, or all, magnet styles. *High Gradient Quadrupoles* addresses the accelerator physics work that is being performed to support the construction of these magnets, which will be built at Fermilab. *Beam splitting dipoles* focuses on the only other magnets that are at sensitive high β locations, and which must be included in the integrated design of a compensation and correction scheme. *RF section magnets* introduces the analysis of the beam splitting D3A, D3B, D4A, and D4B dipoles which will be built at Brookhaven, and that further separate the beams in the interaction region containing the radio frequency cavities. *Alignment* discusses the need for accurate alignment and surveying, not only during cold mass assembly and cryostating, but also in preparation for shipping and installation. *Quality review of production magnets* describes the process that will be put in place to monitor the (short) production run of each magnet style*.* *Beam induced energy deposition* reports results from a preliminary analysis of the inner triplet magnets and internal absorbers, and in the immediate vicinity of the interaction region. Last but not least, *Neutral absorber ionization chamber* describes how the TAN neutral beam absorber can be instrumented to measure the neutral particle flux from the IP.

II.4.2.1 Dynamics analysis and simulation

Various methods are employed for the performance analysis of the IR (and other) magnets, both at the design stage with reference harmonic errors, and (later) at the production stage with measured errors. Key features of this analysis include:

II.4.2.1.1 Reference harmonics

Reference harmonics (or *expected harmonics*) lie at the center of communications between accelerator physicists and magnet builders. Preliminary values of reference harmonics are tabulated, below, for each magnet style being produced in the US-LHC Accelerator project. In every case the values of these numbers are provided by a magnet physicist who acts as a liaison between the magnet builders and the accelerator physicists, and who presents the harmonics as a consensus of the magnet builders. Reference harmonics are publicly posted and maintained on the web.

These harmonic values will evolve modestly and slowly through additional revisions, as more information becomes available about realistic magnets – for example, when magnet prototypes are measured - and perhaps as minor modifications to the magnet design are made. It is in this spirit that the expected harmonics are called references, and not specifications. They are the basis for accelerator physicists and magnet builders to jointly discuss and determine the optimum design for the highest performance magnets that may practically be built within realistic resources.

Expected harmonic tables include separate information on body harmonics and on end multipoles. Body errors at injection and at storage come from multiple sources, including cross section geometry, superconductor magnetization, magnetic saturation, magnetic measurement errors, pre-stress fluctuations between magnets, and manufacturing tolerances. Lead end and return end errors are tabulated as harmonic integrals B_n and A_n , (where $B_n = \int_{end} b_n ds$, $A_n = \int_{end} a_n ds$) which act approximately as delta function multipoles. It is expected that systematic harmonics – some of which are significantly large - will dominate the total error in the ends. Systematic errors are reliably calculated by 3-D magnetic modeling programs.

II.4.2.1.2 Action-kick analysis

The relative action kick $|\Delta J_{x,y}/J_{x,y}|$ received during passage through a magnet (or through an assembly of magnets such as the inner triplet) is a figure of merit for magnet design and error compensation that should be minimized. Both horizontal and vertical action kicks are important. For example, a typical rule of thumb is that the total action kick accumulated by particles with a betatron amplitude of 8σ, due to all multipoles, should be less than 0.005. Taking into account the separation Δ_{sep} between the beams, this requirement becomes

$$\left|\frac{\Delta J_{\mathrm{x,y}}}{J_{\mathrm{x,y}}}\right| = \frac{1}{4\pi\rho}\int\sum_n \beta_{\mathrm{x,y}}\left[(2\beta_{\mathrm{x,y}}J)^{1/2} + \frac{\Delta_{\mathrm{sep}}}{2}\right]^{n-2} c_n ds < 0.005, \qquad (1)$$

where $J = 8^2\varepsilon/2\beta\gamma$ is the action of the 8σ particle, ε is the RMS normalized emittance, and β is the beta function in the magnet (or magnets) of interest. The coefficients c_n are expressed in terms of the normal (b_n) and skew (a_n) body harmonics measured in units of 10^{-4} of the nominal magnetic field at a reference radius of R_0, through

$$c_n = \begin{cases} \dfrac{10^{-4} b_n}{R_0^{n-1}}; \quad \text{or} \quad \dfrac{10^{-4} a_n}{R_0^{n-1}}, & \text{(for dipoles)} \\ \\ \left(\dfrac{\mathrm{G}_0}{B_0}\right)\dfrac{10^{-4} b_n}{R_0^{n-2}}; \quad \text{or} \quad \left(\dfrac{\mathrm{G}_0}{B_0}\right)\dfrac{10^{-4} a_n}{R_0^{n-2}}, & \text{(for quadrupoles)} \end{cases} \qquad (2)$$

The term ρ in the denominator of Equation 1 is either the bending radius (for dipoles), or is $B_0/(B\rho)$ for quadrupoles, where B_0 is defined in Equation 2 and $B\rho$ is the magnetic rigidity.

This semi-analytic method provides rapid physical insight, and allows a quick assessment of the impact of magnetic errors and compensation schemes. Table II.4.2.2-2 and Table II.4.2.3-1 are examples of this kind of analysis. Strictly speaking there are two sensitivity values – one horizontal and one vertical. The sensitivity tables show only the larger of the two values for each harmonic.

II.4.2.1.3 Tune footprint analysis

Tune footprints for a beam of specified emittance and momentum deviation, driven by magnet errors and lattice nonlinearities, are extracted from short-term computer tracking using codes like TEAPOT and COSY. Detailed information is incorporated in the simulations, including expected harmonics, non-zero crossing angles, random misalignments, compensation and corrections schemes, and beam-beam collisions. Specific compensation and correction schemes being investigated include amplitude-weighted body-end compensation, tuning shims, and local correctors. Both normal form and tracking post-processing methods are used to calculate tune footprints. The increased accuracy of using thick fringe fields (instead of delta functions) to model magnet ends is being investigated.

II.4.2.1.4 Dynamic aperture analysis

Relatively long-term computer tracking is used to confirm the short-term results, and to determine the dynamic aperture of the machine. Results obtained with tracking codes are compared with LHC-standard codes like MAD. It is essential to establish and maintain the compatibility of the input model with CERN codes, both for the error free “bare” lattice, and also for the flat instantiated “machine” lattice including field errors, alignment errors, and correctors. It is also essential to be able to “filter” the flat instantiated lattice by performing realistic simulations of machine tuning algorithms.

Although analysis results rely on all of these methods, the action kick analysis and the tune footprint analysis will be used most frequently to ensure rapid feedback between accelerator physicists and magnet builders. This is especially desirable during the early production stage.

II.4.2.1.5 Summary of future work

Action-kick sensitivity calculations and tune footprint analyses will be used to address magnet design issues. They will also be expanded to include other LHC operational scenarios, such as heavy ion operation, when the corresponding optics designs are completed by CERN in the future. These techniques will also be more fully used to evaluate RF section magnets that fall within the scope of the US-LHC program.

In addition to these methods of analysis, frequency map techniques will be developed to gain further insight into long time scale LHC dynamics.

Occasional 6-D dynamic aperture tracking will be performed, including beam-beam effects and reference errors of the arc region magnets provided by CERN. The purpose of such efforts is to ensure the performance of US-built magnets under a fully realistic spectrum of operational conditions.

II.4.2.2 High Gradient Quadrupoles

Because of the high β values and the large beam separations that occur in IR1 and IR5 inner triplets during low-β* operation, the field quality of the HGQ magnets in the triplets is most crucial. The most demanding conditions are $\beta^* \approx 0.5$ m with a total crossing angle of $\Phi \approx 200$ μr.

II.4.2.2.1 Reference harmonics

Table II.4.2.2-1 shows the preliminary "reference" or "expected" harmonics (version 1.0) which apply to the High Gradient Quadrupoles (HGQ) that are being built at FNAL [87]. Body harmonics in the version 1.0 tabulation are mostly derived from discussions during the LHC mini-workshop on IR design that was held in October 1997 at Fermilab, attended by both accelerator physicists and magnet builders. The version 1.0 end harmonics are derived from two independent studies, which are in relatively good agreement [88, 89, 90]. The baseline design for the HGQ coil end design features an external splice connecting the inner and outer coil. An internal splice design is currently being developed, which is expected to improve the field quality. If the results of beam tracking studies show that a further reduction of the field errors in the end regions is necessary, a re-optimization of the conductor group geometry will be performed.

II.4.2.2.2 Action kick analysis

Table II.4.2.2-2 shows the sensitivity of the machine performance to body harmonics in a single composite Q2 magnet under collision conditions with $\beta^* = 0.5$ m and $\Phi = 200$ μr, as measured by the relative action kick figure of merit. For simplicity it is assumed that the beam separation is at its maximum value, given by

$$\Delta_{\mathrm{sep,max}} \approx \Phi\sqrt{\beta^* \beta_{\max}}, \qquad (3)$$

throughout the Q2 magnet.

Table II.4.2.2-1. Reference harmonics (version 1.0) for HGQ magnets. “Units” for the body harmonics are 10^{-4} of the quadrupole field at a reference radius of 10 mm. “Unit-meters” for lead and returns ends represent delta function multipole kicks, also using a 10 mm reference radius. Harmonics are numbered in the European convention: $n = 1$ is dipole, etc. The mean systematic value is labeled by $\langle b_n \rangle$, the uncertainty in the systematic by $\Delta(b_n)$, and the standard deviation of the random error by $\sigma(b_n)$. See G. Sabbi, TD-97-050, Nov 1997.

Order, n	*Normal*			*Skew*		
	$\langle b_n \rangle$	$\Delta(b_n)$	$\sigma(b_n)$	$\langle a_n \rangle$	$\Delta(a_n)$	$\sigma(a_n)$
BODY (collision)						
[Units]						
2	-	-	-	-	-	-
3	.0	.2	.5	.0	.2	.5
4	.0	.09	.3	.0	.09	.3
5	.0	.04	.07	.0	.04	.07
6	.0	.02	.03	.0	.02	.03
7	.0	.01	.008	.0	.01	.008
8	.0	.004	.003	.0	.004	.003
9	.0	.002	.0016	.0	.002	.0016
10	.0003	.0009	.0005	.0	.0009	.0005
BODY (injection)						
[Units]						
as above, except ..						
3			1.3			1.3
6	-.1	.04				
10	.0001					
LEAD END	$\langle B_n \rangle$	$\Delta(B_n)$	$\sigma(B_n)$	$\langle A_n \rangle$	$\Delta(A_n)$	$\sigma(A_n)$
[Unit-meters]						
2	.0			16.0		
6	.270			.008		
10	-.0013			-.0005		

RETURN END [Unit-meters]	$\langle B_n \rangle$	$\Delta(B_n)$	$\sigma(B_n)$	$\langle A_n \rangle$	$\Delta(A_n)$	$\sigma(A_n)$
6	.046			.0		
10	-.0013			.0		

Table II.4.2.2-2. Action-kick sensitivity of 8σ amplitude particles to body harmonics from one (Q2A+Q2B) quadrupole magnet at collision in the absence of error compensation. The second column records the value of the larger of the horizontal and vertical values of $|\Delta J/J|$ produced when 1 unit of error (b_n/a_n) of multipole order *n* at a reference radius of 10 mm acts on a particle of 8σ amplitude ($\beta^* = 0.5$ m and $\Phi = 200$ μr).

Multipole	$|\Delta J/J|$ *(× 10^{-3})*
b_3/a_3	4.7
b_4/a_4	7.6
b_5/a_5	12.3
b_6/a_6	19.9
b_7/a_7	32.2
b_8/a_8	52.4
b_9/a_9	85.3
b_{10}/a_{10}	139.0

II.4.2.2.3 Correction and compensation schemes

Without error compensation or correction, the condition of Equation 1 is not satisfied even when a single sextupole harmonic is present in one Q2 magnet at twice the expected random value recorded in Table II.4.2.2-1. Compensation of the magnet errors needs to take into account the significant variation of the amplitude (β) function across each HGQ magnet [91, 92]. On the other hand, although amplitude weighted compensation is necessary, the betatron phase advance across each inner triplet is negligible, and integrated local triplet compensation is effective. Two types of correction strategies can be envisaged to further reduce the deleterious effects of field errors in the IR regions. The first category includes methods for improving the field quality of the main magnets, while the second category includes methods for compensating the magnet errors through optimization of the IR configuration and/or the use of corrector magnets.

In the first category, the main correction scheme consists of modifying the coil geometry using pole and mid-plane shims in each octant, independently for the inner and outer coil layers. Larger corrections may be obtained by changing the thickness of the bearing strips, while insulation layers 25 μm thick can be added or removed to fine tune the harmonics. Analysis shows that corrections of the systematic harmonics within the predicted range of variation (Δb_n) are possible at the nominal operating gradient using the available tuning capability. A coil cross section iteration will only be required if correction for larger effects becomes necessary.

The random spread in harmonics between magnets could be reduced by coil re-shimming after warm magnetic measurements. This would provide a correction that is quite current independent, but would be labor-intensive and subject to some uncertainty as the harmonics are not exactly reproducible after collared coil re-assembly. Alternatively, tuning shim methods are very attractive in terms of required effort and reproducibility, but the resulting correction is current-dependent due to saturation effects. Preliminary calculations indicate that only 50% of the tuning shim correction capability at low current is preserved at nominal gradient. Tuning shims are discussed further below.

The second approach to IR field quality improvement relies on the use of correction magnets, on the optimization of the configuration layout, and on sorting. Due to the tight spatial constraints inside the inner triplet, the number of corrector coils must be kept to a minimum. However, one correction magnet can have many – say 4 – independent layers.

Fig. II.4.2.2-1. Schematic layout of the LHC inner triplet and common dipole assembly, in version 5.0 optics. The layout shows the dipole (D1), quadrupoles (Q1, Q2A, Q2B, and Q3) and their lead-end orientation, triplet correctors (MCBX, MCDD, MCQS, and MCDDS), and BPMs for the two counter-circulating beams.

Table II.4.2.2-4. The nominal list of correctors to be installed in the IR triplets, in version 5.0 optics [83, 93].

Name	*Type*	*Nominal Field at x,y [m]*	*L_m [m]*	*No.*
MCBX	H/V Dipole			2
	(horizontal)	3.2	0.31	
	(vertical)	3.2	0.30	
MCQS	Skew quadrupole	28 y	0.36	1
MCDD	Dodecapole	$3.2\ 10^6\ x^5$	0.50	2
MCDDS	Skew Dodecapole	$3.2\ 10^6\ y^5$	0.50	1

The objective during configuration optimization is to place the correctors at locations where the β function is relatively large, and to move those systems that generate large field errors toward locations where the β function is small. Fig. II.4.2.2-1 shows the layout of the IR inner triplet in the current lattice version 5.0, including correctors that can be used to further improve the quality of the optics. Table II.4.2.2-4 lists some of the basic properties of these correctors.

Correction tactics that can be used to improve triplet performance include:

lead end orientation

Orient the HGQ magnets so that the lead ends of Q1 and Q2A face each other, and so that the lead ends of Q2B and Q3 face each other, as shown in Fig. II.4.2.2-1. Such an arrangement maximizes the error cancellation between focusing and defocusing quadrupoles and, consequently, minimizes the effect of lead-end systematic errors. It also places the magnet lead ends, which have larger end errors, away from the Q2A-Q2B drift where the β function reaches a peak value [94]. This effectively reduces the optimal value of body b_6 by a factor of 2.3, if a body-end compensation scheme is implemented [95]. A similar advantage is obtained by orienting the lead end of the D1 dipole away from the IP.

Accelerator physicists at Fermilab studied the effect that the end fields of HGQ magnets have on the tune footprint and the short-term dynamic aperture. The tune shift with amplitude was obtained using the DA normal form routine in COSY, and the tracking was performed using a 10th-order one-turn map, also with COSY. Preliminary results confirm the conclusion independently reached by BNL, in that the lead end orientation affects the tune shift with amplitude. The same simple statement can not be made about the effect on the 1000-turn dynamic aperture.

body/end compensation

Adjust the design value of the body b_6 to compensate for the end errors across each triplet according to the amplitude-weighted expression

$$b_{6B} = -0.10 \quad B_{6L} - 0.23 \quad B_{6R} = -0.038(\text{unit}). \qquad (4)$$

where subscript B refers to the body, L to the lead end, and R to the return end. This choice of body b_6, the same for all the HGQ magnets, is insensitive to lattice optics changes as long as β^* is small. The coefficients for the lead end B_{6L} and return end B_{6R} reflect the choice of magnet orientation shown in Fig. II.4.2.2-1.

tuning shims

Tuning shims provide a way to correct the harmonics of an individual HGQ magnet after it is constructed and measured for the first time, but before it is assembled into a cryostat. [96, 97]. For each HGQ magnet, tuning shims are inserted into 8 slots to correct as many as 8 multipole harmonics. The performance of the HGQ tuning shims is being explored jointly by FNAL magnet builders and accelerator physicists, using simulation software to determine the multipole candidates for optimization. Preliminary predictions for the performance of HGQ tuning shims have already been established [98]. Tuning shim correction becomes most effective only if the measurement uncertainties are small, and if the harmonic variations with quench and thermal cycles are small.

local correctors

The optics can be further improved after magnets have been installed and commissioned by powering local correctors in the triplets. Transverse misalignments of the triplet quadrupoles generate dipole kicks in both planes, and will be compensated by vertical and horizontal dipole correctors at locations where the appropriate β function is large. Due to the strong influence that low-β quadrupole roll angles have on the minimum tune split, a local skew quadrupole corrector is necessary. Preliminary studies indicate that a single skew quadrupole is sufficient for correcting these errors [99]. It may be necessary to calculate the strength of these skew quadrupole correctors based on a local de-coupling correction scheme.

The optimum settings of the nonlinear local correctors may be established either by dead reckoning or by beam-based correction schemes. Dead-reckoning schemes based on design lattice functions and bench-measurements of multipole errors are simple to apply. Beam-based schemes using local correctors become more attractive than dead reckoning if measurement uncertainties, and/or harmonic fluctuations with quench or thermal-cycle history, are found to be large. As a rule of thumb, effective correction for each inner triplet in both horizontal and vertical directions requires two correctors for each normal harmonic (at locations of significantly different β_x and β_y), and one for each skew harmonic. The performance of the nominal a_2, b_6 and a_6 correctors (Fig. II.4.2.2-1) will be evaluated using simulation software. Additional b_3/a_3 and b_4/a_4 correctors appear to be highly desirable. Beam-based correction schemes for high-order multipoles are being explored.

sorting

The HGQ magnets with the highest field quality will be selected for use at IR1 and IR5. The remaining magnets will be used either at IR2 or IR8, or as spare magnets. Magnet cold masses (quadrupoles and correctors) will also be selected and matched before cryostat assembly in order to minimize the relative magnetic center offset and roll angle.

Table II.4.2.2-5. One possible integrated correction strategy for the inner IR triplet, consistent with version 5.0 optics.

Order, n	*Normal, b_n*	*Skew, a_n*
1	MCBX	MCBX
2	trim	MCQS
3	S	S
4	B, S	S
5		
6	B+, MCDD (2)	B+, MCDDS
8	B	
10	B	

Table II.4.2.2-6. Key to symbols used in Table II.4.2.2-5.

Symbol	*Meaning*
B	coil cross-section iteration
B+	coil cross-section iteration plus body-end compensation
S	tuning shims
MCBX	local normal/skew dipole corrector
MCQS	local skew quad corrector
MCDD	local b_6 corrector (2 per IR)
MCDDS	local a_6 corrector

The optimum correction and compensation strategy will incorporate tactics using most or all of these schemes. Table II.4.2.2-5 and Table II.4.2.2-6 summarize one integrated correction strategy that is possible in version 5.0 optics, according to order of the multipole being addressed.

II.4.2.3 Summary of future work

Ongoing study is required in order to assess the efficiency and the relative advantages of potential HGQ compensation and correction schemes. The optimum inner triplet design will be continuously reviewed as new information becomes available from field quality measurements of the HGQ magnets, from beam tracking studies, and from improved knowledge of the precision of the alignment procedures. Studies will be performed to support decisions on the IR corrector package including the number of layers of each package, choice of multipole components, and the required corrector strengths. Since error compensation of D1 dipoles also relies on inner triplet correctors, their performance requirements will also be integrated into inner triplet design studies.

II.4.3 Beam splitting dipoles, D1

The superconducting D1 dipoles placed at IR2 and IR8 may be built at Brookhaven. At these locations the β values are not nominally expected to become very large, since the β^* values shown in Table II.4.1.2-1 are relatively large. However, future upgrades could lower these β^* values as low as 0.5 m. It is necessary to pay close attention to the field quality of all the D1 magnets, including the warm dipoles in IR1 and IR5 locations, wherever they are to be constructed.

Table II.4.2.3-1 shows version 1.0 of the expected magnet harmonics for D1 dipoles at collision energy. In lieu of expected harmonics from a known design, the values tabulated are derived from actual harmonics of RHIC arc dipoles, with a few minor modifications [100]. If BNL builds the D1magnets, these harmonics are the appropriate starting point for discussions with magnet builders. A replacement table will be established if the D1 magnets are built elsewhere. In either case it is also necessary to establish expected harmonics for the warm D1 dipoles that will be built at CERN.

Table II.4.2.3-2 shows the impact that 1 unit of magnetic error (b_n/a_n) in a single D1 dipole has on machine performance if β^* is reduced to 0.5 m, under collision conditions with $\Phi = 200\ \mu$r. Note that the reference radius used here is 25 mm. The action-kick sensitivity shown, defined by Equation 1, is for a particle of 8σ amplitude.

Table II.4.2.3-1. Expected magnetic errors (version 1.0) at collision energy for the body, lead end, and return end of D1 dipoles, derived from measurements of RHIC arc dipoles [100]. Units are 10^{-4} of the dipole field at a reference radius of 25 mm. Harmonics are numbered in the European convention: $n = 1$ is dipole, et cetera. The mean systematic value is labeled by $\langle b_n \rangle$, the uncertainty in the systematic by $\Delta(b_n)$, and the standard deviation of the random error by $\sigma(b_n)$. See A. Jain, RHIC/AP/147, February 1998.

Order, n		*Normal*			*Skew*	
BODY (collision) [units]	$\langle b_n \rangle$	$\Delta (b_n)$	$\sigma (b_n)$	$\langle a_n \rangle$	$\Delta (a_n)$	$\sigma (a_n)$
2	.1	.8	.28	.6	3.5	1.55
3	-3.3	3.4	1.82	-.3	.6	.21
4	.0	.3	.09	.0	1.1	.42
5	.5	.8	.41	-.1	.2	.06
6	-.1	.1	.04	-.1	.6	.17
7	1.1	.2	.11	.0	.1	.03
8	.0	.1	.01	.0	.2	.05
9	.0	.1	.05	.0	.1	.01
10	.1	.1	.02	.0	.1	.02
11	-.6	.1	.02	.0	.1	.01
LEAD END [unit-m]	$\langle B_n \rangle$	$\Delta(B_n)$	$\sigma(B_n)$	$\langle A_n \rangle$	$\Delta(A_n)$	$\sigma(A_n)$
2	-.5	2.3	.99	-1.4	4.3	1.77
3	22.4	2.9	1.10	-9.9	1.0	.39
4	.0	.7	.23	.1	.8	.29
5	-.4	.7	.22	2.2	.3	.13
6	.0	.3	.12	.0	.3	.10
7	.9	.1	.05	-.9	.1	.06
8	.0	.1	.03	.0	.1	.03
9	.0	.1	.03	.3	.1	.02
10	.0	.1	.03	.0	.1	.02
11	-.1	.1	.01	.0	.1	.01
RETURN END [unit-m]	$\langle B_n \rangle$	$\Delta(B_n)$	$\sigma(B_n)$	$\langle A_n \rangle$	$\Delta(A_n)$	$\sigma(A_n)$
2	.2	1.8	.66	.9	4.5	1.91
3	6.1	2.7	1.16	.3	1.0	.34
4	.0	.4	.16	.2	.7	.31
5	.0	.7	.23	.0	.3	.11
6	.0	.2	.06	.0	.2	.10
7	.0	.1	.06	.0	.1	.05
8	.0	.1	.03	.0	.1	.04
9	-.2	.1	.03	.0	.1	.02
10	-.1	.1	.04	.0	.1	.05
11	-.1	.1	.01	.0	.1	.01

Table II.4.2.3-2. Action-kick sensitivity to body harmonics in one D1 magnet at collision in the absence of error compensation. The second column records the value of the maximum horizontal or vertical action kick |ΔJ/J| produced when 1 unit of error (b_n/a_n) of multipole order *n* at a reference radius of 25 mm acts on a particle of 8σ amplitude ($\beta^* = 0.5$ m and $\Phi = 200$ μr).

Multipole	$\lvert\Delta J/J\rvert$ ($\times 10^{-3}$)
b_2/a_2	4.08
b_3/a_3	2.48
b_4/a_4	1.51
b_5/a_5	.93
b_6/a_6	.57
b_7/a_7	.35
b_8/a_8	.21
b_9/a_9	.13
b_{10}/a_{10}	.08
b_{11}/a_{11}	.05

II.4.3.1 Correction and compensation schemes

Applying the D1 expected body harmonics from Table II.4.2.3-1, it is found that the condition of Equation 1 can not be satisfied even when only with the systematic body sextupole is present, without error compensation or correction. The possible compensation schemes are similar to those discussed for HGQ magnets. Strictly speaking, the D1 and HGQ field quality issues are not separable, since it is the integrated performance of both D1 and inner triplet magnets that is a concern.

II.4.3.1.1.1 lead-end orientation

Orient the D1 dipoles so that the lead end faces away from the IP, as shown in Fig. II.4.2.2-1. Such an arrangement minimizes the effect of the lead-end systematic errors.

II.4.3.1.1.2 body-end compensation

Adjust the design value of the body b_3 to compensate for the end errors (Table II.4.2.3-1) across each D1 according to the amplitude-weighted expression

$$b_{3B} = -0.095 \quad B_{3L} - 0.116 \quad B_{3R} = -2.8 \,\text{(unit)}. \qquad (5)$$

This choice of body b_3 is optimized for low β^* operation, but is not sensitive to the exact value. Note the strong influence of the lead end sextupole harmonic.

II.4.3.1.1.3 tuning shims

Tuning shims may be used to provide individual magnet correction after a D1 magnet is constructed and measured, if provision is made in the D1 magnet design. The desirability of D1 tuning shims will be explored jointly by magnet builders and accelerator physicists, using simulation software to determine the multipole candidates for optimization. Just as in the HGQ case, tuning shim correction is most effective when the measurement uncertainties are small, and if the harmonic variations with quench and thermal cycles are small.

II.4.3.1.1.4 local correctors

Since the betatron phase advance between the inner triplet and the nearby D1 is negligibly small at low-β^* IPs, the same local correctors for the inner triplets (shown in Fig. II.4.2.2-1) can also be employed to compensate for D1 field errors. In this case, however, appropriate corrector layers need to be present to respond to a different set of dominant allowed harmonics.

II.4.3.2 Summary of future work

Efforts will be made to evaluate the impact of D1 dipoles, warm and cold. Improved reference harmonics will be established both for the warm D1 beam splitting dipoles being built by CERN, and also for the superconducting D1 magnets to be installed at IR2 and IR8. The effects of multipole feed-down due to non-zero crossing-angle and due to beam splitting will be studied and incorporated in standard LHC analyses.

The effectiveness of local and non-local correctors will be studied, at injection and at collision energies. In conjunction with HGQ work, an optimum integrated correction strategy will be incorporated into the design of IR triplet corrector packages. This strategy will be continuously re-assessed as improved knowledge of the realistic performance of D1 dipoles becomes available.

II.4.3.3 RF section magnets

Only the HGQ and the D1 magnets will experience the rigors of very large β values. Nonetheless, field quality and alignment assurance also needs to be applied to the other magnets that are to be built by the US-LHC collaboration. This list currently includes D3A, D3B, D4A, and D4B dipoles for the RF straight section at IR4. The same computer software and analysis methods are employed to study the performance of all of these magnets. Reference harmonics will be developed and maintained for all these magnet types.

While the field and alignment quality issues in these magnets are not so stringent as in HGQ and D1 magnets, there are additional issues that need special attention. For example, cross talk and magnet saturation between the two bores in the common yoke D3 and D4 dipoles with different separations will be studied.

Table II.4.3.3-1. Expected magnetic errors, version 1.0, for D3A, D3B, D4A, and D4B dipoles at IR4 at injection [100]. Units are 10^{-4} of the dipole field at a reference radius of 25 mm. Harmonics are numbered in the European convention *n* = 1 is dipole, et cetera. The mean systematic value is labeled by $\langle b_n \rangle$, the uncertainty in the systematic by $\Delta(b_n)$, and the standard deviation of the random error by $\sigma(b_n)$. Later versions of expected harmonics for these magnets will be split into 4 tables, since there are significant variations between them. See A. Jain, RHIC/AP/147, February 1998.

Order, n	*Normal*			*Skew*		
INTEGRAL [units]	$\langle b_n \rangle$	$\Delta(b_n)$	$\sigma(b_n)$	$\langle a_n \rangle$	$\Delta(a_n)$	$\sigma(a_n)$
D3A and D3B						
2	.1	.8	.28	-.1	3.7	1.53
3	-11.3	5.5	1.95	-1.1	.5	.17
4	-.1	.2	.08	.1	1.2	.42
5	.6	.8	.40	.2	.2	.06
6	.0	.1	.03	.0	.5	.15
7	-.3	.2	.10	-.1	.1	.02
8	.0	.1	.01	.0	.2	.05
9	.1	.1	.04	.0	.1	.01
10	.0	.1	.02	.0	.1	.02
11	-.7	.1	.02	.0	.1	.01
D4A and D4B						
2	.1	.8	.28	-.1	3.7	1.53
3	-9.9	5.5	1.95	-1.1	.5	.17
4	-.1	.2	.08	.1	1.2	.42
5	.6	.8	.40	.2	.2	.06
6	.0	.1	.03	.0	.5	.15
7	-.3	.2	.10	-.1	.1	.02
8	.0	.1	.01	.0	.2	.05
9	.1	.1	.04	.0	.1	.01
10	.0	.1	.02	.0	.1	.02
11	-.7	.1	.02	0	.1	.01

{{{ADD D3/4 REFERENCE HARMONIC TABLE HERE}}

Table II.4.3.3-2. Action-kick sensitivity to body harmonics for RF region D3 dipoles, at injection. The second column records the value of: $|\Delta J_{x,y}/J_{x,y}|$ produced when 1 unit of error (b_n/a_n) of multipole order *n* at a reference radius of 25 mm in a single D3A + D3B magnet pair acts on a particle of 11σ amplitude.

Multipole	$|\Delta J/J|$ ($\times 10^{-3}$)
b_2/a_2	.350
b_3/a_3	.170
b_4/a_4	.090
b_5/a_5	.040
b_6/a_6	.020
b_7/a_7	.010
b_8/a_8	.005
b_9/a_9	.003
b_{10}/a_{10}	.001
b_{11}/a_{11}	.001

Table II.4.3.3-3. Action-kick sensitivity to body harmonics for RF region D4 dipoles, at injection. The second column records the value of: $|\Delta J_{x,y}/J_{x,y}|$ produced when 1 unit of error (b_n/a_n) of multipole order *n* at a reference radius of 25 mm in a single D4A + D4B magnet pair acts on a particle of 11σ amplitude.

Multipole	$|\Delta J/J|$ ($\times 10^{-3}$)
b_2/a_2	.220
b_3/a_3	.089
b_4/a_4	.035
b_5/a_5	.014
b_6/a_6	.006
b_7/a_7	.002
b_8/a_8	.001

II.4.3.4 Summary of future work

Individual reference harmonic tables will be generated and evaluated for each of the four RF dipole magnet styles. The impact of persistent current sextupole b_3 harmonics in dipoles like the RF section dipoles will be studied, including the time dependence of coil generated b_3, partial compensation by geometric b_3, and the effectiveness of global sextupole correction.

II.4.4 Alignment

II.4.4.1 Alignment requirements

The HGQ magnets, correctors, and Beam Position Monitors (BPMs) in the inner triplets must be carefully aligned relative to each other, and relative to the outside world, to avoid degradation of the desired accelerator performance [101]. Magnet misalignments (low-β quadrupoles and correctors) irrevocably affect the beam. In contrast, BPM misalignments are easily removed in accelerator controls software, so long as they are accurately measured and recorded. The sizes of typical HGQ and corrector misalignments are approximately identical, while the HGQs are much stronger than the correctors. Thus, most of the accelerator physics issues arise from HGQ misalignments.

Transverse misalignments of HGQ magnets primarily affect the closed orbit, while roll misalignments primarily affect the linear coupling between horizontal and vertical motion. Pitch and yaw rotation errors and longitudinal translation errors are relatively unimportant. In calculating the strengths of closed orbit and linear coupling distortions an HGQ magnet is often well parameterized by its integrated magnetic field strength. Similarly, it is often sufficient to consider the integrated values of the transverse field displacement and the field roll angle, including the effects of the magnet ends.

Sometimes, however, it is necessary to pay attention to the variation of the field displacement and the field roll angle along the considerable length of these magnets. To fully characterize a magnet it is therefore necessary to measure the center of the magnetic field in the transverse x, y plane and the roll angle ϕ at many places along its length. Transverse misalignment and roll measurements are usually made relative to surveying fiducials attached to the cold mass. During magnet assembly these cold mass fiducials are related to externally available cryostat fiducials. Care must also be taken at this point to minimize the relative misalignments between magnets and correctors. Cryostat fiducials are used during tunnel installation to place the cryostat in the optimum location in the global coordinate system.

The strengths of dipole and skew quadrupole correctors must be carefully adjusted to compensate for the closed orbit distortions and linear coupling which are caused by transverse misalignments and rolls of inner triplet quadrupoles. In contrast, the feed down distortions caused by corrector misalignments are only second order in the main magnet strength, and so are relatively easy to correct by minor adjustment of the strengths of the nonlinear correctors themselves.

Extensive studies have already been performed on the effect of transverse misalignments of low-β quadrupoles on accelerator performance [102]. For example it has been shown that a 1mm offset of the inner triplet cryostats on both sides of an IP results in a vertex displaced by 0.6 mm, and exterior closed orbit distortions of approximately one beam sigma. Similarly, relative misalignments of 0.35 mm amongst HGQ magnets inside the inner triplets correspond to saturation of the dipole corrector, but introduce essentially no change in the value of the dynamic aperture. Short term displacements which cannot be corrected (vibrations) should be limited to a few μm for a single quadrupole to ensure no more than 10% degradation of the luminosity. Common mode vibrations of the entire inner triplet should be limited to a few tenth of one micron, in order not to perturb the closed orbit by more than one beam sigma.

II.4.4.2 Operational realignment and cold mass sensors

Since the alignment tolerances are quite tight it has been proposed that a movable support system be used to make it possible to re-adjust individual quadrupole positions, thus eliminating undesired orbit perturbations at their source [102]. Beam based alignment monitoring, as well as any initial beam based alignment procedure, rely strongly on the accuracy of the beam based monitors [103]. In this context an external reference system would be very useful to give additional redundant information about the position of the quadrupoles. The CERN survey group has proposed using a wire based monitoring system that would provide such information [104]. Occasional re-adjustment of the inner triplet cryostats will also be made easier by the presence of cold mass sensors, which will provide information about where the cold mass is relative to the cryostat fiducials.

The relationship between cold mass fiducials and cryostsat fiducials changes from that observed during bench measurement as the triplet is cooled down. Worse, these movements may not be the same on two subsequent cool-downs, or after a quench [105]. The relationship between cold mass and cryostat fiducials may also change during shipping from the US to CERN, or during local transportation. Fortunately it appears possible to avoid these ambiguities by monitoring the movement of the HGQ cold mass relative to the cryostat using a system of capacitative cold mass sensors [105].

II.4.4.3 Summary of future work

The impact of misalignments of HGQ, D1, and other magnets within the scope of the US-LHC program will be continually assessed during magnet design and production using analysis and tracking codes like TEAPOT. Non rigid body deviations including magnet twist and pitch will be evaluated using modeling techniques including machine file manipulation. The effects of corrector misalignment and the corresponding feed down harmonics will be studied. The potential performance of plausible cold mass sensor designs will be evaluated.

II.4.5 Quality review of production magnets

The quench performance, the field quality, and the alignment of the production magnets built at FNAL and at BNL will be jointly monitored and routinely reviewed by the magnet builders, surveyors, and the accelerator physicists. The review process includes:

II.4.5.1.1 SYBASE documentation of individual measurement data

Measurement data include information such as the minimum and plateau quench currents for each magnet, warm and cold integral transfer functions, field angles, harmonics, magnetic center offsets, and field roll misalignments. These data will be stored in one or more SYBASE databases at FNAL and at BNL. Other commercial database platforms may also be used. The measurement data will be freely accessible to all interested parties at CERN and US laboratories.

II.4.5.1.2 quench performance and field quality

Production line measurement data that is incrementally added to the databases at FNAL and BNL will be jointly and promptly reviewed by magnet builders and accelerator physicists, using software similar to that used for the RHIC Magnet Acceptance Committee [106, 107]. Statistical trends will be monitored and analyzed. Individual magnet data will be compared with expected harmonics and with the statistics of the previously built population. Possible production flaws and problems will be identified.

II.4.5.1.3 alignment-based sorting

Magnet cold masses will be selected and matched in order to minimize the relative magnetic center offsets and roll angles in their common cryostats, based upon measured transverse offsets and integral field angles. Individual cold masses will be assembled into cryostats while correcting the average offset and roll angle using SYBASE documented data. The amount of correction will be specified by accelerator physicists and recorded in a database.

II.4.5.1.4 review of assembly alignment

Magnetic center offsets and roll angles will again be measured and recorded into a database after each individual cold mass is assembled into a cryostat. Using software similar to that used for RHIC magnet review and acceptance, the measurement data documented in databases at FNAL and BNL will be jointly and promptly reviewed by magnet builders and accelerators physicists [107]. Trends will be analyzed and monitored, and individual magnet data will be compared with the statistics of the previously built population to identify possible production flaws and problems.

II.4.5.1.5 feedback during (early) production

If undesirable trends or individual problems are noticed in production, it may be possible to invoke magnetic design iterations or production and assembly alignment modifications to improve later magnets. It is often possible to do this without interrupting the production line [106, 107]. Design iterations will be jointly discussed, with every effort made to improve the final quality of the product while minimizing the impact on the production line schedule, and costs.

II.4.5.2 Field quality and alignment review dataflow

The first parts of Table II.4.5.2-1 list the database structures necessary for recording the field quality and quench performance data (MAGLHC) and also alignment data (SURVLHC). The second part lists production line analysis software needed for monitoring field (maganal) and alignment (survanal) quality. Full fledged simulation tracking codes will also be used to assess the overall impact of magnetic and misalignment errors. In order for such tracking codes to be as realistic as possible, the LHC model will be prepared by simulating the actual IR compensation schemes, using “IR filters”. Measurements of the magnetic field centers, and roll angles relative to cryostat fiducials, are recorded in the database table CENTERS. This information will be used for later tunnel installation at CERN.

Table II.4.5.2-1. Summary of IR production magnet database structures and analysis software for field and alignment quality review and ring installation.

Databases/tables:	
MAGLHC	Database structure to record magnetic measurement data
SURVLHC	Database structure to record survey and alignment data
CENTERS	Table structure containing instructions for ring installation
Analysis software:	
Maganal	Analysis of measurement data - Integral Transfer Function, Integral Field Angle, harmonics, et cetera. This includes population statistics, trends, and 2σ and preset limit flags.
Survanal	Analysis of alignment data - center offset, roll, et cetera. This includes statistics, trends, and 2σ and preset limit flags.
IR Filters	Tuning shims, local corrector settings, crossing angle (simulating measurement errors and shimming optimization, set corrector strength within preset limits, et cetera.)

II.4.6 Beam induced energy deposition

The LHC is designed to produce p-p collisions at $\sqrt{s}$ =14 TeV and $L=10^{34}cm^{-2}s^{-1}$. With a total cross section of 106 mb, these parameters give rise to 1190 W of power in collision products leaving an IP in each direction. Calculations with the DPMJET event generator and the MARS hadronic and electromagnetic shower code show that elastically scattered protons carry off 290 W into the multi-turn beam halo [108, 109]. With σ_{in}=80 mb, the inelastic interaction rate of $8 \times 10^8 s^{-1}$ represents a power of 900 W per beam leaving an IP in each direction.

The calculated collision power *P* deposited in inner triplet components on either side of a high-luminosity interaction point depends on the component and on the beam crossing parameters:

- *P*=250-320 W – in the TAS front absorber 19 m from the IP. The exact value depends on the TAS inner aperture, outer radius, configuration, and material. For copper absorbers with a inner aperture of 17 mm and an outer radius of 0.25 m the power is *P*=270 W.

- *P*=150-200 W – in the low-β quadrupoles (including internal absorbers). For each inner triplet with 70 mm aperture HGQ magnets and internal absorbers, TAS aperture 17 mm, and a half crossing angle of 150 μrad in a 45° crossing plane, the power is *P*=200 W.
- *P*=210 W – in the TAN neutral absorber 149.5 m from the IP, for the above case, deposited mainly by neutral hadrons and photons.
- the rest (about *P*=220 W) – in beam pipes inside and downstream of D1, such as the D2 separation dipole, Q4 and other components in the dispersion suppressor region, and farther from the IP, deposited by energetic protons and the products of their interactions.

Preliminary studies at CERN and Fermilab identified this as a potentially serious problem, especially with the indicated amount of power deposited in the superconducting components of the low-β insertions [110, 111, 112, 113, 114]. The quadrupole fields sweep secondary particles into the coils preferentially along the vertical and horizontal planes, giving rise to a local peak power density *P(max)* about 4 times larger than the average and as much as an order of magnitude larger than the azimuthal minimum. The estimated quench limits for LHC magnets are 0.7-1.2 mW/g, defined as the longitudinal and azimuthal peak power density averaged radially over the first superconducting cable. From this one derives *P(max)* ≤0.4 mW/g as a design goal. Energy deposition calculations show that without protection *P(max)* could easily exceed 0.4 mW/g and prevent the low-β quadrupoles from reaching their required gradient. Tests of porous cable insulation systems and calculations concerning the insulation system to be used in the HGQ magnets have shown that up to about 1 mW/g of heat can be removed while keeping the coil below the magnet quench temperature, partially mitigating the problem [115, 116]. Statistical errors on the Monte Carlo calculation are estimated to be ±15% for *P(max)*, based on comparison of results from different runs with independent random seeds.

Energy deposition studies concentrate on beam-induced effects in the IR1 and IR5 interaction regions, due to both pp-collisions at $\sqrt{s}$ =14 TeV and radiation coming towards an IP from beam loss in the IP vicinity [117]. Full scale simulations have been used to optimize the TAS front absorber, the inner triplet absorbers, and the TAN neutral beam absorber, as well as to study accelerator related backgrounds in the CMS and ATLAS detectors. Simulation results depend on the optical layout in general, and the inner triplet configuration in particular.

II.4.6.1 Inner triplet configuration

Fig. II.4.6.1-1 shows the inner triplet configuration in version 5.0 optics, including the positions and apertures of each magnet as well as internal absorbers that define the limiting aperture [113]. Fig. II.4.6.1-1 also indicates the minimum mechanical half aperture, accounting for all the various errors considered in reference [83]. Each internal absorber has an inner radius at this limit, and has an outer radius 2 mm less than the coil radius.

{{{FIGURE 2 GOES HERE. Nikolai Mokhov says "get 'triplet5.eps' file from Jim Strait".}}}

Fig. II.4.6.1-1. The LHC low β* insertions (version 5.0) including internal absorbers. The solid (dashed) line is the approximate allowed beam envelope for injection (collision) optics, including closed orbit and mechanical tolerances.

Version 5.0 of the LHC optics eliminated trim quadrupoles in the inner triplet, lengthened Q1 and Q3 to 6.3 m, decreased the HGQ gradients to 200 T/m, and increased the separation between D1 and D2 to allow the use of lower field or shorter dipoles. At the high luminosity IRs (IR1 and IR5) D1 is now a conventional warm magnet. Under injection optics β* = 12 m, but might be increased further.

To understand the impact of these changes on the energy deposition and to guide future work, the dependence of *P(max)* on internal absorber thickness has been studied. The optimal internal absorber apertures tend to increase in going from version 4.2 to version 5.0 optics, mainly due to the larger crossing angle. The distance of the triplet from the interaction point is the same and the overall length of the triplet is only slightly greater in version 5.0 than in version 4.2 (30.6 m versus 29.6 m). Thus, the relation between power density and absorber thickness is the same for the two configurations, within calculation uncertainties. The final optimization of absorbers consistent with these lattice parameters is the subject of on-going studies [118, 119].

II.4.6.2 The energy deposition model

All the details of the CMS and ATLAS detector near beam components, the layouts of the high-luminosity insertions at IR1 and IR5, the dispersion suppressors, and nearby arc half-cells which might affect both luminosity and beam loss induced energy deposition in the IR components, are taken into account. Three-dimensional geometries and material descriptions of the lattice and tunnel components are used. This includes a 0.4 m horizontal shift of the beam line with respect to the tunnel axis, a floor level 0.95 m beneath the magnet string, the TAS front absorber, and a proposed flared beam pipe between the D1 dipole and the TAN neutral beam absorber. The solenoid field in the collider detectors is included in the simulations, as well as POISSON derived 2-D magnetic fields in the full cross-sections of the HGQ magnets, the separation dipoles (D1 and D2), the arc dipoles, and the arc quadrupoles. Shower and muon transport simulations are performed for a clockwise beam in one octant of the LHC lattice adjacent to the IR including the tunnel components and surrounding rock (molasse), with a density of $\rho=2.24$ g/cm^3.

Proton-proton collisions and showers in the IR components are simulated with the DPMJET event generator and the MARS code, respectively [108, 109]. Charged particles are tracked through the lattice and the fields within each magnetic element, their cryostats, tunnel equipment, shielding, detector components and surrounding rock. The cut-off energies are 1 MeV (charged hadrons and muons), 0.2 MeV (photons and electrons) and 0.5 eV (neutrons). Magnet coils are modeled with 4 radial bins of 8.5 mm depth, with azimuthal bins ranging from 5° wide at the horizontal and vertical planes to 15° in between, and with axial bins ranging between 0.5 m and 3 m long. The magnet coils, which are a mixture of NbTi, copper, insulation and helium, are simulated as a homogeneous material with A=50, Z=23 and ρ=7 g/cm^3. Details such as cooling channels in the yoke and coil ends are not included.

II.4.6.3 Front absorbers, TAS

The TAS external front absorbers are located in front of the Q1 quadrupoles, ±19 m from the interaction points at IP1 and IP5. They protect the inner triplet quadrupoles against intense particle fluxes from the IP. The TAS aperture should be at least 10σ, where σ is the RMS beam size. In early studies the aperture radius was assumed to be 14 to 14.5 mm, but recently a more desirable nominal aperture of 17 mm has been established.

The TAS absorber is made of a copper core 1.8 m long and about 0.25 m in radius, surrounded with massive steel and concrete shielding. An albedo trap is used to minimize the background rates in the CMS and ATLAS detectors, to avoid groundwater activation, and to reduce residual dose rates in the TAS vicinity to acceptable levels. The power deposited in a copper absorber with aperture 17 mm and outer radius 0.25 m by showers induced by particles from the collision point is P=270 W. Table II.4.6.3-1 shows the calculated mean number of particles emitted from the collision point, their mean energy, and the total energy deposited, in the assumption of an open aperture upstream TAS. It shows that most of the total power dissipation in TAS is due to charged pions and photons. The total power dissipation is shown as a function of the front absorber radius and length in Fig. II.4.6.3-1 and Fig. II.4.6.3-3.

Table II.4.6.3-1. The mean number, mean energy, and total energy of particles per proton-proton interaction striking the TAS front absorber (R_{in}=17 mm and R_{out}=0.25 m).

Particle Type	*<n>*	*<E> (GeV)*	*<n><E> (GeV)*
Neutral hadrons	.58	261	152
Protons	.29	292	83
Charged pions	6.80	159	1081
Photons	8.33	87	725
Muons	.06	33	2

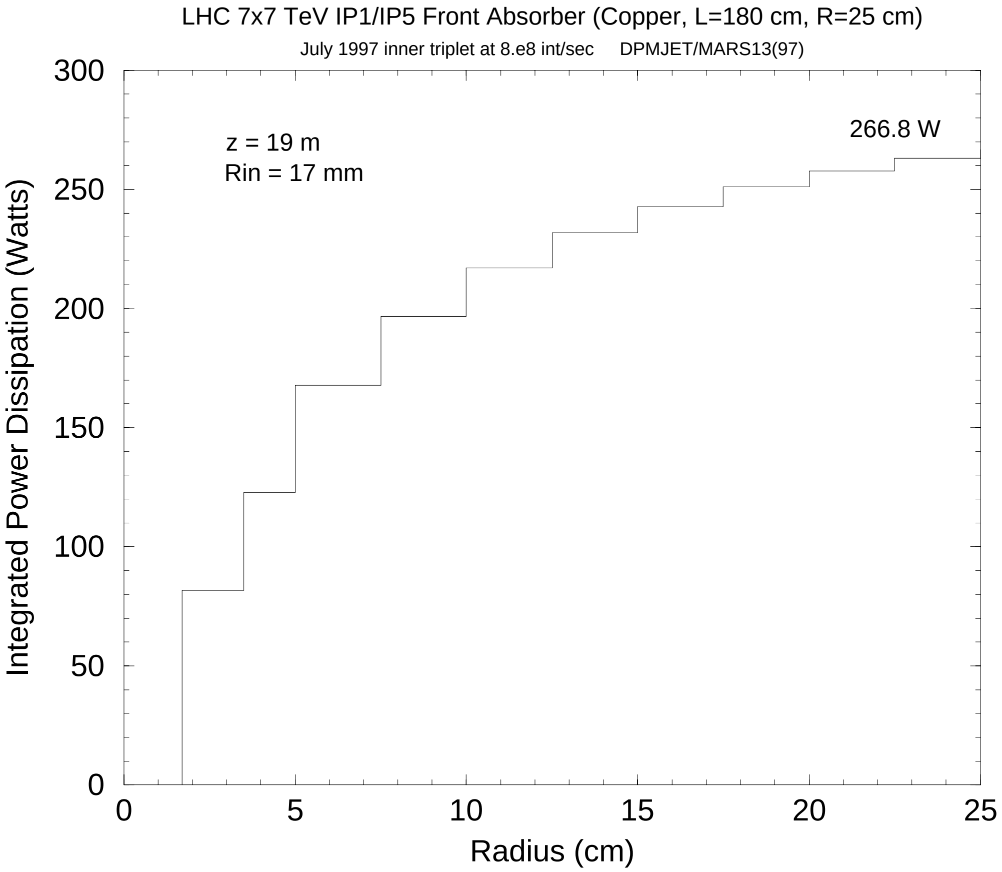

Fig. II.4.6.3-1. The longitudinally integrated total power dissipation in the TAS front absorber, versus its radius.

Fig. II.4.6.3-3. The longitudinally integrated total power dissipation in the TAS front absorber, versus its length.

Longitudinal distributions of TAS power density show that the peak power density is about 10 mW/g at an absorber depth of about 0.15 m. It decreases to 0.2 mW/g at a depth of 1.8 m, a factor of two below the design limit in the Q1 quadrupole immediately downstream of TAS. The TAS dose rate levels after 30 days of irradiation at the design luminosity followed by 1 day of “cooling” are much higher than both the emergency (1-2 mSv/hr) and routine (0.1 mSv/hr) human access limits. Thus, TAS requires massive external shielding and remote handling.

II.4.6.4 Internal absorbers

Stainless steel internal absorbers are to be placed within the HGQ magnet bores to minimize the energy deposition in the coils. Apertures of 8σ and 10σ were studied for the nominal 35 mm coil radius, to evaluate the effectiveness of the internal absorber [114, 114]. With no internal absorber (not even a beam pipe) *P(max)* = 1.2±0.2 mW/g, at or above the allowable limit. With individually sized 10σ absorbers the peak is a factor of

3 smaller, giving a reasonable safety margin. The use of 8σ absorbers reduces *P(max)* in Q1, but there is little overall improvement. Increasing the inner aperture of the absorbers in Q1 to match those in the other quadrupoles results in a 25% increase in *P(max)*. However, this increase may not be statistically significant and further study is required to determine if it is necessary to use different absorbers in the Q1 and Q1-Q2 regions than in the rest of the triplet.

An unacceptably large *P(max)* is observed at the downstream end of a superconducting D1 even with a 10σ absorber. This problem is eliminated in version 5.0 optics by making D1 a conventional warm magnet at IR1 and IR5 (but not at IR2 and IR8). Since the integrated strength of the warm D1 is lower, the outer D2 dipole is moved an additional 90 m farther from the IP at IR1 and IR5. D2 remains superconducting at all locations.

Studies with a TAS front absorber aperture of inner radius 17 mm show that the total power deposited in the inner triplet components on either side of an IP is about 200 W [118, 119]. Up to half of this power is deposited in the internal absorbers, and it is tempting to consider cooling them at a higher temperature than the beam pipe. However, the insulating space required between the absorber and the vacuum pipe would reduce the absorber thickness, making this option impractical. Averaged over each element, the power density varies from 3 to 12 W/m. However, the variation within one magnet can be as large as a factor of 8.

An inner absorber configuration has been designed which keeps *P(max)* below the design limit of 0.4 mW/g in version 5.0 optics, even with the enlarged aperture of the TAS front absorber. Its layout has the following sequence. A uniform beam pipe 3 mm thick is inserted between TAS and Q1. An internal absorber in Q1 occupies the radial region $23.5<r<33$ mm. A 1.5 m long supplementary beam absorber begins 0.25 m downstream of Q1 ($25<r<60$ mm). A second 1.5 m long supplementary beam absorber is placed upstream of Q3 ($30<r<60$ mm). Lastly, a uniform beam pipe 3 mm thick ($30<r<33$ mm) is inserted between Q2 and Q4, and between the second supplementary beam absorber and D1.

II.4.6.5 Neutral beam absorbers, TAN

The TAN neutral beam absorbers are located between the separation dipoles D1 and D2, 149.5 m from the interaction points at IP1 and IP5. The absorber has twin apertures in a copper core 3 m long and about 0.15 m in radius surrounded by steel shielding up to a radius of 0.55 m. A power of P=210 W is deposited in the central part with $r<0.20$ m by showers induced mainly by neutral hadrons and photons. This takes into account particle interactions and showering in all the preceding components through the entire 149.5 m region. Table II.4.6.5-1 shows the calculated mean number of particles emitted from the collision point, their mean energy, and the total energy deposited in TAN per proton-proton interaction. It shows that neutral hadrons – principally neutrons and some K_L – and photons contribute most of the total power. The total power dissipation is shown as a function of the neutral absorber radius and length in Fig. II.4.6.5-1 and Fig. II.4.6.5-3.

Table II.4.6.5-1. The mean number, mean energy, and total energy of particles per proton-proton interaction striking the TAN neutral beam absorber.

Particle type	*<n>*	*<E> (GeV)*	*<n><E> (GeV)*
Neutral hadrons	.33	2185	725
Protons	.06	1215	73
Charged pions	.71	125	88
Photons	150.80	5	736
Electron/positron	12.50	1	8
Muons	.01	25	.4

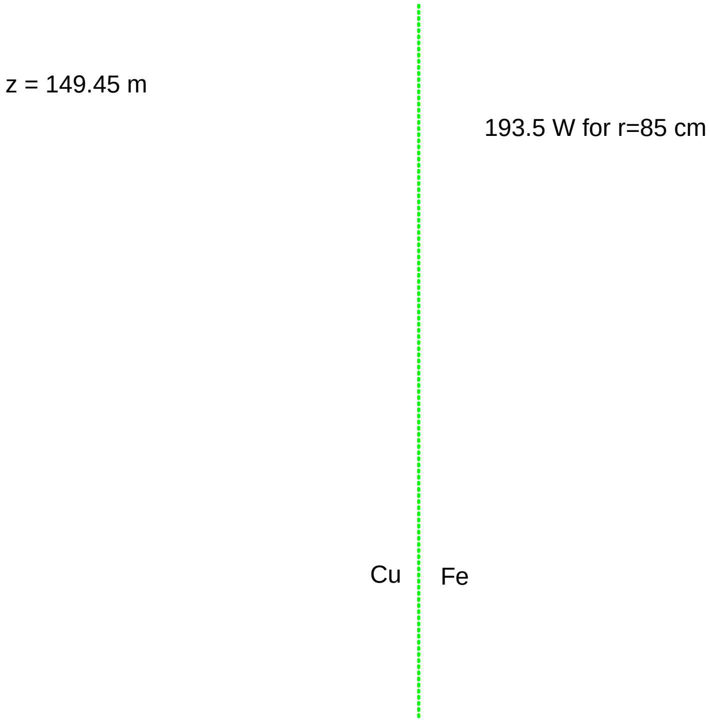

Fig. II.4.6.5-1. The longitudinally integrated total power dissipation in the TAN neutral absorber, versus its radius.

Fig. II.4.6.5-3. The longitudinally integrated total power dissipation in the TAN neutral absorber, versus its length.

Longitudinal distributions of the TAN power density show that the peak power density is about 5 mW/g at an absorber depth of about 0.25 m. It decreases to 10^{-3} mW/g at the far end, well below the quench limit in the D2 dipole and the Q4 quadrupole downstream of TAN. The dose rate levels after 30 days of irradiation at the design luminosity followed by 1 day of “cooling” are about 0.4 mSv/hr, at a radius of about 0.55 m on the back surface. This is below the emergency human access limit. Lengthening the TAN core by 0.4 m would reduce the dose rate to 0.1 mSv/hr.

II.4.6.6 Summary of future work

If the optics and configuration of the lattice changes significantly, the energy deposition analysis will be redone to ensure that the absorber design is still valid, and that the power deposition in the accelerator structure is within acceptable limits.

II.4.7 Neutral absorber ionization chamber

The TAN neutral beam absorber can be instrumented to measure the neutral particle flux. This enables it to be used as a luminosity monitor, and as a diagnostic for low frequency closed orbit correction feedback.

At a design luminosity of 10^{34} cm^{-2}sec^{-1} there are approximately 10^9 collisions per second at the high luminosity interaction points IP1 and IP5. These interactions give rise to about 1.2 kW of power in collision products leaving an IP in each direction. Some of this power is carried off by small angle elastic and diffraction scattering of the primary protons, and stays inside the beam tube until leaving the interaction regions. However, a significant fraction of the power is carried off by neutral particles leaving the beam tube in the interaction region. The inelastic collision power carried off by neutrals is estimated to be 330 W leaving an IP in each direction. These particles are not deflected by the magnetic field of the separation dipoles or of the inner triplet quadrupoles. Because of the high incident flux of neutral collision products near zero degrees, it is natural to locate a radiation hard ionization detector in the TAN neutral beam absorber downstream of the D1 beam splitting dipole.

A preliminary physics analysis of such a detector has been made. A flux of approximately 9 neutral hadrons (mostly neutrons) per bunch crossing is estimated to be incident on each absorber, with a mean energy 2.3 TeV. In addition there are approximately 35 photons with a mean energy 0.63 TeV [112]. On axis ionization detectors of the shower products can be used to infer at least three things from these energetic particles:

(1) the luminosity,

(2) the beam-beam separation at the IP, and

(3) the transverse beam shape and size.

The signal from the detector can be also used to regulate to a negligible level (through feedback) the beam-beam closed orbit drift at the IP, due to ground motion or other slow effects [120]. The behavior of the signal at large beam-beam separation or with only a single circulating beam can also be used to estimate the non-IP background due to beam-gas and beam halo-wall collisions. The methods that are proposed for analysis are similar to those previously used for luminosity by van der Meer [121] and considered for beam-beam centering by Jostlein [122].

II.4.7.1 Measurement performance

Consider round Gaussian beams at the IP, with an RMS beam size of $\sigma^* = 15.9\ \mu$m in each transverse direction, and with beam centers separated by a transverse displacement of $\vec{D} = D_x\hat{e}_x + D_y\hat{e}_y$. Suppose that the transverse displacement is the sum of an intentional time dependent displacement ($\vec{d}(t) = d\cos(\omega t)\hat{e}_x + d\sin(\omega t)\hat{e}_y$) produced by horizontal and vertical dipole correctors, and a quasi-static steady-state error

($\vec{\varepsilon} = \varepsilon\cos(\varphi)\hat{e}_x + \varepsilon\sin(\varphi)\hat{e}_y$). Assuming that the error and the intentional displacements are small compared to σ* the luminosity becomes

$$L = L_0\left(1 - \frac{\varepsilon^2 + d^2}{4\sigma_*^2}\right) - L_0\,\frac{\varepsilon d}{2\sigma_*^2}\cos(\omega t - \varphi)\,. \tag{6}$$

The circular sweep $\vec{d}(t)$ introduces a sinusoidal luminosity modulation that vanishes when the error offset is reduced to zero. A detector signal proportional to *L* then has a quasi-dc component proportional to L_0 and a time varying component proportional to the scalar product of the error offset $\vec{\varepsilon}(t)$ and the time dependent displacement $\vec{d}(t)$. The time varying component is used to estimate the magnitude and phase of the error offset and is used in a feedback scheme to reduce it to zero. The integration time required to resolve the magnitude of the error offset in the presence of statistical fluctuations of the quasi-dc term is discussed below.

Additional information can be obtained once the error offset is reduced to a magnitude that is small compared to the RMS beam radius. The beam profile and the RMS beam size in the two transverse dimensions are measured by changing the sweep mode to linear scans in the x and y planes. The absolute measurement of luminosity can be calibrated two ways:

(1) against simultaneous ATLAS/CMS measurements of absolute luminosity, and

(2) measuring the beam size and the beam current, and using the usual formula

$$L_0 = \frac{1}{kf}\left(\frac{I}{e}\right)^2 \frac{1}{4\pi\sigma_*^2} \tag{7}$$

where *k* is the number of bunches in a beam, *f* is the revolution frequency, and *I* is the beam current. This equation is valid for round Gaussian beams. If the beam profiles found by scanning do not satisfy this assumption then it can be extended to treat the general case [123].

The current from an ionization detector in the neutral absorber is written as

$$\begin{aligned} I(t) &= e\sum_j \alpha_j \varepsilon_{\det,j} m_j N_p \\ &= e\sum_j \alpha_j \varepsilon_{\det,j} m_j \sigma_{inel} L \end{aligned} \tag{8}$$

where N_p is the rate of inelastic p-p interactions at the IP, m_j is the multiplicity of particles of type j falling within the acceptance of the detector per interaction, $\varepsilon_{det,j}$ is the detector efficiency, α_j is the detector gain, and σ_{inel} is the inelastic cross section. Integrating over time T readily gives expressions for the luminosity and luminosity error. It is assumed that T is either an integer multiple of the modulation period, or is very large compared to it.

$$L_0 = \frac{\int_0^T I(t)dt}{e\sum_j \alpha_j \varepsilon_{\det,j} m_j \sigma_{inel} T} \tag{9}$$

Similarly, when Equation 6 is multiplied by $\cos(\omega t)$ or $\sin(\omega t)$ and integrated one obtains estimates for the components of the displacement error.

$$\begin{aligned} \varepsilon_x &= \varepsilon\cos(\varphi) = \frac{-\int_0^T dt\cos(\omega t)I(t)}{\left(\frac{d}{4\sigma_*^2}\right)e\sum_j \alpha_j \varepsilon_{\det,j} m_j \sigma_{inel} L_0 T} \\ \varepsilon_y &= \varepsilon\sin(\varphi) = \frac{-\int_0^T dt\sin(\omega t)I(t)}{\left(\frac{d}{4\sigma_*^2}\right)e\sum_j \alpha_j \varepsilon_{\det,j} m_j \sigma_{inel} L_0 T} \end{aligned} \tag{10}$$

Expressions for the statistical measurement errors of L_0 and $\vec{\varepsilon}$ can be derived assuming Poisson counting statistics for N, α and m, and binomial statistics for ε_{det} [124]. It can be shown that the magnitude of the intentional sweep offset d which minimizes the integration time is equal to the allowable RMS measurement error σ_ε of the displacement ε established from considerations of allowable luminosity degradation.

Table II.4.7.1-1. Estimated integration time for the measurement of luminosity and beam-beam separation.

L	T ($\sigma_L/L = .01$)		T ($\sigma_\varepsilon = 0.1\sigma_*$)	
$cm^{-2}sec^{-1}$	*ms*	*turns*	*ms*	*turns*
10^{31}	54	610	860	9,700
10^{32}	5.4	61	86	970
10^{33}	.54	6.1	8.6	97
10^{34}	.054	.61	.86	9.7

Table II.4.7.1-1 shows the integration time required to achieve 1% statistical errors for measurements of the luminosity, or 10% accuracy of the beam-beam displacement in units of σ*, under different luminosity assumptions. At the highest luminosity it is necessary to integrate over approximately 0.61 turns (or 1730 bunch crossings) in order to achieve 1% luminosity accuracy, and 9.7 turns (27,500 bunch crossings) to achieve 10% displacement accuracy. The inelastic cross section is taken to be σ_{inel} = 80 mb and the statistical errors have been estimated assuming that only the hadron showers initiated by neutrons with energy between 0.2 TeV and 7 TeV contribute significantly to the detector signal. Contributions from other particle species will reduce the statistical errors somewhat. If the detector is placed 0.30 m behind the front face of the absorber, and the absorber material is copper with a hadronic interaction length 151 mm, then most (86%) of the incident hadrons will interact, and the detector is near the shower maximum.

II.4.7.2 An Argon ionization chamber

It is necessary to integrate over many bunch crossings in order to obtain reasonable statistical accuracy. A relatively slow detector that integrates over many bunch passages can therefore be considered. A parallel plate Argon ionization chamber at atmospheric pressure seems to be a good choice, since a simple design constructed for high reliability will not degrade with exposure to radiation. Argon has low recombination and is free of electrically induced chemical reactions. The incident radiation is normal to the plates of the ionization chamber and the electric field strength between plates is $E = V/a$, with V the applied voltage and a the separation between plates.

The main problems to avoid in the choice of operating parameters are gas multiplication and space charge saturation. Gas multiplication will not be a problem if the chamber is operated with an applied electric field of less than 0.15 kV/mm at atmospheric pressure. The criterion for avoiding space charge saturation is

$$a \le 2\left(\frac{V}{a}\right)\sqrt{\frac{\varepsilon_0 k^+}{\dot{q}}} \tag{11}$$

where k^+ = 1.7 cm^2/sec is the Argon ion mobility [124].

The ion production rate, expressed as the current per unit volume, is

$$\dot{q} = eF_{mip} N_{ion/mip} \tag{12}$$

where F_{mip} is the flux of ionizing particles (assumed to be minimum ionizing) and $N_{ion/mip}$ is the number of ion-electron pairs per unit length produced by an ionizing particle. The mean energy loss per ion pair is W_i = 26 eV and the minimum ionization energy loss is dE/dX_{Ar} = 1.52 MeV/gm/cm^2. For a pressure of 760 Torr at a temperature of 294 K the density of Argon is $\rho = 1.66\text{x}10^{-3}$ gm/cm^3. Thus, the number of ion pairs produced by a minimum ionizing particle is

$$\begin{aligned} N_{ion/mip} &= \frac{\rho_{Ar} \left.\frac{dE}{dX}\right|_{Ar}}{W_i} \\ &= 97 ion\, pairs/cm/mip \end{aligned} \quad . \tag{13}$$

The flux of minimum ionizing particles incident on the ionization chamber is

$$\begin{aligned} F_{mip} &= \frac{\left.\frac{dP}{dm}\right|_{Cu}}{\left.\frac{dE}{dX}\right|_{Cu}} \\ &= 2.2\times10^{10} / cm^2 \end{aligned} \tag{14}$$

where dP/dm_{Cu} = 5x10^{-3} W/gm is the maximum power deposited in the copper absorber per unit mass and dE/dX_{Cu} = 1.4MeV/gm/cm2 is the specific energy loss in copper.

Putting all this together, the maximum ion production is 0.35 µA/cm^3. Substituting this value into Equation 11 with an applied electric field of 0.1 kV/mm, the condition on gap length for avoiding space charge saturation becomes $a < 13.2$ mm.

Table II.4.7.2-1. Typical parameters for a Neutral Absorber Argon ionization chamber

Parameter	*Value*
Voltage, kV	0.3
Electrode gap, mm	3
Time resolution, ms/turns	180/2
Electrode area, cm^2	100
Current, µA @ L=10^{34} cm^{-2}sec^{-1}	1.1

Some typical physical parameters are summarized in Table II.4.7.2-1. The applied voltage is 0.3 kV and the electrode gap is 3 mm, chosen for convenience and to satisfy the gas multiplication and space charge constraints. The detector area is chosen to be 10 cm x 10 cm so the chamber fits in the copper septum between the two beam tubes. The total ionization current of 1.1 µA at design luminosity is estimated assuming the detector is placed at a depth of 0.30 m and integrates over the radial profile of the power density. The time resolution of approximately 180 ms (2 turns) is determined by the ion drift time across the electrode gap. At design luminosity the flux of energetic neutrons incident on the neutral absorber is 2.9x10^8/sec, and the ionization chamber current gain defined in Equation 8 is α =2.8x10^4.

II.4.7.3 Summary of future work

Future work on the ionization detectors will evaluate the magnitudes of background effects due to beam gas interactions and beam halo scraping. The effect of small variations of the beam crossing angle on the ionization chamber current will also be evaluated. In addition the following areas will be addressed:

(1) improved evaluation of the flux of ionizing hadronic shower particles crossing the ionization chamber

(2) inclusion of photon induced showers in the statistical analysis

(3) analysis of the time resolution needed for measurement of luminosity and beam-beam separation

(4) design of appropriate horizontal and vertical steering magnets and

(5) design of a prototype test in an extracted low intensity p beam.

II.4.8 Beam Physics Issues

Beam Physics Issues describes topics that invoke unique US capabilities to investigate areas of joint interest to current and future generations of superconducting hadron colliders at the US labs and at CERN. Although these topics are less directly related to physical deliverables, they are also important in optimizing LHC performance.

The first sub-section, *The electron cloud effect*, presents a simulation approach to an effect that may limit the performance of the LHC, and may also constrain RHIC and the Tevatron in plausible upgrade scenarios. *PACMAN closed orbit correction* proposes a bunch-by-bunch closed orbit correction scheme that would compensate for the atypical long-range beam-beam interactions encountered at the end of a bunch train. *Beam collimation* reports a preliminary analysis of the performance of the LHC beam cleaning system. *Software maintenance and development* describes the codes and environments used by accelerator physicists. It also addresses the effort to ensure smooth accelerator modeling data flow between the US labs and CERN. *Local chromaticity correction* looks at the possibility of local correction of the second order chromaticity generated by the low β^* interaction regions. Finally, *Ground motion and external noise* outlines a set of studies and experimental measurements that can be made to evaluate this problem for the LHC.

II.4.8.1 The electron cloud effect

It has become apparent that the new generation of e^+e^- "factories" faces a new kind of coupled-bunch effect called the electron-cloud instability (ECI) [125]. This instability affects only positively charged, high-current, multi-bunch beams. A closely related instability has long been observed and analyzed at the CESR collider [126]. This instability continues to be the object of intense theoretical and experimental studies [127, 128, 129]. It may also arise in the LHC [130].

The ECI is caused by the cloud of photoelectrons that are generated inside the vacuum chamber as an unavoidable consequence of the synchrotron radiation that accompanies the beam. This cloud couples the transverse motion of successive bunches, sometimes leading to a coupled-bunch instability. A proton traversing a single arc dipole in the LHC emits approximately 0.4 photons on average, whose spectrum has a critical energy of about 44 eV. There will therefore be a substantial number of photoelectrons in the vacuum chamber. In addition, secondary electron emission from the walls of the beam screen will contribute even more electrons to the cloud. The related phenomenon of beam-induced multipacting was first observed at the ISR, and may play a role in the ECI at the LHC [131]. Preliminary simulations show that the ECI has a growth time on the scale of about 100 msec at the top beam energy of 7 TeV [83]. Continuing studies of the electron-cloud effect in the LHC are developing further refinements of the calculation techniques used, and the physical model being simulated. The instability now appears to have slower growth times than earlier estimates suggested.

The
from the
so large
depositi
seconda
compute
beam-in
SEY=1.
vanishir
the valu
change
and inde
estimate

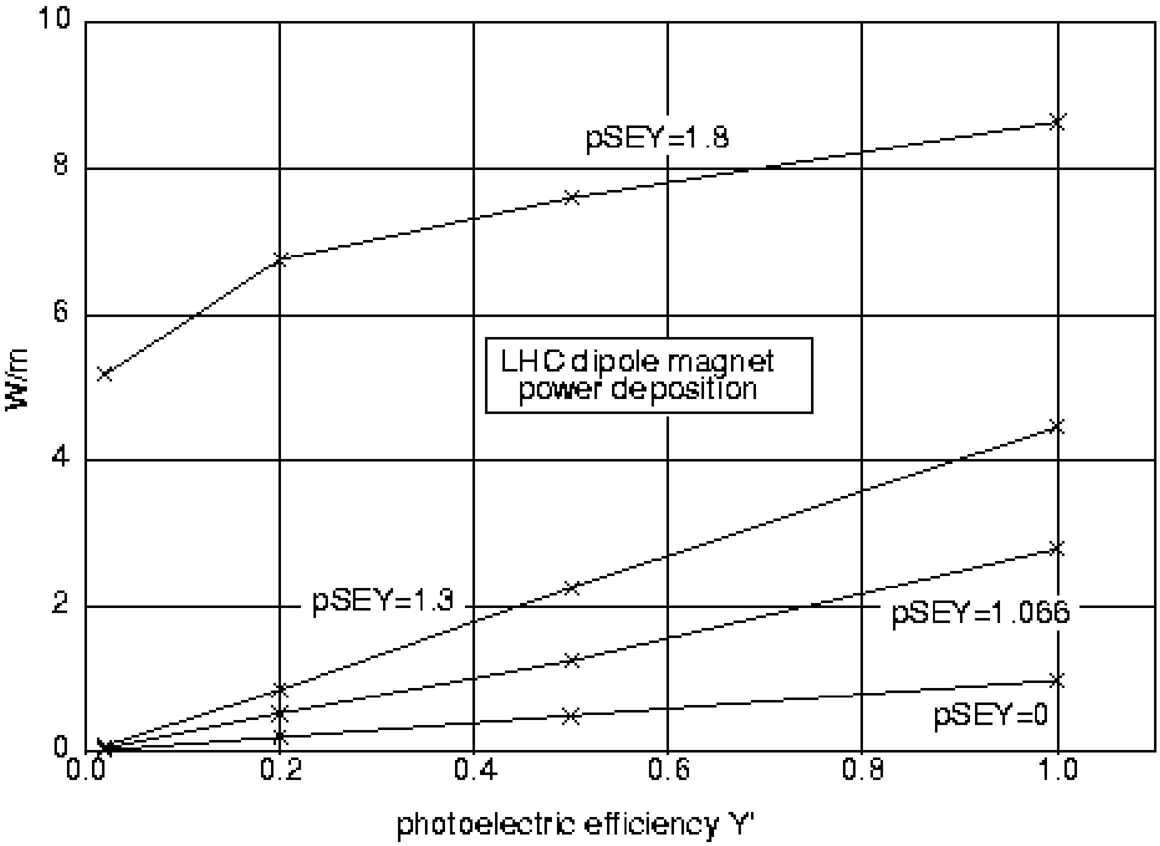

Fig. II.4.8.1-1. The average power deposition of the electron cloud upon bombarding the beam screen of an LHC arc dipole.

While these results are clearly of great concern, simulation details need to be refined and, more importantly, input parameters need to be sharpened before definitive conclusions can be reached. Theoretical issues that are currently being investigated include bunch length effects and image charges [133]. Preliminary indications are that lower estimates for the power deposition are obtained when these refinements are taken into account. However, these estimates are still much higher than the LHC heat-load specification [83].

A low rate of heat deposition requires low values of the secondary emission yield and the photoelectric quantum efficiency. The value of the photon reflectivity *R* also needs to be low. The vacuum chamber beam screen in the nominal design is made of stainless steel about 1 mm thick, coated by a 50 μm thick layer of roll-bonded copper. Current values with the roll-bonded copper layer are *Y'*~ 0.2 and *R* ~ 0.8, respectively, in the absence of a magnetic field [134]. The value of *R* could be lowered by roughening the surface of the copper layer, or by electro-depositing it. In this case, the reflectivity has been measured to be about 0.08 [134]. However, it is not yet clear what the SEY value SEY and *Y'* are in this case. Other ideas to lower *R* and *Y'* include making subtle changes to the beam screen, such as making tiny longitudinal grooves on the horizontal "edges" of the beam screen and/or affixing tiny, regularly-spaced irises. Obviously, all these ideas need to be assessed by simulations and experiments before proceeding.

The LHC accelerator physics group has launched an experimental program to determine the three main parameters of the beam screen relevant to the electron-cloud effect (*Y'*, *R*, and the SEY) with and without the presence of a magnetic field. A direct measurement of the SEY in the presence of a strong magnetic field, such as the 8.6 T field in the LHC dipoles, is practically impossible. An indirect approach is being attempted by the LHC group, based on a standing-wave tube with a coaxial cable.

II.4.8.1.1 Summary of future work

The following topics will be investigated by simulation:

(1) Explore heat deposition in parameter space, such as *Y'*, *R*, the SEY, bunch spacing, bunch current, et cetera.

(2) Quantify what can be gained from longitudinal grooves and/or irises.

(3) Evaluate the heat deposition in other regions of the ring.

(4) Incorporate the curvature of the trajectory, beam size variation, et cetera

(5) Evaluate the effects of natural beam divergence and the transverse bunch shape.

II.4.8.2 PACMAN closed orbit correction

The long-range beam-beam interactions that the beams experience as they approach each other on either side of an IP give each bunch a deflecting kick, which distorts the closed orbit. The average closed orbit distortion experienced by a nominal bunch is readily corrected using dipole correctors, to keep the beams in the middle of the vacuum chamber in the arcs, and in collision at the IP. The PACMAN effect results from bunches near the ends of a bunch train, which experience substantially fewer long-range beam-beam collisions than "nominal" bunches within a train. This causes the deflecting kick to vary on a bunch-by-bunch basis along the front and back of the bunch trains, resulting in different closed orbits for these PACMAN bunches. Since the deflecting kicks are almost equal and opposite on either side of the IP, the closed orbit offset effects are largest at other IPs and elsewhere in the lattice. PACMAN bunch separations as large as one sigma have been predicted to occur in the case of high-luminosity operations [135].

In addition to the linear closed orbit effect, PACMAN bunches also undergo anomalous tune shifts and spreads and nonlinear effects, which may cause them to suffer enhanced loss rates. The loss of one of these bunches will create more such bunches, in an ongoing zipper-like process which may eventually destroy the beam, and that explains the origin of the "PACMAN" label [136].

A bunch encounters the same counter circulating bunch (or gap) at two points separated by half the circumference. In principle it is possible to compensate for the PACMAN closed orbit and tune shift differences by arranging for cancellation between these two points, including an appropriate choice of phase advance between IPs. For example, partial closed orbit cancellation is achieved by arranging for the crossings planes near IP1 and IP5 to have a relative angle of 90° (assuming equal β^* values). There is an optimum phase difference that minimizes but does not completely cancel the orbit displacements at the IPs. PACMAN tune shift effects are also, in principle, completely eliminated by using crossing planes tilted by 90° relative to each other, independent of the phase advance between IPs.

In practice it is inconvenient to set additional optical constraints on the phase advance between IPs. Another way to correct for the bunch-by-bunch orbit offsets, and to avoid the substantial luminosity reduction that would result, is to use a high-frequency closed-orbit correction scheme.

II.4.8.2.1 Bunch by bunch closed orbit correction

Fig. II.4.8.2-1 shows the bunch train fill pattern in the LHC, which is determined by the rise times of various kickers in the machine and injection complex. Fig. II.4.8.2-3 shows the kick distribution along a bunch train that has been calculated for long-range collisions with this fill pattern [135]. It is the difference in orbits arising from these kicks which must be compensated at each IP in order to achieve the highest possible luminosities.

Fig. II.4.8.2-1. The nominal LHC bunch fill pattern.

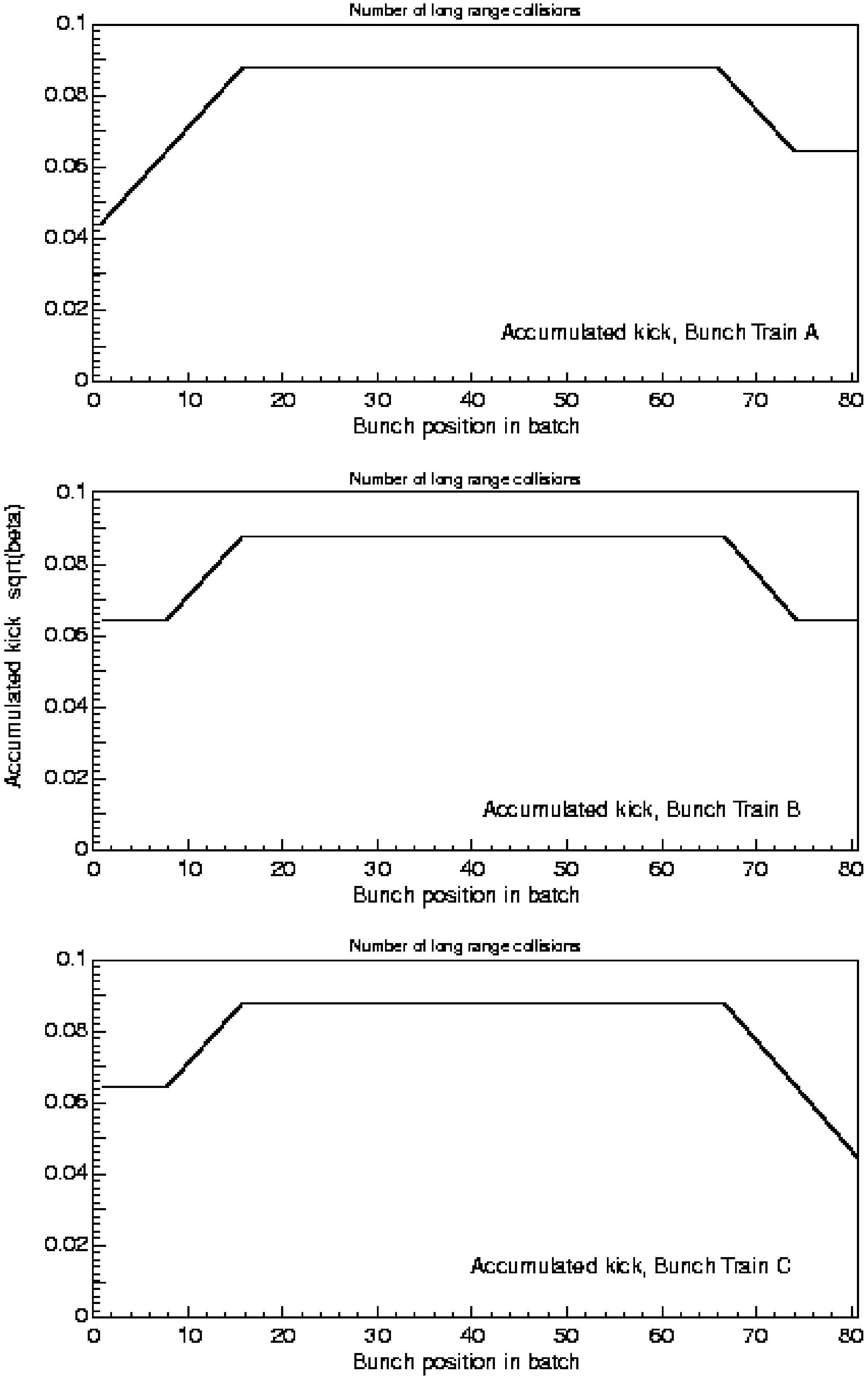

Fig. II.4.8.2-3. The distribution of the accumulated kick from long-range beam-beam interactions along a bunch train.

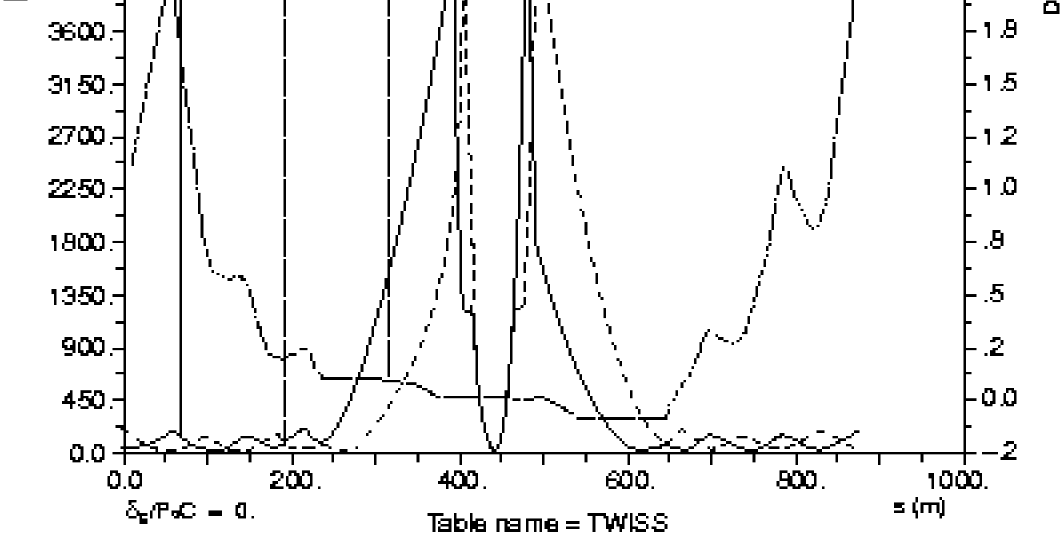

The propo
closed orbit de
compensate fo
must be locate
arc quadrupole
independent co
an average val
closed orbit er
show the layou

Fig. II.4.8.2-5. Schematic layout of components around IP1.

Fig. II.4.8.2-7. Lattice functions around IP1 when β* = 0.5 m.

Fig. II.4.8.2-9 shows the proposed correction system. The product of bunch current and transverse position of each bunch is measured and digitized at the full bunch rate of

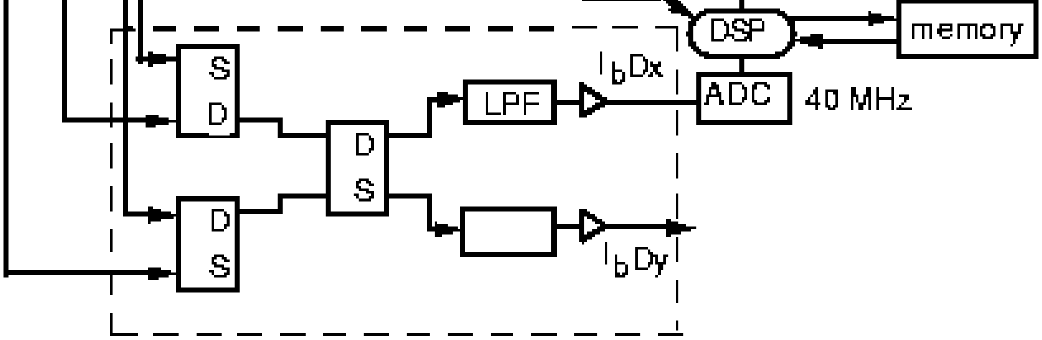

40 MHz. T and is used This proces determined characterist effects of coherent bunch oscillations. A corrective bump is calculated independently for each bunch from the value of its position stored in memory, and is sent to each of the kickers with an appropriate phase and amplitude. The system is designed to hold its output signal level until the next populated bucket arrives.

Fig. II.4.8.2-9. Schematic of the proposed fast closed-orbit correction scheme.

Bandwidth requirements are determined by the necessity to respond within the time period of the PACMAN bunches, about 400 ns, and the settling time thereafter. A bandwidth of 2.5 MHz will probably be sufficient, but actual bandwidth may be determined by the availability of power amplifiers, and requires further consideration.

Significant advantages in power requirements are obtained by constructing the kick signal as a modulation about an average of zero. The variation between minimum and maximum angular kicks is estimated to be 0.16 mrad, based on the information represented by Fig. II.4.8.2-1 and Fig. II.4.8.2-3. The power requirement for the kickers is independent of β if the kicker aperture is scaled with the square root of β for a given angular deflection. The shunt impedance of a strip-line electromagnetic kicker is high, and increases with the length of the structure. Fig. II.4.8.2-11 shows the shunt impedance versus frequency for such a kicker, using a length of 10 m for illustrative purposes. Four 6 kW power amplifiers are required to drive two such kickers on either side of an IP. A further set of power amplifiers is required for the second beam, and additional duplication is needed for the vertical plane.

Fig. II.4.8.2-11. Shunt impedance versus frequency for a typical strip-line kicker.

II.4.8.2.2 Summary of future work

The following topics will be investigated:

(1) Assess the practical extent to which the closed-orbit distortion can be minimized by appropriate phasing between IPs, and update the feedback-kicker system design accordingly

(2) Examine kicker aperture requirements (for injected beam).

(3) Examine possible alternate kicker locations.

(4) Investigate crossing angle in both planes.

(5) Investigate the possibility of having one system to damp effects of all IPs.

(6) Investigate cross-talk between IPs.

II.4.8.3 Beam collimation

In collision mode, it is estimated that 2.4 x 10^9 protons per second leave the stable central core of each beam at nominal luminosities. This halo must be removed with a dedicated beam cleaning system embedded in the lattice, in order for the LHC design performance to be achieved [137 - 141]. At the beginning of the acceleration ramp, about 5% of the beam (1.4 x 10^{13} protons) may be lost in as little as 0.2 seconds, even under good operational conditions [142]. If these losses are sufficiently localized they can cause a magnet quench. Even if they are not highly localized, such losses can cause serious problems for the cryogenic system, and for the lifetime of accelerator components. Detector components may also be subject to undesirable levels of irradiation at injection

The beam loss distribution around the entire machine needs to be evaluated in all these scenarios, with particular attention paid to the two high luminosity insertions.

II.4.8.3.1 Preliminary simulation results

Preliminary Monte-Carlo simulations have been performed, including a model for beam halo interactions with collimators and other components, multi-turn particle tracking, beam-gas scattering, and hadronic and electromagnetic shower simulations, using the MARS code [109]. In accordance with the nominal LHC plan, the model included a betatron cleaning system in IR3 and a momentum cleaning system in IR7 [83].

The high energy physics of collisions at IP1 and IP5 and interactions of the beam halo with primary collimators were modeled using the DPMJET and STRUCT codes, respectively [108, 143]. Shower simulations in the IRs and arc components took into account all the lattice details, including the three-dimensional geometry and material and magnetic field descriptions. This enabled energy deposition distributions in the machine components and particle fluxes in the CMS and ATLAS detectors to be calculated.

Primary and secondary collimators were set at displacements of 6σ and 7σ, respectively. Under these conditions the momentum cleaning system in IR7 intercepts approximately 10^9 protons per second, and the beam cleaning system contributes about 10% to the total heat load in the inner triplet components [117]. A comparison of primary collimators constructed from different materials showed that beryllium and graphite have great advantages compared to tungsten, with loss rates almost an order of magnitude lower in the superconducting magnets. Although loss rates are about 60% larger than with beryllium, pyrolytic graphite might still be considered for use in the primary collimators, taking into consideration alignment and safety issues.

A preliminary study was also performed with the collimators slightly withdrawn – with the primaries placed at 7σ and the secondaries at 8.2σ. Large amplitude particles that escape from the cleaning system are able to circulate without hitting the aperture in the cold part of the machine, before being captured by the collimators on later turns. Fig. II.4.8.3-1 shows that the tails of this halo extend up to about 10σ. Fig. II.4.8.3-3 shows the distribution of hits on the primary collimators, when a skew collimator is used to intercept the "corner" halo protons. Preliminary indications are that the beam cleaning system still defines the geometric aperture of the LHC, even with the collimators partially withdrawn.

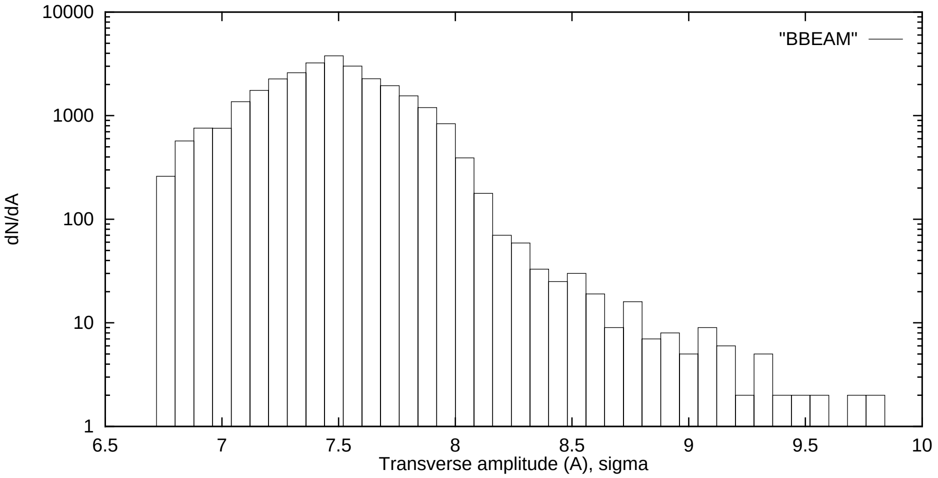

Fig. II.4.8.3-1. Tail distribution of halo particles that have temporarily escaped from the beam cleaning system.

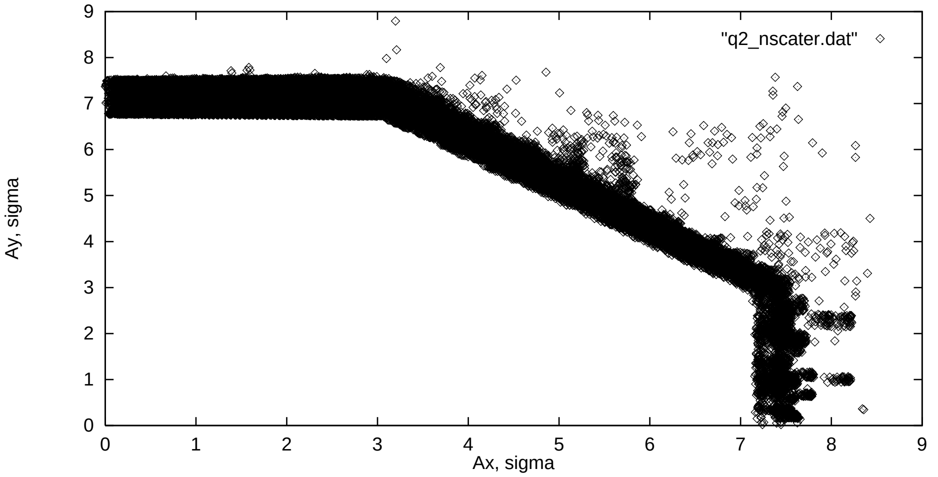

Fig. II.4.8.3-3. Distribution of hits on the primary collimators, with primary and secondary collimators partially withdrawn.

II.4.8.3.2 Summary of future work

Further simulation will be performed to finalize the collimation design results. As the lattice evolves, simulations will occasionally be made to revalidate the collimator design.

II.4.8.4 Software maintenance and development

The CERN tracking codes MAD and SIXTRACK are maintained on US lab computers, as well as standard US tracking codes such as TEAPOT and COSY. Tracking studies will be performed using these codes, and others, in order to perform direct and indirect comparisons.

The C++ version of TEAPOT incorporates an object template that can be instantiated either to reproduce the original thin element functionality of TEAPOT, or to use a differential algebra (DA) integrator [144]. TEAPOT is the major part of a larger Unified Accelerator Libraries (UAL) environment that is constructed so that it can share its common data structures and services with other codes. UAL also includes DA, Survey, and other data structures. UAL is under continuing development in an ongoing collaboration between Cornell University and BNL [145].

UAL uses an accelerator model that includes realistic errors and corrector settings, in the Standard Machine Format (SMF). An SMF parser developed for MAD format files allows the automatic generation of SMF input structures (without errors or corrections) based on standard CERN releases of LHC design optics. This SMF description of the LHC allows tracking to proceed with SMF compliant codes like TEAPOT. It also allows magnet errors to be attached to the model from lists of expected harmonics or from magnet measurement databases. LHC optics model files will be generated in the SMF input format, complete with all the standard errors and imperfections.

A group of physicists from Michigan State University is developing a model of the LHC lattice with detailed end field information. A converter from the MAD9 format to COSY has been completed and tested. Preliminary result shows that quadrupole fringe field has a sizable effect on the tune shift with amplitude. In collaboration with magnet builders at FNAL, they are working on obtaining the field map directly from the coil using differential algebraic techniques.

II.4.8.4.1 Standard Exchange File

Significant efforts are being expended to ensure that there is good data communication between CERN and among the US-LHC institutions. Of primary importance is the lattice description file. A Standard Exchange File lattice format is under active discussion. Tentative agreement on a preliminary format was reached at the “UAL/LHC” mini-workshop that was held at BNL in February 1998. The CERN DOOM database will also be used at several US sites and at CERN, to maintain two way communications between files in this format and standard CERN codes. In this way the unique features of a particular analysis code, or correction algorithm, will be shared among others, without the unnecessary duplication of software development effort.

The existence of a fully instantiated “machine” file in a standard format allows for corrections and other manipulations to be applied through stand alone code “filters” [145, 146]. Used in this sense, a filter is a piece of code that reads in a machine file, performs an operation upon it (such as simulating the insertion of tuning shims) and then writes out a modified machine file. LHC specific “IR filters” are being developed to generate off-axis closed orbits under non-zero crossing angles, to simulate tuning shim performance with expected measurement uncertainty and quench/thermal-cycle dependence, to simulate local IR corrections, et cetera. All filters will use a Standard Exchange File interface.

Standard LHC descriptions will be maintained and made freely available, so that compliant codes may connect with detailed and realistic LHC models.

II.4.8.4.2 Summary of future work

Good data communication will be established between the US labs and CERN, and between accelerator physicists and the magnet designers, using both real and simulated data.

Standard Exchange Files will be developed and shared for use by analysis and tracking codes including TEAPOT and COSY, as well as standard CERN codes via the DOOM database. Based on this flat, instantiated file, US-LHC specific procedures including shimming simulation and corrector strength setting will be evaluated. Appropriate filters will be developed.

Code benchmarks will be developed to be able to compare different codes. A list of “standard” calculations will be developed so that, as the magnet design and lattices evolve, the same calculation results can be made and compared.

II.4.8.5 Local chromaticity correction

The peak β functions in the inner triplet of the LHC are about 4.5 km when β^* is 0.5 m in collision optics. Each such IR generates a natural linear chromaticity ($dQ/d\delta$) of about –30, equal in both planes due to the anti-symmetric powering of the quadrupoles. When all four IRs have a β^* of 0.5 m the linear chromaticity of the entire ring is about -200, with the IRs being responsible for more than half of the total. The characteristic second order chromaticity ($d^2Q/d\delta^2$) of each low-beta insertion is about 3×10^3 and the third order coefficient is less than the second order.

The nominal LHC chromaticity correction scheme employs four families of sextupoles (two per plane) in a regular and global distribution in the arc octants [147]. For comparison purposes, preliminary studies have been conducted that consider local approaches to both linear and second order chromaticity corrections.

In the simplest local scheme for canceling linear chromaticity, 2π-pairs of sextupoles are established in the arc cells closest to the IR. The resulting sextupole strengths are unrealistic. An optical insert that raises the beta functions at local sextupoles to about 1 km has also been tried. Although sextupole strengths are then reduced to nominal values, the insertion proves difficult to impose on the existing lattice structure, requiring either quadrupole moves or quadrupole strength increases of as much as 50%. This approach is not practical and has been abandoned in favor of global correction of linear chromaticity.

A local correction scheme for second-order chromaticity has also been simulated on top of version 5.0 optics, and its impact on the momentum aperture has been studied [148]. Ideally, such a scheme would enable a more accurate operational determination of the linear chromaticity, and also would increase the momentum aperture.

Second order correction is more complicated than simply establishing local sextupoles. Additional optical considerations play a significant role, including correctly setting the phase advance between IPs, and the global tunes. Second-order chromaticity is particularly sensitive to phases and the use of sextupoles in π pairs. The first step in creating an effective local correction scheme is to properly phase sextupole families with respect to the IP and the final-focus triplet by adjusting the strengths of matching and trim quadrupoles (Q4-Q7 and QT8-QT11). Given the 90 degree phase advance across an arc module, the existing sextupoles then divide naturally into two families per plane: those nπ from the IP and those (2n+1)π/2 from the IP.

Although both families are equally effective in canceling linear chromaticity, only the latter family of sextupoles is effective in correcting second-order chromaticity. Furthermore, members of the nπ set which interleave the (2n+1)π/2 local correction pair must be turned off, because powered interleaving would disrupt the "aberration-free" geometry of the correction. On the other hand, since the beta functions are sufficiently disparate in version 5.0 optics, sextupoles for opposite planes may be successfully interleaved with little cross correlation. Sextupoles outside the local correction section are used to cancel the linear chromaticity.

It proves difficult to correct the vertical second order chromaticity in this scheme, due to the coherent vertical phasing of the four IPs in collision optics. One way to avoid this difficulty is to change the vertical tune while holding the horizontal tune constant. If this is done, and the first and second order chromaticities are reduced to zero, the tuneshift versus momentum dependence with four IRs in collision mode (with a β^* of 0.5 m) is equivalent to the use of global chromaticity correction when only IP1 and IP5 are in collision mode [149].

Studies so far conclude that the second-order chromaticity can be locally corrected without generating higher-order aberrations. If lower β^* values are implemented (for example, in a 0.25 m upgrade), local chromaticity correction will probably prove to be important, especially to the momentum aperture.

II.4.8.5.1 Summary of future work

Chromatic correction and other momentum dependent effects will be studied as the LHC lattice evolves.

II.4.8.6 Ground motion and external noise

Time-varying alignment and field fluctuations in the hundreds of magnets that comprise the LHC may seriously affect proper machine operation. This is especially true of magnets in the interaction regions, where the beta functions become very large in collision optics. One can distinguish two mechanisms of beam perturbation in circular accelerators, depending on the frequency regime [149]. Processes that are slow with respect to the revolution period produce closed orbit distortions [150]. Rapid fluctuations cause direct emittance growth. Since the LHC revolution frequency is much lower than in all other existing hadron accelerators, and since numerous natural noise sources grow rapidly in strength as the frequency is decreased, fluctuations may dramatically influence beam dynamics.

Investigations into ground motion and external noise in the LHC will be performed using both analytical and experimental tools. The goal of the investigations is the thorough evaluation of the impact that noise sources like ground motion and dipole field fluctuations, et cetera, have on beam dynamics. This includes making estimates of noise spectrum tolerances, and specifying parameters for possible emittance preservation and closed orbit correction feedback systems.

The primary sources of emittance growth are quadrupole jitter (misalignment fluctuations) and high-frequency variations of the bending magnetic field in dipoles. Both sources produce angular kicks and excite coherent betatron oscillations. If this coherent motion is not damped then filamentation or dilution processes due to tune spread within the beam eventually transform them into emittance increases. Transverse feedback allows such emittance growth to be suppressed by damping out the coherent oscillations before filamentation has time to set in - the oscillations should be damped much faster than their decoherence time.

II.4.8.6.1 Future analytical studies

Analytical studies will be pursued in the following areas:

1) Recent accelerator alignment studies at SLAC and Japan show that alignment error statistics may be far from Gaussian, with distributions more like power laws, presumably due to both human and natural factors [151, 152]. Such distributions often have no finite variance value, and demonstrate a significant probability for many-sigma outliers. They can cause difficulties with LHC re-alignment.

2) The applicability of beam-based alignment techniques.

3) Emittance growth rate calculations, which lead to the ability to set tolerances on external noise sources such as ground motion and dipole magnetic field fluctuations due to ripple and liquid helium flow.

4) Requirements for possible transverse feedback systems, including bandwidth, number of pick-ups and kickers, power, and tolerance to pick-up and amplifier noise.

5) Tolerances on orbit jitter in a frequency band from 1 to 100 Hz. Calculate vibration amplitude limits for arc and IR quads. Study designs for feedback systems for orbit correction and stabilization.

6) Address alignment issues at time scales from 1 hour to 10 years, making comparison of tolerances with existing data. Estimate long-term stabilization scheme parameters, such as the number of correctors, strength, location, et cetera.

7) Evaluate mechanical resonances in the design of the LHC inner triplet integrated cryostat structure. If appropriate, make recommendations for possible modifications in the support design

II.4.8.6.2 Future experimental studies

Some experimental studies (for example, of the temporal stability of the magnet alignments) cannot yet be performed at CERN, due the absence of installed superconducting magnets. Nonetheless, they can be performed on the Tevatron and/or RHIC. In addition to being of great importance for the LHC, these experimental topics are also of interest to the Tevatron and RHIC, and for future hadron colliders in general. Experimental topics for study include:

1) Measure ground motion in the frequency band from 0.01 Hz to 5 kHz in the tunnel of a working machine. Focus in particular on the frequency band from 0.1 Hz to 200 Hz. Measure the motion of arc and IR dipole magnets and quadrupoles in the same frequency bands.

2) Test the conventional assumption that quadrupole jitter is mostly uncorrelated between magnets. Measure the correlation of magnet motion in a frequency band from 0.1 to 5 kHz with 0 to 500 m spacing between magnets. Focus in particular on the frequency band from 0.1 Hz to 200 Hz.

3) Search for temporal correlations between particle loss rates and closed orbit fluctuations, magnet vibrations, and ground motion. Focus in particular on the motion of the IR quads.

4) Perform a “beam heating” experiment in transverse and longitudinal by deliberately introducing controlled noise sources. Compare with theoretical predictions and derive recommendations for the LHC.

5) Study of long-term ground motion drifts with a hydrostatic level system at the Tevatron, to determine the constant *A* in the “ATL law” [153].

II.4.8.6.2.1 References

[83] *LHC Conceptual Design*, CERN/AC/95-05, CERN, 1995.

[84] LHC lattice, Version 5.0, CERN, 1997.

[85] CERN/LHC 97-45, CERN, 1997.

[86] J. Wei, *LHC Preliminary IR analysis and compensation schemes,* RHIC/AP/130, BNL, 1997.

[87] G. Sabbi, *HGQ_9711 field quality table,* TD-97-050, FNAL, November 1997.

[88] S. Caspi, K. Chow, *Normal and skew multipoles in the LHC low beta quad - Rev. 1*, SC-MAG-577, LBL, February 1997.

[89] G. Sabbi, *End field analysis of HGQ model S02,* Fermilab TD-97-045, October 1997.

[90] G. Sabbi, *Magnetic field analysis of HGQ coil ends,* Fermilab-TD-97-040, September 1997.

[91] J. Wei, *Error compensation in insertion-region magnets*, Particle Accelerators, **55**:439-448, Montreux proceedings, 1996.

[92] J. Wei and R. Talman, *Theorem on magnet fringe field*, Particle Accelerators, **55**:339-344, Montreux proceedings, 1996.

[93] R. Ostojic et al., *Systems layout of the low-*β *insertions for the LHC experiments,* PAC, Vancouver, May 1997.

[94] R. Ostojic and T. Taylor, *Proposal for an improved optical and systems design of the LHC low-*β *triplets*, CERN AT/94-38 (MA), November 1994.

[95] J. Wei, *Preliminary IR analysis and compensation schemes*, US-LHC TeleVideo Conference, July 14, 1997.

[96] R. Gupta, *Estimating and adjusting field quality in superconducting accelerator magnets,* Particle Accelerators, **55**:375-386, Montreux proceedings, 1996.

[97] R. Gupta et al., *Tuning shims for high field quality in superconducting magnets*, MT-14, Finland, June 1995.

[98] G. Sabbi, *HGQ magnetic shim performance,* Fermilab TD-97-054, December 1997.

[99] S. Peggs, *Report of the interaction region working group*, Workshop on Future Hadron Facilities in the US, Bloomington, Indiana, July 1994.

[100] A. Jain, *Expected harmonics version 1.0 for BNL built LHC dipoles*, RHIC/AP/147, February 1998.

[101] J. Wei et al., *Misalignment evaluation of superconducting magnets in RHIC*, EPAC, Barcelona, 2222-2224, 1996.

[102] S. Weisz, *Alignment of the low-*β *quadrupoles,* LHC Project Note 59, 1996.

[103] A. Verdier and S. Weisz, *Alignment of low-*β *insertion with beam*, CERN-SL-Note 95/118 (AP), November 1995.

[104] J-P Quesnel, private communications.

[105] D. Missiaen, *Metrology of superconducting magnets: LHC test string first experience*, Proc. 4th Int. Workshop on Accelerator Alignment, p 221, November 1995.

[106] S. Peggs, *Feedback between accelerator physicists and magnet builders*, Particle Accelerators, **55**:83-92 Montreux proceedings, 1996.

[107] J. Wei et al., *Field quality evaluation of the superconducting magnets for the Relativistic Heavy Ion Collider*, pp 461-463, PAC, Dallas, 1995.

[108] J. Ranft, Phys. Rev. D51, 64, 1995.

[109] N.V. Mokhov, *The MARS code system user guide*, Version 13(95), Fermilab-FN-628, 1995.

[110] A. Morsch et al., *Progress in the systems design of the inner triplet of 70 mm aperture quadrupoles for the LHC low-beta insertions*, EPAC, London, 1994.

[111] N.V. Mokhov, *Accelerator/experiment interface at hadron holliders: energy deposition in the IR components and machine related background to detectors*, Fermilab-Pub-94/085, 1994.

[112] N.V. Mokhov and G.R. Stevenson, *Radiation considerations in the design of the neutral dump close to LHC interaction regions*, CERN/TIS-RP/IR/94-17, 1994.

[113] N.V. Mokhov and J.B. Strait, *Optimization of the LHC interaction region with respect to beam-induced energy deposition*, EPAC, Barselona, and Fermilab-Conf-96/136, 1996.

[114] N.V. Mokhov and J.B. Strait, *Towards the optimal LHC interaction region: beam-induced energy deposition*, PAC, Vancouver, 1997.

[115] L. Burnod et al., *Thermal modelling of the LHC dipoles functioning in superfluid helium*, EPAC, London, 1994.

[116] R. Bossert et al., *Development of a high gradient quadrupole for the LHC interaction regions*, IEEE Trans. Appl. Superconductivity **7**, 1997.

[117] A.I. Drozhdin et al., *NIM A381*, 531, 1996.

[118] J.B. Strait, *Geometric apertures and internal absorbers in the LHC inner triplet*, Fermilab TD-97-026, July 1997.

[119] A.I. Drozhdin and N.V.Mokhov, *Geometric aperture in LHC for collision conditions*, Fermilab, July 1997.

[120] L. Vos, *Ground motion in LEP and LHC*, PAC, Dallas, p. 3367, 1995.

[121] S. van der Meer, *Calibration of the effective beam height in the ISR*, CERN, ISR, PO/68-31, 1968.

[122] H. Jostlein, *Automatic beam centering at the SSC interaction regions*, Fermilab, TM-1253, 1984.

[123] K. Potter, *Luminosity measurements and calculations*, Proc. CERN Acc. School, CERN 94-01, vol. 1, p. 117, 1994.

[124] W.C. Turner, report in preparation.

[125] M. Izawa et al., *The vertical instability in a positron bunched beam*, Phys. Rev. Lett. 74 (25) p. 5044, 1995.

[126] J.T. Rogers, *Photoemission instabilities: theory and experiment*, CBN 97-26 and PAC, Vancouver, 1997.

[127] K. Ohmi, *Beam photo-electron interactions in positron storage rings*, Phys. Rev. Lett. 75 (8), p. 1526, 1995.

[128] M. A. Furman and G. R. Lambertson, *The electron-cloud instability in PEP-II: an update*, LBNL-40256/CBPNote-224/PEP-II AP note 97.07, PAC, Vancouver, 1997.

[129] Z.Y. Guo et al., *The experimental study on beam-photoelectron instability in BEPC*, PAC, Vancouver, 1997.

[130] F. Zimmermann, *A simulation study of electron-cloud instability and beam-induced multipacting in the LHC*, LHC Project Report 95, 1997.

[131] O. Grobner, *Beam-induced multipacting*, PAC, Vancouver,1997.

[132] O.S. Bruning, *Simulations for the beam-induced electron cloud in the LHC liner*, LHC project note 102, 1997.

[133] S. Berg, *Energy gain in an electron cloud during the passage of a bunch*, LHC project note 97, 1997.

[134] I. Collins and O. Grobner, private communication.

[135] W. Herr, *Effects of PACMAN bunches in the LHC*, LHC Project Report 39, 1996.

[136] P. Morton and J. Schonfeld, *Long range beam-beam effects,* p 54, Acc. Physics issues for an SSC, UM HE 84-1, Ann Arbor, December 1983.

[137] L. Burnod and J.B. Jeanneret, *Beam losses and collimation in the LHC: a quantitative approach*, CERN SL/91-39 (EA), LHC Note 167, 1991.

[138] P.J. Bryant and E. Klein, *The design of betatron and momentum collimation systems*, CERN SL/92-40 (AP), 1992.

[139] T. Trenkler and J.B. Jeanneret, *The principles of two stage betatron and momentum collimation in circular accelerators*, CERN SL/95-03 (AP), LHC Note 312, 1995.

[140] M. Maslov et al., *The SSC beam scraper system*, SSCL-484, 1991.

[141] A. Drozhdin et al., *Toward design of the collider beam collimation system*, SSCL-Preprint-555, 1994.

[142] J.B. Jeanneret, CERN, SL/Note 92-56(EH), 1992.

[143] I. Baishev et al., *STRUCT program user's reference manual*, SSCL-MAN-0034, 1994.

[144] N. Malitsky, private communication, Cornell University, 1997.

[145] F. Pilat et al., *Summary of mini-workshop on UAL and CESR, LHC, RHIC Lattice Description*, RHIC/AP/131, BNL 1997.

[146] R. Talman, private communication, Cornell University, 1997.

[147] F. Schmidt, *Strength requirements for the arc sextupoles of LHC Version 4.1*, LHC Project Note 38, 1994.

[148] C. Johnstone, *Local chromaticity correction of the LHC*, PAC, Vancouver, 1997.

[149] A. Verdier, *Phase between IPs and nonlinear chromaticity*, LHC Project Note 103, 1997.

[150] V. Lebedev et al., *Emittance growth due to noise and its suppression with the feedback system in large hadron colliders*, Particle Accelerators, Vol. 44, No. 3-4, p. 147, 1994.

[151] R. Pitthan, *Realignment: it is the tunnel floor which moves, isn't it*?, Proc. of IV Int. Work. on Accel. Alignment, KEK Proceedings 95-12 p. 382, 1995.

[152] V. Shiltsev, *17-years of hydrostatic level measurements at Sazare mine*, private communication, 1995.

[153] V. Shiltsev, *Space-time ground diffusion: the ATL law for accelerators*, Proc. of IV Int. Work. on Accel. Alignment, KEK Proceedings 95-12 p. 352, 1995.